Stable isotope investigations of atmospheric nitrous oxide

Dissertation

zur Erlangung des Grades
„Doktor der Naturwissenschaften“

am Fachbereich Chemie
der Johannes Gutenberg-Universität
in Mainz

Jan Kaiser
geb. in Hamburg

Mainz, 2002

This thesis is also available as a book from Verlag Dr. Hut, München, www.dr.hut-verlag.de (ISBN 3-934767-90-7).

Datum der mündlichen Prüfung: 1. Oktober 2002

This thesis is also available as a book from Verlag Dr. Hut, München, www.dr.hut-verlag.de (ISBN 3-934767-90-7).

Abstract

The analysis of isotope ratios is of increasing importance to study the sources and sinks of atmospheric trace gases and to investigate their chemical reaction pathways. Nitrous oxide (N_2O) has four mono-substituted rare isotopic species: $^{14}N^{15}N^{16}O$, $^{15}N^{14}N^{16}O$, $^{14}N_2{}^{17}O$ and $^{14}N_2{}^{18}O$. Mass-spectrometric measurement techniques have been developed during the work described here which enable a complete characterisation of abundance variations of these species. The hitherto most comprehensive account of these variations in the troposphere and stratosphere is given and interpreted in detail with reference to a suite of laboratory experiments.

The laboratory experiments represent a major part of this thesis and focus on the isotopic fractionation of N_2O in its stratospheric sink reactions, i.e. ultraviolet photolysis and reaction with electronically excited oxygen atoms, $O(^1D)$. These processes are of dominant influence for the isotopic composition of atmospheric N_2O. Parameters of potential importance such as temperature and pressure variations as well as wavelength changes in case of UV photolysis were considered. Photolysis at stratospherically relevant wavelengths >190 nm invariably showed enrichments in ^{15}N at both nitrogen atoms of the residual N_2O as well as in ^{17}O and ^{18}O. Enrichments were significantly larger for the central N atom than for the terminal N (with intermediate values for ^{18}O) and increased towards longer wavelengths and colder temperatures. For the first time, isotopic depletions were noted for ^{18}O and ^{15}N at the terminal nitrogen site in N_2O photolysis at 185 nm. In contrast, the second important N_2O sink, reaction with $O(^1D)$, causes comparatively smaller isotopic enrichments in stratospheric N_2O. However, its position-dependent fractionation pattern is directly opposite to the one in photolysis corresponding to larger enrichments at the terminal N atom. Hence, both sink processes leave distinct isotope signatures in stratospheric N_2O. Further N_2O photolysis experiments showed that $^{15}N_2{}^{16}O$ is most likely to be present in the atmosphere at its statistically dictated abundance.

Small stratospheric samples required adaptation of mass-spectrometric methods to continuous-flow techniques which were also used for measurements on firn air samples from two Antarctic locations. The firn air "archive" allowed to determine present trend and pre-industrial values of the tropospheric N_2O isotope signature. A global N_2O isotope budget constructed therefrom is in line with current best estimates of total N_2O emissions from soils and oceans.

^{17}O measurements confirmed the presence of an oxygen isotope anomaly in atmospheric N_2O, but also showed that N_2O photolysis enriches oxygen isotopes according to a mass-dependent fractionation law. A tropospheric origin for part of the ^{17}O excess was proposed due to reaction of NH_2 with NO_2 which transfers the oxygen isotope anomaly of O_3 via NO_2 to N_2O.

This thesis is also available as a book from Verlag Dr. Hut, München, www.dr.hut-verlag.de (ISBN 3-934767-90-7).

Table of contents

List of abbreviations and symbols[1]

D	diffusion coefficient
DML	Dronning Maud Land, Antarctica
Dome C	Dome Concordia, Antarctica
ECD	electron capture detector
eqn.	equation
FTIR	Fourier transform infrared (spectroscopy)
FWHM	full width at half maximum
F	flux
GC	gas chromatography/gas-chromatographic
HP	Hermite propagation
h	Planck constant ($6.626 \cdot 10^{-34}$ Js)
I	moment of inertia; ion current
IPCC	International Panel on Climate Change
k	rate constant
k_B	Boltzmann constant ($1.381 \cdot 10^{-23}$ J/K)
K	equilibrium constant
L	loss/sink of N_2O
m	mass; mass number
m/z	mass to charge ratio
M	molar mass
MS	mass spectrometry/mass-spectrometric
n	number of analyses
N	number (of molecules, etc.)
p	pressure
P	production/source of N_2O
Q	partition function
r	correlation coefficient
R	isotope ratio
SAR	Second IPCC Assessment Report
T	temperature (in K)
TAR	Third IPCC Assessment Report
UV	ultraviolet
PDB	Pee Dee Belemnite
RDT	Russian doll trap
SATP	Standard Ambient Temperature and Pressure ($T = 298.15$ K; $p = 10^5$ Pa = 1 bar)
SMOW	Standard Mean Ocean Water
STP	Standard Temperature and Pressure ($T = 273.15$ K; $p = 101325$ Pa)
v	velocity
VPDB	Vienna Pee Dee Belemnite
VSMOW	Vienna Standard Mean Ocean Water
VUV	vacuum ultraviolet
x	molar fraction
y	remaining fraction of substrate
z	charge number
ZPE	zero point energy

[1] Symbols used in a single section only are not included here and are explained rather at the appropriate location.

α	isotope fractionation factor
β	exponent in mass-dependent three-isotope fractionation laws
δ	isotope ratio relative to standard isotope ratio
γ	factor in approximate mass-dependent three-isotope fractionation laws
ε	isotope fractionation constant
Φ	quantum yield
η	ratio between $^{15}\varepsilon_1$ and $^{15}\varepsilon_2$ (fractionation constants of terminal and central N in N_2O)
λ	wavelength
μ	reduced mass; mixing ratio
ν	frequency
π	3.14159265358979...
θ	temperature (in °C)
σ	absorption cross section; symmetry number
τ	lifetime (of an atmospheric trace gas)
ξ	stoichiometric coefficient
ψ	ratio between $^{15}\varepsilon$ and $^{18}\varepsilon$ (fractionation constants of N and O in N_2O)

Preface

The isotopic composition of atmospheric traces gases provides unique information on their origin and their reactions in the atmosphere. Slight variations in the rate constants of production and destruction processes between isotopically substituted and unsubstituted species as well as changes in the isotopic composition of the source material give rise to small changes in the "isotopic fingerprint" of a specific compound which helps to trace its way through atmospheric trace gas cycles.

This thesis presents a comprehensive study of isotope techniques applied to nitrous oxide (N_2O), an important greenhouse gas and source of stratospheric NO_x. The emphasis of the work presented here lies on the detailed investigation of isotopic fractionation in the stratospheric sink reactions of N_2O, i.e. photolysis and reaction with excited oxygen atoms, $O(^1D)$, since the accompanying isotope effects influence the isotopic composition of the entire atmospheric N_2O reservoir. The position-dependent isotopic enrichments of ^{15}N ($^{15}N^{14}NO$ vs $^{14}N^{15}NO$) provide an additional unique characteristic of N_2O. Thus, the characterisation of the corresponding isotope effects in the stratospheric sink processes using laboratory experiments (chapters 3 to 5) as well as measurements of position-dependent isotope ratios in N_2O collected in the stratosphere (chapter 7) and N_2O from Antarctic firn (chapter 9) are essential parts of this thesis. A thorough understanding of the kinetic isotope effects in photolysis and reaction of N_2O with $O(^1D)$ was achieved which constitute crucial ingredients for global atmospheric models (section 7.3). From the firn air data, the present temporal isotope trends in tropospheric N_2O as well as its pre-industrial isotopic composition could be determined (chapter 9). Taking these data together with the stratospheric measurements, allows a characterisation of the present and pre-industrial average N_2O source signature (chapter 11) and a checking of the present understanding of the global N_2O cycle. Furthermore, a number of analytical advances were made in calibration of the N_2O working standard including its position-dependent isotope ratios which involved a revision of the underlying mathematical framework. Corrections for CO_2 interference with N_2O measurements were introduced and a novel technique to analyse ^{17}O isotope ratios in N_2O was developed (chapter 2). The improved precision of the analytical techniques showed the absence of significant variability in tropospheric N_2O isotope ratios (chapter 8). The oxygen isotope anomaly in tropospheric N_2O was confirmed and explained by a small *in situ* source of N_2O in the atmosphere which transfers the well-known O_3 anomaly to N_2O (chapter 10). Finally, we have investigated whether photolysis can induce a deviation from the statistical distribution of ^{15}N in atmospheric N_2O (chapter 6).

1 Introduction

1.1 N_2O in the atmosphere

Nitrous oxide (N_2O) plays two important roles in the atmosphere: In the troposphere, it acts mainly as a greenhouse gas, but is chemically almost inert, whereas its reaction with excited atomic oxygen, $O(^1D)$, represents the dominant source of nitrogen oxides (NO_x) in the stratosphere and regulates stratospheric O_3. These effects are expected to be reinforced in the future owing to the increase in atmospheric N_2O (Figure 1). The globally averaged surface mixing ratio has increased from about 270 nmol/mol in pre-industrial times (1750) to about 314 nmol/mol in 1998, and continues to grow at a current rate of (+0.8±0.2) nmol/(mol·a) or (+0.25±0.05) %/a [*Prather et al.*, 2001]. In view of an atmospheric lifetime of about 120 years, this leads to a perturbation of the total N_2O burden which will persist for centuries[2] even if the increase in emissions was stopped now. The increase was initially attributed to fossil fuel combustion, but estimates of this N_2O source were dramatically reduced after the discovery of a sampling artefact [*Muzio and Kramlich*, 1988]. From our present understanding of the global N_2O budget, none of the various sources can be held solely responsible for the rise in atmospheric concentration (Table 1). Plausible candidates are the increasing use of mineral nitrogen fertilisers in agriculture [*Kroeze et al.*, 1999] and deforestation in the tropics [*Matson et al.*, 1990]. In any case, the increase of N_2O (and other greenhouse gases) seems to be the consequence of anthropogenic perturbations to the global environment. The quasi-exponential expansion of the impact of human activities on all scales in the industrial era led Crutzen [2002] to propose the term "Anthropocene" for a new geological epoch beginning around the second half of the 18th century.

The greenhouse effect due to N_2O was first mentioned by Yung *et al.* [1976]. It is caused by partial trapping of infrared radiation emitted at the earth's surface within the atmosphere. Recent estimates of the direct global warming potential of N_2O indicate that its radiative efficiency per molecule integrated over a time horizon of 100 years is 296 times that of CO_2 [*Ramaswamy et al.*, 2001]. Therefore, the increasing atmospheric N_2O burden has prompted concern, although N_2O is more than three orders of magnitude less abundant than CO_2, the most important anthropogenic greenhouse gas. According to the 2001 IPCC report, the increase of N_2O abundance

[2] Global atmospheric lifetime (*LT*) and perturbation lifetime (*PT*) are not necessarily identical. *LT* characterises the time required to turn over the global atmospheric burden and is defined by the ratio of burden and mean global sink for a gas in steady state. In contrast, *PT* refers to the effective duration of an N_2O addition, which may differ from *LT* in the presence of feedback effects [*Prather et al.*, 2001]. In the case of N_2O, *PT* is 5 % smaller than *LT*.

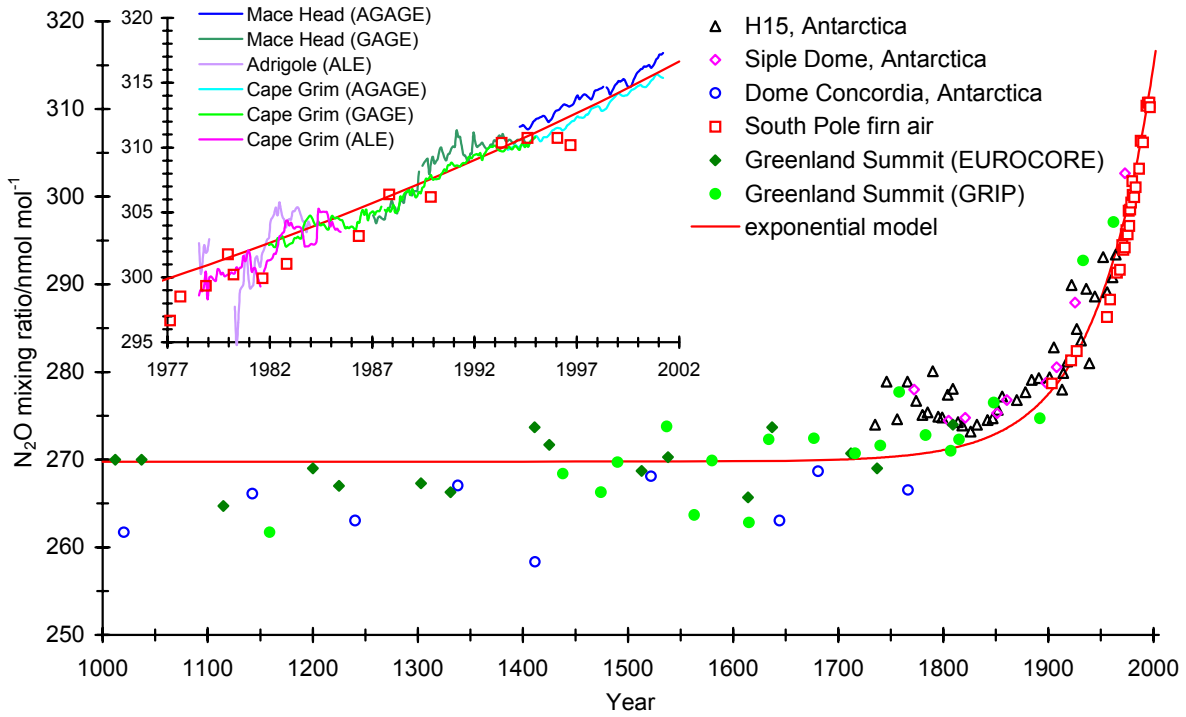

Figure 1: Changes in atmospheric N_2O abundance for the last 1000 years as determined from air trapped in ice cores, firn air, and whole air samples. Data are from Machida *et al.* [1995] (H15), Battle *et al.* [1996] (South Pole firn), Güllük *et al.* [1998] (Siple Dome), Flückiger *et al.* [1999; 2002] (Greenland Summit; Dome Concordia) and Prinn *et al.* [2000] (ALE, GAGE, AGAGE; monthly means from Mace Head (53°N), Adrigole (52°N) and Cape Grim (41°S); see http://cdiac.esd.ornl.gov/ndps/db1001.html). The exponential model was constrained by global mixing ratios of 270 and 315 nmol/mol in 1700 and 2000, respectively, and a growth rate of 0.8 nmol/mol/a in 2000 (see section 9.2 for details of the model).

caused about 0.15 W/m^2 or 6 % of the enhanced radiative forcing by well-mixed greenhouse gases from pre-industrial to present times (total +2.43 W/m^2). The remainder comprises contributions by CO_2 (1.46 W/m^2), CH_4 (0.48 W/m^2) and halocarbons (0.34 W/m^2).

Before the effect of N_2O on the radiative balance of the atmosphere was recognised, Crutzen [1970] had pointed out its importance for stratospheric chemistry. Photooxidation of N_2O is the major source of stratospheric NO_x ("active nitrogen") which is the main catalyst of gas-phase ozone destruction at altitudes between 25 and 40 km [*Brasseur et al.*, 1999]. However, NO_x can also mitigate ClO_x catalysed ozone loss by formation of the stable reservoir species chlorine nitrate ($ClONO_2$) from ClO and NO_2. These opposite effects make a prediction of the impact of rising N_2O levels on stratospheric ozone difficult [*Nevison and Holland*, 1997]. In the future though, stratospheric chlorine levels are expected to decrease thanks to the reduced emissions of organic halogen compounds as called for by the 1987 Montreal Protocol and its subsequent adjustments and amendments [*WMO*, 1999]. The continuing rise of N_2O will likely lead to an enhancement of the NO_x–O_3 destruction cycle. Because coupling to the Cl_x-O_3 destruction cycle

will become less important, the net effect of increasing N_2O is O_3 destruction [*Randeniya et al.*, 2002]. The importance of stratospheric O_3 is evident from its beneficial role in blocking most of the biologically harmful ultraviolet radiation (UV-B in the range $280\ nm < \lambda < 320\ nm$) to penetrate the atmosphere. In addition, the absorption of UV radiation by O_3 is responsible for the very existence of the stratosphere itself, since it represents a source of heat that causes the temperature to rise with altitude. Via the link to NO_x and O_3, increases in N_2O lead to enhanced UV light flux in the atmosphere and at the earth's surface. Note that this involves an interesting negative feedback (or self-healing effect), because N_2O is photolysed more rapidly in the stratosphere due to the enhanced UV light flux. As a consequence, the increase in N_2O mixing ratios is diminished [*Prather*, 1998].

In conclusion, both the role of N_2O as a greenhouse gas and as a source gas for stratospheric NO_x combined with its long atmospheric lifetime call for reductions of its anthropogenic emissions. N_2O is one of the target gases of the 1997 Kyoto Protocol which includes emission limitations and reduction commitments for greenhouse gases not controlled by the Montreal Protocol. A prerequisite for the implementation of efficient control strategies is a good understanding of its global atmospheric budget which is presented in the following section.

1.2 The global N_2O budget

Among the atmospheric nitrogen species, N_2O ranks second to molecular nitrogen (N_2). Despite the importance of N_2O outlined in the previous section, its budget is still not well quantified today (Table 1). Especially the errors in the individual source terms are large.

Two methodologies have been applied to estimate the global N_2O budget: One involves a "bottom-up" approach, the other uses "top-down" constraints. The bottom-up approach consists in summing up individual contributions from various sources and requires upscaling of local flux measurements to the global scale. In contrast, "top-down" constraints on the total N_2O source can be inferred, e.g., from the sum of global sink strength and rate of increase (trend). Thanks to the long lifetime of 120 years, seasonal cycles and inter-hemispheric gradients of N_2O are inconspicuous and only clearly defined in the AGAGE data obtained with improved analytical equipment during the last 6 years (Figure 1). Annually averaged mixing ratios at Mace Head (53°N) and Cape Grim (41°S) are only 1 nmol/mol apart. Therefore, measurements of N_2O mixing ratios at single locations can easily be extrapolated to the global scale, so that the increase of the global N_2O burden is the best known parameter of the N_2O budget. The sink strength can be calculated from photochemical models of the stratosphere [*Minschwaner et al.*, 1993]. Recent estimates from "bottom-up" studies [*Kroeze et al.*, 1999; *Mosier et al.*, 1998] coincide with the "top-down" con-

Table 1: Estimates of the global N_2O budget (Tg N/a)
(adapted from Prather *et al.* [2001] and Houghton *et al.* [1994])

References	Mosier *et al.* [1998] Kroeze *et al.* [1999]		Olivier *et al.* [1998]		SAR†		TAR‡
Base year	1994	range	1990	range	1980s	range	1990s
Sources							
Ocean	3.0	1–5	3.6	2.8–5.7	3	1–5	
Atmosphere (NH_3 oxidation)	0.6	0.3–1.2	0.6	0.3–1.2			
Tropical soils							
Wet forest	3.0	2.2–3.7			3	2.2–3.7	
Dry savannahs	1.0	0.5–2.2			1	0.5–2.0	
Temperate soils							
Forests	1.0	0.1–2.0			1	0.5–2.3	
Grasslands	1.0	0.5–2.0			1		
All soils			6.6	3.3–9.9			
Natural sub-total	9.6	4.6–15.9	10.8	6.4–16.8	9		
Agricultural soils	4.2	0.6–14.8	1.9	0.7–4.3	3.5	1.8–5.3	
Biomass burning	0.5	0.2–1.0	0.5	0.2–0.8	0.5	0.2–1.0	
Industrial sources	1.3	0.7–1.8	0.7	0.2–1.1	1.3	0.7–1.8	
Cattle and feedlots	2.1	0.6–3.1	1.0	0.2–2.0	0.4	0.2–0.5	
Anthropogenic sub-total	8.1	2.1–20.7	4.1	1.3–7.7	5.7		6.7*
Total sources	**17.7**	**6.7–36.6**	**14.9**	**7.7–24.5**	**14.7**	**10–17**	
Imbalance (trend)	**3.9**	**3.1–4.7**			**3.9**	**3.1–4.7**	**3.8**
Total sinks (stratospheric)	**12.3**	**9–16**			**12.3**	**9–16**	**12.6**
Implied total source	16.2				16.2		16.4

† Second IPCC Assessment Report [*Houghton et al.*, 1994]
‡ Third IPCC Assessment Report [*Prather et al.*, 2001]
* corrected according to IPCC Special Report on Emission Scenarios [*Nakicenovic et al.*, 2000]

straint and show that the global N_2O budget can be closed. Previous studies missed some of the impact of agriculture (especially livestock) on the global nitrogen cycle, so that in the Second IPCC Assessment Report (SAR) the best estimate of the total added source was 10 % short of the source implied by the sum of sinks and annual trend (Table 1).

1.2.1 N_2O sources

Natural N_2O is released predominantly by microbial nitrification and denitrification reactions in soils and waters. Biomass burning and industrial sources (combustion processes in power plants and vehicles, nitric acid and nylon production) represent minor anthropogenic sources, but the major share of anthropogenic perturbations is also made up by soil emissions. Well-known applications of N_2O as anaesthetic in medicine, aerosol propellant in canned whipped cream or

fuel gas in racing cars and flame absorption spectroscopy are of negligible importance for the global N_2O budget.

The attribution of individual emission rates to the various sources remains difficult, because of the wide temporal and spatial variability of the main sources, soils and oceans. The long lifetime of N_2O being a strength in the top-down approach is a weakness if it comes to the quantification of emissions: Flux estimates by flux-gradient-relations or eddy correlation techniques are problematic, because they rely on variations in the N_2O mixing ratio which are only small. Scaling-up of direct flux measurements to global dimensions is therefore difficult and entails large errors. A number of parameters influence the emission rates: For example, denitrification (dissimilatory reduction of NO_2^- or NO_3^- to N_2 and N_2O) is controlled by substrate availability, oxygen levels, carbon supply and temperature. Soil moisture and soil texture affect denitrification rates indirectly via their influence on oxygen levels. The proportioning between the obligatory intermediate N_2O and the end product N_2 is both sensitive to oxygen levels and relative supplies of substrate (NO_3^-) and reductant (organic carbon) [*Firestone and Davidson*, 1989]. Complex process-oriented models have been used to simulate relevant physico-chemical and biological processes in a mechanistic way [*Frolking et al.*, 1998], but are often adapted to specific environments only or suffer from large uncertainties in the required parameterisations. Moreover, the response to changes in natural parameters is not necessarily linear: N_2O emissions from tropical forests were shown to increase faster than external nitrogen inputs because the soil was already saturated with nitrogen [*Hall and Matson*, 1999].

Future N_2O emissions are likely to be affected by climate change due to rising temperatures and precipitation (which affects soil moisture content). Widespread use of mineral (artificial) and organic nitrogen fertilisers increases the nitrogen availability in agricultural soils leading to enhanced N_2O emissions [*Mosier et al.*, 1998]. Land-use changes in the tropics may also increase nitrogen losses to the atmosphere [*Matson and Vitousek*, 1990].

1.2.2 N_2O sinks

The established loss mechanisms for N_2O are stratospheric UV photolysis and reaction with electronically excited oxygen atoms, $O(^1D)$:

$$N_2O + h\nu \rightarrow N_2 + O(^1D) \qquad (185\ \text{nm} < \lambda < 230\ \text{nm}) \qquad (90\ \%) \qquad \text{(R1)}$$

$$N_2O + O(^1D) \rightarrow 2\ NO \qquad (6\ \%) \qquad \text{(R2)}$$

$$N_2O + O(^1D) \rightarrow N_2 + O_2 \qquad (4\ \%) \qquad \text{(R3)}$$

The percentages in brackets indicate the approximate relative shares of the individual reactions in the total global N_2O loss [*Minschwaner et al.*, 1993]. Reaction R2 represents the aforementioned major source of stratospheric NO_x. The reaction with $O(^1D)$ is often called "photooxida-

tion", since it involves photolysis of a $O(^1D)$ precursor (primarily ozone) and the subsequent oxidation of nitrous oxide by $O(^1D)$. However, strictly speaking, only the reaction channel to NO (R2) represents a true oxidation from a chemical point of view.

Soils and oceans have been proposed as N_2O sinks [*Cicerone*, 1989; *Elkins et al.*, 1978; *Ryden*, 1981], but these are usually accounted for in the net source term. Moreover, oceans and coastal waters are largely in equilibrium with the atmosphere or supersaturated with N_2O [*Bange et al.*, 1996; *Weiss*, 1981], so that a sink – if it exists – is likely to be small. Another suggested stratospheric destruction mechanism via $N_2O + O_2$ ($b\ ^1\Sigma_g^+$) [*Toumi*, 1993] has not been substantiated by measurements yet.

1.3 Isotope effects

Stable isotope based research in the earth sciences exploits subtle differences in reaction rate coefficients or equilibrium constants of chemical species that differ only in their isotopic composition, but are otherwise identical. These effects are denoted *kinetic isotope effects* if a reaction rate constant changes upon isotopic substitution, and *thermodynamic* (or *equilibrium*) *isotope effects* if the equilibrium constant is affected. Isotope effects can give rise to different isotope distributions of the same element in different substances or at non-equivalent positions within a single substance, and are called *intermolecular* or *intramolecular* isotope effects, respectively [*Müller*, 1994]. Often isotope effects are also referred to as *(isotope) fractionation* or *(isotope) discrimination*.

Many constituents of the earth's atmosphere, but also of the oceans, soils, ice sheets or the earth's crust, show characteristic variations of their isotopic composition which are caused by isotope effects. For elements heavier than hydrogen, these variations are of the order of 10^{-2} to 10^{-4} relative to the average isotopic composition on earth (see Table 2, p. 17, for an overview of isotope ratios of standard materials used for carbon, nitrogen and oxygen). Precise analytical measurements by mass spectrometry or infrared absorption spectroscopy allow to quantify these small differences. In a sense, this goes beyond the "traditional" view of chemistry which states that isotopically substituted molecules display the same chemical behaviour because their electron configuration is identical.

The differences in physico-chemical properties of isotopic compounds (i.e. chemical compounds consisting of molecules containing different isotopes of the same element [*Mook*, 2000]) are mainly due to the mass differences of the atomic nuclei. Hence, the translational, rotational and vibrational energy levels change and as a consequence also the partition functions. This causes heavier molecules to have lower mean velocities, lower collision frequencies and lower

zero point energies. Such changes at the molecular level appear as macroscopic isotope effects in a number of processes, for example

- chemical conversions
- isotope exchange reactions
- photolysis
- diffusion
- gravitational separation
- phase changes, such as evaporation, dissolution, etc.
- chromatography

According to the theory of Bigeleisen and Mayer [1947], isotope effects in exchange reactions and equilibrium processes are expected to vary regularly with mass. This theory of so-called "mass-dependent" isotope effects was extended later to kinetic reaction rates [*Bigeleisen*, 1949; *Bigeleisen and Wolfsberg*, 1958]. The details of these theories are not of interest here. We rather focus on the relations between fractionation laws for elements with three (or more) isotopes, especially oxygen (^{16}O, ^{17}O and ^{18}O). The Bigeleisen-Mayer theory predicts that ^{17}O/^{16}O fractionation effects are about half as large as for ^{18}O/^{16}O, but slight differences are expected for kinetic and equilibrium processes. In the following, we will briefly summarise the fractionation laws for mass-dependent isotope effects and then explain the nature of "mass-independent" isotope effects which give rise to anomalous isotope variations.

1.3.1 Equilibrium mass-dependent isotope fractionation

Isotope exchange between two species is an equilibrium process and can be written as

$$A^{l}X + B^{h}X \rightleftharpoons A^{h}X + B^{l}X$$

Superscripts *h* and *l* refer to the mass numbers of the isotope (16, 17 or 18 in the case of oxygen). In this example of monatomic exchange, the *fractionation factor* $\alpha_{A/B}$ between the two substances AX and BX is simply the ratio of equilibrium constants at a given temperature relative to the high temperature (classical) limit (K_∞), i.e.

$$\alpha_{A/B} = K / K_\infty = \frac{\dfrac{A^{h}X}{A^{l}X}}{\dfrac{B^{h}X}{B^{l}X}} = \frac{\mathcal{Q}(A^{h}X)\mathcal{Q}(B^{l}X)}{\mathcal{Q}(A^{l}X)\mathcal{Q}(B^{h}X)} \qquad (1)$$

where $\mathcal{Q}$ stands for the total partition function of the particular isotopologue. The partition function is defined as $\mathcal{Q} = \sum_n e^{-\varepsilon_n/(k_B T)}$ where the summation extends over all quantum states of energy ε_n (counting a *j*-fold degenerate level as *j* states). The total partition function for a gas-phase molecule is (at least approximately) separable in a product of partition functions for trans-

lation, rotation, vibration and electronic motion, i.e. $Q = Q_{\mathrm{trans}} Q_{\mathrm{rot}} Q_{\mathrm{vib}} Q_{\mathrm{el}}$. Separation of nuclear and electronic motion corresponds to the Born-Oppenheimer approximation which is justified by the fact that the heavy nuclei remain in a virtually fixed position while the electrons move. This is related to the assumption that the potential energy surface for the electronic ground state is the same for isotopically substituted molecules. Moreover, population of excited electronic states is usually negligible, so that Q_{el} cancels if we take partition function ratios [*Richet et al.*, 1977]. The separation of vibrational and rotational modes is valid if we treat the molecules as a rigid rotors.

Inserting Q_{trans}, Q_{rot} and Q_{vib} into partition function ratios of isotopically substituted molecules, for example $Q(\mathrm{A}^h\mathrm{X})/Q(\mathrm{A}^l\mathrm{X})$, results in simplified expressions compared to the original partition functions since constant factors cancel. Assuming that translational and rotational energy levels are closely spaced, integration of the corresponding partition functions is justified and the following expression for K can be derived for a diatomic molecule (one vibrational mode) [*Urey*, 1947; *White*, 2000]:

$$K = \prod_i \left(Q_{\mathrm{trans}} Q_{\mathrm{rot}} Q_{\mathrm{vib}}\right)^{\xi_i} = \prod_i \left(M_i^{3/2} \frac{I_i}{\sigma_i} \frac{e^{-h\nu_i/(2k_{\mathrm{B}}T)}}{1 - e^{-h\nu_i/(k_{\mathrm{B}}T)}} \right)^{\xi_i} \tag{2}$$

Symbols denote index of species participating in the exchange (i), stoichiometric coefficient (ξ), molar mass (M), moment of inertia (I), symmetry number (σ) and vibrational frequency (ν).

By applying the Teller-Redlich product rule [*Redlich*, 1935], this equation simplifies to:

$$K = \prod_i \left(m_i^{3/2} \frac{1}{\sigma_i} \frac{h\nu_i}{kT} \frac{e^{-h\nu_i/(2k_{\mathrm{B}}T)}}{1 - e^{-h\nu_i/(k_{\mathrm{B}}T)}} \right)^{\xi_i} \tag{3}$$

A similar expression can be derived for polyatomic molecules. The Teller-Redlich product rule is valid for harmonic oscillations and assumes equal force constants for isotopically substituted molecules. It states that the expression $\prod_{j=1}^{3n-6} \nu_j^2 \prod_{k=1}^{n} m_k \Big/ \left(M^3 I_{\mathrm{A}} I_{\mathrm{B}} I_{\mathrm{C}}\right)$ is invariant under isotopic substitution where indices j and k indicate vibrational mode and number of atom with n being the total number of atoms in the molecule and I_{A}, I_{B}, I_{C} being moments of inertia.

Bigeleisen and Mayer [1947] deduce an equation similar to (3) in a more informal way and split the ratio of partition functions for two isotopologues into a "quantum mechanical" part (f) arising from molecular vibrations and a "classical" part:

$$\frac{Q(\mathrm{A}^h\mathrm{X})}{Q(\mathrm{A}^l\mathrm{X})} = f \left(\frac{m_h}{m_l} \right)^{3/2} \tag{4}$$

Symmetry numbers have been omitted since they only represent the relative probabilities of forming symmetrical and unsymmetrical molecules and drop out in the final computation of

α from K and K_∞ (eqn. 1). The ratio of masses $(m_h/m_l)^{3/2}$ cancels for equilibrium constants in stoichiometrically balanced reactions, so that the fractionation factor is $\alpha_{A/B} = f(AX)/f(BX)$.

In the geochemical literature [*Fritz and Fontes*, 1980; *Hoefs*, 1997; *Mook*, 2000], l is usually identified with the light isotope (i.e., ^{16}O) whereas h stands for the heavy isotope (^{17}O and ^{18}O). We thus have two fractionation factors, $^{17}\alpha_{A/B}$ and $^{18}\alpha_{A/B}$. Following Urey [1947] and Bigeleisen [1955], it was shown that a simple relationship between $^{17}\alpha_{A/B}$ and $^{18}\alpha_{A/B}$ can be approximated starting from eqn. 3 [*Matsuhisa et al.*, 1978; *Weston*, 1999; *Young et al.*, 2002]:

$$\beta = \frac{\ln {}^{17}\alpha_{A/B}}{\ln {}^{18}\alpha_{A/B}} = \frac{1/m(^{16}O) - 1/m(^{17}O)}{1/m(^{16}O) - 1/m(^{18}O)} = 0.5305 \tag{5}$$

Eqn. 5 is rearranged to give $^{17}\alpha_{A/B} = (^{18}\alpha_{A/B})^{\beta}$. This relationship is valid for any oxygen species; the equilibrium value of β ("three-isotope exponent") is not sensitive to the masses of surrounding atoms. However, it relies on a number of assumptions made in the derivation of eqn. 5, e.g. high temperature ($T \geq 298$ K) or treating the molecular vibrations as harmonic oscillations so that the vibrational frequencies depend only on the masses of the isotopes. Detailed calculations have been made by Matsuhisa *et al.* [1978] for a number of reactions and temperatures giving a range of 0.520 to 0.531 for mass-dependent equilibrium reactions with molecules containing oxygen isotopes.

1.3.2 Kinetic mass-dependent isotope fractionation

In a first-order approach, kinetic isotope effects can be understood by classical mechanics and kinetic gas/collision theory: Molecules with heavier isotopes have lower average velocities ($\bar{v}$) at a given temperature and therefore lower collision frequencies and reaction rates. The Maxwell-Boltzmann velocity distribution gives

$$\bar{v} = \sqrt{\frac{8 k_B T}{\pi \mu}} \tag{6}$$

The reduced mass μ occurs because we are interested in the relative speed of approach. It is defined by $\mu_i = (1/m_i + 1/m_X)^{-1}$ where m_i and m_X are the masses of the reacting molecule containing an isotope of mass number i and the reaction partner, respectively. The simplest case arises for diffusion which corresponds to the limit $\lim_{m_X \to \infty} \mu_i = m_i$. The fractionation factor α equals the rates of the velocities of isotopically heavy and light molecules giving $\alpha = \bar{v}_h / \bar{v}_l = \sqrt{m_l / m_h}$. Thus, the three-isotope exponent β for diffusion of nitrous oxide is

$$\beta = \frac{\ln {}^{17}\alpha}{\ln {}^{18}\alpha} = \frac{\ln \frac{{}^{16}\mu}{{}^{17}\mu}}{\ln \frac{{}^{16}\mu}{{}^{18}\mu}} = \frac{\ln \frac{m(N_2\,{}^{16}O)}{m(N_2\,{}^{17}O)}}{\ln \frac{m(N_2\,{}^{16}O)}{m(N_2\,{}^{18}O)}} = 0.5066 \qquad (7)$$

Theoretically, β values for oxygen isotopes in diffusion processes can vary between 0.501 (heavy molecules) and 0.516 (atomic oxygen).

Another simple example is represented by the reaction $N_2O+O(^1D)$ (R2 and R3, page 5). With the reduced masses of isotopically substituted N_2O and atomic O, one obtains $\beta = 0.511$ (eqn. 7). This can be compared with an experimentally determined value of 0.57 ± 0.05 which may be subject to an analytical artefact though (re-evaluation of data from Johnston *et al.* [1995], see section 10.2).

For a more comprehensive theory of kinetic isotope effects, Bigeleisen [1949] was the first to use transition state theory. It was shown by Young *et al.* [2002] that eqn. 7 is a good approximation for β even in this case, with the only difference that the reduced masses need not correspond to those of the reaction partners, but may refer instead, for example, to a bond being broken within the isotopic molecule. N_2O photolysis giving N_2 and $O(^1D)$ as reaction products (R1, page 5) may serve as such an example. From the reduced masses of N_2 and ^{16}O, ^{17}O and ^{18}O, we compute $\beta = 0.521$ which compares favourably to the measured value of 0.518 ± 0.006 for broadband photolysis (Table 18) and is equal to the value from a more sophisticated quantum-chemical model giving 0.521 ± 0.001 between 185 and 225 nm (re-evaluation of model results from Johnson *et al.* [2001], see section 10.2).

Young *et al.* [2002] have also investigated the validity of eqn. 7 within the framework of RRKM (Rice-Ramsperger-Kassel-Marcus) theory, a quantum mechanical formulation of transition state theory for unimolecular dissociation. They conclude that the β values obtained from this theory are either close to the values of eqn. 7 or somewhere between the values given by equations 5 and 7 (representing equilibrium and kinetic isotope fractionation laws). This conclusion relies on the assumption that the number of quantum states accessible for the transition states is independent of isotopic substitution and that the internal energy is distributed equally over the vibrational-rotational modes of the excited molecule. Recently, it was shown by Marcus and co-workers [*Gao and Marcus*, 2001; *Hathorn and Marcus*, 1999; *Hathorn and Marcus*, 2000] that deviations from the statistical density of states which are different for asymmetric and symmetric O_3 isotopologues can explain the observed "mass-independent" isotope effects observed in ozone formation (cf. next section), but require adjustment of one parameter.

1.3.3 "Mass-independent" isotope effects

Departures from the expected mass-dependent relationships described in the previous section have been termed "mass-independent" isotope effects [*Thiemens and Heidenreich III*, 1983]. This definition is a bit misleading since it might imply that such isotope effects occur without accompanying change of mass. Obviously this is not the case. What was meant is rather an isotope effect deviating from the usual mass-dependent fractionation laws between three isotopes (equations 5 and 7). "Strange", "unconventional" or "anomalous" are probably preferable descriptions of this kind of isotope effect which is dependent on mass indeed. However, N_2O photolysis bears – as will be seen later – a truly "mass-independent" isotope effect (at least as far as molecular mass is concerned), since isotopomers of the same mass ($^{14}N^{15}N^{16}O$ and $^{15}N^{14}N^{16}O$) have clearly different absorption cross sections.

Anomalous isotope effects may also arise from changes of other nuclear properties upon isotopic substitution (such as nuclear spin, size or shape). These changes can cause isotope shifts in the electronic spectra as well as vibrational and rotational energy levels [*Bigeleisen*, 1996; *Fujii et al.*, 1998; *Tiemann et al.*, 1982]. Moreover, stellar nucleosynthesis, radioactive decay or natural nuclear reactors (such as in Oklo, Gabon) may cause exceptional isotopic variations. In fact, anomalous oxygen isotope effects were first detected in meteorites [*Clayton et al.*, 1973] and ascribed to nucleosynthetic process. However, in the present work we shall concentrate on isotope effects of "chemical" origin.

Gas-phase O_3 formation in an electrical discharge was the first chemical reaction in which anomalous oxygen isotope ratios were detected [*Thiemens and Heidenreich III*, 1983]. Other reactions with unconventional isotope effects were recently reviewed by Weston [1999] and include O_3 formation by O_2 photolysis, photolytic and thermal dissociation of O_3, electrodissociation of CO_2, reaction of CO + OH, formation of S_2F_{10} by an electric discharge in SF_4, photopolymerisation of CS_2 and ion-molecule reactions of the type $A^+ + A \rightarrow A_2^+$.

In the atmosphere, oxygen isotope anomalies were first reported for stratospheric O_3 [*Mauersberger*, 1987]. Subsequent measurements found similar anomalies in tropospheric O_3 and showed that the ^{17}O enrichment was about 0.7 times the corresponding ^{18}O enrichment in both stratosphere and troposphere [*Krankowsky et al.*, 1995; *Krankowsky et al.*, 2000]. O_3 is a key trace gas for both tropospheric and stratospheric chemistry and may transfer it oxygen isotope anomaly to other atmospheric trace gases and aerosols, including CO_2 [*Lämmerzahl et al.*, 2002; *Thiemens et al.*, 1991], CO [*Röckmann et al.*, 1998a], sulphate [*Lee and Thiemens*, 2001] and nitrate [*Michalski et al.*, 2001] (reviews in [*Thiemens*, 1999; *Thiemens et al.*, 2001]). Next to O_3 formation, reaction of CO + OH [*Röckmann et al.*, 1998b] and H + O_2 [*Savarino and Thiemens*, 1999b] are other primary sources of excess ^{17}O in tropospheric gases, namely CO and H_2O_2.

Given the wide spread of O isotope anomalies, it is no surprise that N_2O displays an oxygen isotope anomaly, too [*Cliff and Thiemens*, 1997]. At the time of its discovery, the observed anomaly in N_2O oxygen isotopes was regarded as an indicator of missing sources or sinks in the global N_2O budget and diverted research efforts into that direction [*Prasad*, 1997; *Wingen and Finlayson-Pitts*, 1998; *Zipf and Prasad*, 1998]. In section 10.3. we will present a mechanism which can explain the observed anomaly within the current understanding of the global N_2O budget.

1.4 Isotope studies of atmospheric N_2O

Isotope measurements provide additional independent observables to constrain the global budgets of atmospheric trace constituents and have successfully been used for this purpose in the cases of CO_2, CH_4 and CO. Different sources of trace gases often show characteristic variations of their isotopic signature which allow to distinguish them. Atmospheric sink reactions cause kinetic isotope fractionations which contribute to the naturally occurring variations of isotopic composition.

The first measurements of the ^{15}N content of atmospheric nitrous oxide (N_2O) were carried out in the early 1970s [*Moore*, 1974] and already showed that stratospheric N_2O was enriched in ^{15}N relative to tropospheric N_2O. Important foundations for the field were laid in the 1980s with the work of Yoshida and co-workers [*Yoshida*, 1988; *Yoshida and Matsuo*, 1983] for ^{15}N and Wahlen and Yoshinari for ^{18}O [*Wahlen and Yoshinari*, 1985; *Yoshinari and Wahlen*, 1985] as well as in the early 1990s with the first dual isotope measurements (^{15}N and ^{18}O) by Kim and Craig [*Kim and Craig*, 1990; *Kim and Craig*, 1993] and Yoshinari [*Yoshinari*, 1990]. These initial investigations showed that N_2O produced from different sources can have strongly varying isotopic composition. Measurements of soil emissions showed significant isotopic depletions relative to tropospheric N_2O [*Kim and Craig*, 1993; *Mariotti et al.*, 1981; *Mariotti et al.*, 1982; *Wahlen and Yoshinari*, 1985]. In contrast, heavy N_2O isotopes in surface waters of the oceans were only slightly depleted in ^{15}N and slightly depleted or enriched in ^{18}O [*Kim and Craig*, 1990; *Yoshida et al.*, 1984; *Yoshida et al.*, 1989].

It became clear soon that the isotopic composition of N_2O sources is as variable as their fluxes and depended on a large number of environmental variables. However, the annual emissions of N_2O make up only a minor fraction of the global N_2O burden which leads to a very small temporal and spatial variability of tropospheric N_2O isotope as well as mixing ratios. As pointed out above, a top-down approach promises to be the more suitable means to constrain the global budget of atmospheric N_2O. Having consolidated the enrichment of stratospheric N_2O found by Moore [1974], Kim and Craig [1993] suggested that the return flux of isotopically

heavy N_2O should balance the relatively light emissions from surface sources. However, their budget calculations showed that the stratospheric enrichment was too strong to balance the depleted source fluxes. Furthermore, initial laboratory experiments failed to show isotopic enrichments in both stratospheric sink reactions, photolysis (at 185 nm) and reaction with $O(^1D)$ [*Johnston et al.*, 1995]. Thus, the origin of the stratospheric enrichment which was confirmed later [*Rahn and Wahlen*, 1997] remained elusive.

At that time, not only the N_2O isotope budget appeared to be unbalanced, but also the N_2O budget itself suffered from a lack of N_2O sources which were required to explain the observed increase in N_2O mixing ratios [*Watson et al.*, 1992; *Watson et al.*, 1990]. This gave rise to proposals of a suite of "non-standard" chemistry, atmospheric *in situ* N_2O sources [*McElroy and Jones*, 1996; *Prasad*, 1997; *Wingen and Finlayson-Pitts*, 1998]. Finally though, a zero point energy (ZPE) model of N_2O photolysis [*Yung and Miller*, 1997] postulated wavelength-dependent isotopic fractionations due to small blue-shifts of the UV absorption spectra of the isotopically heavy N_2O species as a results of their lower vibrational zero point energies. Near-zero fractionations at the absorption maximum of N_2O (≈182 nm) were expected along with isotope enrichments of the residual N_2O at longer and depletions at shorter wavelengths. This explained both the stratospheric enrichments (at least qualitatively) and the measurements at 185 nm. In retrospect, this was also in agreement with pioneering vacuum ultraviolet (VUV) spectroscopy of ^{15}N-N_2O species [*Selwyn and Johnston*, 1981]. The further prediction of position-dependent enrichments of ^{15}N in the N_2O molecule led to the development of new spectrometric techniques [*Brenninkmeijer and Röckmann*, 1999; *Toyoda and Yoshida*, 1999; *Turatti et al.*, 2000] which are used extensively in the work presented here.

2 Isotope analysis of N_2O

Pioneering mass-spectrometric (MS) investigations of the isotopic composition of N_2O focussed on the average $^{15}N/^{14}N$ ratios [*Mariotti et al.*, 1982; *Moore*, 1974; *Yoshida et al.*, 1984; *Yoshida and Matsuo*, 1983]. Infrared absorption spectroscopy by tuneable diode lasers was developed later for $^{18}O/^{16}O$ [*Wahlen and Yoshinari*, 1985; *Yoshinari and Wahlen*, 1985], but it took another five years before the first MS dual-isotope ($^{15}N/^{18}O$) study was published [*Kim and Craig*, 1990]. $^{17}O/^{16}O$ measurements started in 1994 [*Cliff and Thiemens*, 1994]. The early MS techniques involved decomposition of N_2O with subsequent analysis of the reaction products. Both preparation of N_2 and/or CO_2 [e.g., *Kim and Craig*, 1990; *Moore*, 1974; *Yoshida and Matsuo*, 1983] or conversion to N_2 and O_2 [*Cliff and Thiemens*, 1994] were employed. Large sample sizes and laborious preparation and purification steps were required in any case and limited the amount of data that could be produced in reasonable time.

Direct injection of N_2O into a mass spectrometer was avoided from fear of contamination by CO_2 which has the same molecular masses as N_2O, but is $\approx 10^3$ times more abundant in a typical atmospheric sample. By the same token, corrections for N_2O artefacts had to be applied to CO_2 isotope measurements [*Mook and van der Hoek*, 1983]. In addition, NO_2 production in the ion source of certain mass spectrometers hampered precise determinations of $^{14}N_2{}^{18}O$ since both have mass-to-charge ratios (m/z) of 46. Kim and Craig [1993] were the first to realise the potential of direct N_2O injection and solved the problem of CO_2 contamination by a preparatory GC step, assuming complete removal of CO_2. However, thorough investigations by Tanaka *et al.* [1995] revealed that trace amounts of CO_2 could still be present in the N_2O sample even after this GC purification step and/or be introduced later by diffusion of air into the sample containers. These CO_2 traces lead to significant errors in the determination of N and O isotope ratios in N_2O because of the large differences in relative isotope ratios of CO_2 and N_2O (see section 2.8). The influence of CO_2 can be corrected for by measuring so-called "interfering masses" at m/z 12 or 22, arising from $^{12}C^+$ and $^{12}C^{16}O_2^{2+}$.

Recently, new analytical techniques were developed for the position-dependent ^{15}N analysis in N_2O, both by mass-spectrometry [*Brenninkmeijer and Röckmann*, 1999; *Toyoda and Yoshida*, 1999] and FTIR spectroscopy [*Esler et al.*, 2000]. This allowed a complete characterisation of the elemental isotopic composition of N_2O (^{14}N, ^{15}N, ^{16}O, ^{17}O, ^{18}O) if the common assumption of a statistical isotope distribution for each of the three atoms in N_2O is made. Further insights may be gleaned from non-statistical distributions of the isotopes as found for $^{12}CH_4$ and $^{12}CD_4/^{13}CHD_3$ [*Mroz et al.*, 1989] (chapter 6).

For the present work, a similar GC purification technique as used by Kim and Craig [1993] was developed and adapted to the position-dependent analysis of ^{15}N isotope ratios in the N_2O molecule as well as ^{17}O and ^{18}O measurements (see sections 2.6 and 2.7). "Conventional" ^{15}N and ^{18}O isotope measurements were made by direct injection of N_2O into the mass spectrometer (section 2.5).

2.1 Calibration

Absolute isotope ratio determinations are cumbersome and have to be performed on mass spectrometers which have been carefully calibrated by synthetic mixtures of essentially pure isotopes [*Aregbe et al.*, 1998]. The measured ratios of ion currents can thus be corrected for mass discrimination in sample inlet, ion source and detector.

Relative measurements of isotope ratios are much easier: If sample and reference material are treated in exactly the same way ("identical treatment" or "IT" principle [*Werner and Brand*, 2001]), mass discrimination effects that occur for instance in the inlet capillary or the ion source are the same for both sample and reference and cancel out. To enable comparison between results from different laboratories and to allow for some degree of traceability of results, isotope ratios are reported relative to a common international standard (i.e., an artefact) using the δ notation:

$$\delta = \left(\frac{R}{R_{st}} - 1 \right) \cdot 1000 \text{ ‰} \tag{8}$$

R is the elemental isotope ratio of the sample (i.e., $^{15}N/^{14}N$, $^{18}O/^{16}O$ and $^{17}O/^{16}O$ in the case of N_2O); R_{st} the elemental isotope ratio of the standard. In principle, a "free-floating" reference scale could be conceived without knowledge of the absolute isotope ratio of the international standard. Different laboratories would report their measurement results as δ values relative to this standard. However, absolute isotope ratios are still needed in order to remove the influence of isobars when making the transition from molecular to elemental isotope ratios (see computations in the next section). Table 2 gives an overview of absolute isotope ratios of international standards which are currently in use. These standards were chosen because they are representative for the average isotopic composition of the respective elements in the earth's crust (including the atmosphere). Throughout this doctoral thesis, air-N_2 will be used as reference to report $\delta^{15}N$ values, VSMOW for $\delta^{18}O$ and $\delta^{17}O$ values and VPDB for $\delta^{13}C$ values, unless noted otherwise.

Atmospheric N_2 is the international standard for ^{15}N abundance [*Mariotti*, 1983; *Mariotti*, 1984]. For oxygen isotopes, Vienna Standard Mean Ocean Water (VSMOW), CO_2 derived from Pee Dee Belemnite (VPDB-CO_2) and PDB itself are in use (VPDB) [*Gonfiantini*, 1978; *IAEA*, 1995]. PDB was a fossil calcium carbonate from the Pee Dee formation in South Carolina, but

Table 2: Overview of international scales and absolute isotope ratios used in this thesis

Species	Scale	$R/10^{-6}$	Relative error/‰	Reference
$^{13}C/^{12}C$	VPDB	11179.7±2.8	2.5	Chang and Li [1990][5]
$^{15}N/^{14}N$	Air-N_2	3676.5±4.1	1.1	Junk and Svec [1958][6]
$^{17}O/^{16}O$	VSMOW	379.9±0.8	2.1	Li *et al.* [1988]
	VPDB	385.7		Li *et al.* [1988]; IAEA [1995][7]
	VPDB-CO_2	387.7		Li *et al.* [1988]; IAEA [1995][8]
$^{18}O/^{16}O$	VSMOW	2005.2±0.45	0.2	Baertschi [1976]
	VPDB	2067.2		Li *et al.* [1988]; IAEA [1995]
	VPDB-CO_2	2088.3		Li *et al.* [1988]; IAEA [1995]

the original material became exhausted decades ago. Therefore, the original PDB scale was replaced by a hypothetical VPDB (Vienna PDB) scale which is supposed to be identical to PDB. The VPDB scale was fixed by an internationally agreed assignment of exact δ values to NBS-19 (another carbonate reference material): $\delta^{13}C(\text{NBS-19}) \equiv +1.95$ ‰ and $\delta^{18}O(\text{NBS-19}) \equiv -2.20$ ‰ vs VPDB. A similar agreement was reached for interconversion between the two scales [*Hut*, 1987]: $\delta^{18}O(\text{VPDB}) = 30.9$ ‰ vs VSMOW. VPDB-CO_2 is liberated from VPDB by treatment with 100 % H_3PO_4 at 25 °C. The pertinent fractionation factor between the carbonate and the CO_2 gas was fixed at 1.01025[3], so that $\delta^{18}O(\text{VPDB-CO}_2) = 41.47$ ‰ vs VSMOW[4].

Some authors have also used tropospheric O_2 as a reference [*Cliff and Thiemens*, 1997; *Rahn and Wahlen*, 1997], since O_2 from background air at sites remote from local perturbations is known to have a relatively uniform enrichment of (23.5±0.3) ‰ versus SMOW[9] [*Kroopnick and Craig*, 1972] (although this value might be incorrect, see section 2.7.3).

2.2 Isotope ratio mass spectrometry

As the two N atoms in the linear N_2O molecule are not equivalent (Figure 2), a distinction will be made between the δ value of the terminal N atom in N_2O (designated $^1\delta^{15}N$ or shorter $^1\delta$

[3] A recent study reported a slightly higher value of 1.01050 [*Kim and O'Neil*, 1997].
[4] δ values are non-additive. Sum and difference must be calculated in the following way (δ_{A-B} designating the δ value of sample A vs standard B, etc.):

$$\delta_{A-B}=\delta_{A-C}+\delta_{C-B}+\delta_{A-C}\delta_{C-B} \qquad \delta_{A-C}=(\delta_{A-B}-\delta_{C-B})/(1+\delta_{C-B})$$

[5] This value is 5 ‰ lower than the previously recommended value of $(11237\pm30)\cdot10^{-6}$ [*Craig*, 1957]. However, a recent measurement has found an even lower ratio of $(11094\pm12)\cdot10^{-6}$ [*Nørgaard et al.*, 1999].
[6] This is the value recommended by IUPAC for reporting of nitrogen-isotope abundance [*Coplen et al.*, 1992]. A recent measurement has found $(3678.2\pm1.5)\cdot10^{-6}$ [*De Bièvre et al.*, 1996], in agreement with the recommendation.
[7] Calculated from ^{18}R(VPDB) using $[^{17}R(\text{VPDB})/^{17}R(\text{VSMOW})]^2=^{18}R(\text{VPDB})/^{18}R(\text{VSMOW})$
[8] Calculated from ^{18}R(VPDB-CO_2) using $[^{17}R(\text{VPDB-CO}_2)/^{17}R(\text{VSMOW})]^2=^{18}R(\text{VPDB-CO}_2)/^{18}R(\text{VSMOW})$
[9] VSMOW is believed to be identical in oxygen isotope composition to SMOW [*IAEA*, 1995].

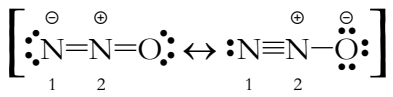

Figure 2: Mesomeric forms of N_2O in resonance with each other. Locants 1 and 2 indicate the position-dependent ^{15}N designations.

[*Brenninkmeijer and Röckmann*, 1999]), the middle N ($^2\delta^{15}N$ or $^2\delta$) and the average of both ($\delta^{15}N$). Likewise the isotope ratios are designated $^{15}R_1$ and $^{15}R_2$ (short R_1 and R_2).

Elemental isotope ratios ($^{15}N/^{14}N$, $^{18}O/^{16}O$ and $^{17}O/^{16}O$) cannot be measured directly by gas isotope ratio mass spectrometry, but must be determined from the observed molecular mass spectrum. In the case of N_2O, the molecular ion N_2O^+ as well as the NO^+ or N_2^+ fragment ions with their pertinent 12 (m/z 44 to 48), 6 (m/z 30 to 33) or 3 (m/z 28 to 30) isotopic species could be used. However, for N_2O at natural abundance isotope levels only species with m/z between 44 and 46 give sufficient ion currents to achieve the desired precision within a reasonable measurement time. Measurements of the NO^+ fragments are restricted to m/z 30 and 31 since masses 32 and 33 are severely perturbed by residual O_2^+ which can be also be produced by ion-molecule reactions in the ion source. In the case of N_2^+, the dominance of $^{14}N^{16}O^+$ at m/z 30 does not allow measurements of $^{15}N_2^+$ so that one is restricted to m/z 28 and 29.

The existing treatments in the literature of the conversion from molecular to elemental isotope ratios often make unnecessary approximations, do not deal with the position-dependent ^{15}N enrichment or assume from the outset a completely statistical isotope distribution. Therefore, a comprehensive discussion of this subject will be presented in the following.

There are two stable nitrogen isotopes (^{14}N, ^{15}N) and three stable oxygen isotopes (^{16}O, ^{17}O, ^{18}O). Since the two N positions in the linear N_2O molecule are non-equivalent there are $2 \cdot 2 \cdot 3 = 12$ possible combinations of these isotopes into different N_2O species (Table 3).

The molecular isotope ratios for the most abundant species of m/z 44 to 46 are defined as:

$$
\begin{aligned}
^{45}R &= \left[x(^{15}N^{14}N^{16}O) + x(^{14}N^{15}N^{16}O) + x(^{14}N_2{}^{17}O)\right] / x(^{14}N_2{}^{16}O) \\
^{46}R &= \left[x(^{15}N^{14}N^{17}O) + x(^{14}N^{15}N^{17}O) + x(^{14}N_2{}^{18}O) + x(^{15}N_2{}^{16}O)\right] / x(^{14}N_2{}^{16}O)
\end{aligned}
\qquad (9a,b)
$$

$x(^iN^jN^kO)$ is defined as the fractional abundance of the individual N_2O species with

$$
\sum_{i=14}^{15} \sum_{j=14}^{15} \sum_{k=16}^{18} x(^iN^jN^kO) = 1 \qquad (10)
$$

However, we are interested in the elemental isotope ratios which are the following for the terminal and central N atoms and the O atom:

Table 3: N_2O isotopologues and isotopomers and their relative abundance (x), assuming statistical isotope distributions for the three atoms in the N_2O molecule (calculated for $^1\delta^{15}N = -3$ ‰, $^2\delta^{15}N = +17$ ‰, $\delta^{17}O = +23$ ‰ and $\delta^{18}O = +45$ ‰)

Species	m	$x/10^{-6}$	share/% (species with same m)
$^{14}N^{14}N^{16}O$	44	990143.61	100.00
$^{14}N^{14}N^{17}O$	45	385.76	4.98
$^{14}N^{15}N^{16}O$		3642.65	47.04
$^{15}N^{14}N^{16}O$		3716.00	47.98
$^{14}N^{14}N^{18}O$	46	2079.94	99.21
$^{14}N^{15}N^{17}O$		1.42	0.07
$^{15}N^{14}N^{17}O$		1.45	0.07
$^{15}N^{15}N^{16}O$		13.67	0.65
$^{14}N^{15}N^{18}O$	47	7.65	49.48
$^{15}N^{14}N^{18}O$		7.81	50.48
$^{15}N^{15}N^{17}O$		0.01	0.03
$^{15}N^{15}N^{18}O$	48	0.03	100.00

$$
\begin{aligned}
{}^{15}R_1^* &= \sum_{i=14}^{15}\sum_{k=16}^{18} x({}^{15}N^{i}N^{k}O) \Big/ \sum_{i=14}^{15}\sum_{k=16}^{18} x({}^{14}N^{i}N^{k}O) \\
{}^{15}R_2^* &= \sum_{i=14}^{15}\sum_{k=16}^{18} x({}^{i}N^{15}N^{k}O) \Big/ \sum_{i=14}^{15}\sum_{k=16}^{18} x({}^{i}N^{14}N^{k}O) \\
{}^{17}R^* &= \sum_{i=14}^{15}\sum_{j=14}^{15} x({}^{i}N^{j}N^{17}O) \Big/ \sum_{i=14}^{15}\sum_{j=14}^{15} x({}^{i}N^{j}N^{16}O) \\
{}^{18}R^* &= \sum_{i=14}^{15}\sum_{j=14}^{15} x({}^{i}N^{j}N^{18}O) \Big/ \sum_{i=14}^{15}\sum_{j=14}^{15} x({}^{i}N^{j}N^{16}O)
\end{aligned}
\qquad \text{(11a-d)}
$$

In theory, optical techniques would allow to determine each N_2O species individually so that the elemental isotope ratios could be computed, but in practice the sensitivity of the detector limits the measurements to $^{14}N_2{}^{16}O$, $^{14}N^{15}N^{16}O$, $^{15}N^{14}N^{16}O$ and $^{14}N_2{}^{18}O$ for unenriched N_2O [*Esler et al.*, 2000; *Uehara et al.*, 2001]. Of course, isotope ratio mass spectrometry suffers from similar restrictions, but in this case it is also principally impossible to distinguish between species of the same molecular mass number (isobars) because the usual isotope ratio mass spectrometers have mass resolutions ($m/\Delta m$) between 100 and 300 only. Therefore, the elemental isotope ratios cannot be derived from the measurement of ^{45}R and ^{46}R alone, without further assumptions. The first step to solve this dilemma is to assume a statistical isotope distribution between the different *isotopologues*[10]. However, different *isotopomers* are still treated separately because the two nitrogen

[10] The terms *isotopologue* and *isotopomer* are used according to their IUPAC definitions [*Müller*, 1994]:
"*isotopologue*: a molecular entity that differs only in isotopic composition (number of isotopic substitutions), e.g. CH_4,

atoms in the N_2O molecule are chemically not equivalent and fragment analysis can provide additional information to calculate the position-dependent ^{15}N enrichment (as shown below).

Assuming statistical distributions, the relative abundance of individual N_2O species can be factorised, e.g. $x(^{14}N^{15}N^{17}O) = {}^{14}x_1\ {}^{15}x_2\ {}^{17}x$, with ${}^{14}x_1$, ${}^{15}x_1$ and ${}^{14}x_2$, ${}^{15}x_2$ being the relative abundance of ^{14}N and ^{15}N at the terminal and central N positions, respectively, and ${}^{16}x$, ${}^{17}x$ and ${}^{18}x$ being the abundance of ^{16}O, ^{17}O and ^{18}O. With $\sum_{i=14}^{15} {}^{i}x_1 = \sum_{j=14}^{15} {}^{j}x_2 = \sum_{k=16}^{18} {}^{k}x = 1$ it follows

$$\begin{aligned} {}^{15}R_1 &= {}^{15}x_1 / {}^{14}x_1 \\ {}^{15}R_2 &= {}^{15}x_2 / {}^{14}x_2 \\ {}^{17}R &= {}^{17}x / {}^{16}x \\ {}^{18}R &= {}^{18}x / {}^{16}x \end{aligned} \qquad (12a\text{-}d)$$

Likewise, the molecular isotope ratios defined in eqn. 9 can be simplified to

$$\begin{aligned} {}^{45}R &= \left[{}^{15}x_1\,{}^{14}x_2\,{}^{16}x + {}^{14}x_1\,{}^{15}x_2\,{}^{16}x + {}^{14}x_1\,{}^{14}x_2\,{}^{17}x \right] / {}^{14}x_1\,{}^{14}x_2\,{}^{16}x \\ {}^{46}R &= \left[{}^{15}x_1\,{}^{14}x_2\,{}^{17}x + {}^{14}x_1\,{}^{15}x_2\,{}^{17}x + {}^{14}x_1\,{}^{14}x_2\,{}^{18}x + {}^{15}x_1\,{}^{15}x_2\,{}^{16}x \right] / {}^{14}x_1\,{}^{14}x_2\,{}^{16}x \end{aligned} \qquad (13a,b)$$

Substitution of equations 12a-d into 13a,b gives

$$\begin{aligned} {}^{45}R &= {}^{15}R_1 + {}^{15}R_2 + {}^{17}R \\ {}^{46}R &= ({}^{15}R_1 + {}^{15}R_2)\ {}^{17}R + {}^{18}R + {}^{15}R_1\,{}^{15}R_2 \end{aligned} \qquad (14a,b)$$

Although we have substantially reduced the number of unknowns, this system of equations is still underdetermined. Without resort to fragment analysis, one can only proceed by definition of an average ^{15}N isotope ratio ${}^{15}R = ({}^{15}R_1 + {}^{15}R_2)/2$ which is then substituted into eqn. 14. However, in order to eliminate the term ${}^{15}R_1\,{}^{15}R_2$ a further assumption has to be made, namely that the arithmetic mean $({}^{15}R_1 + {}^{15}R_2)/2$ is identical to the geometric mean $\sqrt{{}^{15}R_1\,{}^{15}R_2}$. This assumption is not necessarily true as will be seen later from the position-dependent ^{15}N analysis, but it went completely uncommented and unnoticed in the past, because in conventional isotope analysis of N_2O only the ^{18}O and average ^{15}N enrichments were determined and identical isotope ratios at both N positions were implicated from the outset. Fortunately, the error thus introduced appears to be negligible for samples close to natural ^{15}N abundance and small differences in the in-

---

CH_3D, CH_2D_2."

"*isotopomer*: isomers having the same number of each isotopic atom but differing in their positions. The term is a contraction of "isotopic isomer". Isotopomers can be either constitutional isomers (e.g. $CH_2DCH{=}O$ and $CH_3CD{=}O$) or isotopic stereoisomers (e.g. (*R*)- and (*S*)-CH_3CHDOH or (*Z*)- and (*E*)-$CH_3CH{=}CHD$)."

Applied to N_2O this means that e.g. $^{14}N_2{}^{16}O$, $^{14}N_2{}^{17}O$ and $^{14}N_2{}^{18}O$ are different isotopologues of the same molecular entity N_2O, but they are not isotopomers. Conversely, $^{14}N^{15}NO$ and $^{15}N^{14}NO$ are different isotopomers of the same isotopologue. However, we note that it is common in publications on isotopically substituted molecules to extend the definition of "isotopomer" so that it refers to different isotopic compositions or different positions of the isotopic atoms in a molecular entity.

tramolecular ^{15}N distribution. Even for an extreme scenario in which the central N atom is enriched by 160 ‰ against the terminal N atom (i.e., $^{15}R_2 = 1.160 \cdot {}^{15}R_1$), we have

$$\left(\sqrt{{}^{15}R_1\,{}^{15}R_2}\right)^2 = 1.160\ {}^{15}R_1^2$$
$$\left[\left({}^{15}R_1 + {}^{15}R_2\right)/2\right]^2 = 1.080^2\ {}^{15}R_1^2 = 1.166\ {}^{15}R_1^2 \qquad (15a,b)$$

Taking into account that the $^{15}N_2{}^{16}O$ isotopologue makes up about 6 ‰ (Table 3) of mass 46, this 5.5 ‰ difference between arithmetic and geometric mean translates into a difference of only 0.033 ‰ for ^{46}R, i.e. about the internal precision of the mass-spectrometric analysis. Approximation of $^{15}R_1{}^{15}R_2$ by $(^{15}R)^2$ is therefore justified in most cases:

$$^{45}R = 2\ {}^{15}R + {}^{17}R$$
$$^{46}R = 2\ {}^{15}R\ {}^{17}R + {}^{18}R + ({}^{15}R)^2 \qquad (16a,b)$$

Finally, conventional N_2O isotope analysis exploits the covariation of ^{17}R and ^{18}R. In general, their relationship can be cast into a power law

$$^{17}R = A(^{18}R)^{\beta} \qquad (17)$$

If β is close to 0.5, this is considered to be a mass-dependent relationship (see 1.3.3). The three-isotope exponent β (1.3.3) has to be determined by independent experiments whereas A is calculated from β and the isotope ratios of VSMOW (see section 2.7.2). For the present work, $\beta = 0.516$ and $A = 0.00937035$ (exactly) were adopted. Eqn. 17 is then substituted into eqn. 16:

$$^{45}R = 2\ {}^{15}R + A(^{18}R)^{\beta}$$
$$^{46}R = 2\ {}^{15}R\ A(^{18}R)^{\beta} + {}^{18}R + ({}^{15}R)^2 \qquad (18a,b)$$

This system of equations can be solved numerically for ^{15}R and ^{18}R.

Fragment analysis can provide additional constraints to eqn. 14. A typical mass spectrum of N_2O is shown in Figure 3. Next to the N_2O^+ molecule ion, the following fragments are produced upon electron impact ionisation of N_2O (intensity relative to the molecule ion in brackets): NO^+ (32 %), N_2^+ (11 %), N^+ (7 %) and O^+ (3 %)[11]. Most importantly, the intramolecular ^{15}N distribution can be determined by measurements of the ratio of NO^+ fragments at m/z 31 and m/z 30, but also the $N_2{}^+$ fragment (m/z 29 and 28) can be exploited to derive the $^{17}O/^{16}O$ isotope ratio by comparison of the N_2O^+ and N_2^+ measurements. In the case of NO^+, some isotopic scrambling occurs which has to be corrected for: 91.8 % of the nitrogen atoms in NO^+ come from the central N position, but 8.2 % are derived from the terminal N position (cf. section 2.6).

[11] The relative intensity seems to be sensitive to the type of mass spectrometer as well as age and tuning settings of the ion source. We used three types of mass spectrometers: *Finnigan* MAT 252, *Finnigan* DELTA^{plus} XL and *Micromass* Prism II. In dual-inlet mode the MAT 252 and Prism II instruments gave an NO^+ intensity relative to N_2O^+ of 30 to 35 %, the DELTA^{plus} XL yielded between 17 and 25 %. It was verified by multiple measurements of the same sample on different instruments that this variation had no noticeable influence on the measured $^{31}\delta$ values.

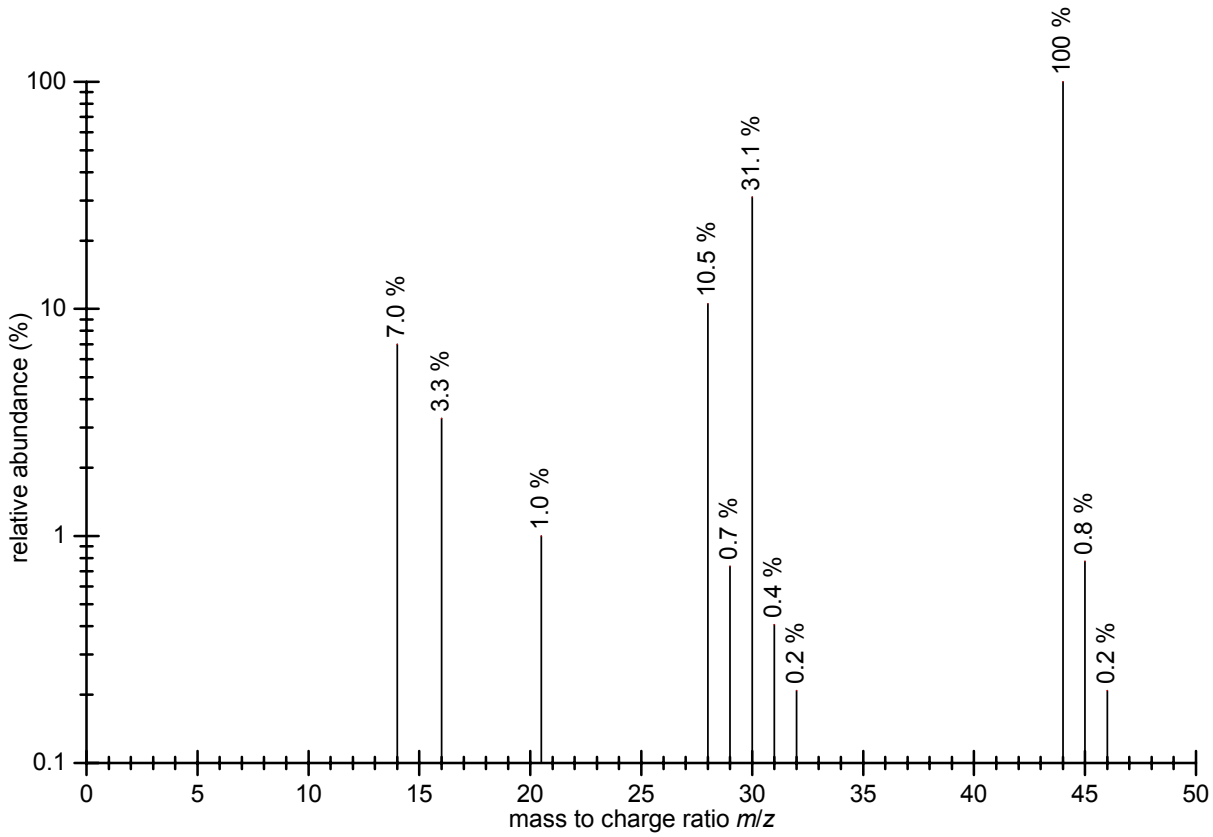

Figure 3: Typical mass spectrum of N_2O working standard. Note the logarithmic ordinate scale. The signal at m/z 20.5 is due to metastable ions from N_2O^+ ions dissociating after being accelerated but before entering the field of the bending magnet [*Begun and Landau*, 1961; *Newton and Sciamanna*, 1970a; *Newton and Sciamanna*, 1970b].

In analogy to the derivation shown for ^{45}R and ^{46}R, the corresponding equations for ^{31}R and ^{29}R are derived, first without, then with consideration of scrambling.

$$^{31}R = \left[x(\mathrm{N^{15}N^{16}O}) + x(\mathrm{N^{14}N^{17}O})\right] / x(\mathrm{N^{14}N^{16}O}) \tag{19}$$

$$^{29}R = \left[x(\mathrm{^{15}N^{14}NO}) + x(\mathrm{^{14}N^{15}NO})\right] / x(\mathrm{^{14}N_2O}) \tag{20}$$

The oxygen isotope speciation is of no relevance for ^{29}R and can therefore be omitted. The same applies to the nitrogen isotopes at the terminal N position Making the same assumptions on the statistical isotope distribution as for ^{45}R and ^{46}R, equations 19 and 20 can be simplified to:

$$^{31}R = {}^{15}R_2 + {}^{17}R \tag{21}$$

$$^{29}R = {}^{15}R_1 + {}^{15}R_2 \tag{22}$$

With these two additional equations it is in principle possible to solve eqn. 14 for $^{15}R_1$, $^{15}R_2$, ^{17}R and ^{18}R. E.g. substitution of eqn. 22 into 14a gives $^{17}R = {}^{45}R - {}^{29}R$; substitution of eqn. 21 into 14a gives $^{15}R_1 = {}^{45}R - {}^{31}R$. In reality, some restrictions apply due to the relatively high error in the ^{29}R measurement (≈ 0.05 ‰) limiting the precision of ^{17}R to about 1 ‰ (since $^{14}N_2{}^{17}O$ makes up only 5 % of the total ion current at m/z 45, cf. section 2.7). In addition, we have to take the

scrambling of NO^+ into account. To this end, a "scrambling coefficient" s is introduced which is the percentage of nitrogen atoms in NO^+ derived from the terminal N position. The coefficient s has to be measured in a separate experimental series and its presence complicates the ^{31}R calculations, so that eqn. 19 now reads with the scrambled ratio $^{31}R_s$:

$$^{31}R_s = \frac{s\left[x(^{15}\mathrm{NN}^{16}\mathrm{O}) + x(^{14}\mathrm{NN}^{17}\mathrm{O})\right] + (1-s)\left[x(\mathrm{N}^{15}\mathrm{N}^{16}\mathrm{O}) + x(\mathrm{N}^{14}\mathrm{N}^{17}\mathrm{O})\right]}{sx(^{14}\mathrm{NN}^{16}\mathrm{O}) + (1-s)x(\mathrm{N}^{14}\mathrm{N}^{16}\mathrm{O})} \tag{23}$$

Again, only the relevant isotopes have been shown. To simplify this, the usual statistical assumption is made, ^{17}R is extracted and the numerator is divided by the denominator:

$$\begin{aligned} ^{31}R_s - ^{17}R &= \frac{s\,^{15}R_1 + (1-s)\,^{15}R_2 + ^{15}R_1\,^{15}R_2}{1 + s\,^{15}R_2 + (1-s)\,^{15}R_1} \\ &= s\,^{15}R_1 + (1-s)\,^{15}R_2 - \frac{s(1-s)(^{15}R_1 - ^{15}R_2)^2}{1 + s\,^{15}R_2 + (1-s)\,^{15}R_1} \end{aligned} \tag{24a,b}$$

Eqn. 24b disagrees in the last term from the result of Yoshida and Toyoda [1999; 2000]. This term is at its maximum for $s = 0.5$ and for large differences in the isotope ratios at the central and terminal nitrogen positions ($^{15}R_2$ and $^{15}R_1$). However, s is only 0.082 in reality (see section 2.4.1) and even the same extreme assumption as above ($^{15}R_2 = 1.160 \cdot ^{15}R_1$) leads to a correction of – 0.006 ‰ only for natural abundance samples. For work with artificially enriched ^{15}N isotopes, this term may become relevant though.

As stated in the first paragraphs of section 2.1, isotope ratios are not measured directly, but are calculated from δ values relative to international standards. Because the supply of calibration materials is limited, it is mandatory to set up an N_2O working standard as intermediary between the sample and a fictitious N_2O standard bearing the nitrogen isotope ratio of atmospheric air and the oxygen isotope ratio of VSMOW. This working standard is not limited by sample size restrictions and several batches of it can be converted for calibration purposes to CO_2 and N_2 or N_2 and O_2. These gases can then be related to isotope reference materials. The conversion is described in section 2.3 of this thesis.

In the conventional N_2O isotope analyses of the past, these steps were sufficient to calibrate the ^{18}O and the average ^{15}N isotope. However, for position-dependent analysis of the N isotope ratios a position-dependent calibration of the standard is also required, because otherwise systematic errors could result from the conversion of $^{31}\delta$ measurements of the NO^+ fragment to ^{31}R or $^{31}R_s$. Following Brenninkmeijer and Röckmann [1999], the position-dependent isotopic composition of the standard is expressed by a parameter f defined as

$$f = \frac{^{15}R_{1,\mathrm{st}}}{^{15}R_{1,\mathrm{st}} + ^{15}R_{2,\mathrm{st}}} \tag{25}$$

Then, the average $\delta^{15}N$ value (derived from the $^{45}\delta$ and $^{46}\delta$ measurements) is

$$\begin{aligned}\delta^{15}\mathrm{N} &= \frac{^{15}R_1 + {}^{15}R_2}{^{15}R_{1,st} + {}^{15}R_{2,st}} - 1 = f\frac{^{15}R_1}{^{15}R_{1,st}} + (1-f)\frac{^{15}R_2}{^{15}R_{2,st}} - 1 \\ &= f(1+{}^1\delta) + (1-f)(1+{}^2\delta) - 1 \\ &= f\,{}^1\delta + (1-f)\,{}^2\delta\end{aligned} \tag{26}$$

The simplest case occurs for $f = ½$, since then $^{15}R_{st} = {}^{15}R_{1,st} = {}^{15}R_{2,st}$ and both $^{31}R_{st}$ and $^{31}R_{s,st}$ are equal to $^{15}R_{st} + {}^{17}R_{st}$ (equations 21 and 24). The average δ^{15}N value is equal to the arithmetic average of $^1\delta^{15}$N and $^2\delta^{15}$N. $f > ½$ means that the average δ^{15}N value is biased towards the enrichment at the terminal N position of the N_2O molecule; $f < ½$ means that δ^{15}N is biased towards the enrichment at the central N position. This is independent of any scrambling and serves to illustrate how a potential asymmetry in the intramolecular ^{15}N distribution in the working standard may influence the average δ^{15}N. As long as we are dealing with average δ^{15}N values *only*, this is irrelevant. However, for position-dependent measurements it has to be taken into account.

To this end, $^2\delta^*$ is defined as the apparent δ value of the central N atom (under the influence of scrambling and a potentially asymmetric standard):

$${}^2\delta^* = \frac{^{31}R_s - {}^{17}R}{^{31}R_{s,st} - {}^{17}R_{st}} - 1 \tag{27}$$

Substitution of equations 24 (neglecting the third term), 25 and 26 into eqn. 27 yields:

$${}^2\delta = {}^2\delta^* + \frac{s({}^2\delta^* - \delta^{15}\mathrm{N})}{(1-f)(1-2s)} \tag{28}$$

$${}^1\delta = {}^2\delta + \frac{\delta^{15}\mathrm{N} - {}^2\delta}{f} = {}^2\delta^* - \frac{(1-s)({}^2\delta^* - \delta^{15}\mathrm{N})}{f(1-2s)} \tag{29}$$

Section 2.7.1 describes a purely mass-spectrometric procedure to perform a position-dependent calibration of a sample of N_2O. It relies on measurements of mixtures of the working standard and $^{15}N^{15}N^{16}O$ against the working standard. A plot of $^{31}\delta$ versus $^{46}\delta$ can be used to derive essentially the ratio $^{31}R_{s,st}/{}^{46}R_{st}$ which allows computation of $^{31}R_{s,st}$ provided $^{46}R_{st}$ has been determined before. Calibration of $^{46}R_{st}$ is possible by conventional techniques as described in 2.3. Via this approach we obtain a value of $f = 0.4899 \pm 0.0002$ for our N_2O working standard which indicates that the terminal N position is about 40 ‰ lighter than the central one. Since the average ^{15}N composition of our standard is close to air-N_2 (+1.0 ‰) this means that $^1\delta_{air}$(working standard) ≈ -19 ‰ and $^2\delta_{air}$(working standard) $\approx +21$ ‰. The sensitivity of $^2\delta$ and $^1\delta$ of a sample (measured against the working standard) to the accuracy of f for the standard is checked by deriving equations 28 and 29 with respect to f:

$$\frac{\partial({}^2\delta)}{\partial f} = \frac{s({}^2\delta^* - \delta^{15}\mathrm{N})}{(1-f)^2(1-2s)} \tag{30}$$

$$\frac{\partial(^1\delta)}{\partial f} = \frac{(1-s)(^2\delta^* - \delta^{15}\mathrm{N})}{f^2(1-2s)} = \frac{1-s}{s}\frac{(1-f)^2}{f^2}\frac{\partial(^2\delta)}{\partial f} \approx \frac{1-s}{s}\frac{\partial(^2\delta)}{\partial f}, \text{ since } f \approx 1-f \approx ½ \quad (31)$$

With $s = 0.082$ it follows that $^1\delta$ is about 11 times more sensitive than $^2\delta$ to any uncertainty in f. For tropospheric samples with typical values of $^1\delta = 15.8$ ‰ and $^2\delta = -4.4$ ‰, it follows that $^2\delta$ and $^1\delta$ are subject to possible systematic errors of ±0.0006 ‰ and ±0.007 ‰ which are negligible considering the external precision of mass spectrometric analysis which is at best 0.03 ‰ for $^2\delta^*$ (section 8.3.1).

In a similar way, the influence of the precision of the scrambling coefficient s on the precision of the δ values can be investigated:

$$\frac{\partial(^2\delta)}{\partial s} = \frac{^2\delta^* - \delta^{15}\mathrm{N}}{1-f}\frac{1}{(1-2s)^2} \quad (32)$$

$$\frac{\partial(^1\delta)}{\partial s} = \frac{^2\delta^* - \delta^{15}\mathrm{N}}{f}\frac{-1}{(1-2s)^2} = -\frac{1-f}{f}\frac{\partial(^2\delta)}{\partial f} \quad (33)$$

Since $f \approx ½$, $^1\delta$ and $^2\delta$ are about equally sensitive to uncertainties in s. Under the standard conditions s is reproducible and amounts to 0.0822±0.0001. Even allowing for a uncertainty of 0.001, gives negligible errors of about 0.02 ‰ for $^1\delta$ and $^2\delta$ of a typical tropospheric sample such as mentioned above.

2.3 Calibration of ^{15}N and ^{18}O in the working standard

Calibration of the working standard gas against which isotope ratios are measured is necessary in order to make the transition from δ values as measured by the isotope ratio mass spectrometer to isotope ratios R which are required for the calculations outlined in the preceding section. Moreover, calibration to international scales (Table 2) facilitates intercomparison of the results between different workgroups.

2.3.1 Calibration procedure

The N_2O working standard (*Messer-Griesheim*, 99.9999 % purity) was calibrated in two different ways: through conversion to N_2 and CO_2 by graphite with Pt mesh as a catalyst and through thermal decomposition to N_2 and O_2 on a gold surface. Table 4 gives an overview on the experimental parameters and final results.

N_2, O_2 and CO_2 from N_2O decompositions are measured in turn against working standards of these gases. They were calibrated against the international standards air-N_2 (section 2.3.2) and NBS-19-CO_2 which has a fixed isotopic composition relative to the international standard VPDB-CO_2. To this end, the O_2 working standard was combusted to CO_2 first (section 2.3.4).

Table 4: Overview on conversion experiments for calibration of the N_2O working standard

experiment	$N_2O + ½\ C \rightarrow N_2 + ½\ CO_2$	$N_2O \rightarrow N_2 + ½\ O_2$
catalyst	Pt	Au
reactor volume	≈ 24 cm^3	≈ 34 cm^3
sample volume (SATP)	≈ 1.2 cm^3	≈ 1.2 cm^3
temperature	(690–713) °C	(930–940) °C
initial reactor pressure	≈ 180 mbar	≈ 200 mbar
duration of conversion	1 h	(3–12) h
yield	(99.3±0.7) %	(100.0±0.1) %
$\delta^{18}O_{CO_2\text{-standard}}$	(27.25±0.13) ‰	
number of analyses	17	
$\delta^{18}O_{O_2\text{-standard}}$		(22.68±0.29) ‰
number of analyses		9
$\delta^{18}O_{VSMOW}$	(38.59±0.20) ‰	(38.15±0.31) ‰
$\delta^{18}O_{VSMOW}$ (weighted mean)	(38.45±0.20) ‰	
$\delta^{15}N_{N_2\text{-standard}}$	(14.25±0.09) ‰	(14.31±0.04) ‰
number of analyses	11	19
$\delta^{15}N_{air}$	(0.96±0.09) ‰	(1.02±0.05) ‰
$\delta^{15}N_{air}$ (weighted mean)	(1.01±0.03) ‰	

A quartz tube with a transition piece to *Duran* glass was used for the graphite conversions. Only the quartz part of the reactor was inserted into a tube furnace (*Carbolite* MTF 10/15/130) and heated to the designated temperature. In order to release all residual gases, the reactor, the graphite and the catalyst were pumped out under high vacuum prior to the conversion for at least one hour. Furthermore, the first conversion of a day was not included in the final evaluation. The amount of N_2O before conversion and the combined amount of CO_2 and residual N_2O after conversion were determined manometrically and used to assess the yield of the reaction. Yields higher than 100 % would indicate incomplete conversions.

In case of the Pt/C reaction, the Boudouard reaction $C + CO_2 \rightleftharpoons 2\,CO$ ($K_p \approx 1$ at 700 °C) produces CO as a by-product. However, most of the CO reacts back to CO_2 when the reaction is stopped by freezing out CO_2, because this effectively shifts the equilibrium to the $C + CO_2$ side of the Boudouard reaction. Any residual CO was removed by Schütze reagent (acidic I_2O_5 on silica gel) [*Schütze*, 1940], because it would otherwise interfere with the N_2 measurement in the isotope ratio mass spectrometer. The absence of any CO or CO_2 contamination in the purified N_2 was checked by measurement of the $^{12}C^+$ ion.

The decomposition to N_2 and O_2 was performed in a gold tube (Au purity: 99.9 %) at 930 to 940 °C. The yield was controlled by manometric measurement of the residual condensable gas which amounted to about 1 % of the initial N_2O. However, after passage over a preparatory GC

column (cf. section 8.1.4) only 1 to 3 % of the residual gas turned out to be N_2O, the rest being CO_2 that was presumably produced by carbon containing impurities in the reactor. Thus, the overall N_2O conversion was 99.97 to 99.99 % and the conversion products should quantitatively reflect the initial isotopic composition of N_2O since kinetic isotope effects are expected to be small at such high temperatures. Indeed, measurements on residual N_2O from incomplete conversion indicate fractionation factors of $\alpha(^{15}N) = 1.005–1.007$ and $\alpha(^{18}O) = 1.010–1.014$ at temperatures between 930 and 940 °C. On some occasions, the N_2O yield was double-checked by determining the amount of N_2 and O_2 in a calibrated volume containing silica gel for freezing in the gas with liquid nitrogen. It agreed with the stoichiometrically expected amount indicating no significant leaks of air into the reactor.

2.3.2 Calibration of the N_2 working standard

Measurements of $\delta^{15}N$ in N_2 were performed against a cylinder of high-purity nitrogen (*Messer-Griesheim*, 99.9999 %). Since $\delta^{15}N$ of the sample was to be given relative to air, this N_2 working standard had to be calibrated against air-N_2. Initial experiments in the year 2000 had shown that N_2 could be analysed directly versus air-N_2, because O_2 and Ar did not interfere with the N_2 measurement as could be ascertained by analysing mixtures of 20 % to 60 % O_2 in N_2 + O_2 and 1 % to 30 % Ar in N_2 + Ar. CO^+ interference from CO_2 in ambient air required only a small correction of about 0.020 ‰. The results of these analyses in the year 2000 can be identified by their date in Figure 4.

However, later checks in 2001/2002 revealed that the above observation must have been a fortunate coincidence since measurements under varying ion source conditions showed that both increases and decreases of the directly measured $\delta^{15}N$ values of O_2/N_2 mixtures versus N_2 could occur. The results shown in Figure 5 were obtained at the end of the lifetime of the filament in the ion source which had been installed in summer 2000. They clearly show a linear increase of $\delta^{15}N$ with O_2 mixing ratio as opposed to the absence of any trend which was noted in October 2000. Subsequent measurements with a new filament installed in March 2002 showed *negative* $\delta^{15}N$ values when O_2 was added to the N_2 standard.

Therefore, two different strategies were followed to avoid the undesired influence of O_2 on the $\delta^{15}N$ measurement in N_2. O_2/N_2 mixtures were either measured relative to samples of the N_2 standard amended with O_2 to give the same O_2 mixing ratio as the sample or the mixtures were separated on a preparatory GC system with a molecular sieve column as used before for oxygen isotope analysis [*Luz et al.*, 1999]. The results of both approaches have been included in Figure 4.

The first approach required a special mixing system which consisted of two glass bulbs ($V \approx$ 1 dm^3) connected in line with a valve in the middle and one valve each on either end. The exact

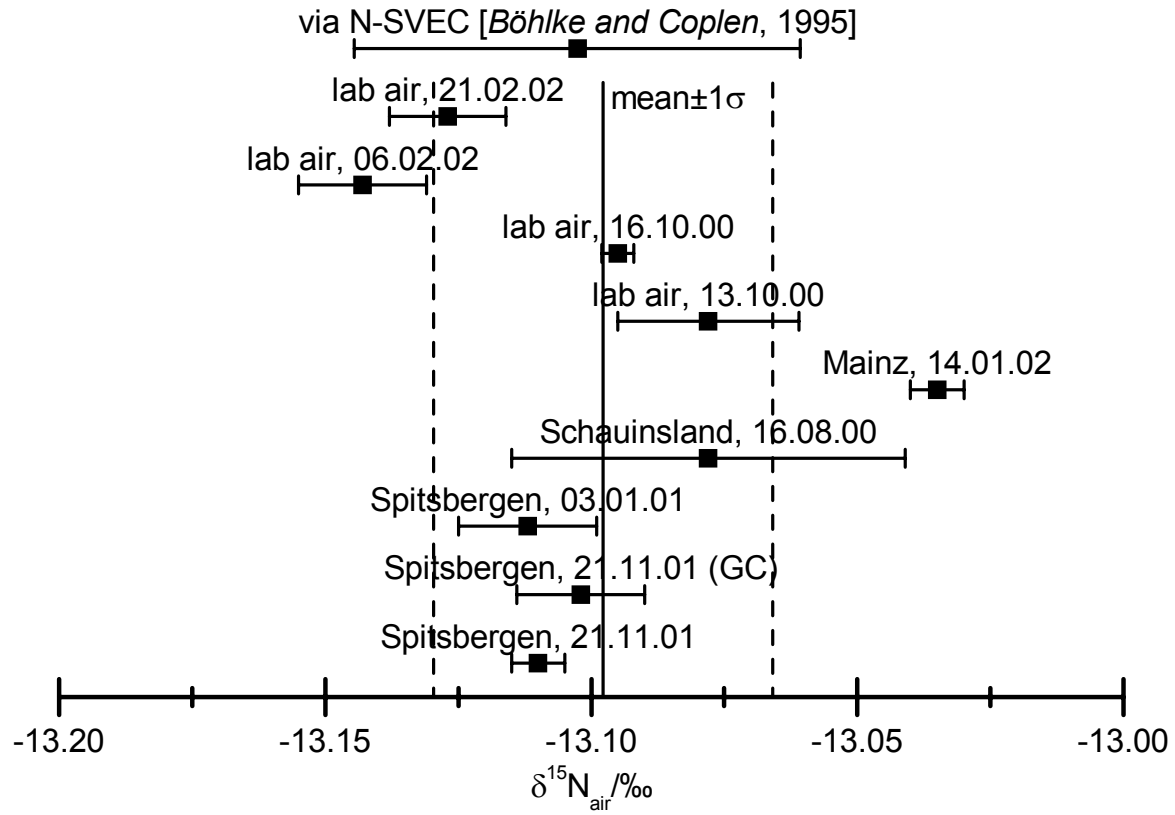

Figure 4: Measurements of the N_2 working standard against air samples from various locations and analysed in different years. The deviations mainly reflect changes in sample treatment rather than variation in $\delta^{15}N$ in air-N_2 which is less than the internal precision of mass-spectrometric analysis [*Mariotti*, 1983; *Mariotti*, 1984]. The analyses of samples from the year 2000 have been performed directly against air. Samples from 2001/2002 have been measured against a mixture of similar $O_2/(N_2+O_2)$ ratios as air (21.14 % and 21.16 % for air and the mixture, respectively) ensuring that any O_2 interference cancels. One Spitsbergen sample has been passed over a preparatory GC system which separates O_2 and N_2 on a molecular sieve column. Vertical lines indicate mean and standard deviation from all of the above analyses. Finally, the N_2 working standard was measured against the gaseous N_2 reference material N-SVEC which has $\delta^{15}N_{air} = (-2.78 \pm 0.04)$ ‰ [*Böhlke and Coplen*, 1995] and the result subsequently transposed to the air-N_2 scale.

volumes of the bulbs were determined gravimetrically with degassed H_2O. After filling the bulbs with manometrically determined amounts of N_2 and O_2, the valve in the middle was opened and the contents of both bulbs were mixed by a miniature rotary vane pump. Samples of different $\delta^{15}N(N_2)$ isotopic composition, but with the same O_2 content, can then be measured against each other and directly give the difference in $^{15}N/^{14}N$ isotope ratios since the O_2 influence cancels.

In principle, the same approach can be used for O_2 isotope analysis. However, the N_2 influence on O_2 analysis is much larger than for the inverse. It could be shown that the apparent $\delta^{17}O$ and $\delta^{18}O$ values correlate linearly with the N_2/O_2 ratio. On a *Finnigan* MAT 252 mass spectrometer we obtained slopes of $\partial\delta^{17}O/\partial(N_2/O_2) \approx 100$ ‰/1 and $\partial\delta^{17}O/\partial(N_2/O_2) \approx 10$ ‰/1.

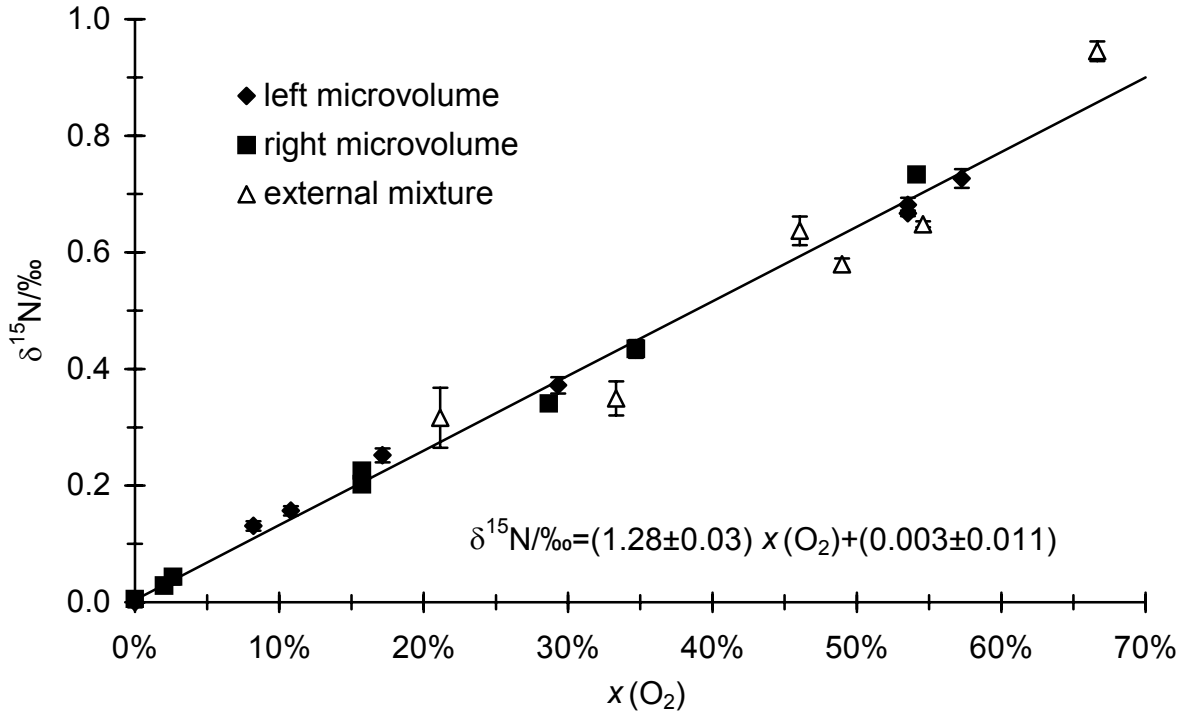

Figure 5: Influence of oxygen mixing ratio on $\delta^{15}N$ of mixtures of O_2 and N_2 working standard measured against the same working standard. Mixtures were both prepared externally and by flowing O_2 through the capillaries of either one of the two microvolume inlets of the mass spectrometer. The microvolumes ($\approx$250 mm^3) are normally used to analyse small aliquots of sample gas which are not sufficient for use with the adjustable bellows (3 to 40 cm^3), but on this occasion serve as a convenient mixing device with very stable flow conditions. Both bellows contain N_2 working standard gas. The O_2 mixing ratio can be varied by changing the pressure in the microvolume and can be calculated from the m/z 32 signal if differences in ionisation efficiency of N_2 and O_2 are taken into account.

However, very precise measurements would have required a major refurbishment of the MS [*Leuenberger et al.*, 2000] and were not necessary because O_2 isotope ratios could be measured directly on pure O_2 samples from the preparatory GC system as explained in the following.

The second approach made use of the same preparatory GC system as used for N_2O purification (Figure 46), but with the Porapak Q column replaced by a 5 Å molecular sieve column (60/80 mesh; diameter: 3.2 mm; length: 5 m). Injection and collection traps were replaced by loops with 5 Å molecular sieve. The efficiency of the set-up was tested by passing mixtures of N_2 and O_2 with know isotopic composition over the GC. This set-up had the advantage that O_2 could be extracted, too, and be analysed for $\delta^{17}O$ and $\delta^{18}O$. No change of isotopic composition by more than 0.01 ‰ was found for $\delta^{15}N$ and $\delta^{17}O$ and no more than 0.02 ‰ for $\delta^{18}O$

From the results of all analyses, a non-weighted mean of $\delta^{15}N_{air} = (-13.10\pm0.03)$ ‰ for the working standard can be calculated (Figure 4). This results was checked by measurement against

the pure N_2 reference material N-SVEC obtained from NIST, Gaithersburg, USA. N-SVEC has been calibrated against air-N_2 in a laboratory intercomparison which resulted in a value of $\delta^{15}N_{air} = (-2.78 \pm 0.04)$ ‰. Measurements of N-SVEC versus the N_2 working standard gave a difference of (10.46±0.01) ‰ which translates into a value of $\delta^{15}N_{air} = (-13.10 \pm 0.04)$ ‰ for the N_2 working standard, in perfect agreement with the direct calibration against air-N_2.

2.3.3 Nitrogen isotope analysis of the N_2O working standard

N_2 from the Pt/C combustion or the N_2/O_2 mixture from the decomposition on gold were frozen out on silica gel and transferred to the isotope ratio mass spectrometer for nitrogen isotope analysis. N_2 could be analysed directly, but the N_2/O_2 mixture (33.3 % O_2, 66.7 % N_2) was analysed against a mixture of the N_2 working standard with the same amount of O_2.

Figure 6 shows the results for the two procedures. For the Pt/C combustion a mean $\delta^{15}N$ of (14.25±0.09) ‰ versus the N_2 working standard is calculated; for the decomposition to N_2 and O_2 one finds (14.31±0.04) ‰ (Table 4). Both values are in good agreement and as a best estimate for $\delta^{15}N(N_2O)$ against the working standard, an error-weighted average of (14.30±0.05) ‰ is computed. With the value of $\delta^{15}N_{air}(N_2$ working standard$) = (-13.10 \pm 0.03)$ ‰ (section 2.3.2), this gives a final value for the average nitrogen isotope composition of the N_2O working standard of $\delta^{15}N_{air} = (1.01 \pm 0.03)$ ‰.

2.3.4 Calibration of the O_2 working standard

The O_2 working standard calibration relies on the calibration of our CO_2 working standard. The latter standard is well characterised by calibration against NBS-19-CO_2 (which isotopic composition has been fixed to establish the VPDB-CO_2 scale; see Table 2), direct intercomparison with other laboratories and by comparison with gaseous CO_2 reference samples (NIST RM 8562, 8563 and 8564). Conversion from the VPDB-CO_2 scale to the VSMOW scale is done using the conversion factors recommended by IAEA, i.e. $^{18}R(\text{VPDB-CO}_2) = 1.041467 \cdot {}^{18}R(\text{VSMOW})$.

The set-up used by two of the three analysts who have calibrated our O_2 working standard has been described before [*Röckmann*, 1998]. In brief, O_2 is combusted at 550 °C by activated charcoal in a platinum mesh cup which itself is placed inside a cup made out of a sheathed thermocouple [*Brenninkmeijer and Hemmingsen*, 1988]. Temperature is controlled by an additional thermocouple sensor. CO_2 is frozen out at the bottom of the reaction vessel (≈ 0.5 dm^3) by liquid N_2. Before transfer of the CO_2 to a sample bottle, the charcoal is cooled down to ≈ 200 °C, in order to reconvert CO to CO_2 via the Boudouard equilibrium ($2\,CO \rightleftharpoons C + CO_2$). The second set-up differs mainly in its dimensions from the one just described, in an effort to reduce the pressure so that the reaction temperature stays as low as possible. In addition, the reaction gas mixture is re-

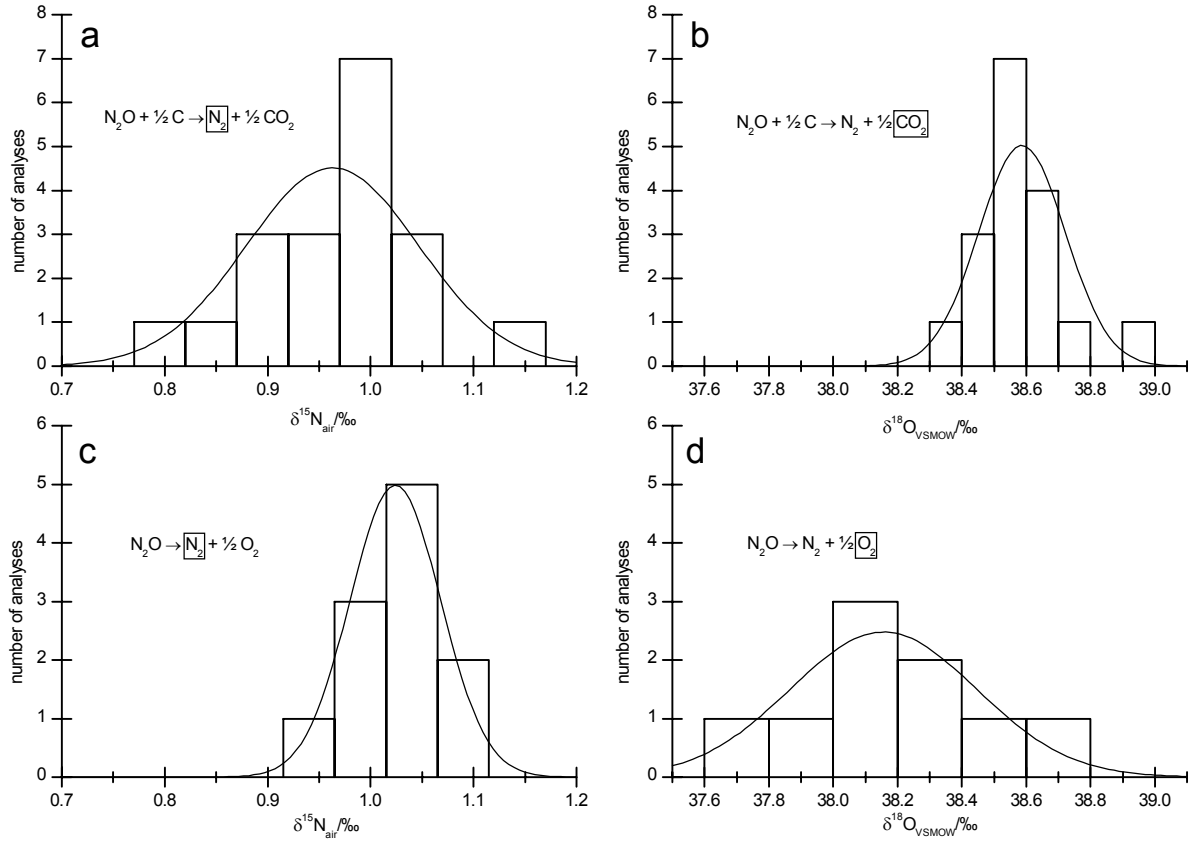

Figure 6: Histograms of the results from the Pt/C conversions and the decompositions of the N_2O working standard on a gold surface. The species which was analysed has been marked by a box. The Gaussian curves have been calculated from mean and standard deviation of the N_2; O_2 and CO_2 analyses against the corresponding working standards, so that they only reflect the variability of the conversions/decompositions, not the uncertainties of the working standard calibration. The Gaussian curves have been scaled to match the area of the histograms.

circulated by thermal convection maintained by alternately cooling and heating the bottom part of the reactor. The results from the three sets of experiments agree reasonably well (Figure 7), so that an weighted average of $\delta^{18}O_{VSMOW}$(O_2 working standard) = (15.14±0.12) ‰ is calculated.

2.3.5 Oxygen isotope analysis of the N_2O working standard

CO_2 from the Pt/C conversion could be measured directly against the CO_2 working standard of known isotopic composition, $\delta^{18}O_{VPDB\text{-}CO_2}$ = (–29.22±0.14) ‰. O_2 from the decomposition on gold was first separated from N_2 on a preparatory GC system (see section 2.3.2 and Figure 46) before it could be analysed against the O_2 working standard. Figure 6 and Table 4 give an overview of the results from both approaches. After conversion to the VSMOW-scale, the results from the Pt/C conversion give $\delta^{18}O_{VSMOW}$(N_2O working standard) = (38.59±0.20) ‰, those from the decomposition on gold yield $\delta^{18}O_{VSMOW}$(N_2O working standard) = (38.15±0.29) ‰. Taking both results together, a weighted average of $\delta^{18}O_{VSMOW}$ = (38.45±0.22) ‰ is assigned to our N_2O

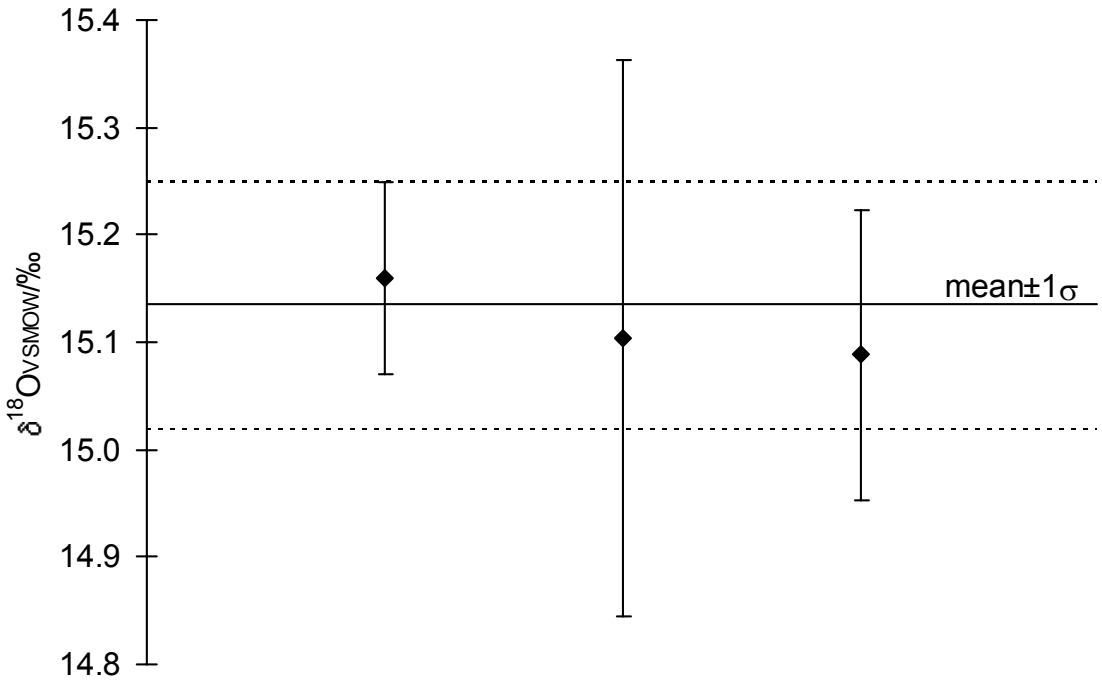

Figure 7: Calibration of the O_2 working standard. Results from three different analysts using two different systems are shown to agree quite well. A weighted average of (15.14±0.12) ‰ can be calculated.

working standard. The precision of the results hinges not only upon the N_2O decomposition reactions, but also on the precision of the calibration of O_2 and CO_2 working standards and is therefore deemed satisfactory. Nevertheless, improvements may be possible in the future.

2.4 Position-dependent calibration

The analysis of position-dependent ^{15}N isotope ratios in N_2O relies on measurements of the NO^+ fragment as noted in 2.2. Therefore, the ion current ratios on m/z 30 and m/z 31 are monitored. Ideally, mass 31 fragments should only stem from $^{14}N^{14}N^{17}O$ or $^{14}N^{15}N^{16}O$. However, some scrambling occurs in the ion source which produces $^{15}N^{16}O^+$ ions next to $^{14}N^{16}O^+$ from $^{15}N^{14}NO$ and vice versa for $^{14}N^{15}N^{16}O$, presumably via a cyclic intermediate. Such an effect was already noted by Friedman and Bigeleisen [1950] and has to be accounted for in the calculation of the position-dependent isotope ratios of N_2O. To this end, a scrambling coefficient *s* was introduced in the relevant equations for the fragment isotope ratio (cf. eqn. 24).

2.4.1 Determination of the scrambling coefficient *s*

The scrambling coefficient *s* was determined by analysis of samples of pure $^{15}N^{14}NO$ and $^{14}N^{15}NO$. The purity of the samples was ascertained by mass-spectrometry and Fourier transform infrared spectroscopy. According to the mass spectrometric analyses the samples contained 0.36

to 0.39 % $^{14}N_2{}^{16}O$, 98.96 to 98.99 % $^{14}N^{15}N^{16}O$ + $^{15}N^{14}N^{16}O$, 0.44 % $^{15}N_2{}^{16}O$ + $^{14}N^{15}N^{17}O$ + $^{15}N^{14}N^{17}O$ and 0.21 % $^{14}N^{15}N^{18}O$ + $^{15}N^{14}N^{18}O$. Contamination by CO_2 was less than 0.01 % and therefore negligible. FTIR proved that the isotopomeric purity (i.e. the contribution of the isotopomer stated on the label compared to the sum of $^{14}N^{15}N^{16}O$+$^{15}N^{14}N^{16}O$) was ≥99.9%. The value of 0.21 % for $^{14}N^{15}N^{18}O$ + $^{15}N^{14}N^{18}O$ showed that oxygen isotope ratios were normal. Because of the low $^{14}N_2{}^{16}O$ abundance, contributions by $^{14}N_2{}^{17}O$ and$^{14}N_2{}^{18}O$ were negligible. The scrambling coefficient can be determined essentially from the ratio of ion currents on m/z 31 and m/z 30 for $^{15}N^{14}N^{16}O$ and the reciprocal ratio for $^{14}N^{15}N^{16}O$. However, corrections have to be applied for the contribution of $^{14}N_2{}^{16}O$ to m/z 30 as well as for $^{15}N_2{}^{16}O$ and $^{15}N^{14}N^{17}O$ to m/z 31 ($^{15}N^{14}N^{17}O$ is only relevant for $^{15}N^{14}N^{16}O$). Assuming a $^{17}O/^{16}O$ ratio of 0.00038 and the above contributions from undesired N_2O species, these corrections amount to a change of the raw 31/30 ratio from, e.g., 8.60 % to 8.23 % for $^{15}N^{14}NO$. Under mass-spectrometric standard conditions, we thus find a very stable value of $s = (8.22 \pm 0.01)$ %. Allowing for a 0.1 % cross-contamination by the other than the desired isotopomer results in a relative decrease of s by about 1 % which is negligible for the precision of the final position-dependent analysis. However, s was significantly lower when an aged filament was in use: (7.89±0.01) %. Other ion source parameters had a minor influence, but this results means that in case of long-term monitoring studies s should be determined on a regular basis in order to avoid systematic errors in the final results. For the present case, such a variation was deemed irrelevant since the experimental studies were of rather short duration (of the order of months rather than years).

2.4.2 Calibration of the working standard

Toyoda and Yoshida [1999] have considered four procedures for a position-dependent calibration of the N_2O working standard:

- synthesis of N_2O from NH_4NO_3 with known $^{15}N/^{14}N$ ratios in ammonium and nitrate
- measurement relative to pure NO of known isotopic composition
- preparation of calibrated N_2O mixtures from $^{14}N^{15}NO$, $^{15}N^{14}NO$ and $^{14}N_2O$
- another analytical method, such as infrared absorption spectroscopy

The authors used the first two methods for calibration of their standard, but encountered experimental difficulties in the second approach. The third approach was rejected because commercially available samples of high isotopic purity were lacking.

Here we describe yet another method to obtain position-dependent information on the N_2O working standard by a purely mass spectrometric technique. It can be implemented in less than a day and gives a comparable precision to the calibration by NH_4NO_3 decomposition. The method consists in addition of pure $^{15}N_2O$ to the N_2O working standard and mass spectrometric meas-

urement of $^{46}\delta$ and $^{31}\delta$, i.e. the isotope ratios of molecular and NO^+ fragment ions in the mixture relative to those in the working standard. $^{45}\delta$ is monitored as control for a possible contamination of $^{15}N_2O$ by $^{14}N^{15}N^{16}O$ and $^{15}N^{14}N^{16}O$. This procedure avoids gravimetric or manometric preparation of calibrated gas mixtures which is difficult to accomplish by standard techniques with the required precision of less than 1 ‰. Rather the isotope ratio mass spectrometer itself is used as a tool for calibration which can measure relative isotope ratios with a precision of $\approx 10^{-5}$.

However, the following calculations demonstrate that the quality of the calibration relies also on the accuracy of the absolute isotope ratios of the standard and therefore ultimately on the accuracy of the isotope ratios of the international standards (Table 2), in this case particularly VSMOW. Fortunately, VSMOW is one of the best characterised international standards with a relative error of 0.2 ‰ in its absolute isotope ratio.

The isotope ratios of the working standard are taken from equations 14b and 24a, i.e.

$$^{46}R_{st} = (^{15}R_{1,st} + ^{15}R_{2,st})\ ^{17}R_{st} + ^{18}R_{st} + ^{15}R_{1,st}\ ^{15}R_{2,st} \tag{14b}$$

$$^{31}R_{s,st} = \frac{s\ ^{15}R_{1,st} + (1-s)\ ^{15}R_{2,st} + ^{15}R_{1,st}\ ^{15}R_{2,st}}{1 + s\ ^{15}R_{2,st} + (1-s)\ ^{15}R_{1,st}} + ^{17}R_{st} \tag{24a}$$

The term $^{15}R_1\,^{15}R_2$ in both equations stem from the statistically expected contribution of $^{15}N_2{}^{16}O$ in the sample. If additional $^{15}N_2{}^{16}O$ is mixed with the standard, this term changes which we express by the symbol $^{15}R_{12}$. Thus, the isotope ratios of the amended standard are

$$^{46}R = (^{15}R_{1,st} + ^{15}R_{2,st})\ ^{17}R_{st} + ^{18}R_{st} + ^{15}R_{1,st}\ ^{15}R_{2,st} + ^{15}R_{12} \tag{34}$$

$$^{31}R_s = ^{31}R_{s,st} = \frac{s\ ^{15}R_{1,st} + (1-s)\ ^{15}R_{2,st} + ^{15}R_{1,st}\ ^{15}R_{2,st} + ^{15}R_{12}}{1 + s\ ^{15}R_{2,st} + (1-s)\ ^{15}R_{1,st}} + ^{17}R_{st} \tag{35}$$

The expected relation between $^{46}\delta$ and $^{31}\delta$ can then be calculated from 14b, 24a, 34 and35:

$$^{46}\delta = \frac{^{46}R}{^{46}R_{st}} - 1 = \frac{^{15}R_{12}}{^{46}R_{st}} \tag{36}$$

$$^{31}\delta = \frac{^{31}R_s}{^{31}R_{s,st}} - 1 = \frac{^{15}R_{12}}{^{31}R_{s,st}\left[1 + s\ ^{15}R_{2,st} + (1-s)\ ^{15}R_{1,st}\right]} \tag{37}$$

Obviously, a plot of $^{31}\delta$ versus $^{46}\delta$ is expected to give a straight line with the slope $^{46}R_{st}/^{31}R_{s,st}$ $[1+s^{15}R_{2,st}+(1-s)^{15}R_{1,st}]^{-1}$. This slope can be used to derive $^{15}R_{2,st}$ and $^{15}R_{1,st}$. $^{46}R_{st}$ is known with a precision of $2.2\cdot10^{-4}$ relative to VSMOW (Table 4) and the absolute isotope ratio of VSMOW itself is known to within $2.2\cdot10^{-4}$ (Table 2) which translates into a precision of $^{46}R_{st}$ of 0.31 ‰. Additional parameters needed for this calculation are the scrambling coefficient s (see section 2.4.1), the average $^{15}N/^{14}N$ isotope ratio of the standard (Table 4), i.e. $^{15}R_{st} = (^{15}R_{1,st}+^{15}R_{2,st})/2$, and $^{17}R_{st}$ (calculated from a mass-dependent relation to ^{18}O, cf. section 2.7.3).

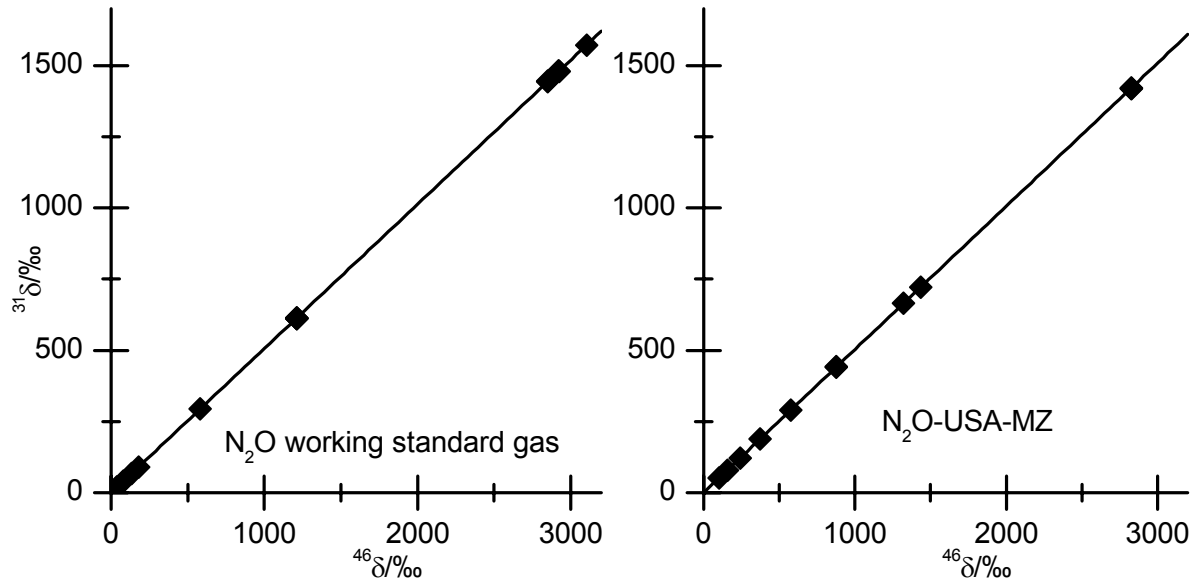

Figure 8: Change of $^{31}\delta$ versus $^{46}\delta$ for addition of $^{15}N_2O$ to N_2O working standard gas (*Messer Griesheim*, grade 6.0) and another sample of N_2O (N_2O-USA-MZ) which is known to be derived from adipic acid production (*Puritan-Bennet Medical Gases*, grade 2.2). Mass-spectrometric errors are smaller than the symbol sizes. The slope of these plots can be used derived to the position-dependent ^{15}N isotope ratios of the initial N_2O as described in the main text. Analysis of N_2O-USA-MZ versus the N_2O working standard gave $\delta^{15}N = (-2.78\pm0.01)$ ‰, $\delta^{18}O = (1.95\pm0.02)$ ‰, $^{1}\delta^{15}N = (-17.76\pm0.10)$ ‰ and $^{2}\delta^{15}N = (11.62\pm0.10)$ ‰.

Plots of $^{31}\delta$ versus $^{46}\delta$ are shown in Figure 8. Linear least squares regression analysis gives slopes of 0.50683±0.00010 and 0.50259±0.00011 for the N_2O working standard and N_2O-USA-MZ, respectively; ordinate offsets are (–0.31±0.16) ‰ and (0.84±0.19) ‰, respectively. However, this analysis does not take into account mass-spectrometric errors of $^{31}\delta$ and $^{46}\delta$. Therefore, a more sophisticated analysis which considers these errors was implemented according to the approach of Williamson [1968]. Slightly larger slopes of 0.50695±0.00012 and 0.50286±0.00015 are derived with ordinate offsets of (–0.32±0.11) ‰ and (0.62±0.17) ‰ for N_2O working standard and N_2O-USA-MZ, respectively. All MS analyses have been performed on a *Finnigan* MAT 252 mass-spectrometer which has a reduced precision for $^{31}\delta$ analysis because measurements had to be done with the cup configuration installed for oxygen isotope analysis (see 2.6 for details). This accounts for the small y-axis offsets.

In principle, one could now proceed to calculate the position-dependent isotope ratios of the two gases. However, it was noted that $^{45}\delta$ increased as well along with the addition of $^{15}N_2O$ (Figure 9). This indicates the presence of a contamination of mass 45 in the $^{15}N_2O$ material. If it is due to $^{15}N^{14}N^{16}O$ and/or $^{14}N^{15}N^{16}O$ this affects also the $^{31}\delta$ measurement, but not the $^{46}\delta$ measurement, thus changing the slope $\partial^{31}\delta/\partial^{46}\delta$. Such an artefact has to be taken into account in

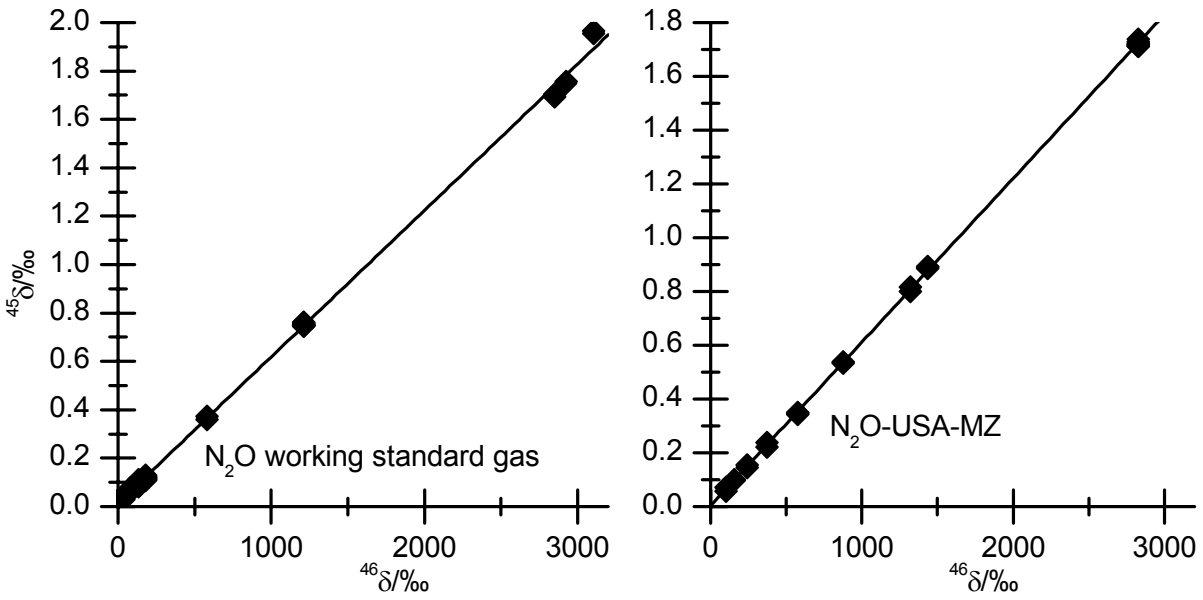

Figure 9: Plots of $^{45}\delta$ versus $^{46}\delta$ for addition of $^{15}N_2O$ to samples of N_2O. Note the change of ordinate scale compared to Figure 8. Linear least squares regression gives:
$^{45}\delta(\text{working standard}) = (605.2\pm3.8)\cdot10^{-6}\ ^{46}\delta(\text{working standard})+(0.014\pm0.006)$ ‰
$^{45}\delta(\text{USA-MZ}) = (608.5\pm1.4)\cdot10^{-6}\ ^{46}\delta(\text{USA-MZ})+(0.003\pm0.003)$ ‰.

calculation of $^{15}R_1$ and $^{15}R_2$. Therefore, the ion currents at m/z 44, 45, 46, 47 and 48 for "$^{15}N_2O$" were determined and normalised to the total ion current of these masses. Contributions of 0.02 %, 0.21 %, 99.52 %, 0.04 ‰ and 0.21 %, respectively could be identified. This documents the high purity of the $^{15}N_2O$ sample, but shows also a small isotopic contamination on m/z 45. The shares of mass 47 and 48 indicate a normal oxygen isotope composition of $^{15}N_2O$. The minor signal on m/z 44 was caused quantitatively by CO_2 as shown through measurement of $^{12}C^+$ and CO_2^{2+}. The signal at m/z 45 must therefore be caused by $^{15}N^{14}N^{16}O$ and $^{14}N^{15}N^{16}O$ since $^{13}C^{16}O_2$ should make only a very minor contribution. A ratio of the contamination to the desired isotopologue $(^{15}N_2{}^{16}O)$ $\left[x(^{14}N^{15}N^{16}O)+x(^{15}N^{14}N^{16}O)\right]/x(^{15}N_2{}^{16}O) = 464$ is calculated. However, this may have been slightly altered by mass discrimination effects in inlet or ion source. A more accurate estimate can be derived from the plot of $^{45}\delta$ vs $^{46}\delta$. By similar considerations as for $^{31}\delta$ and $^{46}\delta$ above the following relation between $^{45}\delta$ and $^{46}\delta$ is found:

$$\frac{^{45}\delta}{^{46}\delta} = \frac{^{46}R_{st}}{^{45}R_{st}}\,\frac{x(^{14}N^{15}N^{16}O)+x(^{15}N^{14}N^{16}O)}{x(^{15}N_2{}^{16}O)} \qquad (38)$$

$^{46}R_{st}/^{45}R_{st}$ is known from the calibration of the N_2O working standard (Table 4) and can be inferred for N_2O-USA-MZ from its δ values measured against the N_2O working standard (see caption of Figure 8). This ratio amounts to 3.692 and 3.675 for the two gases, respectively. Hence, $\left[x(^{14}N^{15}N^{16}O)+x(^{15}N^{14}N^{16}O)\right]/x(^{15}N_2{}^{16}O) = (448\pm3)$ is derived from the N_2O work-

ing standard from the slopes indicated in the caption of Figure 9, in agreement with the value of (447±1) derived from N_2O-USA-MZ.

Assuming a symmetric distribution of ^{15}N in the m/z 45 contamination and using the best estimates for $^{46}R_{st}$, $^{17}R_{st}$, $^{15}R_{st}$ and s one can derive a value of 0.4899 for the parameter $f = R_{1,st}/(R_{1,st}+R_{2,st})$ (eqn. 25). Neglecting the contribution of $^{15}N^{14}N^{16}O$ and $^{14}N^{15}N^{16}O$ in the $^{15}N_2O$ material would have resulted in $f(N_2O$ working standard$) = 0.4907$. An estimate of the cumulative error in f of 0.0003 can be made which takes into account the uncertainties of the slope $\partial^{31}\delta/\partial^{46}\delta$, s, $R^{18}O$(VSMOW) (Table 2), $\delta^{18}O_{VSMOW}(N_2O$ working standard) (Table 4) and allows for an asymmetry of the distribution of ^{15}N in the m/z 45 contamination amounting to an enrichment of $^{14}N^{15}N^{16}O$ over $^{15}N^{14}N^{16}O$ by 100 ‰ or vice versa. This is most likely an overestimate. We rather expect a symmetric distribution of ^{15}N between these two isotopomers, because $^{15}N_2O$ is (by definition) equally enriched at both nitrogen positions in the molecule. Finally, we calculate the values of $^1\delta^{15}N_{air}$ and $^2\delta^{15}N_{air}$ for the N_2O working standard using $\delta^{15}N = (1.01\pm0.03)$ ‰ (Table 4) and $f(N_2O$ working standard$) = 0.4907\pm0.0003$ which results in $^1\delta^{15}N_{air} = (-19.2\pm0.6)$ ‰ and $^2\delta^{15}N_{air} = (21.2\pm0.6)$. This shows an unexpected depletion of the terminal position in ^{15}N relative to the central position by 41.1 ‰.

The validity of this procedure was checked by measurement of a sample of N_2O-USA-MZ which had similar average ^{15}N and ^{18}O isotope ratios as the N_2O working standard, but was enriched at the terminal and depleted at the central position. With $\delta^{15}N = -2.78$ ‰ and $\delta^{18}O = 1.95$ ‰ as bulk isotopic composition of N_2O-USA-MZ versus the working standard and performing the same calculations as for the N_2O working standard above, the value of $\partial^{31}\delta/\partial^{46}\delta = (0.50286\pm0.00015)$ translates into $f(N_2O$-USA-MZ$) = (0.4814\pm0.0004)$. This agrees fairly well with a value of $f(N_2O$-USA-MZ$) = (0.4826\pm0.0004)$ derived from the direct measurement of the position-dependent isotope ratios in N_2O-USA-MZ against the working standard and $f(N_2O$ working standard$) = 0.4907\pm0.0003$.

Toyoda and Yoshida [1999] have measured $^1\delta^{15}N_{air} = (0.2\pm0.8)$ ‰ and $^2\delta^{15}N_{air} = (-4.0\pm0.4)$ ‰ for their N_2O standard which translates into $f = 0.5011\pm0.0002$. The average ^{15}N composition of their standard (–1.9 ‰ from the average of $^1\delta^{15}N_{air}$ and $^2\delta^{15}N_{air}$ or –2.2 ‰ from conversion with graphite) is similar to ours (+1.1 ‰), but the position-dependent enrichment is clearly distinct. The $^{18}O_{VSMOW}$ composition of their standard (23.3 ‰) deviates also clearly from ours (38.5 ‰) and is closer to atmospheric oxygen (23.7 ‰, revised value from [*Kroopnick and Craig*, 1972], cf. section 2.7.3). Commercial N_2O production starts usually from NH_4NO_3 [*Thiemann et al.*, 1991], but some manufacturers also extract it from exhaust gas in adipic acid production (as in the case of our sample of N_2O-USA-MZ obtained from *Puritan-Bennet Medical Gases*). Tracing back the

original source of our N_2O working standard proved to be difficult, because the supplier (*Messer-Griesheim*) only acts as a distributor of batches obtained on the world market. Most likely though, the working standard stems from *Ijsfabriek Strombeek*, Belgium, and is made by decomposition of NH_4NO_3. The ^{15}N and ^{18}O isotopic composition of NH_4NO_3 is expected to be close to air because NH_3 is produced from air-N_2 in the Haber-Bosch process and HNO_3 is made my NH_3 oxidation with air (Ostwald process) [*Thiemann et al.*, 1991]. However, isotopic fractionation may occur in later purification steps which presumably proceeds through distillation to obtain the high-purity (grade 6.0 equivalent to 99.9999 %) of our N_2O working standard. Vapour pressures of isotopic N_2O species are known to increase in the order $^{14}N_2{}^{18}O < {}^{15}N^{14}N^{16}O < {}^{14}N^{15}N^{16}O < {}^{14}N_2{}^{16}O$ [*Jancso and van Hook*, 1974] which may explain the enrichment of $^{14}N^{15}N^{16}O$ over $^{15}N^{14}N^{16}O$ as well as the enrichment of our working standard's $\delta^{18}O = 14.4$ ‰ relative to air-O_2. A future direct comparison of the position-dependent calibration from both groups is desirable to check the results obtained.

2.5 Conventional isotope analyses: $\delta^{18}O$, $\delta^{15}N$

As N_2O is isobaric to CO_2, it is possible to use the same three Faraday cups for both gases on a isotope ratio mass spectrometer. For most analyses, a *Finnigan* MAT 252 instrument was used which was equipped with a dual-inlet system comprising also two cold fingers (or micro-volumes) for analyses of small samples (down to 200 nmol). On some occasions, results were obtained on other machines (*Micromass* Prism II for $^{31}NO^+$ analyses; *Finnigan* DELTA^{plus} XL mainly for online-analysis of stratospheric samples, see section 7). Intercomparison did not show any significant differences for the three machines. Internal precision (1σ) is best on the MAT 252 ($\approx$0.01 ‰ for $\delta^{15}N$, $\approx$0.02 ‰ for $\delta^{18}O$), but only slightly worse on the other two instruments.

The $\delta^{18}O$ and $\delta^{15}N$ (bulk) values are calculated from N_2O isotope ratios of masses 44, 45 and 46 based on equations 18a and b. Due to diffusion of air into the sample flasks a correction for CO_2 interference is necessary, especially for smaller samples (section 2.8).

The corrected $^{45}\delta$ and $^{46}\delta$ values have to be subjected to a ^{17}O correction. It is inferred from the relation $^{17}R = 0.00937035 \cdot (^{18}R)^{0.516}$ (section 2.7.2), but only applies to mass-dependently fractionated N_2O. In contrast, atmospheric N_2O displays an oxygen isotope anomaly (chapter 10). The required downward correction of $\delta^{15}N$ is about 0.05 ‰ and 0.001 ‰ for $\delta^{18}O$, the latter being negligible in view of the internal mass-spectrometric precision of about 0.02 ‰. The magnitude of the correction is calculated from a modification of equations 8 and 18a,b according to Tanaka *et al.* [1995]:

$$\delta^{15}\mathrm{N} = {}^{45}\delta\left(1+\frac{{}^{17}R_{\mathrm{st}}}{2\,{}^{15}R_{\mathrm{st}}}\right)-\delta^{17}\mathrm{O}\frac{{}^{17}R_{\mathrm{st}}}{2\,{}^{15}R_{\mathrm{st}}} \tag{39}$$

$$\begin{aligned}\delta^{18}\mathrm{O} = {}^{46}\delta&\left[1+\frac{2\,{}^{15}R_{\mathrm{st}}\,{}^{17}R_{\mathrm{st}}+({}^{15}R_{\mathrm{st}})^2}{{}^{18}R_{\mathrm{st}}}\right]-\delta^{15}\mathrm{N}\left(2+\delta^{15}\mathrm{N}\right)\frac{({}^{15}R_{\mathrm{st}})^2}{{}^{18}R_{\mathrm{st}}}\\&-\left(\delta^{15}\mathrm{N}+\delta^{17}\mathrm{O}+\delta^{15}\mathrm{N}\delta^{17}\mathrm{O}\right)\frac{2\,{}^{15}R_{\mathrm{st}}\,{}^{17}R_{\mathrm{st}}}{{}^{18}R_{\mathrm{st}}}\end{aligned} \tag{40}$$

The difference between the true value $\delta^{17}O$ and the "mass-dependent" value $\delta^{17}O_{md} = (1+\delta^{18}O)^{\beta}-1$ (calculated according to eqn. 17) is defined as

$$\Delta^{17}\mathrm{O} \equiv \frac{\delta^{17}\mathrm{O}-\delta^{17}\mathrm{O}_{\mathrm{md}}}{1+\delta^{17}\mathrm{O}_{\mathrm{md}}} = \frac{1+\delta^{17}\mathrm{O}}{\left(1+\delta^{18}\mathrm{O}\right)^{\beta}}-1 \tag{41}$$

$\Delta^{17}O$ is neither identical to the conventional definition [*Clayton and Mayeda*, 1988] (cf. 2.7.2)

$$\Delta^{17}\mathrm{O}' \equiv \delta^{17}\mathrm{O}-\gamma\delta^{18}\mathrm{O} \tag{42}$$

nor to an alternative proposed by Miller [2002]

$$\Delta^{17}\mathrm{O}'' \equiv \ln\frac{1+\delta^{17}\mathrm{O}}{\left(1+\delta^{18}\mathrm{O}\right)^{\beta}} \tag{43}$$

but is preferred because it does not involve any approximations and uses standard addition rules for δ values (footnote 4, page 17). The differences/corrections $\Delta^{15}N$ and $\Delta^{18}O$ are defined accordingly. If we assume $\Delta^{17}O \approx 0.9$ ‰ (section 10.1), the following values for $\Delta^{15}N$ and $\Delta^{18}O$ result (neglecting terms with products of δ values):

$$\Delta^{15}\mathrm{N} = -\frac{{}^{17}R_{\mathrm{st}}}{2\,{}^{15}R_{\mathrm{st}}}\frac{1+\delta^{17}\mathrm{O}_{\mathrm{md}}}{1+\delta^{15}\mathrm{N}_{\mathrm{md}}}\Delta^{17}\mathrm{O} \approx -0.05\,‰ \tag{44}$$

$$\begin{aligned}\Delta^{18}\mathrm{O} &\approx -\frac{2({}^{15}R_{\mathrm{st}})^2}{{}^{18}R_{\mathrm{st}}}\frac{\Delta^{15}\mathrm{N}(1+\delta^{15}\mathrm{N}_{\mathrm{md}})}{1+\delta^{18}\mathrm{O}_{\mathrm{md}}}-\frac{2\,{}^{15}R_{\mathrm{st}}\,{}^{17}R_{\mathrm{st}}}{{}^{18}R_{\mathrm{st}}}\frac{\Delta^{15}\mathrm{N}(1+\delta^{15}\mathrm{N}_{\mathrm{md}})+\Delta^{17}\mathrm{O}(1+\delta^{17}\mathrm{O}_{\mathrm{md}})}{1+\delta^{18}\mathrm{O}_{\mathrm{md}}}\\&\approx -0.001\,‰\end{aligned} \tag{45}$$

2.6 NO^+ fragment ion analyses: $^2\delta^{15}N$, $^1\delta^{15}N$

In the beginning stage of the experiments reported on in here, the position-dependent isotopic composition of N_2O was analysed on a *Micromass* Prism II isotope ratio mass spectrometer with one fixed and two adjustable collectors for measurement of the NO^+ ion fragment [*Brenninkmeijer and Röckmann*, 1999]. On our MAT 252 instrument, this is only possible with reduced precision (0.5 ‰ standard deviation, 95 % standard error between 0.1 and 0.2 ‰ for ten measurement cycles) since masses 30 and 31 cannot be resolved sufficiently using the O_2 or N_2

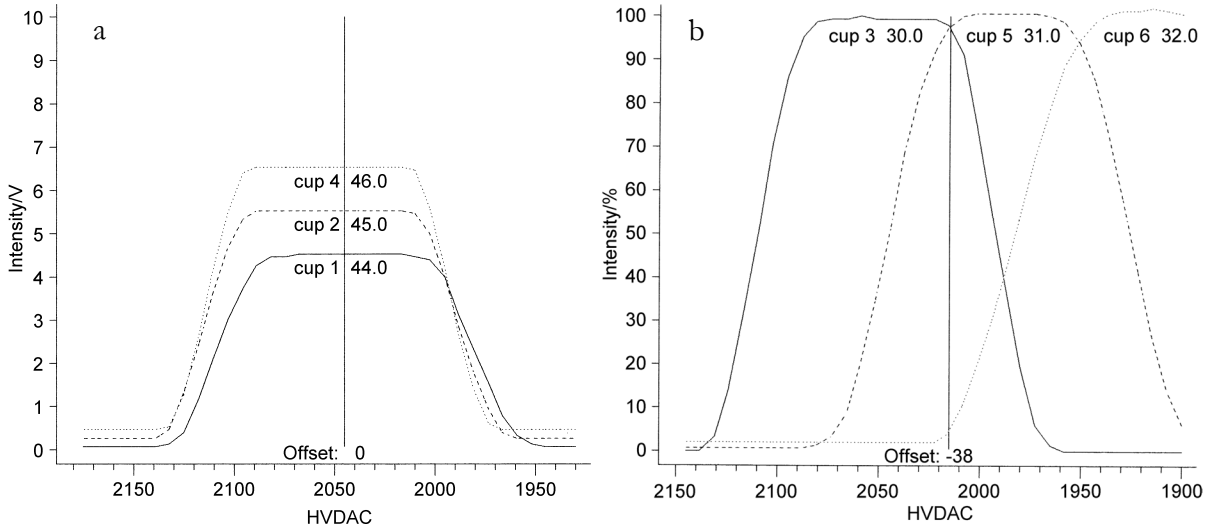

Figure 10: Peak shapes of CO_2 (a) and of NO^+ fragment analysis (b) on the MAT 252 instrument. N_2O looks similar to CO_2, but with inverse order of voltages. In case of NO^+ the centre of the ion beam does not coincide with the centre of the Faraday cup, because the collectors used for NO^+ analysis were initially intended for O_2 analysis (m/z 32 and 33) rather than NO (m/z 30 and 31). In practice, the ion beam is first centred on the mass 30 beam, and then offset to the point of intersection of mass 30 and 31 peaks. This lowers the precision, but does not change the accuracy of the results as was ascertained by intercomparison with 30/31 measurements on the Prism II and DELTA^{plus} XL instruments.

cups installed. One rather measures on the peak flanks (Figure 10b) which has adverse affects on the precision, but does not compromise the accuracy of the results.

In the ion source, the isotope ratios of the individual N atoms of the N_2O molecule undergo minor scrambling ($\approx$8.2 % section 2.4.1), i.e. 8.2 % of $^{15}N^{14}NO$ gives $^{14}N^{15}NO$) which has to be accounted for when calculating the final $^2\delta^{15}N$ value. $^1\delta^{15}N$ can then be inferred from $^2\delta^{15}N$ and $\delta^{15}N$ (bulk) using the formulas stated in section 2.2. Since the raw $^{31}\delta(NO)$ values do not differ significantly on the three isotope ratio mass spectrometers we used, one can assume that the scrambling coefficient s is the same in all cases.

From similar considerations as in the preceding section, it follows that the ^{17}O correction for $^2\delta^{15}N$ is about twice that for $\delta^{15}N$, i.e. $\approx$0.09 ‰ for $\Delta^{17}O \approx 0.9$ ‰.

2.7 Analysis of $\delta^{17}O$

2.7.1 Techniques: N_2^+ fragment analysis

Direct mass spectrometric analysis of the $^{14}N_2{}^{17}O$ isotopologue is not a viable technique for ^{17}R analysis on a conventional isotope ratio mass spectrometer because such instruments only resolve integral masses (mass resolution $m/\Delta m \approx 200$). Thus, the fraction of about 5 % $^{14}N_2{}^{17}O$

contributing to m/z 45 (Table 3) cannot be separated from the dominant isobars $^{14}N^{15}N^{16}O$ and $^{15}N^{14}N^{16}O$. Therefore, three other techniques were considered for $\delta^{17}O$ analysis of N_2O:

- combustion with graphite to CO_2+N_2 (section 2.3.1) followed by CO_2 conversion to CH_4+H_2O and subsequent reaction of H_2O with F_2 to O_2+HF [*Brenninkmeijer and Röckmann*, 1998]
- decomposition on a gold surface to N_2 and O_2 (section 2.3.1) [*Cliff and Thiemens*, 1994]
- N_2^+ fragment analysis

The first two techniques rely on $\delta^{17}O$ and $\delta^{18}O$ analysis of O_2 and make use of established analytical techniques which have been described before while the third approach has not yet been tested and will therefore be described in the following.

The N_2^+ fragment analysis consists in measuring of $\delta^{15}N$ from fragments of mass 29 and 28 derived from N_2O. We make use of equations 14a and 22:

$$^{45}R = {}^{15}R_1 + {}^{15}R_2 + {}^{17}R \tag{14a}$$

$$^{29}R = {}^{15}R_1 + {}^{15}R_2 \tag{22}$$

The difference of these two relations gives ^{17}R directly. ^{45}R and ^{29}R are computed from $^{29}\delta$ and $^{45}\delta$ measurements and the corresponding molecular isotope ratios of the standard ($^{45}R_{st}$ and $^{29}R_{st}$). As in NO^+ fragment analysis, fractionation effects in N_2O fragmentation cancel because only relative measurements are made. However, there are two obstacles to this technique: First, the relative intensity of the N_2^+ fragment ion to the molecular N_2O^+ ion is merely ≈ 10 % which impairs the precision of N_2^+ fragment analysis. Second, $^{14}N_2{}^{17}O$ contributes not more than ≈ 5 % to mass 45 (Table 3) which puts high demands on $^{45}\delta$ precision as well. The influence of uncertainty in $^{45}\delta$ and $^{29}\delta$ can be seen if we rearrange eqn. 39 and substitute $\delta^{15}N = {}^{29}\delta$:

$$\delta^{17}O = {}^{45}\delta \frac{2^{15}R_{st} + {}^{17}R_{st}}{{}^{17}R_{st}} - \frac{2^{15}R_{st}}{{}^{17}R_{st}} \delta^{15}N = {}^{45}\delta \left(1 + \frac{2^{15}R_{st}}{{}^{17}R_{st}} \right) - \frac{2^{15}R_{st}}{{}^{17}R_{st}} {}^{29}\delta \tag{46}$$

Since $2^{15}R_{st}/{}^{17}R_{st} \approx 19$, uncertainties in $^{45}\delta$ and $^{29}\delta$ are amplified 20 and 19 times, respectively. To test the procedure in practice, repeated "zero enrichment" measurements were made of standard gas against standard gas. The raw data from ten alternate measurements gave on average $^{29}\delta = (0.006 \pm 0.063)$ ‰ and $^{45}\delta = (-0.002 \pm 0.003)$ ‰ which translates into an error of more than 1 ‰ for $\delta^{17}O$. However, it was noted that $^{29}\delta$ depended on the balance between sample and standard pressure in the bellows of the dual-inlet system of the MS. Over a small range of voltage differences between sample and standard (Figure 11a), one finds in this example a slope of (3.0±0.5) ‰/V, but over a larger range (Figure 11b) a slope of (5.1±0.1) ‰/V is derived. Detrending the data in Figure 11a with the smaller slope gives $^{29}\delta = (0.003 \pm 0.025)$ ‰, i.e. a much

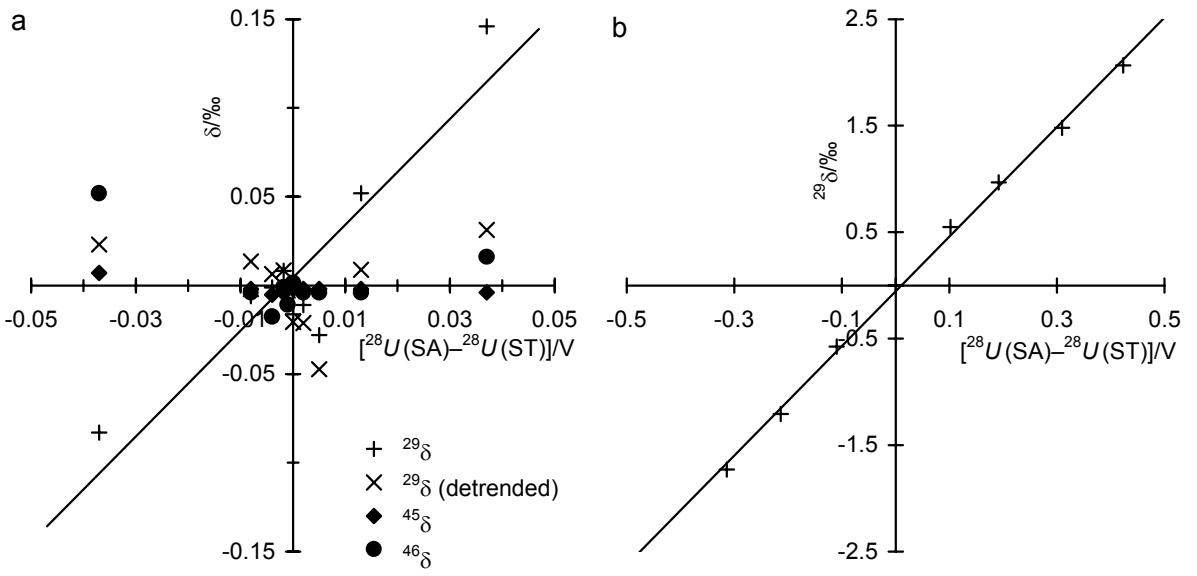

Figure 11: (a) Influence of imbalances in sample and standard signal size (equivalent to pressure) on the measured $^{45}\delta$, $^{46}\delta$ and $^{29}\delta$ values. No influence is discernible for $^{45}\delta$ and $^{46}\delta$ but $^{29}\delta$ is increasing linearly with the difference in mass 28 signal size. Removing the influence of the sample/standard imbalance gives the de-trended $^{29}\delta$ values.
(b) Influence of sample/standard imbalance over a larger range.

smaller standard deviation corresponding to an error in $\delta^{17}O$ of about 0.5 ‰. This is still not precise enough to quantify the oxygen isotope anomaly in atmospheric N_2O of about 1 ‰ (section 10.1). It was also tried to measure $\delta^{17}O$ in photolysis samples, but under these more realistic conditions the achievable precision was only ≈1.0 ‰. Within this error, no anomalous oxygen isotope fractionation by N_2O photolysis was detectable, in line with measurements and theoretical predictions (section 10.2).

2.7.2 Three-isotope exponent β for N_2O oxygen isotopologues

N_2O carries a "mass-independent" enrichment in its O isotopes, i.e. $\delta^{17}O$ is offset by a certain amount from the value expected for a mass-dependent relation to $\delta^{18}O$ [*Cliff and Thiemens*, 1997]. This is commonly expressed as $\Delta^{17}O \equiv \delta^{17}O - \gamma\,\delta^{18}O$ [*Clayton and Mayeda*, 1988] (cf. eqn. 42). γ describes the mass-dependent fractionation law of oxygen isotopologues.

According to this relation, a range of mass-dependently fractionated N_2O samples should have a linear relation between $\delta^{17}O$ and $\delta^{18}O$, but note that this definition bears an inherent problem: From the relation $^{17}R = A\cdot(^{18}R)^{\beta}$ (eqn. 17) one can deduce that

$$(1+\delta^{17}O)=(1+\delta^{18}O)^{\beta} \qquad (47)$$

and $\ln(1+\delta^{17}O) = \beta\ \ln(1+\delta^{18}O)$ [*Li and Meijer*, 1998]. Expansion of the natural logarithm $\ln(1+x) = 1+x+x^2+...$ and neglecting second and higher order terms results in a linear relation-

ship between $\delta^{17}O$ and $\delta^{18}O$, as assumed in the above definition of $\Delta^{17}O$. However, high values of $\delta^{18}O$ would lead to an apparent negative mass-independent fractionation (apparent ^{18}O excess), since the linear relationship is then not valid any more. In general, linear least squares regression of the same data-set of $\delta^{17}O$ and $\delta^{18}O$ values does not give the same values for the coefficients γ and β. The exact relationship between $\delta^{17}O$ and $\delta^{18}O$ (eqn. 47) is preferable for high-precision work and large ranges of $\delta^{18}O$.

In practice, the difference between γ derived from the linear slope γ of a $\delta^{17}O$ vs $\delta^{18}O$ plot and β from 47 might be small. It depends on the range of $\delta^{18}O$ being used for deriving the relationship between ^{17}O and ^{18}O isotope ratios. If the $\delta^{18}O$ values are distributed evenly about the origin of the $\delta^{17}O$–$\delta^{18}O$ co-ordinate system, linear least squares regression shows that the offset of the linear approximation from the curved exact relationship cancels, so that $\gamma = \beta$. Cliff and Thiemens [1997] report a slope of $\gamma = 0.515$ for a $\delta^{17}O$ vs $\delta^{18}O$ plot of mass-dependently fractionated N_2O samples spanning a range of $-9\text{ ‰} < \delta^{18}O < 19\text{ ‰}$ relative to atmospheric O_2. Assuming that the samples are spread evenly over this range of $\delta^{18}O$ with a spacing of 0.5 ‰, one can simulate that $\beta = 0.5162$ yields $\gamma = 0.5150 \pm 0.0001$, a y-axis offset of (-0.005 ± 0.001) ‰ and a correlation coefficient $r^2 = 0.999997$. Accordingly, the deviation of the approximation from linearity between $\delta^{17}O$ and $\delta^{18}O$ is quite small in this example. However, if the same set of δ values relative to air-O_2 is converted to $\delta^{18}O_{VSMOW}$ and $\delta^{17}O_{SMOW}$ (using $\delta^{18}O_{VSMOW}(\text{air}) = 23.50$ ‰ and $\delta^{17}O_{VSMOW}(\text{air}) = 11.92$ ‰ [*Luz et al.*, 1999] for the sake of argument, but see section 2.7.3), a $\delta^{17}O$ vs $\delta^{18}O$ plot returns a slope of $\gamma = 0.5092$. Of course, the relationship between $\delta^{17}O$ and $\delta^{18}O$ must not depend on the choice of reference standard. Eqn. 47 in contrast is standard independent.

From these considerations, we adopt $\beta = 0.516$ for use in eqn. 17. Hence, the parameter A in eqn. 17 is $A = ({}^{17}R_{VSMOW}/{}^{18}R_{VSMOW})^{\beta} = 0.00937035$ which implies that VSMOW and N_2O are lying on the same mass-dependent fractionation line.

2.7.3 Calibration of ^{17}O in the N_2O working standard

^{17}O calibration of N_2O is complicated by the fact that no gaseous international ^{17}O standard exists. The numbers quoted in Table 2 for the ^{17}O isotope composition of VPDB-CO_2 have been calculated rather than measured assuming a mass-dependent relation between ^{17}O and ^{18}O with $\beta = 0.5$. VSMOW/SMOW is the only existing standard with known $^{17}O/^{16}O$ isotope ratios. However, atmospheric oxygen was shown to have a rather constant enrichment of $\delta^{18}O = (23.5 \pm 0.3)$ ‰ against SMOW [*Kroopnick and Craig*, 1972] (measured on CO_2 from reaction

of carbon with air against CO_2 equilibrated with SMOW, i.e. SMOW-CO_2). This so-called Dole effect is caused mainly by isotopic fractionation in respiration and is expected to be constant over at least time-scales close to the atmospheric residence time of O_2 of about 1200 years [*Bender et al.*, 1994]. Based on a seasonal variation of the O_2/N_2 ratio in air of about 0.1 ‰ (with a maximum in northern hemisphere summer) and the fact that photosynthetic oxygen is close to the isotopic composition of the water from which it is produced, a seasonal variation of the $^{18}O/^{16}O$ ratio in air of 0.002 ‰ is expected [*Keeling*, 1995]. Therefore, the ^{17}O and ^{18}O isotopic composition of atmospheric O_2 may serve as a secondary reference material for gaseous samples. Its low variability was confirmed by recent measurements: Thiemens *et al.* [1995] report a value of $\delta^{18}O_{VSMOW} = (23.50\pm0.04)$ ‰ for tropospheric O_2 and show ten stratospheric and mesospheric samples with an average $\delta^{17}O_{VSMOW}$ of (11.90±0.14) ‰ (excluding two samples from the total of 12 with a significantly different $\delta^{18}O$ value of 23.1 ‰). According to Luz *et al.* [1999] the value of $\delta^{17}O_{VSMOW}$ for tropospheric air is (11.92±0.08) ‰, taking the standard deviation from footnote 18 in [*Thiemens et al.*, 1995] since the latter paper is given as reference for $\delta^{17}O_{VSMOW}$(air). These papers did not state how the O_2 working standards used have been calibrated against VSMOW.

Using the GC separation system for N_2 and O_2 (section 2.3.4), we have measured the oxygen isotopic composition of air-O_2 against our O_2 working standard. Mean values from 15 measurements give $\delta^{17}O = (4.34\pm0.04)$ ‰ and $\delta^{18}O = (8.42\pm0.03)$‰. With the ^{18}O calibration of the O_2 working standard against VSMOW ($\delta^{18}O_{VSMOW}/‰ = 15.14\pm0.12$) this results in $\delta^{18}O_{VSMOW}$(air) = (23.68±0.12) ‰, apparently higher than the "established" value of 23.5 ‰. However, we note that the value of 23.5 ‰ stated in [*Kroopnick and Craig*, 1972] has been measured against SMOW-CO_2 assuming an isotopic fractionation constant of (40.9±0.3) ‰ for the CO_2–H_2O isotope exchange. Meanwhile, the recommended value for this quantity has been revised upwards to 41.2 ‰ [*IAEA*, 1995]. In fact, Kroopnick and Craig themselves note that the uncertainty of this fractionation constant is the main source of uncertainty for their measurements. Their raw data rather give an uncertainty of only 0.14 ‰. Adopting the recommended value of 41.2 ‰, we derive from Kroopnick and Craig's data a revised estimate of (23.80±0.14) ‰ which agrees slightly better with our own measurements, but even exceeds them now. Moreover, direct fluorination of VSMOW gave O_2 with –23.205 ‰ against air-O_2 translating into $\delta^{18}O_{VSMOW}$(air) = 23.76 ‰ (*Boaz Luz*, personal communication, 2000). In conclusion, an upward revision of the "established" value of $\delta^{18}O_{VSMOW}$(air) may be needed, but additional measurements are required to improve the precision and check the accuracy of the results.

To calculate $\delta^{17}O_{VSMOW}$(N_2O working standard), we adopt the value of $\delta^{17}O_{VSMOW}$(air) = 11.92 ‰ from [*Luz et al.*, 1999], but scale it upwards to $\delta^{18}O_{VSMOW}$(air) = 23.68 ‰ using a three-

isotope exponent of $\beta = 0.510$ for atmospheric O_2 derived from ln(1.01192)/ln(1.02350). This yields $\delta^{17}O_{VSMOW}$(air) = (12.01±0.08) ‰. For $\delta^{17}O$(N_2O working standard) versus the O_2 working standard a value of (11.82±0.15)‰ was determined. Taken together with $\delta^{17}O_{air}$(O_2 working standard) = (4.34±0.04) ‰, this gives $\delta^{17}O_{VSMOW}$(N_2O working standard) = (19.55±0.18)‰. This value is compared with the one derived from the assumed mass-dependent relationship between ^{18}R and ^{17}R with $\beta = 0.516$ (cf. 2.7.2). With $\delta^{18}O_{VSMOW}$(N_2O working standard) = (38.45±0.22) ‰ (Table 4) one obtains $\delta^{17}O_{VSMOW}$(N_2O working standard) = (19.66±0.11) ‰ which agrees well with the value derived from the ^{17}O measurement against air-O_2. Had we assumed $\beta = 0.5$ instead, $\delta^{17}O_{VSMOW}$(N_2O working standard) would have been only (18.90±0.14) ‰.

2.8 CO_2 correction for N_2O isotope analysis

The CO_2 correction for N_2O analyses is accomplished in analogy to Tanaka *et al.* [1995]. So-called interfering masses are analysed by peak jumping to m/z 12 and 46 after measurement of the δ values. Tanaka *et al.* derived equations of the form

$$^{45}\delta(N_2O) = {}^{45}\delta'(N_2O) - A' \cdot {}^{12}I/{}^{44}I \quad (48)$$

$$^{46}\delta(N_2O) = {}^{46}\delta'(N_2O) - B' \cdot {}^{12}I/{}^{44}I \quad (49)$$

where $^{45}\delta(N_2O)$ is the correct value for the uncontaminated sample relative to the N_2O working standard. $^{45}\delta'(N_2O)$ is the measured value for the CO_2 contaminated sample. ^{12}I and ^{44}I are the ion currents of $^{12}C^+$ at m/z 12 and of $CO_2^+ + N_2O^+$ at m/z 44. A' and B' are constants. A' is defined as $^{12}I_r/{}^{44}I_r \cdot [1 + {}^{45}\delta(CO_2)]$ where $^{12}I_r$ is the relative ion intensity of $^{12}C^+$ to total CO_2, $^{44}I_r$ is the relative ion intensity of $^{14}N_2{}^{16}O$ to total N_2O and $^{45}\delta(CO_2)$ corresponds to CO_2 measured against the N_2O working standard. The definition of B' is analogous to the one of A'.

A dilution series of CO_2 standard gas in N_2O showed that the expected linear relationship is reproduced in the experiment [*Tanaka et al.*, 1995]. However, the derived expressions for the coefficients appear to be not correct which can be verified when one inserts representative quantities for $^{12}I_r$, $^{44}I_r$ and $^{45}\delta(CO_2)$ (deduced from MS measurements). Furthermore, the calculated ratio A'/B' of 0.779 is not reproduced in Figure 3 of Tanaka *et al.* [1995] where ratios of 0.496 and 0.497 are found.

Therefore, the theoretical CO_2 correction is recalculated here. Since we measure m/z 12 and m/z 46 for both standard and sample as interfering masses, the formulas were adapted to this case, but transformations to other masses do not invalidate the general linear relationship as proposed above.

First of all, an exact solution was derived for calculating the correct $^{45}\delta(N_2O)$ and $^{46}\delta(N_2O)$ value from the measured $^{45}\delta'(N_2O)$ and $^{46}\delta'(N_2O)$ values. They are defined as follows:

$$^{45}\delta(N_2O)=\frac{\frac{^{45}U}{^{44}U}}{\frac{^{45}V}{^{44}V}}-1;\quad ^{46}\delta(N_2O)=\frac{\frac{^{46}U}{^{44}U}}{\frac{^{46}V}{^{44}V}}-1;\quad ^{45}\delta'(N_2O)=\frac{\frac{^{45}U'}{^{44}U'}}{\frac{^{45}V'}{^{44}V'}}-1;\quad ^{46}\delta'(N_2O)=\frac{\frac{^{46}U'}{^{44}U'}}{\frac{^{46}V'}{^{44}V'}}-1$$

U' and V' are the actually measured voltages (produced by the ion currents on the amplifier feedback resistors) for sample and standard, respectively at the ion masses 44, 45 and 46. They are the sum of the true voltages U and V for N_2O only and the voltages from the CO_2 contamination, u and v due to CO_2 interference, e.g. $^{45}U'=^{45}U+^{45}u$. The present treatment is totally symmetric and applies to possible CO_2 contamination of both sample and standard. No assumption was made on the absence of such a contamination in the standard. ^{45}u, ^{46}u, ^{45}v and ^{46}v can be inferred from the voltage of interfering mass 12 if the relative intensity of C^+ to $^{12}C^{16}O_2^+$ is known. Defining $^{12}r=^{12}u/^{44}u$, we find that ^{12}r equals (3.9±0.1) % on our instrument. Substituting U by $U'–u$ and V by $V'–v$ and extracting $^{45}U'/^{44}U'\,^{44}V'/^{45}V'=1+^{45}\delta'(N_2O)$ yields:

$$\begin{aligned}^{45}\delta(N_2O)&=\left[1+^{45}\delta'(N_2O)\right]\frac{1-\frac{^{45}u}{^{45}U'}}{1-\frac{^{44}u}{^{44}U'}}\frac{1-\frac{^{44}v}{^{44}V'}}{1-\frac{^{45}v}{^{45}V'}}-1\\ ^{46}\delta(N_2O)&=\left[1+^{46}\delta'(N_2O)\right]\frac{1-\frac{^{46}u}{^{46}U'}}{1-\frac{^{44}u}{^{44}U'}}\frac{1-\frac{^{44}v}{^{44}V'}}{1-\frac{^{46}v}{^{46}V'}}-1\end{aligned}\qquad(50a,b)$$

If one assumes that the contaminating CO_2 is always of the same isotopic composition one can derive ^{45}u and ^{46}u from ^{44}u by calculating $^{45}u=^{44}u\,^{45}R(CO_2)\,^{45}k$ and $^{46}u=^{44}u\,^{46}R(CO_2)\,^{46}k$. $^{45}R(CO_2)$ and $^{46}R(CO_2)$ are the molecular isotopic ratios of CO_2 while ^{45}k and ^{46}k are the ratios of resistances for the mass 45/46 and mass 44 cups (being 100 and 333 within 1 ‰ in our case, but their exact values are of no importance as will be demonstrated in the next paragraph). $^{44}U'$, $^{45}U'$, $^{46}U'$, $^{44}V'$, $^{45}V'$ and $^{46}V'$ are all measured and thus an exact calculation of the CO_2 correction is possible provided ^{12}r, ^{45}k, ^{46}k and the isotopic composition of CO_2 are known.

However, one will mostly find rather a small contamination of both sample and standard. Then, it is possible to expand equations 50a and b and omit terms of second and higher order:

$$\begin{aligned}^{45}\delta(N_2O)&=^{45}\delta'(N_2O)-\frac{^{45}u}{^{45}U'}-\frac{^{44}v}{^{44}V'}+\frac{^{44}u}{^{44}U'}+\frac{^{45}v}{^{45}V'}\\ ^{46}\delta(N_2O)&=^{46}\delta'(N_2O)-\frac{^{46}u}{^{46}U'}-\frac{^{44}v}{^{44}V'}+\frac{^{44}u}{^{44}U'}+\frac{^{46}v}{^{46}V'}\end{aligned}\qquad(51a,b)$$

A further approximation is viable since for a small contamination of the standard (i.e., $v << V'$), so that ${}^{44}v/{}^{44}V' = {}^{44}v/({}^{44}V + {}^{44}v) \approx {}^{44}v/{}^{44}V$. Furthermore, ${}^{45}V$ and ${}^{46}V$ are derived from ${}^{44}V$: ${}^{45}V = {}^{44}V\,{}^{45}R_{st}(N_2O)\,{}^{45}k$ and ${}^{46}V = {}^{44}V\,{}^{46}R_{st}(N_2O)\,{}^{46}k$. One obtains:

$$
\begin{aligned}
{}^{45}\delta(N_2O) = {}^{45}\delta'(N_2O) \\
- \frac{{}^{46}R_{st}(N_2O)}{{}^{12}r}\left[\frac{{}^{45}R(CO_2)}{{}^{45}R_{st}(N_2O)}\left(\frac{1+{}^{46}\delta'(N_2O)}{1+{}^{45}\delta'(N_2O)'}\frac{{}^{12}u}{{}^{46}U'} - \frac{{}^{12}v}{{}^{46}V'}\right) - \left[1+{}^{46}\delta'(N_2O)\right]\frac{{}^{12}u}{{}^{46}U'} - \frac{{}^{12}v}{{}^{46}V'}\right] \qquad (52a,b) \\
{}^{46}\delta(N_2O) = {}^{46}\delta'(N_2O) - \frac{{}^{46}R_{st}(N_2O)}{{}^{12}r}\left[\frac{{}^{46}R(CO_2)}{{}^{46}R_{st}(N_2O)}\left(\frac{{}^{12}u}{{}^{46}U'} - \frac{{}^{12}v}{{}^{46}V'}\right) - \left[1+{}^{46}\delta'(N_2O)\right]\frac{{}^{12}u}{{}^{46}U'} - \frac{{}^{12}v}{{}^{46}V'}\right]
\end{aligned}
$$

Now, the final approximation is the assumption ${}^{45}\delta'(N_2O) << 1$ and ${}^{46}\delta(N_2O)' << 1$ giving

$$
\begin{aligned}
{}^{45}\delta(N_2O) &= {}^{45}\delta(N_2O)' - \frac{{}^{46}R_{st}(N_2O)}{{}^{12}r}\,{}^{45}\delta(CO_2)\left(\frac{{}^{12}u}{{}^{46}U'} - \frac{{}^{12}v}{{}^{46}V'}\right) \\
{}^{46}\delta(N_2O) &= {}^{46}\delta(N_2O)' - \frac{{}^{46}R_{st}(N_2O)}{{}^{12}r}\,{}^{46}\delta(CO_2)\left(\frac{{}^{12}u}{{}^{46}U'} - \frac{{}^{12}v}{{}^{46}V'}\right)
\end{aligned} \qquad (53a,b)
$$

Hence, we obtain two correction factors, A and B, being the factors before the brackets in equations 53a,b. Furthermore, their ratio, A/B, is given by ${}^{45}\delta(CO_2)/{}^{46}\delta(CO_2)$, which is approximately 0.5 in our case, in accordance with the findings in Figure 3 of [*Tanaka et al.*, 1995].

Note that if both ion beams are well balanced, the equation ${}^{44}U' = {}^{44}V'$ holds, and with the above approximations for small enrichments and contamination ${}^{46}U' = {}^{46}V'$ is valid, too.

In an actual mass spectrometric analysis, ${}^{12}u$, ${}^{12}v$, ${}^{46}U'$ and ${}^{46}V'$ were measured after the measurement of ${}^{45}\delta(N_2O)'$ and ${}^{46}\delta(N_2O)'$ and the corrections were calculated using equations 53a,b.

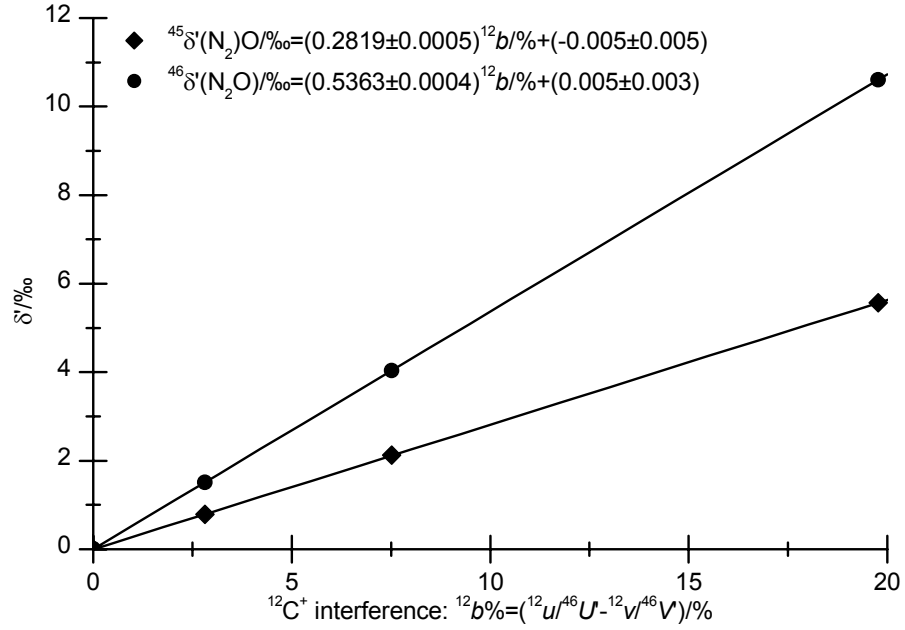

Figure 12: Mixtures of CO_2 in N_2O: ${}^{45}\delta'(N_2O)$ and ${}^{46}\delta'(N_2O)$ versus ${}^{12}C^+$ interference

$^{45}\delta(CO_2)$ and $^{46}\delta(CO_2)$ were measured for a sample of our CO_2 working standard ($\delta^{13}C_{VPDB} = -42.504$ ‰ and $\delta^{18}O_{VPDB\text{-}CO_2} = -29.217$ ‰) and found to be 492 ‰ and 939 ‰, respectively. Hence, the ratio of correction factors (A/B) is $^{45}\delta(CO_2)/\ ^{46}\delta(CO_2) = 0.524$, which is in agreement with results from mixing experiments shown in Figure 12. Here one obtains a ratio of 0.526±0.001. For convenience, the bracket terms with the measured voltages in equations 53a,b are abbreviated as ^{12}b. Similar plots of δ against ^{22}b (from CO_2^{2+}) or against the mixing ratio of CO_2 in the artificial CO_2+N_2O mixture give the same ratios, but higher standard deviations of ±0.005, because CO_2^{2+} is about five times less abundant than $^{12}C^+$ in the CO_2 mass spectrum.

Atmospheric CO_2 has a slightly different composition than the CO_2 standard gas used for calibration of the CO_2 correction curve. Therefore the actual coefficients for CO_2 correction are $A = 29.5$ ‰/100 % and $B = 54.7$ ‰/100 %.

3 Isotope fractionation by $N_2O + O(^1D)$

It was already mentioned in section 1.3 that atmospheric N_2O is enriched in heavy oxygen and nitrogen isotopes relative to its tropospheric sources. This enrichment is traced back to kinetic isotope effects in the two stratospheric N_2O sink mechanisms, i.e. photolysis and reaction with $O(^1D)$. Most of the previous studies on the cause of isotopic enrichment in N_2O have focussed on photolysis and additional data on that process will be presented in chapters 4–6. In this chapter, we present results on the ^{18}O and the position-resolved ^{15}N kinetic isotope effects in the reaction of nitrous oxide with $O(^1D)$ obtained by recently developed mass spectrometric techniques (section 2.6). Just as in the photolysis sink, a heavy isotope enrichment in the residual N_2O was found, but of smaller magnitude. Moreover, the fractionation pattern of nitrogen isotopes at the two non-equivalent positions in the molecule is clearly distinct from that in photolytic N_2O destruction. The larger influence of the $O(^1D)$ sink at lower stratospheric altitudes may help to explain the lower ratio of fractionation constants for the central and terminal nitrogen sites observed there, which is shown to be only marginally influenced by transport (section 7.1).

To date, only Johnston *et al.* [1995] have treated the oxygen isotope fractionation in the photooxidation of N_2O by $O(^1D)$, but no information at all is available about ^{15}N fractionations so far. This demands an accurate and precise determination of the nitrogen and oxygen isotope effects in the "photooxidation" of N_2O with $O(^1D)$. In order to investigate more completely the relevance of this reaction for the isotopic composition of N_2O in the stratosphere, we have also determined the position-dependent fractionation of nitrogen isotopes.

3.1 Kinetic isotope effects: Rayleigh fractionation

Kinetic isotope fractionation in a chemical reaction is described by the fractionation factor α (introduced in 1.3.1 and 1.3.2). In its most general definition, it is the ratio of instantaneous changes in concentrations of heavy and light isotopes [*Rayleigh*, 1896], e.g.

$$^{15}\alpha \equiv \frac{\mathrm{d}c(^{15}\mathrm{N})}{c(^{15}\mathrm{N})} \Big/ \frac{\mathrm{d}c(^{14}\mathrm{N})}{c(^{14}\mathrm{N})} \tag{54}$$

This definition is inverse to an IUPAC recommendation [*Müller*, 1994] we used previously [*Kaiser et al.*, 2002a; *Röckmann et al.*, 2000; *Röckmann et al.*, 2001]. It was adopted by many studies of photo-induced isotopic fractionation in N_2O [*Griffith et al.*, 2000; *Johnson et al.*, 2001; *Rahn et al.*, 1998; *Toyoda et al.*, 2001a; *Toyoda et al.*, 2001b; *Turatti et al.*, 2000; *Umemoto*, 1999; *Yoshida and Toyoda*, 2000; *Yung and Miller*, 1997; *Zhang et al.*, 2000] and is widespread in the geochemical literature

[*Fritz and Fontes*, 1980; *Hoefs*, 1997; *Mook*, 2000]. For consistency, this inverse definition is also adopted here. Moreover, definition 54 simplifies kinetic calculations with atomic isotope ratios (R), because R is defined similarly, e.g. $R \equiv c(^{15}\mathrm{N})/c(^{14}\mathrm{N})$. For a reaction which is of first order with respect to the isotopically substituted molecule α can be identified with the ratio of reaction rate constants of heavy and light isotopomer, i.e.

$$\alpha = \frac{k^h}{k^l} \tag{55}$$

For all atoms except hydrogen, α is close to one. Therefore, the fractionation constant ε is defined as a related quantity by $\varepsilon \equiv \alpha - 1$. It follows from definition 54:

$$^{15}\varepsilon = \frac{\mathrm{d}R}{R} \Big/ \frac{\mathrm{d}c(^{14}\mathrm{N})}{c(^{14}\mathrm{N})} \tag{56}$$

The consequence of this definition is that for a normal kinetic isotope effect (i.e., the isotopically light molecule reacts faster than the heavy ones) the fractionation constant ε is negative. This is counter-intuitive at first sight, since the substrate gets enriched in the reaction, but it makes sense as the product is depleted relative to the substrate. Actually, the initial isotope ratio of the product is $\lim_{t\to 0} R_\mathrm{p}(t) = (1+\varepsilon)\, R_0$ with R_0 being the initial isotope ratio of the substrate. Thus, using δ notation with R_0 as reference ($\delta = R/R_0 - 1$): $\lim_{t\to 0} \delta_\mathrm{p}(t) = \varepsilon$ (< 0 for normal isotope effects).

For a closed system with initial $R(t=0) = R_0$ and $c(^{14}\mathrm{N},\ t=0) = c_0(^{14}\mathrm{N})$, eqn. 56 can be integrated:

$$\ln\frac{R}{R_0} = \ln(1+\delta) = {}^{15}\varepsilon \ln\frac{c(^{14}\mathrm{N})}{c_0(^{14}\mathrm{N})} = {}^{15}\varepsilon\left(\ln y + \ln\frac{1+R_0}{1+R}\right) \approx {}^{15}\varepsilon \ln y \tag{57}$$

where y is the total remaining N_2O fraction. To a very good degree of approximation, we can assume $\ln\frac{1+R_0}{1+R} \approx 0$ (e.g., for a typical R_0 of 0.0037 and $\varepsilon = -60$ ‰, the relative error in the calculated ε is less than 1 ‰ for δ up to 11000 ‰). The further approximation $\ln(1+\delta) \approx \delta$ which was often made in application of eqn. 57 leads to significant errors already for moderately high δ values of about 20 ‰, and is therefore not used here. ε is derived from a fit through all data points in a Rayleigh plot of $\ln(R/R_0)$ vs $\ln y$. Alternatively, one can calculate the fractionation constant directly for each individual experiment. This approach will be used in chapters 4 and 5. Given sufficient experimental precision and provided the y-axis offset in a Rayleigh plot is zero, this approach is more suitable to detect influences of reaction parameters on ε.

3.2 Experimental methods

In general, we follow the experimental approach of Cantrell *et al.* [1994]. Mixtures of N_2O and O_3 with and without He as bath gas were irradiated by UV light from low pressure mercury lamps (254 nm) to photolyse O_3 according to $O_3 + h\nu \rightarrow O_2 + O(^1D)$. Part of the photolysis product $O(^1D)$ then reacts with N_2O, the rest is electronically quenched to $O(^3P)$ which does not react with N_2O. Helium was chosen as bath gas because its electronic quenching rate constant is very small ($< 7 \cdot 10^{-16}$ cm^3 s^{-1}) [*Heidner III and Husain*, 1974]. In the experiments with He, the mixing ratio of N_2O varied between 0.51 and 2.2 mmol mol^{-1}, the mixing ratio of O_3 between 6.7 and 102 mmol mol^{-1} and the total pressure between 203 and 1215 mbar. The experiments without He were performed at total initial pressures between 1.2 and 37.2 mbar with N_2O mixing ratios between 0.02 and 0.63 mol mol^{-1}, respectively (the balance comprises ozone and traces of oxygen).

Two different reaction chambers (A and B) were used. Reaction chamber A consisted of a cylindrical three-walled quartz glass tube. The total length of 1.6 m was illuminated over 1.2 m by eight radially mounted low-pressure mercury lamps (*Philips* TUV 40 W, type G 40T 12) with a monochromatic light flux at 253.7 nm. The 3.5 cm wide core constituting the actual reactor was surrounded by an interior mantle through which ethanol was circulated from a laboratory thermostat (*Huber* HS90). The temperature was varied between –78.6 °C and +25.0 °C and could be controlled to within ±0.2 °C. The outer mantle was evacuated in order to prevent condensation of moisture from laboratory air in case of the low temperature experiments.

It is imperative to have a homogeneous reaction mixture due to the inherent non-linearity of Rayleigh fractionation (exponential relation between mixing ratio and isotope ratio). Therefore, the gas mixture was circulated through the reactor by a small oil-free rotary vane pump (delivery rate: 4.5 dm^3 min^{-1}). A spiral cold trap was mounted in series for trapping the remaining N_2O after termination of the reaction. Finally, a shunt filled with silver wool was incorporated that could be used to remove remaining O_3 from the reaction mixture after completion of an experiment. It also removes NO_2 through formation of $AgNO_2$ and $AgNO_3$ [*Matsuta and Hirokawa*, 1986], but is inert towards NO at room temperature [*Brown et al.*, 1995]. Heating destroys Ag_2O, $AgNO_2$ and $AgNO_3$ and regenerates the pristine silver surface.

The net volume of the reactor was measured by consecutive expansion of gas from a calibrated volume and found to be 1.31 dm^3. The volume of the gas transfer lines connecting the ends of the reaction chamber was 0.16 dm^3, so that the total volume was 1.47 dm^3. All transfer lines were made from borosilicate glass (*Duran*), sealed at the joints by fluorocarbon (*Viton*) o-rings.

Reaction chamber B was simpler in design and consisted of a spherical *Duran* glass bulb. A quartz tube insert extended from the outer circumference to the centre of the bulb and contained a low pressure mercury vapour double bore lamp ("Pen-Ray", *Jelight*). The lamp had a *Vycor* glass window material (basically silicate) that effectively blocks the 185 nm radiation from the mercury discharge, thus avoiding N_2O photolysis. The reactor volume amounted to 2.14 dm^3. A Russian doll-type trap [*Brenninkmeijer and Röckmann*, 1996] was connected and used for cryogenic N_2O extraction after each experiment.

Three mixtures of pure N_2O standard gas (99.9999 %) in He (99.999 % or 99.9999 %) were prepared in an aluminium cylinder (*Scott Marrin*). The mixing ratios were 0.054, 0.094 and 0.22 mmol mol^{-1}. Ozone was produced in advance by conversion of O_2 in a silent discharge [*Siemens*, 1857]. It was stored on silica gel in a U-shaped tube ($V \approx 1$ dm^3) at ≈–80 °C.

A typical experiment proceeded as follows: The U-tube with ozone and a cylinder with the N_2O/He gas mixture were connected to the inlet system (A) or directly to the reactor (B). The entire system was evacuated to $< 10^{-4}$ mbar. The desired amount of ozone was admitted to the reactor by removing the cold bath from the U-tube. Next, the N_2O/He gas mixture was admitted to a final pressure of ≈ 1 bar in most cases. In some cases, lower pressures (200 to 300 mbar) where used in order to check for a pressure influence on the fractionation constants. For the thermostatted experiments, reactor A was now cooled down to the designated temperature. To achieve thorough mixing, the reactant gases were circulated for 1 to 3 min through the entire glass system (only reactor A). To start $O(^1D)$ production, the UV lamp(s) were turned on for 5 min to 21 h. The increase of pressure in the system due to both heating from the lamps and photolysis of O_3 was monitored. After the experiment the gas mixture was circulated via the silver wool shunt for 7 min, then the spiral loop trap was cooled down with liquid nitrogen (-196 °C) and the gas was circulated another 7 min to trap the residual N_2O (reactor A). For reactor B, the reactant gases were pumped off slowly by the turbomolecular pump of the vacuum system, having passed through a silver wool plug and the Russian doll-type trap. The extracted samples were stored in glass sample flasks equipped with glass/o-ring stop-cocks (*Glass Expansion* or *Louwers-Hapert*).

Three types of control experiments ("blank runs") were performed: Type 1) no addition of O_3, no UV irradiation; type 2) O_3, but no UV; type 3) no O_3, but UV. Type 1 runs were used to check the "zero" yield of N_2O to which the other experiments were referenced. Type 2 and type 3 blank runs served as a check for unwanted N_2O producing or destroying reactions.

To facilitate comparability with a previous study [*Johnston et al.*, 1995] some experiments in reactor B were also conducted without He bath gas. The total pressure in these cases was much lower than in the previously described experiments (see Figure 17).

After extraction of the remaining N_2O, it was purified by a preparatory GC system (section 8.1.4). Other observed condensable gases were CO_2, and in some early experiments (when the silver wool shunt was not used) also NO_2/HNO_3. NO_2 was produced by reaction of NO with O_3 or in a three-body reaction with $O(^3P)$. The production of HNO_3 was attributed to hydrocarbon contamination on the walls as noted by Cantrell *et al.* [1994]. This may also have produced the observed CO_2. In a few of the early experiments, repeated GC purification runs were necessary, because NO_2/HNO_3 were still present after the destruction step with silver wool and a single GC run, which led to high errors in the $\delta^{46}N_2O$ measurements. The additional purification steps have remedied this problem in most cases without significant loss of accuracy. Three possible exceptions are discussed later.

The yield of N_2O (y) was determined from the amount of purified N_2O sample as measured manometrically in a calibrated volume, and corrected for a small loss in the GC purification step of (0.7±0.1) % ("GC correction") (section 8.1.4). The error of $\ln y$ is estimated as 0.01 with relative contributions of 70 %, 26 % and 4 % from the precision of pressure (0.3 %) and temperature (0.5 °C) measurements and the GC corrections, respectively.

Dual-inlet isotope mass spectrometric measurements of the purified sample were performed on *Finnigan* MAT 252, *Finnigan* DELTA^{plus} XL and *Micromass* Prism II instruments. On the MAT 252 machine, $\delta^{18}O$ and average $\delta^{15}N$ were determined from $^{45}\delta$ and $^{46}\delta$ with correction for traces of CO_2 and the influence of isobaric isotopomers ("^{17}O correction") (sections 2.5 and 2.8). Measurements of the NO^+ fragment ion ($^{31}\delta$) were done initially on the Prism II, but were transferred later to the MAT 252 (section 2.6). Some samples were cross-checked for both $^{45}\delta/^{46}\delta$ and $^{31}\delta$ on a DELTA^{plus} XL instrument with no detectable difference in results. $^{31}\delta$ was corrected for isobaric CF^+ (originating from fluorocarbons in o-rings and vacuum grease; measurement of interfering masses at m/z 69, corresponding to CF_3^+, section 8.3.3) on all instruments and for nonlinearity effects on the DELTA^{plus} XL. $^1\delta^{15}N$ and $^2\delta^{15}N$ were calculated from $^{31}\delta$ and the average $\delta^{15}N$ as described in section 2.2.

3.3 Results

The pooled results of all 99 experiments (54 normal and 45 blank runs) are shown in Figure 13. The highest enrichments are found in ^{18}O, followed by the terminal nitrogen atom ($^1\delta^{15}N$) and the central nitrogen atom ($^2\delta^{15}N$). From the $\ln(1+\delta)$ vs $\ln(y)$ plots, we calculate the fractionation constants (±2σ) and the y-axis interceptions in Table 5.

Table 5: Fractionation constants derived from linear least squares fits to a Rayleigh plot of all experiments

isotope	ε/‰	2σ	y-axis intercept	2σ	r^2
^{18}O	–12.23	0.14	0.13	0.09	0.997
terminal ^{15}N	–8.79	0.14	–0.05	0.09	0.993
^{15}N	–5.51	0.05	0.02	0.03	0.998
central ^{15}N	–2.21	0.12	0.09	0.08	0.927

The precision of the inferred average fractionation constant in ^{15}N is higher than for ^{15}N at the individual positions, since it does not involve the lower precision of $^{31}\delta$ measurements: In general, the precision of the fractionation constant is comparable to the precision of individual isotope ratio measurements. Deviations from the linear fit are sometimes larger than expected from the precision of individual measurements, which may indicate sample handling errors or contamination by HNO_3/NO_2 in some of the earlier experiments. This contamination proved to be quite sticky, and the walls of the glass sample flasks used for sampling had to be heated to

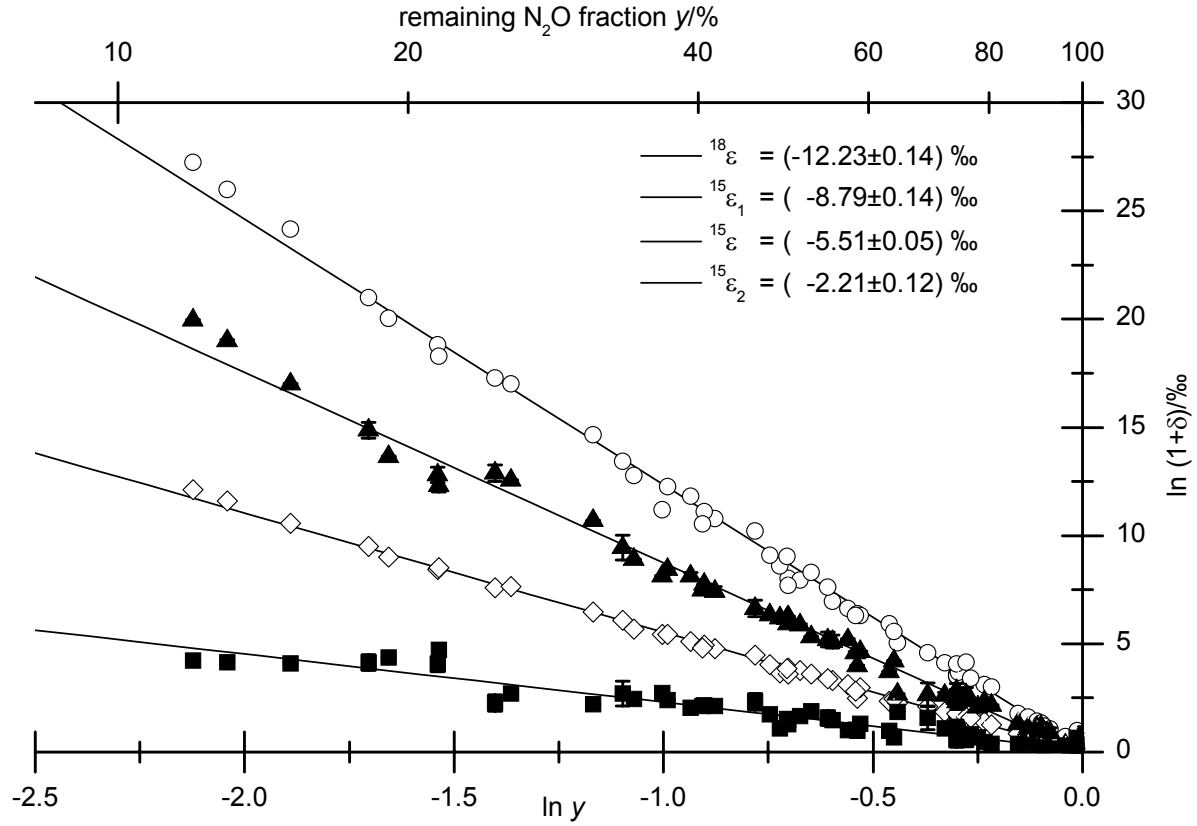

Figure 13: Rayleigh fractionation plot for all 99 experiments. Fractionation constants (±2σ) are calculated from the slopes derived by linear least-squares regression. Mass spectrometric errors of ln(1+δ) and estimated errors of ln *y* are usually smaller than individual symbol sizes, except for a few $^1\delta^{15}N$ and $^2\delta^{15}N$ values where error bars are shown.

remove it entirely. Three experiments (points with lowest ln *y* in Figure 13) suffered from this problem initially, which may be the reason for their larger offset from the least squares fit. However, since the standard deviations of MS measurements after repeated GC purification were as low as normal, we have not excluded them from the calculation of fractionation constants.

The y-axis intercept is close to zero in all cases (Table 5), in line with the results from the blank runs. Recovery of N_2O was better than 99.5 % for blank run types 1 to 3. On average, the isotope ratios in the blank runs were not altered by more than (0.04±0.04) ‰ in $\delta^{15}N$, and not more than (0.21±0.18) ‰ in $\delta^{18}O$ compared to the reference gas. Therefore, it appears that the 185 nm Hg line which photolyses N_2O is effectively shielded in both lamp/reactor combinations. As expected, no change of N_2O mixing ratios was caused by ozone either (in the absence of UV irradiation). For $\delta^{15}N$, the observed shift is equal to the enrichment caused by the preparatory GC system for N_2O purification (8.2.3). The same process accounts for only 0.08 ‰ of the enrichment in $\delta^{18}O$, but this is covered by the higher standard deviation. Additional shifts could be caused by small NO_2 impurities (0.2 ppm NO_2 in N_2O would cause an increase of $\delta^{18}O$ by 0.1 ‰, assuming equal ionisation efficiencies. In any case, the fractionation constants are derived from the slopes of ln(1+δ) vs ln(*y*) plots only, so that the y-axis intercept has no influence on ε.

3.3.1 Influence of mixing ratio and reactor type

Figure 14 shows the fractionation constants from the experiments, assigned to reactor A and B and sorted according to similar mixing ratios. No significant influence of mixing ratio or reac-

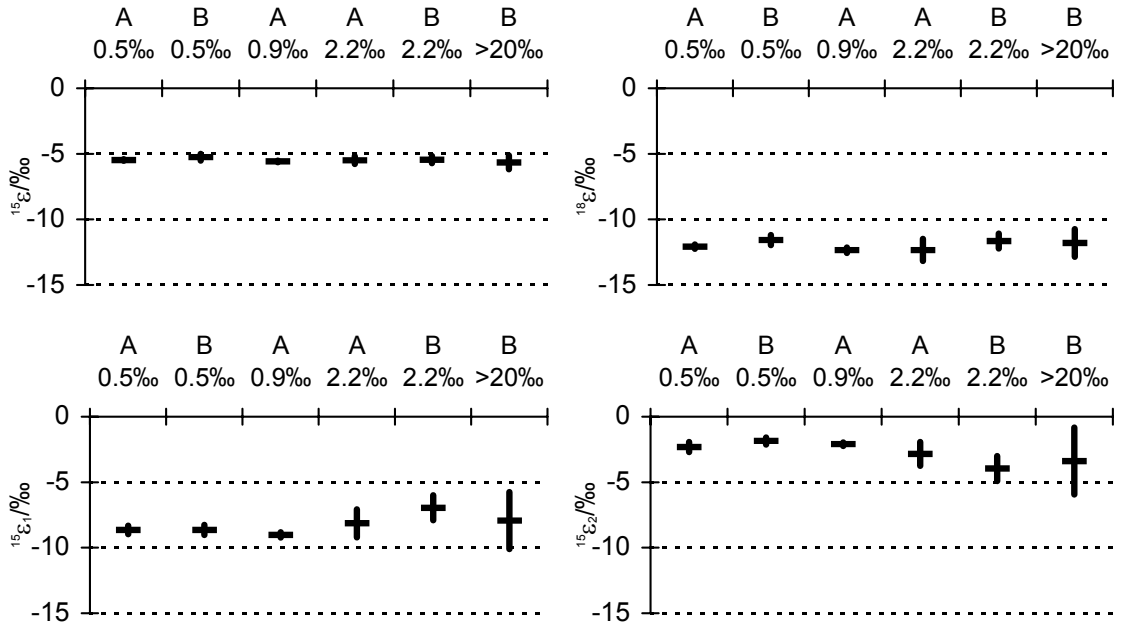

Figure 14: Influence of reactor type and mixing ratio on the observed fractionation constants.

tor type compared to the pooled results from all experiments is apparent within the mutual range of errors, except for the position-dependent nitrogen fractionation constants of the 0.22 % experiments in reactor B. However, the number of experiments is small in this case ($n = 4$) and $^{15}\varepsilon$ and $^{18}\varepsilon$ do not significantly deviate from the pooled results of all experiments, so that we attribute this deviation to the imprecision of the δ^{31}NO measurement.

3.3.2 Influence of temperature

Temperature was lowered from room temperature down to –79 °C in experiments with N_2O mixing ratios of 0.054 % and 0.094 %. With the good precision of individual measurements, it was not deemed necessary to cover a range of different ln *y*-values for all low temperatures. Fractionation constants were rather calculated individually for each of the 28 measurements, assuming that the corresponding Rayleigh fractionation lines pass through the origin.

If the temperature dependence of the reaction rate can be described by the Arrhenius form $k(T) = A\mathrm{e}^{-\frac{E}{RT}}$, then ε is given by

$$\varepsilon = \frac{A'}{A}\mathrm{e}^{-\frac{E'-E}{RT}} - 1 \tag{58}$$

where primed and unprimed quantities refer to the heavy and light isotope, respectively. A plot of ln(1+ε) against $1/T$ is therefore expected to give a straight line. The linearised results are shown in Figure 15, and the fit parameters are displayed in Table 6.

There is a slight negative correlation with 1/T for ^{18}O, terminal ^{15}N and average ^{15}N as well as a very weak positive correlation for central ^{15}N. However, the measurements at lower temperatures do not seem to depart from the observed range of the room temperature experiments, so that the observed temperature influence is merely random and in line with the estimated activation temperature of (0±100) K for the reaction of N_2O with $O(^1D)$ (200-350 K) [*Atkinson et al.*, 1997; *DeMore et al.*, 1997]. The y-axis intercept ln A'/A is in satisfactory agreement with ln (1+ε) derived from the pooled set of 99 experiments.

Table 6: Temperature coefficients calculated from weighted least squares-fits to the Arrhenius equation

isotope	ln A'/A (‰)	2σ	$(E'-E)/R$ (K)	2σ	r^2
^{18}O	–11.15	0.75	–265	171	0.28
terminal ^{15}N	–7.38	0.98	–314	215	0.25
^{15}N	–5.22	0.26	–73	58	0.20
central ^{15}N	–2.67	0.67	+98	154	0.06

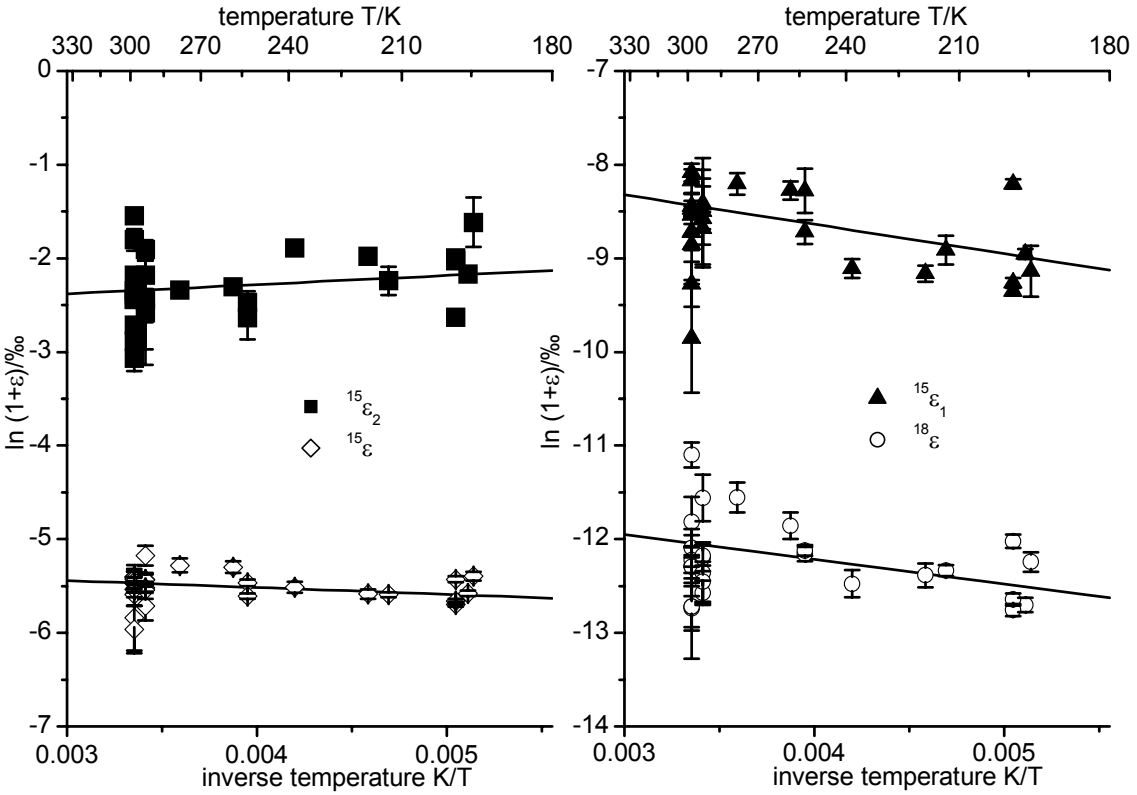

Figure 15: Temperature dependence of fractionation constants between -79 °C and +25 °C. Error bars are ±1σ. Weighted least squares fits are applied to the Arrhenius model of eqn. 58. The fit results are shown in Table 6.

3.3.3 Influence of pressure

No significant pressure dependence can be deduced from the experiments in which helium was used as bath gas although the pressure was varied between 200 and 1130 mbar (Figure 16). To attain even lower pressures, ten runs were performed without helium bath gas. In those cases, ozone and nitrous oxide were introduced cryogenically into reactor B, using the cold finger at its bottom. The results are shown in Figure 17. Again no discernible effect on isotope fractionation constants of pressure is seen over a range from 1 to 37 mbar.

3.4 Discussion

The results are discussed from three viewpoints: First, possible measurement artefacts are considered, then we discuss the nature of the isotope effect in the reaction investigated and finally, we make conclusive remarks on the implications for the stratospheric N_2O signature.

3.4.1 Measurement artefacts

Based on our experimental results and on the measured rate constants of possible side reactions, we rule out that there was *in-situ* N_2O production during the experiments.

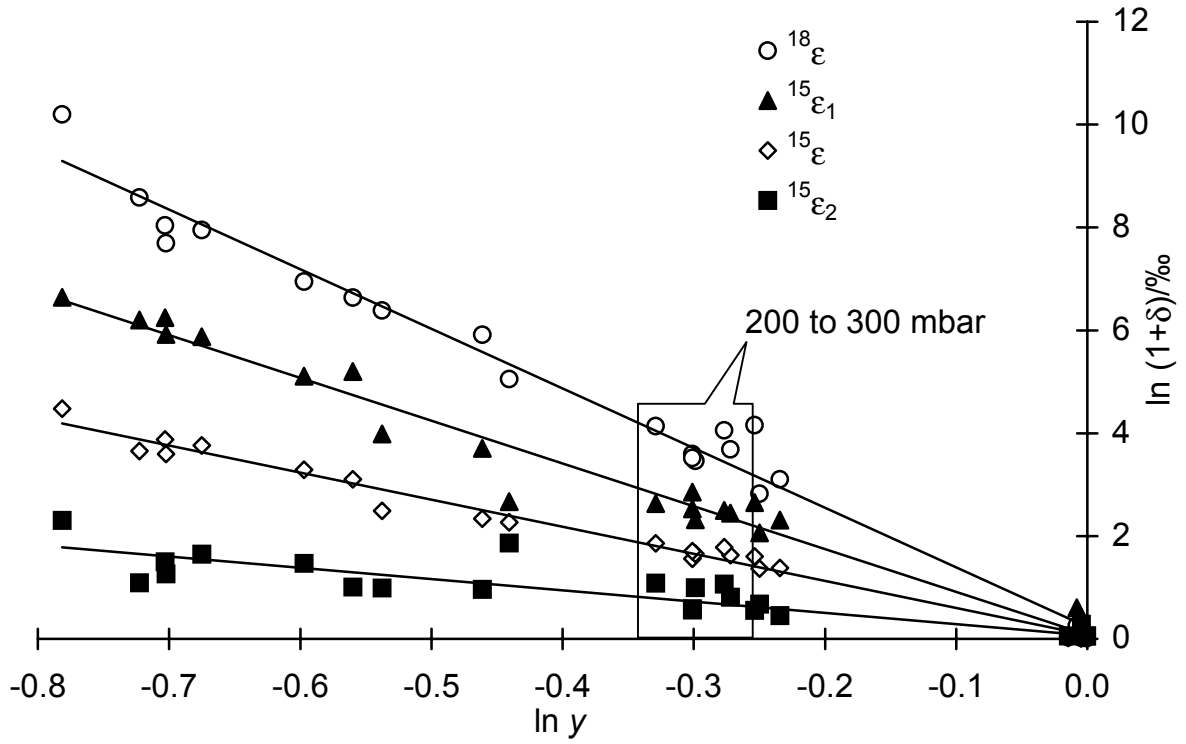

Figure 16: Rayleigh fractionation plot for the experiments with He as bath gas. The data points are for initial total pressures around 1000 mbar at the start of the experiment, except for those labelled "200 to 300 mbar".

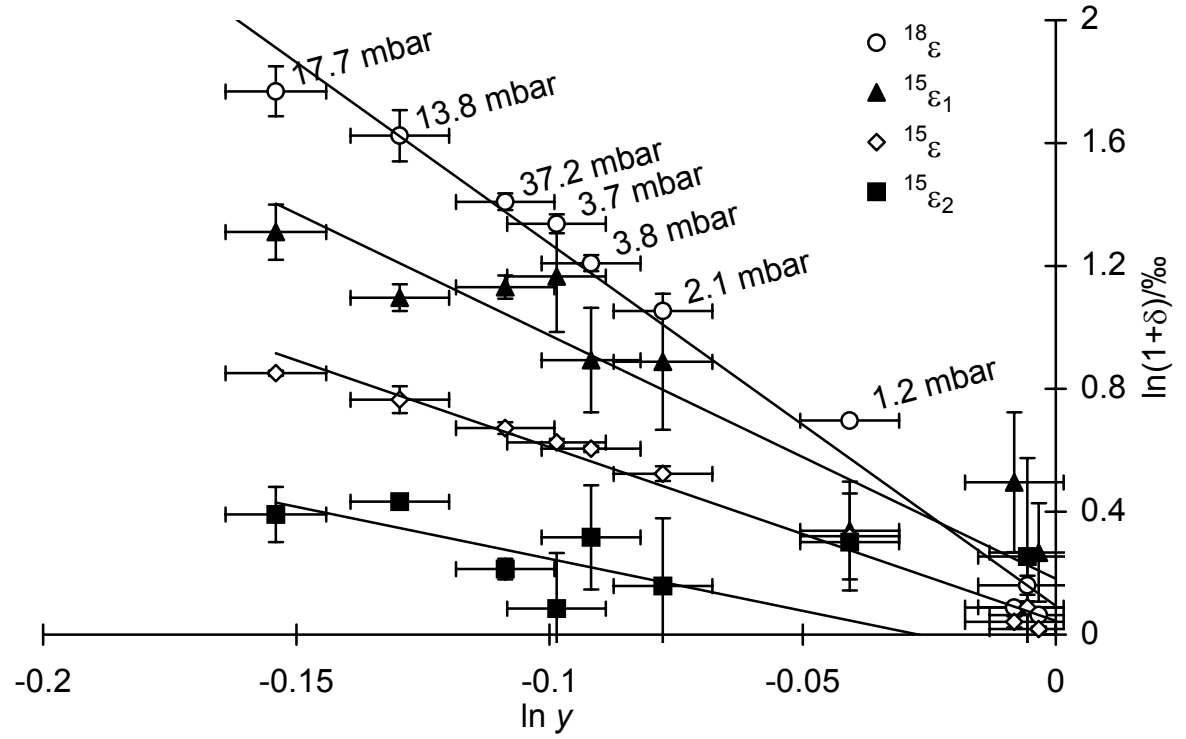

Figure 17: Rayleigh fractionation plot for the experiments in reactor B, without bath gas. The data points are labelled with the initial total pressure at the start of the experiment. Results of the linear regression fits are in Figure 14 (data labelled reactor B, > 2.0%).

The irradiation time has been varied over a range from 5 min to almost 23 h. If there had been a non-negligible amount of *in-situ* N_2O production, a deviation from the Rayleigh fractionation line would have been expected for experiments of long duration. Such a deviation was not apparent. This is in accordance with estimates of relevant reaction rates. The termolecular rate constant for formation of N_2O from N_2 and $O(^1D)$ is $3.5 \cdot 10^{-37}$ cm^6 s^{-1} at 300 K [*DeMore et al.*, 1997] and therefore even the reaction rate in 1 bar nitrogen (number concentration: $2.4 \cdot 10^{19}$ cm^{-3}) is several orders of magnitude smaller than the reaction rate of N_2O with $O(^1D)$ ($1.16 \cdot 10^{-10}$ s^{-1}), [*DeMore et al.*, 1997]. Even smaller rate constants ($< 5 \cdot 10^{-38}$ cm^6 s^{-1}) apply for $O(^3P) + N_2$ [*Stuhl and Niki*, 1971]. Formation of N_2O from $NO_2 + N_2$ is also too slow to be relevant: Estupiñán *et al.* [2000] recently reported a quantum yield of less than $4 \cdot 10^{-8}$ for the reaction $NO_2^* + N_2 \rightarrow N_2O + NO$. In some cases, heterogeneous production of N_2O has been observed [*Marić et al.*, 1992], but even for a 20 h irradiation time and the highest reported production rates (7.5 ppt/s) the yield would be smaller by three orders of magnitude or more than the mixing ratios used in this study.

In spite of the above considerations on the absence of measurement artefacts, there is a disagreement between our results and the single previous measurement of kinetic isotope effects in the reaction of $O(^1D)$ with N_2O [*Johnston et al.*, 1995]. The latter was restricted to ^{17}O and ^{18}O isotopes and stated that $\varepsilon(^{18}O)$ was –6 ‰. $\varepsilon(^{17}O)$ was ≈ -3 ‰, in line with expectations for a mass-dependent fractionation process. Evaluation of the original data shows that they do not pass through the origin as demanded by a Rayleigh fractionation process. (linear least-squares regression of the $\delta^{18}O(N_2O)$ data gives an ordinate offset of (0.27±0.40) % and a slope of (-4.5±2.6) ‰; $r^2 = 0.86$; $n = 4$). Furthermore, the slope bears a significant error even if a blank value of zero is included (slope: (-5.9±1.4) ‰; $r^2 = 0.73$; $n = 5$). No bath gas was used for the experiments, and the initial total pressure and mixing ratios were varied only slightly (*Jeffrey C. Johnston*, personal communication, 2001). We tried to imitate the conditions of this previous study as far as possible considering the differing reactor sizes, but did not see any difference to the results of our other experiments. The origin of the difference between the present study and the previous measurements remains unclear. However, we believe that our set of 99 experiments represents a more accurate and precise measurement of the isotope effects in the reaction of $O(^1D)$ with N_2O, since we tested a by far larger parameter space in terms of mixing ratio, reactor type, temperature and pressure.

3.4.2 Nature of the isotope effect

As expected from the zero activation energy reported for the reaction of N_2O with $O(^1D)$ [*Atkinson et al.*, 1997; *DeMore et al.*, 1997] there is no statistically significant temperature depend-

ence (Figure 15) of the isotope effect. This indicates only a small energy barrier from reactants to products. The absence of any pressure dependence points in the same direction, in contrast to the reaction of another unsaturated molecule with a neutral radical, CO + OH, which clearly exhibits a pressure dependence on its rate constant and isotope effect [*Röckmann et al.*, 1998b]. One can compare the reaction rate constant of $N_2O + O(^1D)$ at 298 K ($k = 1.16 \cdot 10^{-10}$ cm^3 s^{-1} [*Atkinson et al.*, 1997; *DeMore et al.*, 1997]) with that expected from kinetic gas theory (k_{kg}). Van der Waals radii of N_2O and $O(^1D)$ are assumed to be $r_{N_2O} = 236$ pm and $r_{O(^1D)} = 145$ pm [*Simonaitis et al.*, 1972]. With the collisional cross section, $\sigma_c = \pi(r_{N_2O} + r_{O(^1D)})^2$, and the average relative speed of N_2O and $O(^1D)$, $\hat{v} = \sqrt{8RT/(\pi\mu)}$, we have $k_{kg} = \sigma_c \cdot \hat{v}\,(298\text{ K}) = 3.3 \cdot 10^{-10}$ cm^3 s^{-1} for zero activation energy, i.e. significantly larger than the measured reaction rate. This disagreement can be qualitatively understood by the fact that not all relative orientations of N_2O and $O(^1D)$ lead to a reaction. A more comprehensive study of neutral/neutral reactions concluded that *any* reaction with a room temperature rate constant within about an order of magnitude of the collisional value is probably not limited by a potential barrier [*Smith*, 1995]. Moreover, rate constants may even increase as temperature is lowered, but the available data for the reaction $N_2O + O(^1D)$ have not shown any significant temperature dependence yet and no measurements at very low temperatures (< 77 K) have been reported to date. Transition state theory was used to correctly quantify the reaction constant from the ground state potential energy surfaces calculated *ab initio* at the CASPT2//CASSCF level (complete active space second-order perturbation theory//complete active space self-consistent field) [*González et al.*, 2001]. This approach can be simplified significantly for intramolecular isotope effects if the difference in the free energy function for a pair of isotopomers is negligibly small [*Bigeleisen*, 1952]. Good agreement with experimental data was often found in the past, and we therefore tried this approach out for the reaction studied here.

First, the "gas-kinetic" isotope effect was calculated. Since the collisional cross section is not influenced by the nucleus, the fractionation constant is merely dependent on the reduced mass μ: $^{15}\varepsilon = [\mu(^{15}N^{14}NO+O)/\mu(^{14}N_2O+O)]^{1/2} - 1 = [\mu(^{14}N^{15}NO+O)/\mu(^{14}N_2O+O)]^{1/2} - 1 = 2.97$ ‰ and $^{18}\varepsilon = [\mu(^{46}N_2O+O)/\mu(^{44}N_2O+O)]^{1/2} - 1 = 5.85$ ‰, i.e. the predicted isotope effects are significantly smaller than the measured ones. Therefore, we slightly modified our approach taking into consideration the recent results on the potential energy surface of the reaction of N_2O with $O(^1D)$.

The reaction $O(^1D) + N_2O$ has two exit channels: one giving NO + NO (R2; page 5), the other $N_2 + O_2$ (R3). González *et al.* [2001] show correspondingly that there are two possible approaches of $O(^1D)$ to the N_2O molecule: either from the terminal nitrogen or from the terminal oxygen, leading to R2 or R3, respectively. A wide range of approach angles around the collinear

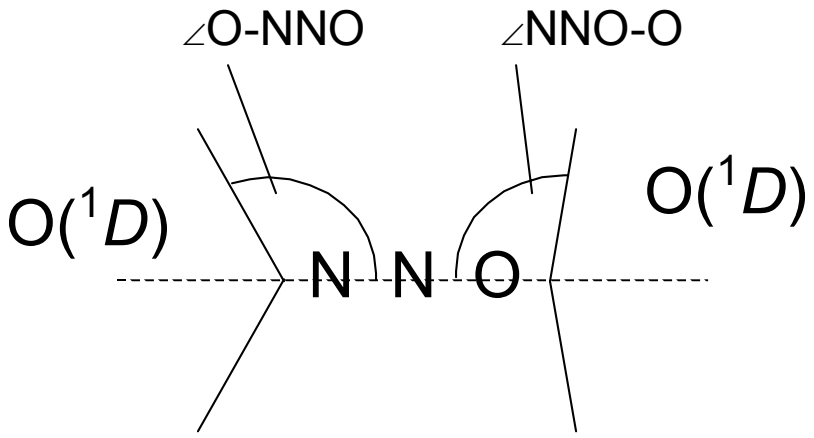

Figure 18: Designation of approach angles for $O(^1D)$ to the N_2O molecule. Attack of $O(^1D)$ from the left hand side corresponds to reaction R2 leading to NO + NO; attack from the right hand side corresponds to reaction R3 leading to $N_2 + O_2$.

configuration is energetically accessible in the R2 channel, with a minimum energy-profile for an ∠O-NNO angle of about 120° (Figure 18). In contrast, the minimum energy approach in the R3 channel is more confined to ∠NNO-O angles close to 100°. There is practically no energy barrier in the entrance zone of both reactions. The main energy release is in the exit valley for R3, but in R2 the energy profile follows a more complex path passing through either predominant *cis*- or *trans*-arrangements in the transition states. For the *trans*-path connecting directly with reactants, the main energy release is in the entrance valley. González *et al.* [2001] calculate rate constants for these reactions using transition state theory. They find a good agreement with the experimental data in the temperature range between 200 and 350 K and predict a non-Arrhenian temperature dependence within a 100-1000 K temperature range. However, they do not make any predictions on isotope effects in this reaction. Therefore we try to grasp the nature of the isotope effect by the following simple considerations:

Bonds between equal atoms are *formed* in R3: Molecular oxygen stems from the terminal oxygen atom and the incoming $O(^1D)$, whereas the two nitrogen atoms give N_2. Since the main energy release is in the exit channel in this case, the isotope effect should be governed by the newly formed bond between oxygen atoms, leaving the N_2 entity in the role of a "spectator". In terms of the theory of intramolecular isotope effects by Bigeleisen [1952], this means that the reduced mass of the molecule in the transition state should be calculated from the masses of O and the different N_2O isotopomers. The isotope effect calculated hereby corresponds to the "gas-kinetic" one discussed above, and does not show any dependence on the position of ^{15}N in the molecule.

To check whether this model is correct, isotope ratio measurements of N_2 produced by the reaction of $N_2O + O(^1D)$ are necessary.

In contrast, bonds between equal atoms are *broken* in R2: The bond between the nitrogen atoms of N_2O is broken, while a new bond between the incoming oxygen atom and the terminal nitrogen atom is formed. Assuming that the exit channel of the reaction is responsible for the isotope effect in the framework of Bigeleisen's theory, we calculate the reduced mass of the transition complex from the NO entities formed in the reaction. Thus, $^{15}\varepsilon = [\mu(^{15}NO+^{14}NO)/\mu(^{14}NO+^{14}NO)]^{½} - 1 = 8.16$ ‰ and $^{18}\varepsilon = [\mu(N^{18}O+N^{16}O)/\mu(N^{16}O+N^{16}O)]^{½} - 1 =$ 16.00 ‰. Again the isotope effect is not dependent on the position-dependent of ^{15}N because of the symmetry of the transition state (in both $^{15}N^{14}NO$ and $^{14}N^{15}NO$ bonds are broken between ^{14}N and ^{15}N).

The overall isotope effect of the reaction is calculated from the partitioning of the overall reaction rate between pathways R2 and R3, i.e. $7.2 \cdot 10^{-10}$ cm^3 s^{-1} and $4.4 \cdot 10^{-10}$ cm^3 s^{-1} according to an IUPAC evaluation [*Atkinson et al.*, 1997] and $6.7 \cdot 10^{-10}$ cm^3 s^{-1} and $4.9 \cdot 10^{-10}$ cm^3 s^{-1} according to a NASA report [*DeMore et al.*, 1997]. The average $^{15}\varepsilon$ is 6.2 ‰ or 6.0 ‰, respectively, while the average $^{18}\varepsilon$ is 12.1 ‰ or 11.7 ‰. Given the crude assumptions made, this is an astonishing agreement between the measured average fractionation constants of (5.5±0.1) ‰ and (12.4±0.1) ‰. However, no predictions on the position-dependent ^{15}N fractionation can be made. Since accurate potential energy surfaces have become accessible lately, more precise calculations of the isotope effect should be possible.

Qualitatively, the position-dependent ^{15}N fractionation can be understood from the following considerations: In R2, ^{15}NO from $^{15}N^{14}NO$ is expected be formed more slowly than ^{14}NO from $^{14}N^{15}NO$ due to the lower zero-point energy, resulting in a relative enrichment of the residual N_2O with the $^{15}N^{14}NO$ isotopomer. The influence of isotopic substitution at the oxygen position is expected to be of secondary importance. In contrast, we have already noted the role as a "spectator" of the N_2 entity in R3. The ^{15}N partitioning should have no influence on the intramolecular ^{15}N fractionation of this pathway.

3.4.3 Atmospheric implications

We finally consider the implications of the reaction of N_2O with $O(^1D)$ on the stratospheric N_2O isotope signature. For all positions of the molecule, enrichments of heavy isotopes are found ("normal" isotope effect). There is no significant temperature dependence for the whole range of relevant stratospheric temperatures (down to 196 K). Moreover, there seems to be no pressure effect either on the fractionation constant in the range between 1 and 1130 mbar. Pressure could have an influence on the observed isotopic fractionation, as discussed for the reaction

of $O(^1D)$ with HD [*Laurent et al.*, 1995], since under the conditions of the low-pressure experiments $O(^1D)$ displays a superthermal translational energy distribution. This means that the translational relaxation rate of $O(^1D)$ by collisions with surrounding gas molecules is not fast enough compared to electronic quenching, $O(^1D) + M \rightarrow O(^3P) + M^*$ [*Matsumi and Chowdhury*, 1996; *Matsumi et al.*, 1994]. For altitudes of 40 km and temperatures of 260 K, $O(^1D)$ is expected to have an average translational energy (7.7 kJ/mol) that is about two times higher than that of the corresponding Boltzmann distribution (3.2 kJ/mol). However, from our experiments we can exclude a direct influence of pressure on the observed isotopic fractionation in the atmosphere.

All the fractionation constants measured for the reaction $N_2O + O(^1D)$ are relatively small compared to those encountered in photolysis experiments conducted at various wavelengths ≥193 nm (see Figure 28). The largest fractionation occurs in ^{18}O, followed by the terminal and finally the central nitrogen atom. This order is clearly distinct from that in photolysis. In photolysis, experimental observations [*Rahn et al.*, 1998; *Röckmann et al.*, 2000; *Röckmann et al.*, 2001; *Toyoda et al.*, 2001a; *Turatti et al.*, 2000; *Umemoto*, 1999; *Zhang et al.*, 2000] (see also chapters 4 and 5) and theoretical calculations [*Johnson et al.*, 2001; *Miller and Yung*, 2000] point to an order $^{15}\varepsilon_2 < {}^{18}\varepsilon < {}^{15}\varepsilon_1$, with the overall nitrogen fractionation, $^{15}\varepsilon$, being larger than $^{18}\varepsilon$ (i.e., $^{15}\varepsilon$ is more negative). The $O(^1D)$ sink is therefore expected to attenuate the apparent N_2O isotope fractionation compared to the effects expected from photolysis only. Moreover, the different pattern in position-dependent ^{15}N isotope fractionation opens up the possibility to distinguish both stratospheric N_2O sink reactions by the isotopic signature of N_2O. This concept will be discussed in greater detail in conjunction with the actual stratospheric measurements (chapter 7).

4 Temperature dependence of isotope fractionation in N_2O photolysis

Stratospheric ultraviolet (UV) photolysis is the dominant sink reaction and main origin of isotopic enrichment for atmospheric nitrous oxide (N_2O) (1.2.2; 1.3). To date all experimental studies of isotopic enrichment in N_2O photolysis have been performed at room temperature only. In this chapter, the first temperature-dependent (193 K < T < 295 K) measurements of ^{18}O and position-dependent ^{15}N fractionation constants obtained by broadband photolysis at wavelengths of relevance to the stratospheric "UV window" are reported. For a given extent of reaction, we find higher enrichments at lower temperatures, qualitatively in agreement with theoretical predictions. The relative changes are in the order $^{14}N^{15}NO > N_2{}^{18}O > {}^{15}N^{14}NO$, similar to the absolute values. The measurements are compared with model predictions of the temperature dependence and the limited data on temperature-dependent absorption cross sections of N_2O isotopomers. We also investigate a hitherto unexplained artefact in laboratory measurements of N_2O photolysis: At high degrees of conversion, N_2O loss by the reaction with $O(^1D)$ becomes important, presumably due to the photochemical production and subsequent photolysis of NO_2 in the reaction cell. The effect gains importance with increasing concentration and in the present study, it caused decreases of the measured fractionation constants requiring correction for initial N_2O mixing ratios of 4 mmol/mol [*Kaiser et al.*, 2002b].

4.1 Experimental methods

Mixtures of N_2O in N_2 bath gas were irradiated by the same 1 kW antimony lamp (*Heraeus*, Hanau) used before [*Röckmann et al.*, 2001]. The lamp features a continuous emission spectrum from 190 to 225 nm which was used both unfiltered and modified by a (207±10) nm interference filter. The water filter employed in previous experiments as IR absorber was found unnecessary and potentially caused problems as will be shown later. The relative shape of the lamp emission spectrum is similar to the actual stratospheric irradiance curve except for the absent Schumann-Runge band structures.

In contrast to the $N_2O + O(^1D)$ (chapter 3), fractionation constants for ^{18}O and ^{15}N at both N positions in the N_2O molecule are calculated directly for single photolysis experiments from eqn. 57 (see section 3.1). For oxygen, we only consider the more abundant rare isotope (^{18}O),

since the isotopic variation in N_2O photolysis is most probably a mass-dependent process and therefore the variation in ^{17}O is closely coupled to that in ^{18}O (section 10.2).

Pilot experiments were performed in four different reactors (A to D) to validate the direct calculation of fractionation constants. Each reactor consisted of a cylindrical body (A: quartz, B: stainless steel, C, D: borosilicate glass with volumes of 125 cm^3, 366 cm^3, 492 cm^3 and 4.71 dm^3, respectively) with synthetic silica windows (*Heraeus* Suprasil) and a shut-off valve. Two different mixing ratios were used: 4.0 mmol/mol and 1.0 mmol/mol. Irradiation lasted for 16 to 192 hours and 4 to 30 hours with and without the interference filter, respectively. The initial total pressure in the reactors was usually 1.0 to 1.2 bar. In three experiments with reactor B 2.8 mmol/mol to 6.6 mmol/mol of oxygen were added in order to check for the influence of O_2 photolysis and O_3 chemistry.

For the low-temperature experiments at 193 to 273 K we used only reactor A equipped with a cooling-jacket through which ethanol at the desired temperature could be circulated by a thermostat (*Huber* HS90). The actual temperature was measured by a calibrated thermocouple and could be controlled to within 0.2 °C. Double-front windows with interstitial vacuum and forced air ventilation prevented condensation of ambient humidity. During the 193 K-experiments, the pressure in the reactor dropped to roughly ⅔ of the initial pressure at room temperature. The absence of an influence of pressure on the fractionation constant has already been established by extensive photolysis experiments at 193 nm [*Röckmann et al.*, 2000] and was confirmed by additional experiments. The low-temperature experiments in the small reactor A had to be performed with the higher mixing ratio of 4.0 mmol/mol in order to have sufficient pressure in the bellows of the dual-inlet system of the isotope ratio mass spectrometer (*Finnigan* MAT 252).

The exact experimental procedures for photolysis and sample extraction through a ultra-high efficient Russian doll-type trap [*Brenninkmeijer and Röckmann*, 1996] have already been described before [*Röckmann et al.*, 2000]. To achieve the required precision for direct calculation of the fractionation constant from a single experiment, several small corrections were applied, namely pressure and temperature corrections for the amount of gas filled into and recovered from the reactor (up to ±1 % each) as well as a correction for a small N_2O loss of (0.7±0.1) % in the preparatory GC purification step (section 8.1.4). The reactor volumes were determined gravimetrically (using degassed *MilliQ* water) except for reactor D which size was estimated manometrically. The other reactor sizes were also cross-checked against each other manometrically and by comparing the relative N_2O yields from the same N_2O/N_2 mixture. The agreement was within 0.2 % in each case. To test the procedure for N_2O extraction from the reaction mixtures, known amounts of N_2O in N_2 were extracted from a glass bulb ($V \approx 2$ dm^3) at a mixing ratio more than two times lower than encountered at the end of any photolysis experiment. Recovery was (100.0±0.2) %

with negligible isotopic fractionation (< 0.02 ‰ in $\delta^{15}N$ and $\delta^{18}O$). "Blank" runs without photolysis provided the mixing ratios of the N_2O/N_2 mixtures and served as a benchmark for the overall precision of the extraction procedure. The standard deviation of ln *y* (as a measure of extraction efficiency; *y* being the remaining N_2O fraction) was determined as 0.012 for the small reactor A and < 0.005 for reactors B, C and D. The average δ values of the extracted N_2O (from 28 extractions) are all zero (within the range of mass-spectrometric precision, see below), but with a larger standard deviation for the "blanks" from reactor A than for those from the larger reactors (0.13 ‰ and 0.03 ‰, respectively – equally for $\delta^{18}O$ and average $\delta^{15}N$) which is a direct consequence of the greater variability of the extraction efficiency for reactor A.

Dual-inlet isotope ratio mass spectrometric measurements of the purified sample were performed on a *Finnigan* MAT 252 instrument. $\delta^{18}O$ and average $\delta^{15}N$ were determined from $^{45}\delta$ and $^{46}\delta$. $^{1}\delta^{15}N$ and $^{2}\delta^{15}N$ were calculated from $^{31}\delta$ of the NO^+ fragment ion and the average $\delta^{15}N$. 95 % standard errors of the $^{45}\delta/^{46}\delta$ measurements were less than 0.02 ‰/0.04 ‰ absolutely and about 0.15 ‰ for $^{31}\delta$ (sections 2.5 and 2.6)

4.2 Dependence of ε on the degree of conversion

4.2.1 Results from pilot experiments at high N_2O mixing ratio

The pilot experiments with a high mixing ratio (4.0 mmol/mol) show a dependence of the fractionation constants on the remaining N_2O fraction (*y*) (Figure 19) which was not noticed in our previous broadband photolysis experiments with the same antimony lamp. Moreover, a shift of the spectrum towards longer wavelengths by introduction of an interference filter yielded a small, but reproducible increase in fractionation which may have been disguised by experimental noise before. We believe that these new findings are a consequence of the improved experimental precision and a more systematic variation of the experimental parameters. In three experiments, we added aliquots of oxygen. Despite the large oxygen excess, there was only a slight increase in $|\varepsilon|$, i.e. the value change in the opposite direction to that needed to explain the decreasing values of $|\varepsilon|$. Oxygen was therefore deemed irrelevant or at least not crucial for the complication discussed here.

A linear fit describes the dependence of ε on ln *y* quite well. The fit parameters are shown in Table 7. The results for photolysis without interference filter agree for reactors B and C which are of similar geometry, but of different material. Fractionation constants are clearly larger for the experiments with a (207±10) nm interference filter than for those without, but the slope

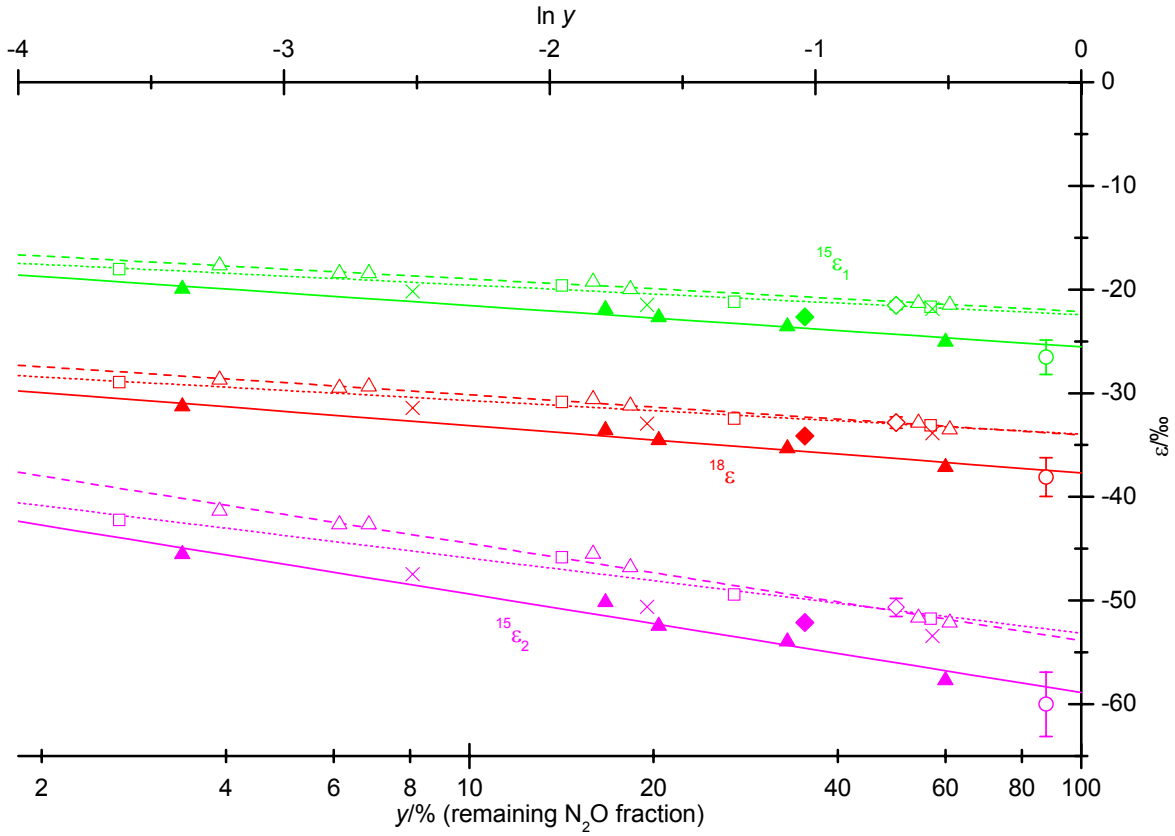

Figure 19: Directly calculated fractionation constants of broadband photolysis experiments with different reactors (A to D) and an N_2O mixing ratio of 4.0 mmol/mol. Additional experiments with an interference filter and with addition of O_2 are also shown. For clarity, average ^{15}N fractionation constants ($^{15}\varepsilon$) have been omitted. Error bars are smaller than symbol sizes unless indicated.
◇ A; △ (- - - -) B; □ (· · · · ·) C; O D: all without filter
× B: without filter, added O_2 (2.8 to 6.6 mmol/mol)
▲ (———) B: with (207±10) nm interference filter

$\partial\varepsilon/\partial(\ln y)$ is almost the same in both cases. The slope is largest for $^{15}\varepsilon_2$ and smallest for $^{15}\varepsilon_1$. The regression coefficients show that $\ln y$ explains at least 96 % of the variation in ε. It is not clear *a priori* whether the y-axis offset (ε_0) can be equated with the "true" fractionation constant as $\partial\varepsilon/\partial(\ln y)$ may be different at the beginning of the reaction ($\ln y > -0.5$). Indeed, the one experiment with reactor D shown here seems to indicate such a behaviour, but reactor geometry and window thickness are also different for this reactor compared to reactors B and C.

4.2.2 Results from pilot experiments at low N_2O mixing ratio

Additional experiments at a lower mixing ratio of 1.0 mmol/mol were performed with the larger reactors C and D (Figure 20). The results show almost constant fractionation constants for the entire range of $\ln y$. The extrapolation to $\ln y = 0$ gives slightly higher $|\varepsilon|$ values than for the mixing ratio of 4.0 mmol/mol Table 7), but there is no indication for a change of the slope

Table 7: Linear regression parameters for the data from Figure 19 and Figure 20 (*n* indicates number of experiments)

	Filter	Reactor	$x(N_2O)$/‰	ε_0	$\partial\varepsilon/\partial(\ln y)$	r^2	*n*
$^{15}\varepsilon$	no	B	4.0	–38.0±0.3	–2.7±0.1	0.988	7
	no	C	4.0	–37.8±0.6	–2.1±0.3	0.963	4
	no	C	1.0	–40.4±0.2	–0.3±0.1	0.636	6
	207 nm	B	4.0	–42.3±0.6	–2.9±0.3	0.962	5
	207 nm	C	1.0	–43.4±0.5	–0.4±0.4	0.177	6
$^{15}\varepsilon_2$	no	B	4.0	–53.9±0.5	–4.1±0.2	0.987	7
	no	C	4.0	–53.1±1.0	–3.1±0.4	0.963	4
	no	C	1.0	–57.8±0.4	–0.8±0.2	0.806	6
	207 nm	B	4.0	–58.9±0.9	–4.1±0.5	0.962	5
	207 nm	C	1.0	–60.9±0.8	–0.7±0.6	0.278	6
$^{15}\varepsilon_1$	no	B	4.0	–22.1±0.2	–1.4±0.1	0.986	7
	no	C	4.0	–22.4±0.4	–1.2±0.2	0.961	4
	no	C	1.0	–23.0±0.2	0.0±0.1	0.036	6
	207 nm	B	4.0	–25.5±0.4	–1.7±0.2	0.963	5
	207 nm	C	1.0	–25.9±0.3	–0.3±0.2	0.282	6
$^{18}\varepsilon$	no	B	4.0	–34.0±0.2	–1.7±0.1	0.985	7
	no	C	4.0	–34.0±0.3	–1.4±0.2	0.976	4
	no	C	1.0	–35.5±0.2	–0.2±0.1	0.358	6
	207 nm	B	4.0	–37.7±0.4	–2.0±0.2	0.965	5
	207 nm	C	1.0	–38.4±0.3	–0.4±0.2	0.458	6

$\partial\varepsilon/\partial(\ln y)$ at smaller degrees of conversion. The y-axis offsets for the filtered spectrum are almost identical for the high and low mixing ratios. We therefore assume that the y-axis offsets in Figure 20 represent the "true" fractionation constants for this system. Additional measurements with reactor D and the unfiltered lamp spectrum at low N_2O mixing ratio give fractionation constants that are close to those with reactors B or C and the filtered spectrum, in agreement with the results at higher N_2O mixing ratio. This indicates that the characteristics of reactor D without filter and reactors B/C with filter are similar, possibly due to the long N_2O column of reactor D (140 cm as compared to 40/50 cm for reactors B/C) acting as a self-absorbing filter.

4.2.3 Origin of the dependence of ε on the degree of conversion

We believe that the decrease in the fractionation constant at higher degrees of conversion is caused by the reaction $N_2O + O(^1D)$. This seems to be surprising at first glance, since the great excess of N_2 bath gas should quench most $O(^1D)$ produced in N_2O photolysis (R1) via

$$O(^1D) + N_2 \rightarrow O(^3P) + N_2 \qquad k_4 = 2.6\cdot10^{-11}\ \mathrm{cm^3 s^{-1}} \qquad \text{(R4)}$$

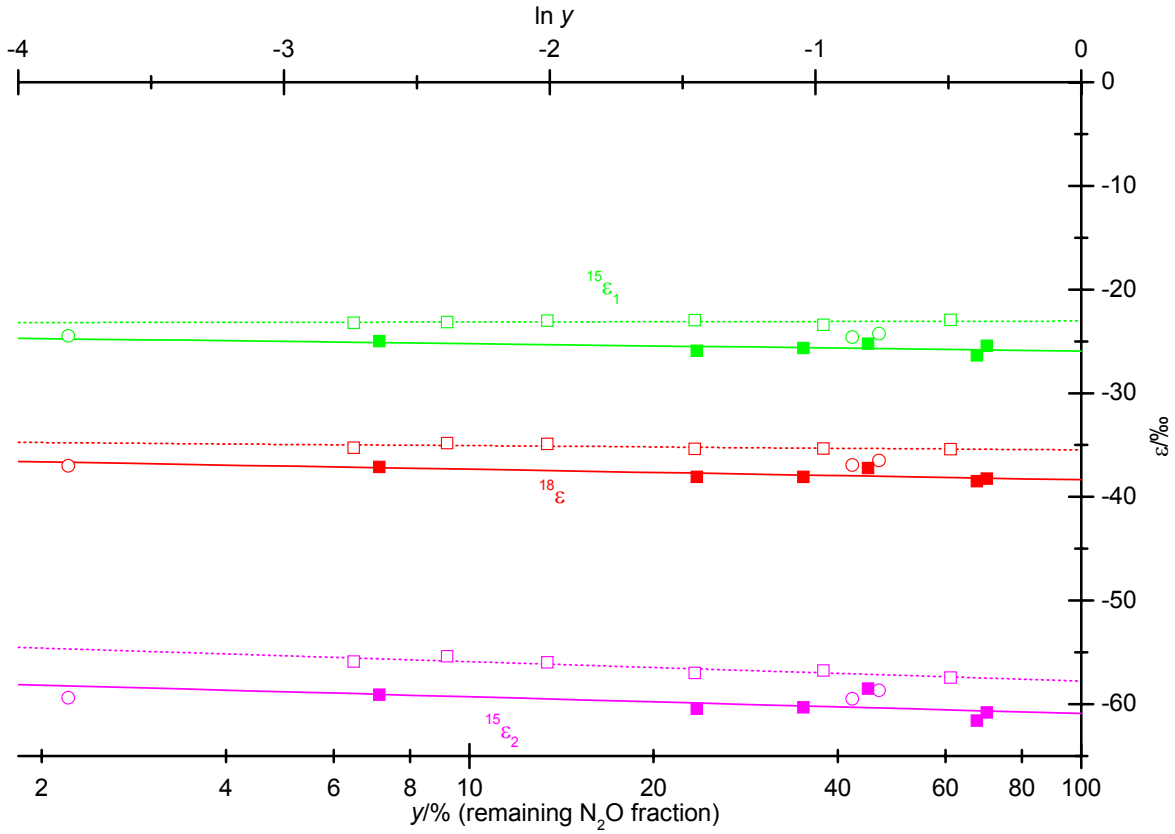

Figure 20: Directly calculated fractionation constants (purple: $^{15}\varepsilon_2$, green: $^{15}\varepsilon_1$, red: $^{18}\varepsilon$) of broadband photolysis experiments with different reactors (C, D) and an N_2O mixing ratio of 1.0 mmol/mol. Additional experiments with an interference filter are also shown. For clarity, average ^{15}N fractionation constants ($^{15}\varepsilon$) have been omitted.
□ (· · · · ·) C; ○ D: without filter
■ (———) C: with (207±10) nm interference filter

The quoted reaction rate constants are calculated from the latest IUPAC evaluation [*Atkinson et al.*, 2001] for 298 K and a N_2 number concentration of $2.9 \cdot 10^{19}$ cm^{-3}. Notwithstanding the dominant $O(^1D)$ quenching, a small fraction of the $O(^1D)$ may react with N_2O according to reactions (R2) or (R3) with rate constants of $k_2 = 7.2 \cdot 10^{-11}$ cm^3s^{-1} and $k_3 = 4.4 \cdot 10^{-11}$ cm^3s^{-1}. With an initial N_2O mixing ratio of 4.0 mmol/mol at most 1.8 % of the $O(^1D)$ from N_2O present in the reactor can react with N_2O. Considering the measured fractionation constants for N_2O + $O(^1D)$ of $^{15}\varepsilon_1 = -8.8$ ‰, $^{15}\varepsilon_2 = -2.2$ ‰ and $^{18}\varepsilon = -12.2$ ‰ (chapter 3), the $O(^1D)$ produced directly be photolysis is not sufficient to explain the observed trends of ε. Therefore an indirect source of $O(^1D)$ must be responsible which is strongly supported by the experimental evidence as shown in next section. Candidates for this source are O_3 and NO_2 photolysis, but as will be demonstrated later, NO_2 photolysis is the more likely cause.

4.2.4 Empirical correction function for photolysis at high N_2O mixing ratio

The differences between the experiments at 1.0 and 4.0 mmol/mol can be used to derive an empirical correction for the measurements of the temperature dependence which had to be performed at high mixing ratios (see above). The correction is based on the measured fractionation constants for $N_2O + O(^1D)$ (chapter 3). For two simultaneous, independent fractionation reactions in a closed system, the total ε value is equal to the sum of the individual fractionation constants weighted by the relative reaction rates, so that

$$\varepsilon = \frac{k_o}{k_o + k_p}\varepsilon_o + \frac{k_p}{k_o + k_p}\varepsilon_p \tag{59}$$

In the present case, the subscripts refer to $N_2O + O(^1D)$ ("o") and photolysis ("p"). ε and ε_p are the fractionation constants ($^{15}\varepsilon_1$, $^{15}\varepsilon_2$, $^{18}\varepsilon$) for photolysis at 4.0 and 1.0 mmol/mol, respectively; values for ε_o are the fractionation constants for $N_2O + O(^1D)$ (chapter 3). The apparent $O(^1D)$ contribution, $x_o = k_o/(k_o+k_p)$, is calculated for all isotopes. Similar results are found for the different fractionation constants ($^{15}\varepsilon_1$, $^{15}\varepsilon_2$, $^{18}\varepsilon$). This strongly supports the assumption that $O(^1D)$ is indeed responsible for the observed trends in ε. x_o is calculated for all experiments performed at high mixing ratios.

The averaged results (Figure 21) show a roughly linear increase with ln *y*, i.e. the "contamination" increases with longer photolysis times. The results for reactors B and C without interference filter are in good agreement. Linear fits give the same y-axis offset of $x_o = 0.06$ for reactors B and C. The slopes are different, but this deviation is due to one ample from reactor C. The slope for the experiments with reactor B and interference filter is slightly steeper. The y-axis offset is zero in this case. This absence of an $O(^1D)$ contribution is a direct consequence of the previous notion that the fractionation constants for the filtered lamp spectrum at 4 mmol/mol and 1 mmol/mol are almost identical. However, at high degrees of conversion, the $O(^1D)$ contribution reaches roughly 30 % which needs to be corrected for. The empirical relations for reactor B without filter and reactor C with filter will be used later to remove the influence of $O(^1D)$ on the observed fractionation constants at lower temperatures.

4.2.5 Relevance of the $O(^1D)$ artefact in other studies

Considering the number of experimental studies published on isotopic fractionation in the UV photolysis of N_2O, it appears surprising that a similar effect as presented here was not found before. This has several reasons: Johnston *et al.* [1995] measured at a wavelength where there is hardly any fractionation at all, optical techniques [*Turatti et al.*, 2000; *Umemoto*, 1999; *Zhang et al.*, 2000] suffer from a lack of precision, the degree of conversion was not large enough in some studies (e.g. Toyoda *et al.* [2001a] did not exceed $-\ln y = 0.25$) or the difference between photo-

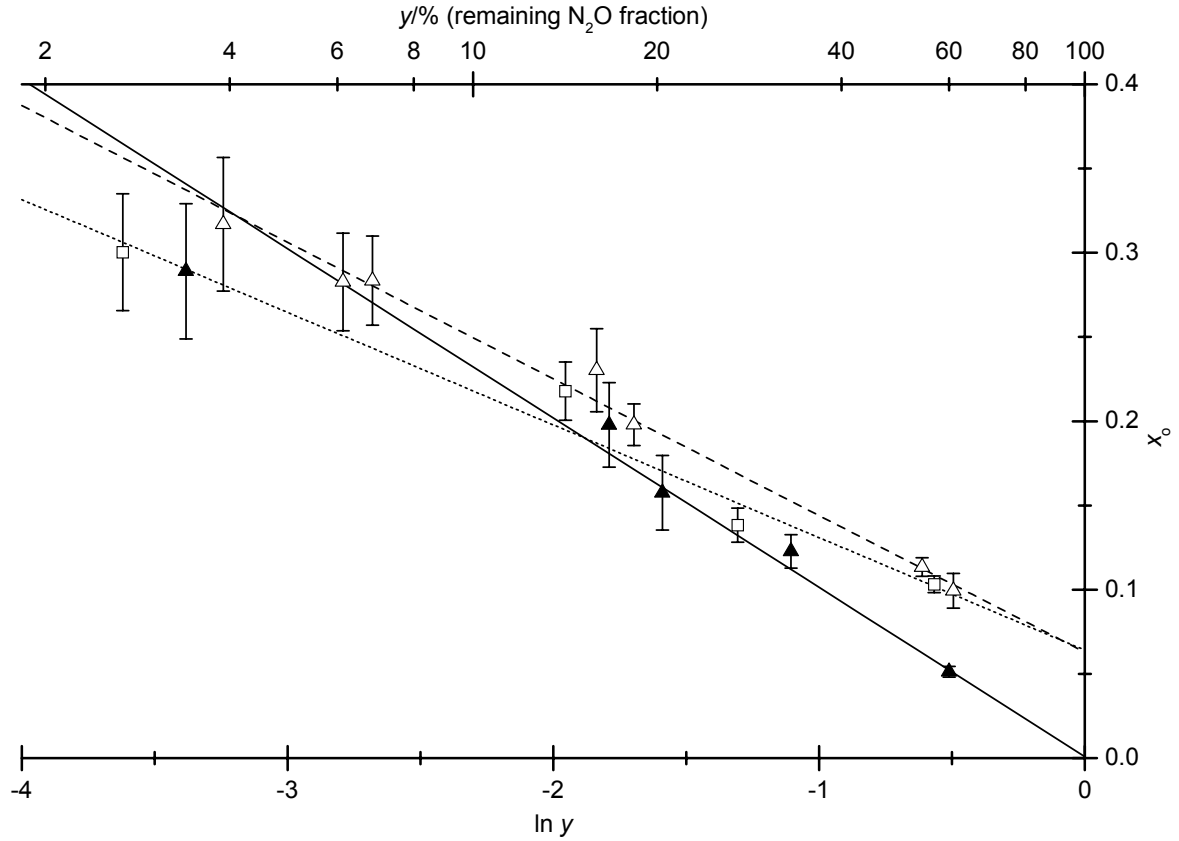

Figure 21: Apparent contribution of N_2O + $O(^1D)$ to observed fractionation constants for experiments with 4.0 mmol/mol N_2O at different degrees of conversion.
△ (- - - -) reactor B; □ (· · · · ·) C: without filter
▲ (———) reactor B: with (207±10) nm interference filter
Weighted linear fits are applied:
x_o(B, without filter) = (–0.081±0.003) ln y + (0.063±0.003) (r^2 = 0.994)
x_o(B, with filter) = (–0.101±0.010) ln y + (0.001±0.007) (r^2 = 0.973)
x_o(C, without filter) = (–0.067±0.011) ln y + (0.064±0.010) (r^2 = 0.952)

lytic and artefactual fractionation constant was only small. On the other hand, it is advantageous not to exceed a certain degree of conversion, because artefacts from the building up of reaction products are likely to be reduced. As stated above, we did not find such an effect in previous experiments with the same lamp as used here and a mixing ratio of 3.7 mmol/mol [*Röckmann et al.*, 2001], even at high –ln y; just a close re-examination of the original data gives similar trends of ε with ln y, but only for reactor B.

There is only one set of previous measurements in which a similar artefact as discussed here can be found: It was already noted by Röckmann *et al.* [2000] that their values of ε for N_2O photolysis at 193.3 nm are in reasonable agreement with Rahn *et al.* [1998] for low degrees of conversion, but are larger for higher degrees of conversion. This could in principle be a real difference if the laser wavelength had been slightly different in both cases since the fractionation constants vary strongly in the region of vibrational structure around the maximum in the N_2O absorption

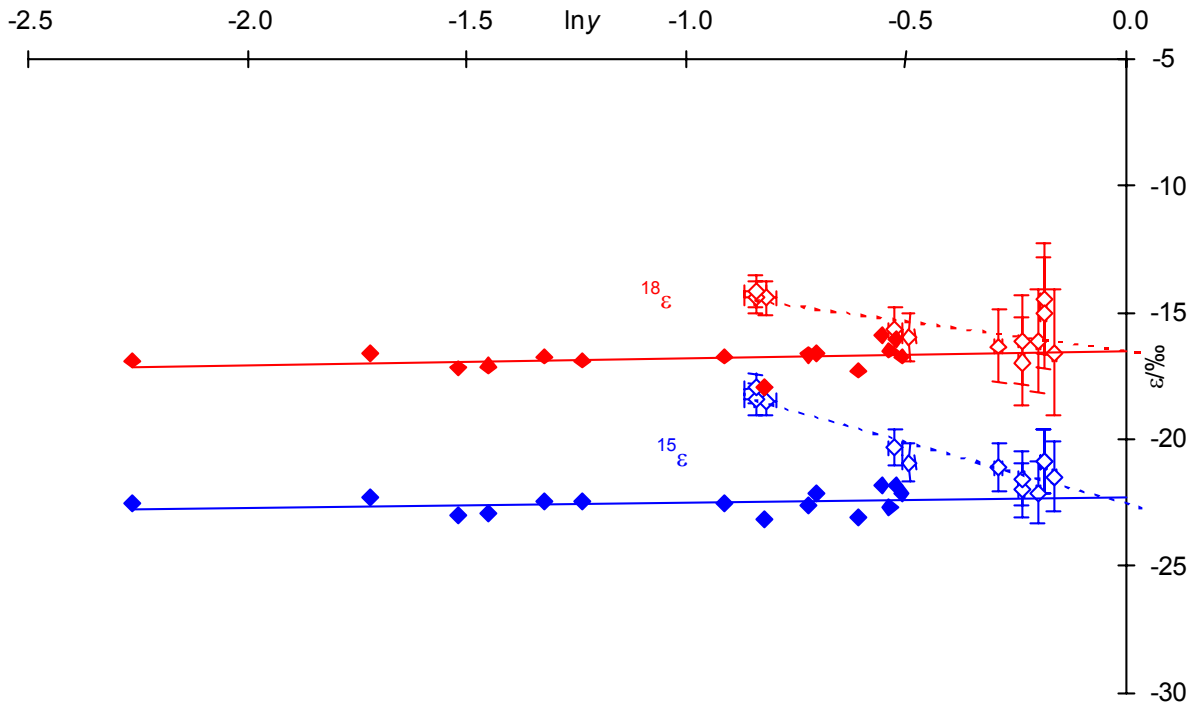

Figure 22: Reanalysis of the data for N_2O photolysis with ArF lasers at 193.3 nm with N_2O mixing ratios of 6.7 mmol/mol [*Rahn et al.*, 1998] and 3.7 mmol/mol [*Röckmann et al.*, 2000]. Fractionation constants are derived directly from individual experiments.
◇ data from Rahn *et al.* [1998]; ◆ data from Röckmann *et al.* [2000]

$^{18}\varepsilon$/‰(Rahn) = (–2.3±0.8) ln y + (–16.5±0.4) $r^2 = 0.445$
$^{18}\varepsilon$/‰(Röckmann) = (+0.2±0.3) ln y + (–16.5±0.3) $r^2 = 0.067$
$^{15}\varepsilon$/‰(Rahn) = (–4.8±0.6) ln y + (–22.5±0.3) $r^2 = 0.873$
$^{15}\varepsilon$/‰(Röckmann) = (+0.2±0.2) ln y + (–22.3±0.3) $r^2 = 0.058$

spectrum [*Selwyn and Johnston*, 1981], but in both experiments the natural bandwidth of the ArF excimer radiation (≈0.7 nm FWHM [*Saito and Ito*, 1998]) was used. However, reanalysis of the data from Rahn *et al.* (obtained with a mixing ratio of 6.7 mmol/mol) and Röckmann *et al.* (3.7 mmol/mol) by direct calculation of the fractionation constants shows that both data sets collapse into a single point at ln $y = 0$ (Figure 22).

In addition, the 6.7 mmol/mol data [*Rahn et al.*, 1998] clearly show a trend to lower fractionation constants at higher degrees of conversion, just as described for broadband photolysis here. Interestingly, the slopes of –2.3 for $^{18}\varepsilon$ and –4.8 for $^{15}\varepsilon$ (Figure 22) are much steeper than for broadband photolysis (Table 7), but this could also be an artefact of the direct calculation method if the N_2O extraction procedure causes a systematic shift in the δ values and thus a non-zero y-axis offset. Such shifts are not relevant for the study of Röckmann *et al.* [2000] and for the present one, as estimated from the results of the blank runs (< 0.02 ‰/0.04 ‰ for $\delta^{15}N/\delta^{18}O$), but may be present in the study of Rahn *et al.* [1998]. Estimates for these systematic offsets can be calculated from linear fits to Rayleigh plots of Rahn's data (i.e., ln(1+δ) vs ln y) and give +0.40

at $\ln y = 0$ for $\ln(1+\delta^{18}O)$ and +0.24 for $\ln(1+\delta^{15}N)$. It should be stressed that these numbers are really upper limits since they can be caused both by a systematic offset of the extraction procedure and by any non-linearity of the Rayleigh plot. Taking these offsets into account, one obtains smaller slopes from an ε vs ln *y* plot: $\partial^{18}\varepsilon/\partial\ln y = (-0.8\pm0.9)$ ($r^2 = 0.07$) and $\partial^{15}\varepsilon/\partial\ln y = (-2.3\pm0.8)$ ($r^2 = 0.45$), with y-axis offsets of –15.0 ‰ and –21.0 ‰. Therefore, the $^{15}\varepsilon$-trend with ln *y* seems to be statistically very robust. Röckmann *et al.* [2000] have also measured at mixing ratios of 6.7 mmol/mol, but their data give smaller slopes of $\partial^{18}\varepsilon/\partial\ln y = (-0.4\pm0.1)$ ($r^2 = 0.96$) and $\partial^{15}\varepsilon/\partial\ln y = (-0.9\pm0.1)$ ($r^2 = 0.97$).

We currently cannot explain these differences in slope, but note that the error estimates for the latter study are much reduced compared to the former one. The larger slope for ^{15}N compared to ^{18}O is due to the larger difference of the photolytic fractionation constants to the ones for $N_2O + O(^1D)$ ($^{15}\varepsilon = -5.5$ ‰ and $^{18}\varepsilon = -12.2$ ‰;). In conclusion, the trend presented here is deemed to be not unique for the specific photolytic set-up used here, but is rather an artefact which can manifest itself in any isotope study of N_2O photolysis if sufficiently high mixing ratios and degrees of conversion are studied.

4.2.6 Tentative explanation of the O(^1D) artefact

In this section we will discuss systematically the possible causes for the deviation of N_2O broadband photolysis from the expected Rayleigh equation at high degrees of conversion (large $|\ln y|$). In order to investigate the nature of this artefact, we will subsequently analyse the reaction kinetics of the N_2O photolysis system.

First of all, it is imperative to have a homogeneous reaction mixture due to the inherent non-linearity of Rayleigh fractionation (exponential relation between mixing ratio and isotope ratio). Otherwise, mixing of photolysed and unphotolysed gas will result in a decrease of the measured fractionation constant. However, in view of N_2O lifetimes of the order of ten hours in the experiments reported here diffusion is certainly sufficient to remove any inhomogeneity in the reactor, even more so since it was noted to be insignificant in the fast laser photolysis experiments at 193 nm [*Röckmann et al.*, 2000].

Second, photolysis channels other than production of $O(^1D)$ should not be present. Although other photolysis products are energetically accessible, namely $N_2 + O(^3P)$, $N(^4S) + NO(^2\Pi)$ and $N_2 + O(^1S)$, the latest evaluations of kinetic rate data for atmospherically relevant reactions recommend a primary quantum yield of 1.0 for the $O(^1D)$ channel [*Atkinson et al.*, 2001; *DeMore et al.*, 1997]. Furthermore, such an effect should not depend on the N_2O mixing ratio in the photolysis gas mixture, but the data from the experiments with 1 mmol/mol N_2O/N_2 are clearly in-

dependent of the degree of conversion and therefore rule out an effect of other reaction channels at 4 mmol/mol.

Third, quenching of $O(^1D)$ by N_2 has to be efficient enough. As discussed above, at most 1.8 % of the N_2O photolysis product $O(^1D)$ reacts directly with N_2O. This effect should become less important at higher degrees of conversion since the N_2O mixing ratio becomes increasingly smaller in the course of a photolysis experiment whereas N_2 remains almost constant. Indeed, simulations with the Gear solver FACSIMILE show that the directly calculated fractionation constants do not deviate significantly from their nominal value for photolysis if no other reactions than N_2O photolysis, $O(^1D)$ quenching and reaction of $O(^1D)$ with N_2O are involved. However, this does not take into account $O(^1D)$ production from other processes which seems to be relevant indeed as shown below.

In conclusion, the complications do not arise from the primary steps in the reaction sequence of N_2O photolysis, but must be produced in a more indirect way. The building up of some reaction product seems to be a likely explanation since the influence on the measured fractionation constant increases with the extent of reaction. From reactions (R1) to (R4), there are two candidate species: NO and O_2. O_2 is also produced from the $O(^3P)$ self-reaction:

$$O(^3P) + O(^3P) + N_2 \rightarrow O_2 + N_2 \qquad k_5 = 1.4\cdot10^{-12}\ \mathrm{cm^3 s^{-1}} \qquad \text{(R5)}$$

The absorption cross sections of NO and O_2 are too low at $\lambda > 190$ nm to render their photolysis significant in this system [*Murray et al.*, 1994; *Yoshino et al.*, 1992], but these species may undergo further reactions with $O(^3P)$ to produce NO_2 and O_3:

$$NO + O(^3P) + N_2 \rightarrow NO_2 + N_2 \qquad k_6 = 2.5\cdot10^{-12}\ \mathrm{cm^3 s^{-1}} \qquad \text{(R6)}$$

$$O_2 + O(^3P) + N_2 \rightarrow O_3 + N_2 \qquad k_7 = 1.7\cdot10^{-14}\ \mathrm{cm^3 s^{-1}} \qquad \text{(R7)}$$

Part of the NO_2 and O_3 is lost again by reaction with $O(^3P)$

$$NO_2 + O(^3P) \rightarrow NO + O_2 \qquad k_8 = 9.7\cdot10^{-12}\ \mathrm{cm^3 s^{-1}} \qquad \text{(R8)}$$

$$O_3 + O(^3P) \rightarrow 2\ O_2 \qquad k_9 = 8.0\cdot10^{-15}\ \mathrm{cm^3 s^{-1}} \qquad \text{(R9)}$$

or may be interconverted:

$$NO + O_3 \rightarrow NO_2 + O_2 \qquad k_{10} = 1.7\cdot10^{-14}\ \mathrm{cm^3 s^{-1}} \qquad \text{(R10)}$$

Finally, NO_2 and/or O_3 can also be photolysed and produce additional $O(^1D)$ via

$$NO_2 + h\nu \rightarrow NO + \Phi_{O(^1D)}(NO_2)\ O(^1D) + \Phi_{O(^3P)}(NO_2)\ O(^3P) \qquad \text{(R11)}$$

$$O_3 + h\nu \rightarrow O_2 + \Phi_{O(^1D)}(O_3)\ O(^1D) + \Phi_{O(^3P)}(O_3)\ O(^3P) \qquad \text{(R12)}$$

where the sum of the quantum yields ($\Phi_{O(^1D)}+\Phi_{O(^3P)}$) equals 1.

In contrast to N_2O which is continuously removed, NO_2 and O_3 may build up during the course of N_2O photolysis and their own photolysis produces additional $O(^1D)$ which can subsequently react with the remaining N_2O, affecting its isotopic signature. Previous publications al-

ready noted the presence of NO_2 in the reaction mixture [*Röckmann et al.*, 2000; *Zhang et al.*, 2000]. O_3 photolysis probably does not play a role because our experiments with added O_2 did not show a stronger influence from $O(^1D)$. Therefore, we conclude that NO_2 is the most important secondary $O(^1D)$ source.

At first sight, it is not clear how $O(^1D)$ production from NO_2 photolysis should explain the observed dependence of ε on $\ln y$, because most of the $O(^1D)$ should be quenched again by N_2, just as the $O(^1D)$ from N_2O photolysis. However, if the NO_2 photolysis rate is much faster than the N_2O photolysis rate and if sufficient NO_2 builds up, such an effect seems to be possible. In an attempt to verify this mechanism, we calculated the expected photolysis rates from the emission spectrum of the antimony lamp we measured previously [*Röckmann et al.*, 2001] and data of absorption cross-sections and quantum yields from the literature (IUPAC Subcommittee on Gas Kinetic Data Evaluation: Data Sheet PNOx4 & Data Sheet POx2_O3_hv, http://www.iupac-kinetic.ch.cam.ac.uk, and references therein). $\Phi_{O(^1D)}(O_3)$ is assumed to be 0.9 for $\lambda < 220$ nm (not covered by the IUPAC evaluation). For $\Phi_{O(^1D)}(NO_2)$ we adopt a value of 0.5 [*Sun et al.*, 2001] for $\lambda < \lambda_{threshold} = 244$ nm. The results indicate that the photolysis rate $J_{O(^1D)}(NO_2)$ is 30 times larger than $J_{O(^1D)}(N_2O)$ for the experiments with filter and 60 times larger for the experiments without interference filter; $J_{O(^1D)}(O_3)$ is 300/9000 times larger (with/without filter). This supports the likelihood of the suggested mechanism.

Unfortunately, we did not measure the O_3 and NO_2 concentrations in our system and therefore cannot calculate the $O(^1D)$ production rates. We tried to simulate the system by FACSIMILE using the precalculated photolysis rates and NO_x chemistry as outlined above. However, we were only able to reproduce the observed dependence of the fractionation constant on the degree of conversion qualitatively. At a mixing ratio of 4 mmol/mol, NO_2 and O_3 production were too low in the model. A similar dependency of ε on $\ln y$ as measured could only be simulated assuming initial N_2O mixing ratios > 15 mmol/mol. Since no spectroscopic analyses other than isotope mass spectrometry were done of the reaction mixtures, it is difficult to say why we cannot simulate our system quantitatively. Inclusion of NO_3, N_2O_5, $O_2(^1\Delta)$ and $O_2(^1\Sigma)$ chemistry/photolysis did not make any difference.

Nevertheless, we believe that the experimental evidence accumulated so far is sufficient to invoke the influence of $N_2O + O(^1D)$ on the isotopic fractionation in N_2O photolysis at 4.0 mmol/mol. A similar influence can be perceived in at least one other study [*Rahn et al.*, 1998], but may have biased the results of others as well. Retrospectively, quenching of $O(^1D)$ by N_2 seems to be *not* efficient enough to avoid the reaction of $N_2O + O(^1D)$. As shown here, a deviation of the measured from the "true" fractionation constant does not necessarily show up as a

deviation from a Rayleigh plot if the range of ln *y* that has been investigated is small. At wavelengths >190 nm, a possible artefact from $N_2O + O(^1D)$ will likely reduce the measured fractionation constant. The failure to simulate this effect is unfortunate, but the reaction system also appears to be underdetermined since we have not measured *in situ* NO_2 and O_3 concentrations.

4.3 Temperature dependence of ε

The fractionation constants before applying the $O(^1D)$ correction for experiments at temperatures between 193 K and 273 K with and without interference filter are shown in Figure 23a. There is a marked increase of $|\varepsilon|$ for all isotopes towards lower temperatures, but with relatively large scatter at a single temperature. The relative increase is most pronounced for $N^{15}NO$, fol-

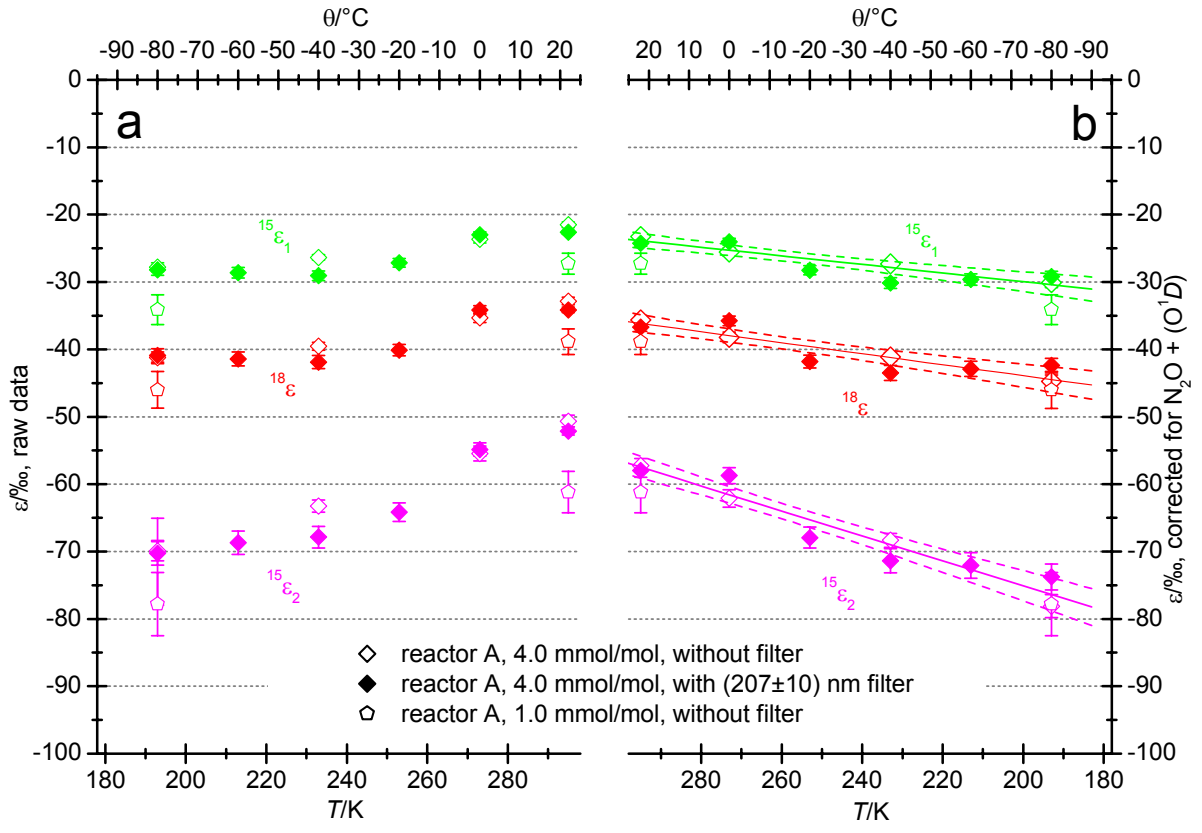

Figure 23a: Directly calculated fractionation constants ($^{15}\varepsilon_2$, $^{15}\varepsilon_1$, $^{18}\varepsilon$) from low-temperature experiments with and without interference filter. Most of the experiments were performed with N_2O mixing ratios of 4.0 mmol/mol, but two were also performed with 1.0 mmol/mol as verification.

Figure 23b: Data from Figure 23a after application of the correction for the contribution of $N_2O + O(^1D)$. Weighted linear fits are applied and plotted together with 95 % confidence limits:

$^{15}\varepsilon_2/‰ = (-61.6\pm0.6)+(0.185\pm0.015)\cdot\theta/°C$ ($r^2 = 0.940$)

$^{15}\varepsilon_1/‰ = (-25.3\pm0.4)+(0.064\pm0.010)\cdot\theta/°C$ ($r^2 = 0.817$)

$^{18}\varepsilon/‰ = (-38.0\pm0.4)+(0.082\pm0.011)\cdot\theta/°C$ ($r^2 = 0.836$)

lowed by $N_2{}^{18}O$ and ^{15}NNO. The final N_2O yields were between 35 and 62 %, corresponding to $-1.0 < \ln y < -0.5$. Figure 21 shows that even at these relatively low degrees of conversion some influence of $N_2O + O(^1D)$ must be corrected for. Therefore, the empirical equations derived above are applied to the data, neglecting a possible temperature dependence of this correction. This is justified by the absence of any temperature dependence of the fractionation constants for $N_2O + O(^1D)$ (chapter 3), but may be subject to errors if the relative rate of the $N_2O + O(^1D)$ reaction (denoted k_o in eqn. 59 above) is temperature dependent. The corrected data are shown in Figure 23b.

Surprisingly, the small difference for photolysis with and without interference filter that was found at room temperature is not evident in the corrected low-temperature data. However, the precision of the data is also reduced compared to the experiments with reactors B and C because of the smaller sample size (reflected by the lower precision of ln y derived from the "blank" experiments with reactor A) and because of additional errors from the $O(^1D)$ correction.

In order to check the validity of our assumption that the empirical $N_2O + O(^1D)$ correction is also valid for reactor A and at lower temperatures, experiments were made at 296 K and 193 K with the 1 mmol/mol N_2O mixture. The results for $^{18}\varepsilon$ and $^{15}\varepsilon_2$ agree within the combined range of errors, and are only slightly off for $^{15}\varepsilon_1$.

In retrospect, our approach to measure the fractionation constant of broadband N_2O photolysis yields reliable data, even at 4.0 mmol/mol, but the results are more variable than expected from the precision of the room temperature measurements. The influence of the reaction of $N_2O + O(^1D)$ was not anticipated and could be a potential source of errors in any photolysis experiment on isotopic fractionation of N_2O.

4.4 Comparison with models and other experiments

The measured temperature dependence can be compared with predictions of the zero point energy (ZPE) [*Miller and Yung*, 2000; *Yung and Miller*, 1997] and Hermite propagation (HP) models [*Johnson et al.*, 2001] (Figure 24). The HP theory uses a quantum-chemical approach to calculated the absorption cross sections of isotopic N_2O molecules. Generally higher enrichment constants are predicted than by the ZPE model. A further prediction of this theory is an increase of the absolute values of the enrichment constants with decreasing temperature.

We have calculated the overall fractionation constants for photolysis with the antimony lamp (once without, once with 207 nm filter) from the wavelength-dependent fractionation constants returned by the models. They were weighted by photolysis rates, i.e. the parameterised, tempera-

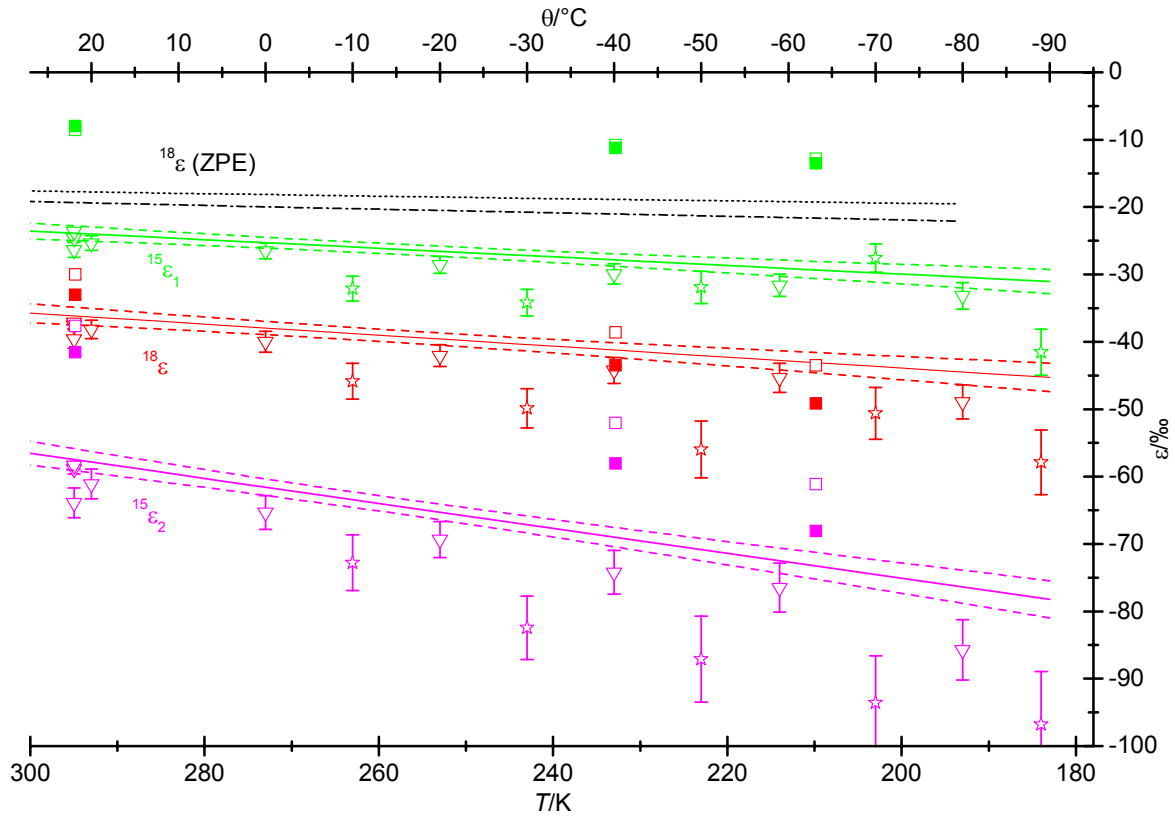

Figure 24: Comparison of the temperature dependence of ε for broadband UV photolysis. The fractionation constants predicted by the Hermite propagation (HP) and zero point energy (ZPE) theories have been calculated by eqn. 60. Also shown are two additional sets of low-temperature measurements which were obtained using a water filter as IR absorber between lamp and photolysis reactor.

- □ HP theory, without filter
- ■ HP theory, with (207±10) nm filter
- · · · · · ZPE theory, without filter
- · – · – · ZPE theory, with (207±10) nm filter
- ——— reactor A, with and without (207±10) nm filter (linear fit)
- ▽ reactor A, with IR filter filled with *MilliQ* water
- ☆ reactor A, with IR filter filled with aged water

ture-dependent N_2O absorption cross-sections [*DeMore et al.*, 1997; *Selwyn et al.*, 1977] and the emission spectrum of the lamp (eqn. 60).

$$\varepsilon(T) = \frac{\int \varepsilon(\lambda,T) I(\lambda) \sigma(\lambda,T) d\lambda}{\int I(\lambda) \sigma(\lambda,T) d\lambda} \qquad (60)$$

The agreement between the temperature dependence predicted by the HP model and the measured values is satisfactory for $^{18}\varepsilon$, as noted already for room temperature in the original publication. However, the measured absolute $^{15}\varepsilon_2$ and $^{15}\varepsilon_1$ fractionation constants are much larger than predicted by this theory. Only at the lowest temperature (210 K), the predictions come closer to the measured values again. For $^{18}\varepsilon$, $^{15}\varepsilon_2$ and $^{15}\varepsilon_1$, the difference between the values cal-

culated for the filtered and unfiltered spectrum match the measurements at room temperature quite well.

Temperature-dependent fractionation constants predicted by the ZPE theory were calculated from the same parameterisation of $\sigma(N_2O)$ as above [*DeMore et al.*, 1997; *Selwyn et al.*, 1977]. Previous reports [*Miller and Yung*, 2000; *Yung and Miller*, 1997] have not mentioned that such a temperature-dependence was predicted by the ZPE theory or assumed it to be absent [*Johnson et al.*, 2001]. In any case, the predicted fractionation constants are a factor of two or more too low (Figure 24). The discrepancy to the measurements increases even at temperatures below room temperature. Zhang *et al.* [2000] suggested that inclusion of vibrationally excited N_2O molecules would increase the predicted fractionation constant, because the spacing between different vibrational energy levels is larger for the heavier isotopologues. However, this correction would be less relevant at lower temperatures and according to our own calculations (not shown), it is too small to account for the difference at room temperature anyway. We note in passing that the HP theory actually predicts lower enrichments for vibrationally excited states, in contrast to the ZPE theory. Accordingly, the temperature dependence must arise from the upper, not the ground state.

Two sets of low-temperature measurements with a water filter between lamp and photolysis reactor (to absorb IR radiation) give an impression how the temperature dependence varies at longer wavelengths, because the water filter also absorbs at the short wavelength shoulder of the lamp emission spectrum. These measurements were discarded for the present study since they did not represent the measured emission spectrum of the lamp. Obviously, absorption of the short-wave UV light by the water filter increases the measured fractionation constants at low temperatures. Even high purity water which has passed through a special treatment system to remove both ions and organic impurities (*MilliQ* water) seems to have a noticeable influence on the light spectrum. One set of measurements was performed with aged water in the IR filter. In this case, the effect on the low-temperature fractionation constants is even more dramatic. Unfortunately, the transmission spectrum of this specific "water" was not measured so that we cannot derive direct information about the wavelength-dependence of $\varepsilon(T)$.

In Figure 25 the wavelength-dependent (175 to 205 nm) predictions of the HP and ZPE theories are compared with the data from this work, with two room-temperature studies at 193.3 nm and with the fractionation constants derived from VUV spectroscopic measurements of ^{15}NNO, $N^{15}NO$ and $^{14}N_2O$ [*Selwyn*, 1974; *Selwyn and Johnston*, 1981]. The direct measurements at 193.3 nm [*Röckmann et al.*, 2000; *Turatti et al.*, 2000] serve as a check of the quality of the VUV spectroscopic data which appears to be very good, supported by additional measurements at 185 nm (chapter 5). For the wavelength range 175 to 205 nm models and measurements are in relatively good agreement for $^{15}\varepsilon_1$, although the HP model does not reflect the vibrational struc-

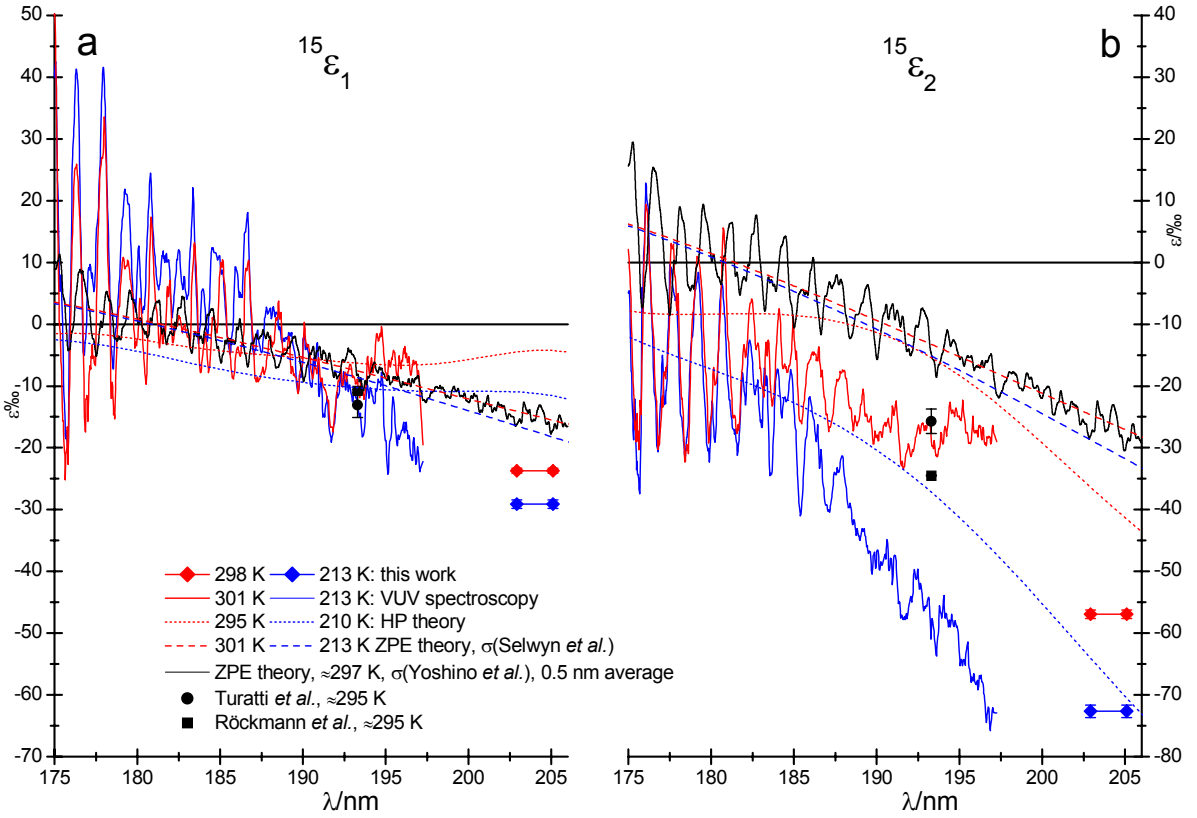

Figure 25: Modelled and measured wavelength-resolved ^{15}N fractionation constants near room temperature and at 210 K/213 K. The data from this work are plotted at the median wavelengths of the spectral photolysis rates (202.9 nm/205.1 nm without/with (207±10) nm interference filter.) VUV spectroscopic data are calculated from measurements of $\sigma(^{15}NNO)$, $\sigma(N^{15}NO)$ and $\sigma(^{14}N_2O)$ [*Selwyn*, 1974; *Selwyn and Johnston*, 1981]. HP theory values were obtained from the authors [*Johnson et al.*, 2001] (at 210 K: unpublished data). ZPE values were calculated from the ZPE differences [*Yung and Miller*, 1997] and polynomial fits of the absorption cross-sections [*Selwyn et al.*, 1977] or high-resolution data [*Yoshino et al.*, 1984] (averaged subsequently averaged over 0.5 nm intervals) Two measurements with ArF lasers at room temperature are shown for comparison [*Röckmann et al.*, 2000; *Turatti et al.*, 2000].

ture superimposed on the nearly Gaussian shape of the N_2O absorption spectrum. It does show up though in the ZPE theory values if a high-resolution N_2O spectrum [*Yoshino et al.*, 1984] is used as input, but is not always in phase with the VUV spectroscopic data. At $\lambda > 195$ nm, the 213 K values start to digress from the model predictions. The measurements from this work at even longer wavelengths seem to coincide with a linear extrapolation of the VUV beyond 197 nm for both 213 K and ≈ 300 K.

Discrepancies between the different data sets are much more prominent for $^{15}\varepsilon_2$. ZPE predictions come mostly not even close to the measurements. Below 185 nm the predictions of the HP theory approach the actual measurements, but are too low in terms of $|^{15}\varepsilon_2|$ at longer wavelengths. At 210 K/213 K however, the predictions of the HP theory for $^{15}\varepsilon_2$ nearly agree with the

measurements from this work. The VUV spectroscopic data indicate similar values of $^{15}\varepsilon_2$ at 197 nm as for broadband photolysis with centre wavelengths of 203 to 205 nm, in disagreement to a linear extrapolation of their trend. The reason for this is at present not clear.

Further investigations of the temperature dependence at other wavelengths are necessary since the theoretical predictions are not yet good enough and the experimental data do not cover all relevant temperatures and wavelengths. Extension of the high-quality VUV spectroscopic measurements are certainly the fastest way to remedy this gap of knowledge and should also include O isotopes.

5 Wavelength dependence of isotope fractionation in N_2O photolysis

N_2O isotope fractionation by photolysis at various wavelengths was the subject of at least eight experimental studies (including part of the results presented here) [*Johnston et al.*, 1995; *Rahn et al.*, 1998; *Röckmann et al.*, 2000; *Röckmann et al.*, 2001; *Toyoda et al.*, 2001a; *Turatti et al.*, 2000; *Umemoto*, 1999; *Zhang et al.*, 2000]. In line with theoretical calculations [*Johnson et al.*, 2001; *Miller and Yung*, 2000], they showed a dependence of fractionation constants on the wavelength of photolysing radiation. Photolysis comprises approximately 90 % of the global N_2O sink (R1, p. 5) and is the major cause of the observed isotopic enrichment of N_2O in the stratosphere [*Griffith et al.*, 2000; *Kim and Craig*, 1993; *Moore*, 1974; *Rahn and Wahlen*, 1997; *Toyoda et al.*, 2001b; *Yoshida and Toyoda*, 2000] (which is confirmed in chapter 7).

Maximum stratospheric N_2O photolysis rates occur at 195–205 nm [*Minschwaner et al.*, 1993], but depending on altitude and latitude there are contributions down to 185 nm and up to 230 nm. Below 185 nm absorption by O_2 prohibits the penetration of solar light, above 230 nm the photolysis rates are constrained by O_3 absorption and the decrease of the N_2O cross section.

In this chapter, we present high-precision measurements of the ^{18}O and of the position-dependent ^{15}N fractionation in N_2O photolysis at 185 nm. They also serve to validate the existing VUV spectroscopic measurements [*Selwyn and Johnston*, 1981] and are supplemented by additional measurements with broadband UV light sources. Together with the data from previous reports, a comprehensive view of the wavelength-dependent isotope fractionation in N_2O photolysis is created which is then used to evaluate the effects of N_2O photolysis in the region of the Schumann-Runge bands on the overall isotopic fractionation.

5.1 Experimental methods

The calculation of fractionation constants ε was based on eqn. 57 using either the ratio of $\ln(1+\delta)/\ln y$ in each individual experiment or least squares fits to Rayleigh plots of $\ln(1+\delta)$ vs $\ln y$. Given sufficient experimental precision and provided the y-axis offset in a Rayleigh plot is zero, the latter approach is more suitable to detect influences of reaction parameters on ε.

N_2O in N_2 bath gas was irradiated by different light sources using four reactor types. All gases used were of 99.9999 % chemical purity. Reactors A, B and C consist of quartz, stainless steel and borosilicate glass tubes, respectively, and were already used in previous photolysis ex-

periments (chapter 4). No significant influence of reactor type on the experimental results was found. Reactor E is a borosilicate glass bulb ($V \approx 2.2$ dm^3) with a quartz insert (chapter 3).

The photolysis experiments at 185 nm were performed in reactor E. A pencil style, low-pressure Hg(Ar) lamp ("Pen Ray lamp", *LOT Oriel*) was put in the quartz insert and usually operated at 18 mA (AC). The spectral output of Pen Ray lamps is known to be remarkably stable and temperature-insensitive [*Reader et al.*, 1996; *Sansonetti et al.*, 1996]; even the total irradiance is reproducible to within 15 %. The wavelengths of 19 spectral lines in the range 253 to 579 nm were within ±0.002 nm of published values for Hg emission lines. However, the 185 nm-line was not investigated. Its intensity relative to the 253.65 nm-line is stated as 3 % (*LOT Oriel*), but may vary from lamp to lamp. Therefore, additional experiments were performed with a second lamp. The precise wavelength of the "185 nm"-line for the natural Hg isotope mixture is given as 184.950 nm [*Lide*, 1999]. Other sizeable Hg lines in the emission spectrum of these lamps are located at wavelengths > 250 nm and are not of importance for N_2O photolysis.

The irradiation by the lamp led to temperatures of about 50 °C at the inner wall of the quartz inset and as high as 100 °C at the lamp itself. Therefore, one experiment was conducted at a reduced current of 10 mA, giving only ≈ 40 °C and ≈ 85 °C, respectively. The temperature of the gas mixture itself was measured with a thermocouple at different positions of the reactor and amounted to fairly homogeneous values of 28 °C/25.5 °C for 18/10 mA. To check for any influence of O_2 photolysis and subsequent O_3 production on the irradiation spectrum, the quartz cavity was flushed with N_2 during three experiments. The photolysis times varied from 2.1 to 40.9 h, resulting in final yields of 3.5 to 84.5 %.

A mixture of 1.0 mmol/mol N_2O/N_2 was used for the experiments at initial pressures of about 1000 mbar. Higher mixing ratios can lead to artefacts which were traced back to $O(^1D)$ production by NO_2 photolysis and subsequent reaction of N_2O with $O(^1D)$ (section 4.2). Pressures were corrected for temperature and non-linearity of the sensor. The remaining N_2O fraction (y) was determined by quantitative extraction in an ultra-high efficient Russian Doll-type trap [*Brenninkmeijer and Röckmann*, 1996]. Blank experiments without photolysis give an indication of the precision of degree of conversion ($\sigma_{\ln y} = 0.009$) and δ values ($\sigma_{\delta^{15}N} = 0.1$ ‰; $\sigma_{1\delta^{15}N} = \sigma_{2\delta^{15}N} = 0.25$ ‰; $\sigma_{\delta^{18}O} = 0.15$ ‰) from which the fractionation constants are calculated. Isotope analyses were performed on our *Finnigan* MAT 252 isotope ratio mass spectrometer (sections 2.5 and 2.6).

Photolysis experiments with broadband light sources were performed with a 4.0 mmol/mol N_2O/N_2 mixture using reactors A to C. Unlike the measurements at 185 nm, the $^{31}\delta$ values for the NO^+ fragment were measured on a *Micromass* Prism II mass-spectrometer with adjustable cups, so that the standard-deviation of $^{31}\delta$ is comparable to that of $^{45}\delta$ and $^{46}\delta$.

5.2 Isotopic depletions by N_2O photolysis at 185 nm

The results for photolysis at 185 nm are shown in Figure 26. Up to the largest degrees of conversion, the fractionation constants give a consistent picture of isotopic depletions at the terminal positions of the residual N_2O ($\delta^{18}O$ and $^1\delta^{15}N$). There is no clearly discernible influence of lamp specimen, operating current or nitrogen flushing. The absence of any significant variation of ε with $\ln y$ indicates that most probably no other than the desired fractionation process was taking place, as opposed to the artefacts noticed at higher mixing ratios (section 4.2.1). The absence of artefacts was also confirmed by irradiation of an O_2/N_2 mixture (0.62 mmol/mol) for 13.5 h. After extraction and purification, 0.38 µℓ N_2O (SATP) were recovered corresponding to the system blank of ≈0.3 µℓ N_2O. N_2O production from $N_2 + O(^1D)$ can thus be neglected, in agreement with its low rate constant of $2.8 \cdot 10^{-36}$ $c(N_2)$ $cm^6 s^{-1}$ [*Estupiñán et al.*, 2002].

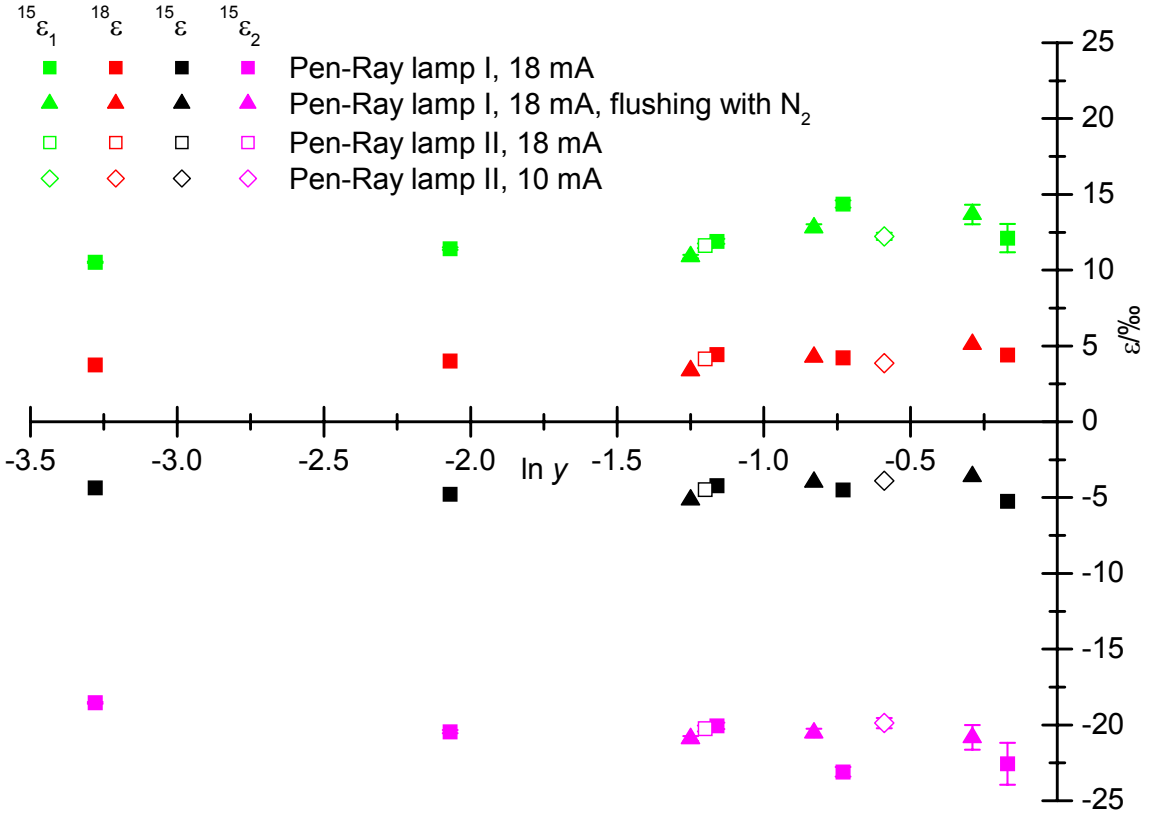

Figure 26: Directly calculated fractionation constants (ε) for photolysis with low-pressure Hg(Ar) lamps at 185 nm. Fractionation constants for the terminal and central nitrogen positions in the N_2O molecule are designated $^{15}\varepsilon_1$ and $^{15}\varepsilon_2$; the ^{18}O fractionation is represented by $^{18}\varepsilon$ and the average ^{15}N fractionation by $^{15}\varepsilon = (^{15}\varepsilon_1 + ^{15}\varepsilon_2)/2$. Two different lamps were used at operating currents of 10 or 18 mA, with or without N_2 flushing. Errors from N_2O extraction and isotope analysis are smaller than the symbol size, unless indicated.

Table 8: Fractionation constants for N_2O photolysis at 185 nm, different ways of calculation

	"mean direct"		"Rayleigh plot"		
	ε/‰	y-axis offset	ε/‰	y-axis offset	r^2
$^{15}\varepsilon$	–4.4±0.5	0	–4.5±0.2	0.0±0.2	0.989
$^{15}\varepsilon_1$	12.2±1.2	0	10.3±0.3	–1.5±0.5	0.992
$^{15}\varepsilon_2$	–20.7±1.3	0	–18.6±0.5	1.7±0.7	0.994
$^{18}\varepsilon$	4.2±0.5	0	3.7±0.1	–0.3±0.2	0.990

Figure 26 shows the directly calculated fractionation constants for each experiment. We argue that the best estimate of the "true" fractionation constants is not the mean of these directly calculated fractionation constants since they are subject to a small error if the y-axis offset in a Rayleigh plot is not exactly zero, especially if the degree of conversion is small ($\ln y \approx 0$). However, the slope in a Rayleigh plot is a more reliable estimate of the fractionation constant and is therefore adopted as "true" ε. The results of two calculation methods ("mean direct" and "Rayleigh plot") are shown in Table 8, together with errors at the 1σ level. The positive values for $^{15}\varepsilon_1$ and $^{18}\varepsilon$ are the first documented cases of isotopic depletion in the residual gas by N_2O photolysis.

In contrast to the results presented here, Johnston *et al.* [1995] did not find any significant oxygen isotope fractionation at 185 nm. Reanalysis of their original data gives $^{18}\varepsilon = (0.2\pm0.2)$ ‰. Although Johnston and co-workers used a low-pressure mercury resonance lamp powered by a microwave discharge, differences between the light sources are very unlikely to account for the differences in $^{18}\varepsilon$. In principle, contributions from Hg lines at other wavelengths could have caused the discrepancy in $^{18}\varepsilon$ values, but were not observed for the Pen Ray lamps at wavelengths relevant to N_2O photolysis (i.e., $\lambda < 240$ nm) and were also absent in the spectrum of the microwave powered lamp (*Jeffrey C. Johnston*, personal communication, 2002). Under exceptional conditions such as dramatically increased nitrogen purge flows and reduced plasma voltages, 194.2 nm-emission from Hg^+ was noticed with intensities of up to 20 % relative to the 185 nm-line [*Cantrell et al.*, 1997; *Lanzendorf et al.*, 1997], but under thermally normal operating conditions the relative emission intensity does not exceed a few percent. Analytical errors are more probable to be blamed for the discrepancy between the two studies: Rather than analysing N_2O directly, Johnston *et al.* decomposed it first to N_2 and O_2 in a quartz tube with gold inset at > 800 °C and separated N_2 and O_2 afterwards [*Cliff and Thiemens*, 1994], since they wanted to analyse $^{17}O/^{16}O$ variations as well. If separation of N_2 from O_2 is not quantitative, this may compromise the accuracy of the $\delta^{18}O$ and especially $\delta^{17}O$ values, because N_2 interferes strongly with O_2 isotope meas-

urements (section 2.3.2). The unlikely three-isotope exponent of $\beta = (-1.5 \pm 0.4)$ (section 10.2) derived from re-analysis of Johnston *et al.*'s data set lends support to this interpretation.

5.3 Photolysis with broadband light sources

Additional photolysis experiments were performed with a set of different broadband light sources. Some results obtained with an Sb lamp, partly used in combination with a 207±10 nm interference filter, have already been reported in section 4.2.2. Additional results were obtained with 200 nm, 214 nm and 220 nm interference filters, a D_2 and a Hg/Xe lamp. The corresponding spectral photolysis rates (Figure 27) were calculated from direct measurements of the emission spectra of the Sb [*Röckmann et al.*, 2001] and Hg/Xe lamps [*Sauerssig*, 1999], convoluted (where appropriate) with transmission spectra of four interference filters (*Melles Griot*) and the N_2O absorption spectrum at room temperature [*Selwyn et al.*, 1977; *Yoshino et al.*, 1984]. The emission spectrum of the D_2 lamp was not measured directly, but was calculated from measurements of the spectral radiant intensity of a D_2 calibration lamp (*Mathias Richter*, personal communication,

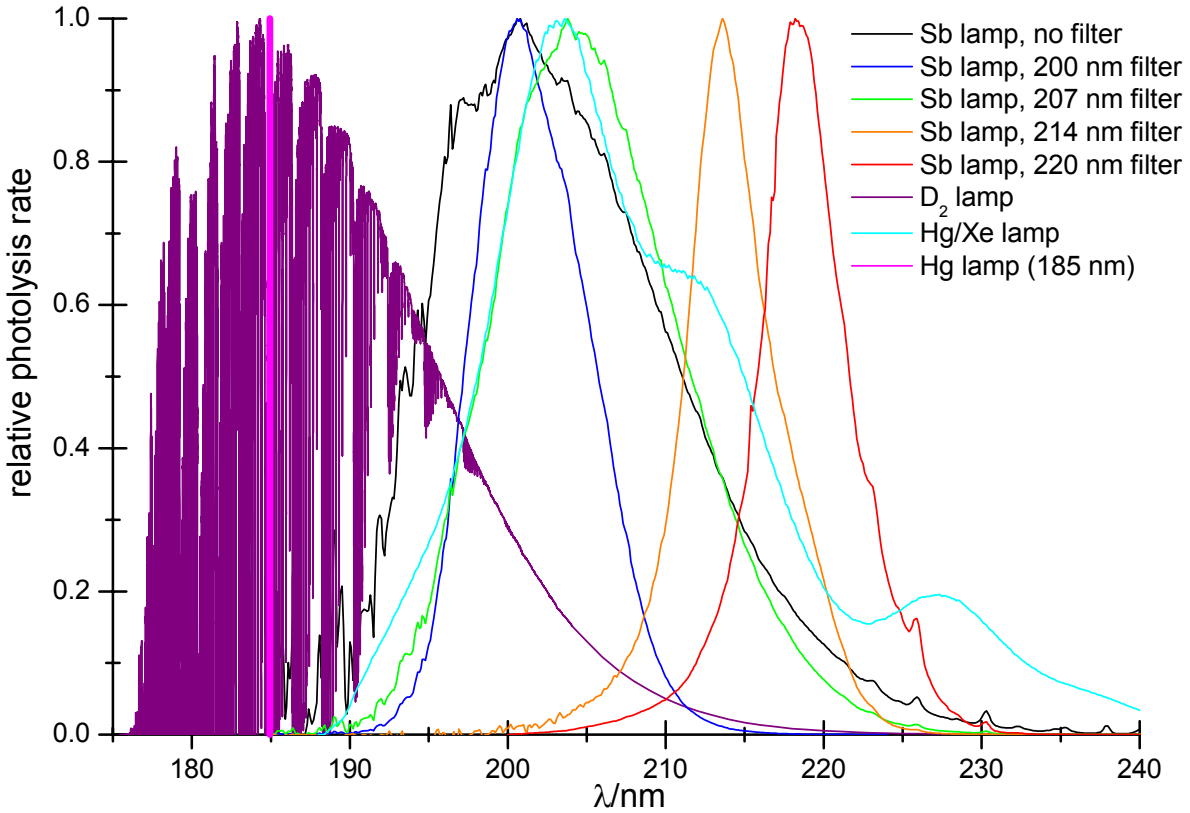

Figure 27: Relative N_2O photolysis rates for filtered and unfiltered light from different broadband lamps. The photolysis rates have been normalised by division through their maximum values so that they can be compared more easily. The closely spaced O_2 Schumann-Runge bands account for the structured appearance of the D_2 lamp spectrum.

Table 9: Fractionation constants for N_2O photolysis with broadband light sources

ε/‰	D_2 lamp	HgXe lamp	Sb lamp, 200 nm filter	Sb lamp, 214 nm filter	Sb lamp, 220 nm filter
$^{15}\varepsilon$	–20.0±0.1	–48.9±1.5	–39±7	–59±10	–69±5
$^{15}\varepsilon_1$	–8.4±0.4	–28.1±2.1	*n.a.*†	–41± 7	–43±3
$^{15}\varepsilon_2$	–31.4±0.3	–69.5±2.8	*n.a.*†	–74±13	–95±7
$^{18}\varepsilon$	–15.9±0.1	–46.9±1.9	–43±8	–52± 9	–61±5
ln $\hat{y}$ ‡	–1.2	–0.39	–0.040	–0.034	–0.076

† *n.a.*: not analysed
‡ $\hat{y}$: maximum degree of conversion

2001), transmission functions of synthetic silica windows (*Hamamatsu*) and high-resolution O_2 absorption cross sections [*Minschwaner et al.*, 1992].

Photolysis half-life times were about 11 hours for the D_2 lamp and 63 hours for the Hg/Xe lamp. Thus, sufficient degrees of conversion were achieved within reasonable irradiation time (up to 22 and 33 hours, respectively), and the fractionation constants derived from Rayleigh plots have low errors (Table 9). Due to the strong infrared radiation from the Hg/Xe lamp, it was used together with a water filter which protected the photolysis reactor from excessive heating. The filter was filled with high-purity water (*MilliQ*) and was cooled continuously by water.

The fractionation constants measured with the unfiltered Sb lamp and in combination with the 207 nm filter (20 nm FWHM) have been presented in Table 7 and Figure 20. To confine the spectrum of the Sb lamp to narrower wavelength regions, the 200, 214 and 220 nm filters were used in spectral bandwidths of 10 nm (FWHM). However, this also reduced the light available for photolysis and considerably lengthened the required irradiation times. This was aggravated by the low peak transmissions of the filters (13 to 18 %) and by light loss due to the fact that the extensive discharge of the Sb lamp could not be well focussed on the filter diameter of 25 mm. Therefore, only small extents of photolysis could be achieved within reasonable times, e.g., after 216 hours of irradiation with the 220 nm filter ln y was only -0.076. Furthermore, the 200 nm filter went blind after 72 hours total irradiation time. Rayleigh plots of ln(1+δ) are still well approximated by linear fits to ln y, but the error introduced by the extraction procedure is not negligible anymore at these low extents of photolysis. Determined from blank runs, the average standard deviation of ln y is $\sigma_{\ln y} = 0.004$ for reactors A to C. This is smaller than for reactor E, probably because of the better reproducibility of the manual extraction procedure for smaller reactor sizes. Following Williamson [1968] and York [*York*, 1966] linear least-squares fits are applied to the data that take into account the mass-spectrometric errors of ln(1+δ) and assume an invariable error of 0.004 for ln y. Therefore the calculated fractionation constants for the experi-

ments with Sb lamp and the 200, 214 and 220 nm filters have larger errors (Table 9). The approach by Williamson/York has the advantage over a simple linear least squares fit that it is symmetric with respect to co-ordinate exchange.

We note that these broadband photolysis measurements were obtained with an N_2O mixing ratio of 4.0 mmol/mol. This may introduce artefacts by interference of the reaction of $N_2O + O(^1D)$ as discussed for high-precision measurements at 1.0 and 4.0 mmol/mol with the Sb lamp (section 4.2). The necessary upward corrections depend on ln *y*, the "true" values for ε and the lamp spectrum. Extrapolating the empirical formula derived in section 4.2 to correct the fractionation constants measured here, gives upward revisions of $\Delta|^{15}\varepsilon_2| = 6$ ‰ at $\ln y = -0.39$ for the Hg/Xe lamp as the worst case. However, considering the different emission spectra, a direct extrapolation might not be justified. Therefore and since the estimated correction is only $2\sigma_{^{15}\varepsilon_2}$, we leave the measurements uncorrected. It should be noted that corrections could be warranted for the results of other studies, too, but are difficult to quantify in retrospect.

5.4 Synoptic view of the wavelength dependence

Figure 28 is an overview of measured and theoretically predicted ε values plotted against wavelength, including this chapter's data. In general, both experimental data and theoretical predictions agree on increasing enrichments at higher wavelengths and the order $^{15}\varepsilon_2 < {}^{18}\varepsilon < {}^{15}\varepsilon_1$, but differ in the magnitudes of ε as well as in its sign near the absorption maximum at 182 nm. The experimental results are approximated by a linear fit from 190 to 220 nm (Table 10).

Data were adopted from the original publications and are presented with 1σ y-error bars as stated by the authors. Experimental data from laser photolysis mostly represent "single wavelengths" except for the measurements with ArF lasers at 193.3 nm which were performed at the natural linewidth of 0.7 nm (FWHM). In case of the broadband photolysis experiments, data points are located at the median wavelengths for 50 % photolysis. The "x-error bars" indicate the

Table 10: Parameters for a y-error weighted linear fit of the wavelength dependence of ε derived from the results of N_2O photolysis experiments (Figure 28).
$\varepsilon = \varepsilon(200\text{ nm}) + \partial\varepsilon/\partial\lambda\ (\lambda - 200\text{ nm})$

	$\partial\varepsilon/\partial\lambda$ (‰/nm)	2σ	ε(200 nm) (‰)	2σ
$^{15}\varepsilon$	–1.57	0.03	–34.1	0.2
$^{15}\varepsilon_1$	–1.18	0.04	–19.2	0.2
$^{15}\varepsilon_2$	–1.94	0.05	–48.1	0.4
$^{18}\varepsilon$	–1.48	0.03	–28.6	0.2

25 % and 75 % quartiles. If these quartiles are symmetric about the median and if the slope $\partial\varepsilon/\partial\lambda$ does not change too much over the range of photolysis, the fractionation constant is close to a hypothetical "single wavelength" measurement at the median λ. Since the actual slope $\partial\varepsilon/\partial\lambda$ appears to be almost constant between 190 and 220 nm and the spectral photolysis rates of the broadband light sources are fairly symmetric indeed about their median wavelength (Figure 27), this explains the relative good agreement between broadband and "single wavelength" data. The weighted linear fit shown in Figure 28 therefore only considers the errors of ε.

The fractionation constants of the ^{15}N isotopomers measured by direct photolysis experiments are complemented by VUV spectroscopic measurements between 173 and 197 nm [*Selwyn and Johnston*, 1981]. The cross-sections are used to calculate ε. The "fine-structure" of ε is in good agreement with the "single wavelength" measurements at 185 and 193.3 nm (Figure 29) and lends support to the view that the VUV spectroscopic data are most probably adequate to represent the "true" fractionation constants within their wavelength range. Unfortunately, this range ends at 197 nm, short of the 195–205 nm region most important for stratospheric N_2O photolysis.

The fractionation constants predicted by the zero point energy (ZPE) theory [*Miller and Yung*, 2000; *Yung and Miller*, 1997] have been derived by blue-shifting the high resolution absorption spectrum of Yoshino *et al.* [1984] in addition to the polynomial approximations of ln σ proposed by Selwyn *et al.* [1977] and Mérienne *et al.* [1990], assuming that these spectra represent essentially the absorption cross section of the most abundant N_2O species, $^{14}N_2{}^{16}O$. Although the relative order of ^{18}O and position-dependent ^{15}N fractionations is predicted correctly, their magnitudes are about a factor of 2 too low. Also, at wavelengths close to the absorption maximum, the theoretical "fine structure" is not in phase with VUV spectroscopic measurements (Figure 29).

Figure 28: (next page) Measured and theoretically predicted fractionation constants for N_2O photolysis at room temperature (unless indicated):

mass spectrometry:
+ Johnston *et al.* [1995]
■ this work, 301 K
▬ Röckmann *et al.* [2000]
● Toyoda *et al.* [2001a]
× *Rahn et al.* [1998]
▲ this work
◆ Röckmann *et al.* [2001]

optical spectroscopy:
△ Turatti *et al.* [2000]
○ Umemoto [1999]
□ Zhang *et al.* [2000]

weighted linear fit:
– – – this work

VUV spectroscopy:
—— Selwyn and Johnston [1981], 301 K

ZPE theory:
—— σ(Yoshino *et al.* [1984]), 0.0006 nm resolution
—— σ(Yoshino *et al.* [1984]), 0.5 nm adjacent average
—— σ(Mérienne *et al.* [1990]), polynomial fit
—— σ(Selwyn *et al.* [1977]), polynomial fit

HP theory:
—— Johnson *et al.* [2001], 1 nm resolution

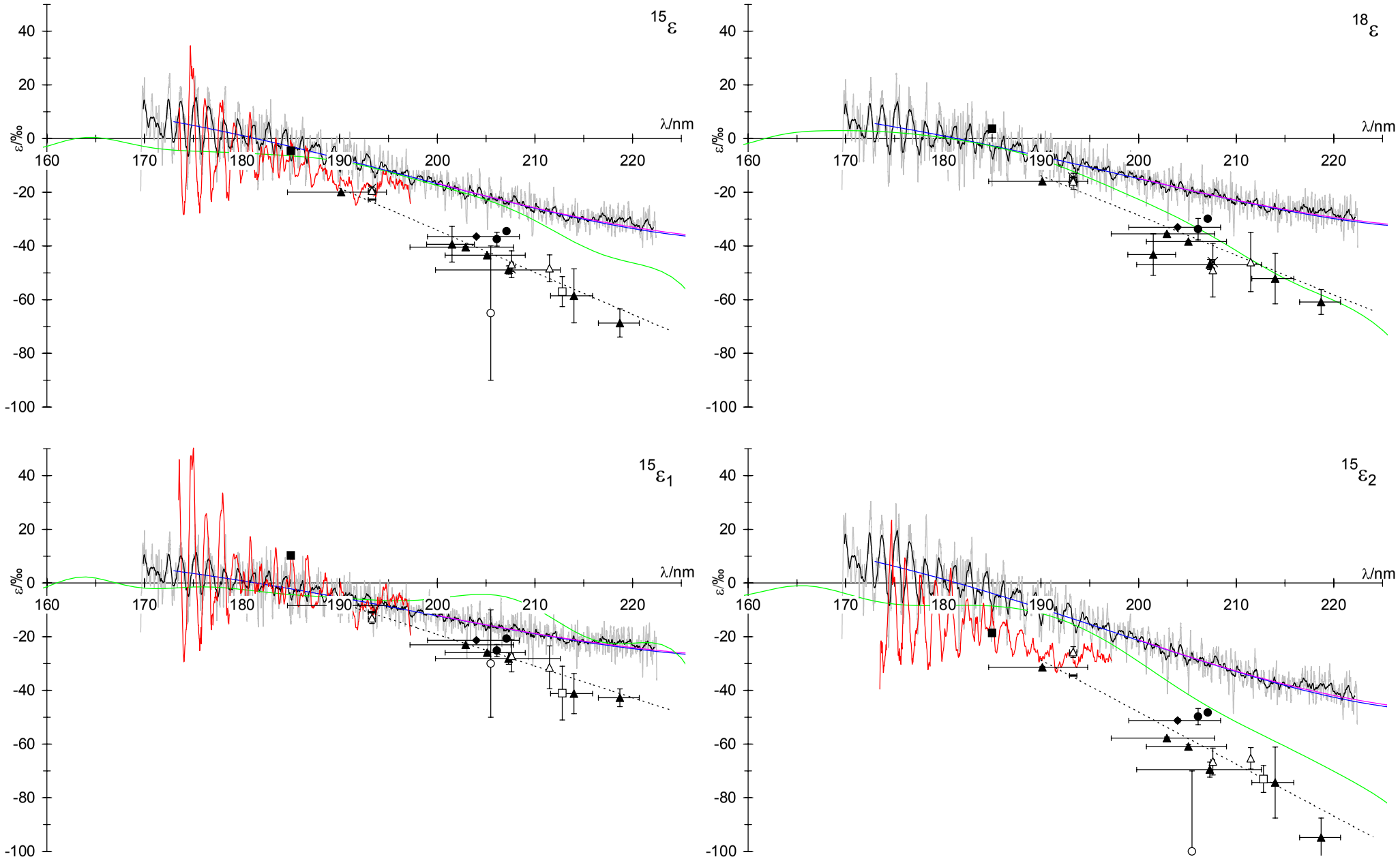
$^{15}\varepsilon$
$^{18}\varepsilon$
$^{15}\varepsilon_1$
$^{15}\varepsilon_2$
ε/‰
λ/nm
40
20
0
-20
-40
-60
-80
-100
160
170
180
190
200
210
220

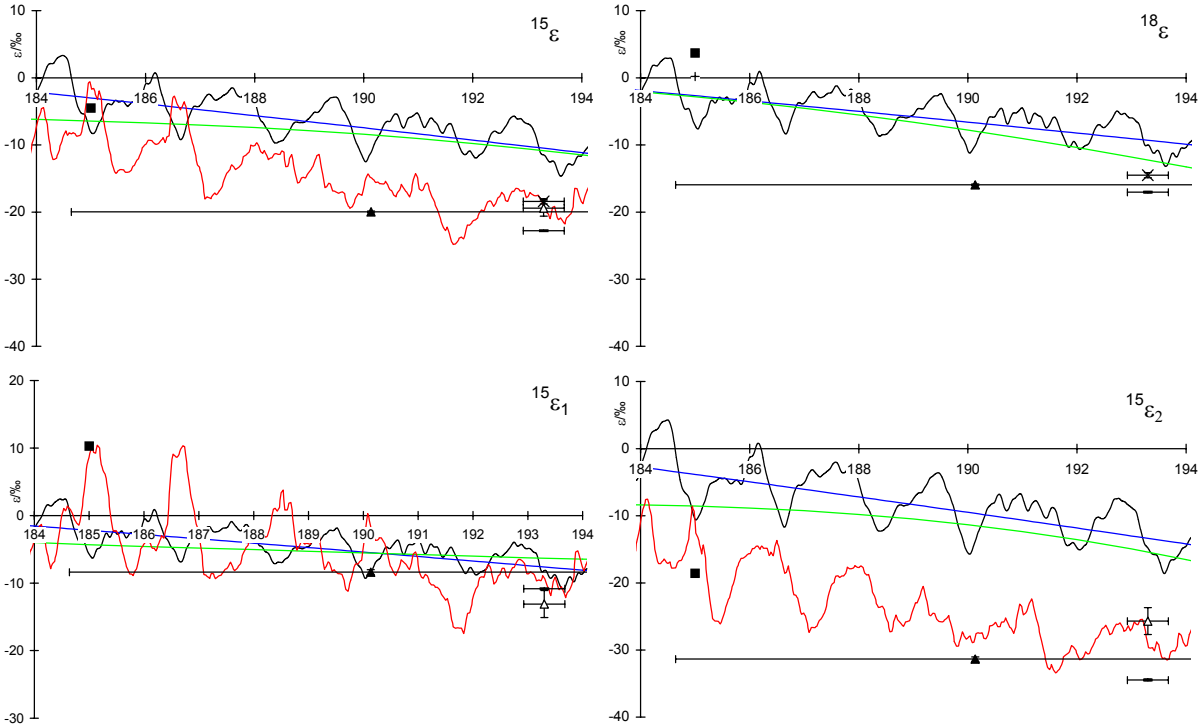

Figure 29: Comparison between fractionation constants derived from theoretical predictions, direct measurements and VUV spectroscopy in the range from 184 to 194 nm. The same symbols as in Figure 28 have been used, but the high-resolution ZPE calculation has been omitted for clarity.

Ab initio calculations with the Hermite propagation (HP) theory [*Johnson et al.*, 2001] were performed at 1 nm resolution on a two-dimensional (2D) potential energy surface (PES) (spanned by NN–O distance and bending angle) and therefore lack the "fine structure" seen in the ZPE predictions and VUV spectroscopic measurements (*Matthew S. Johnson*, personal communication, 2002). The agreement with the measurements is good for $^{14}N_2{}^{18}O$ and better than the ZPE theory for $^{14}N^{15}N^{16}O$, but $^{15}N^{14}N^{16}O$ is not adequately modelled, also as a consequence of the 2D-PES.

5.5 Implications for the stratosphere and modelling

For stratospheric modelling, one now has the choice between various data sets. Considering the underestimated fractionation constants of the theoretical predictions (except for $^{18}\varepsilon$ in the HP model), it seems that the linear fit through the experimental data represents the wavelength dependence of ε more adequately. This fit also agrees reasonably well with the VUV spectroscopic measurements up to 197 nm. In chapter 4, temperature dependent measurements of fractionation constants for broadband photolysis with the Sb lamp (median wavelength: 203 nm) were presented. At lower temperatures, the HP theory predictions compared slightly better to the experimental measurements than at room temperature, but were still off by more than a factor of

two for $^{15}N^{14}N^{16}O$, underscoring the deficiencies of the model. However, one has to be careful in extrapolating the derived temperature dependence to other wavelengths. E.g., values of $^{15}\varepsilon_2$ derived from the VUV spectroscopic measurements at 197 nm and 213 K were identical to those for broadband photolysis at the same temperature and longer wavelengths, in disagreement to the observed wavelength-dependence at room temperature.

With the validation of the VUV spectroscopic measurements, we have to consider additional complications for atmospheric modelling from the "oscillations" and changes of sign of ε below 190 nm. Due to the strong variation of actinic flux over narrow wavelength regions in the Schumann-Runge bands below 200 nm (Figure 30), this may have noticeable influences on the fractionation constants. We have therefore calculated the expected fractionation constants for photolysis using actinic fluxes at 20, 40 and 80 km (US standard atmosphere, solar zenith angle 30°). The data were averaged to about 0.1 nm resolution in the Schumann-Runge region and to about 1 nm above 200 nm. This is more than sufficient to sample the maximum and minimum values of the N_2O fractionation constants which occur with a period of about 2 nm. Altitudes of 20 and

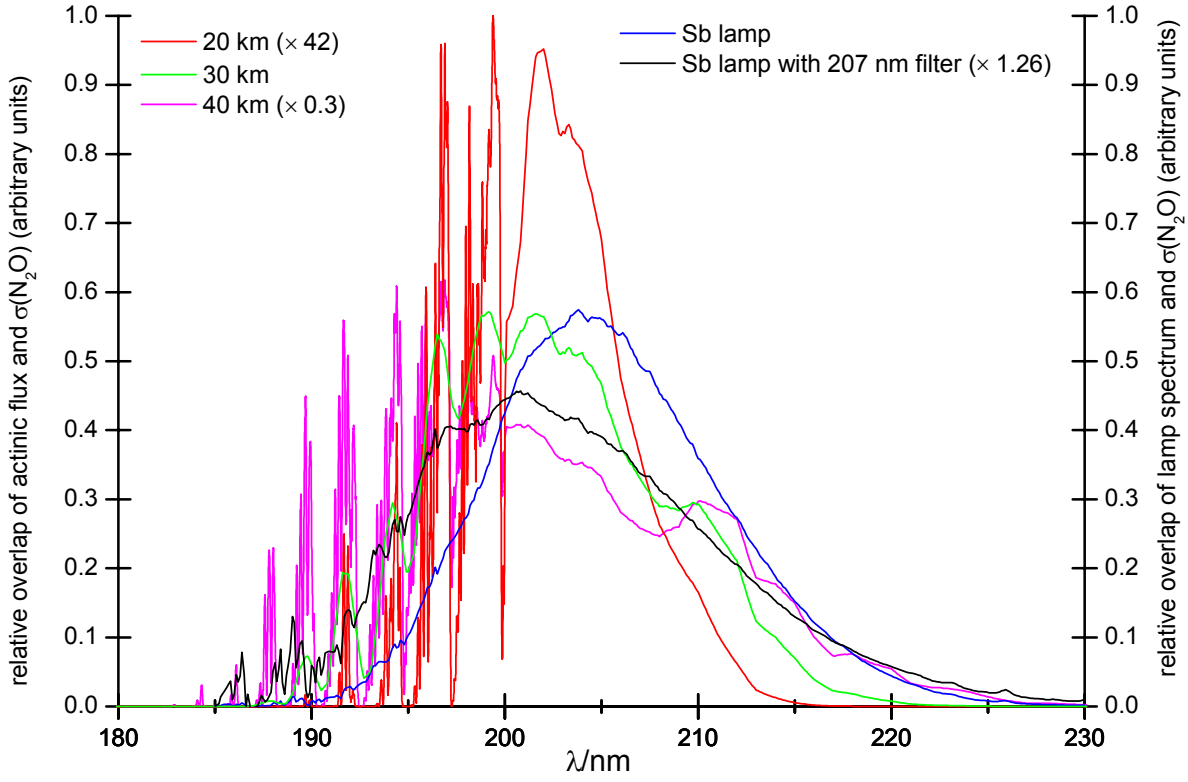

Figure 30: Relative photolysis rates of N_2O calculated with broadband UV lamp emission spectra and actinic fluxes at three altitudes. The influence of O_2 absorption in the Schumann-Runge band region between 175 and 200 nm is shown for the 20 and 40 km data. Data have been re-scaled to give equal areas in the plot (i.e. integrated photolysis rates). Peaks and spectral distribution of photolysis by the UV lamp and in the atmosphere values are similar, making the lamp a suitable tool for simulation of N_2O photolysis in the atmosphere.

40 km are below and above the region of maximum N_2O photolysis in the atmosphere and should therefore provide limits for the fractionation constants. Mesospheric N_2O photolysis at 80 km is negligible, but has been included for comparison. Given the sparse database at lower temperatures, we restrict our calculations to room temperature, although this is clearly not representative for the stratosphere and mesosphere. However, the vibrational structures in the N_2O absorption spectrum become less intense with lower temperatures [*Selwyn and Johnston*, 1981] and so should the oscillations in ε. Therefore, the room temperature calculations are a "worst-case" scenario for any interference of Schumann-Runge bands and N_2O isotope fractionation.

Two scenarios have been investigated: The first one was created from the high-resolution VUV spectroscopic data for $^{15}\varepsilon_2$ and $^{15}\varepsilon_1$ [*Selwyn and Johnston*, 1981] up to 190 nm, complemented by the linear fit (Figure 28) for higher wavelengths. In the second scenario, the linear fit is extrapolated also to wavelengths below 190 nm. For the sake of argument, the linear fit is extended in both scenarios to wavelengths up to 240 nm. Any errors thus introduced will be minor due to the small contribution of this wavelength range to the total N_2O loss at all three altitudes. Table 11 shows the results of the calculations.

Interestingly, the differences between scenario 1 and 2 are negligible for both fractionation constants and all altitudes. More surprising is the small altitude dependence of ε. There is barely any variation in ε at 20 km and at 40 km due to the change of actinic flux, but the minute increase of $|\varepsilon|$ with altitude is in line with previous qualitative considerations which postulated an increase of $|\varepsilon|$ with altitude due to the decreasing influence of O_3 absorption in the Hartley band [*Yoshida and Toyoda*, 2000].

Summarising, changes of actinic flux with altitude affect the average fractionation constants only negligibly between 20 and 40 km. The contribution of isotopic fractionation by photolysis in the region of O_2 Schumann-Runge bands can be well approximated by an extension of the linear fit derived from photolysis experiments in the range from 190 to 220 nm. Section 7.3 discusses variations of actinic flux in the context of stratospheric samples.

The new measurements at 185 nm have demonstrated for the first-time heavy isotope deple-

Table 11: Calculated fractionation constants for N_2O photolysis at 20, 40 and 80 km (US standard atmosphere, solar zenith angle: 30°)

	Scenario	ε(20 km)	ε(40 km)	ε(80 km)
$^{15}\varepsilon_1$/‰	1	–21.88	–22.56	–16.25
	2	–21.88	–22.53	–16.32
$^{15}\varepsilon_2$/‰	1	–52.57	–53.52	–43.11
	2	–52.57	–53.63	–43.42

tions in the residual gas of N_2O photolysis experiments. Obviously, the absorption cross-sections of N_2O species with isotopic substitutions at the terminal positions of the molecule are larger than for the most abundant $^{14}N_2{}^{16}O$ isotopologue, corresponding to an inverse kinetic isotope effect. In contrast, isotope enrichments are observed at the central nitrogen position as found at longer wavelengths in other studies. Taken together with measurements of "single wavelength photolysis" at 193.3 nm and of broadband photolysis by a D_2 lamp with a median wavelength for N_2O photolysis of 190 nm, these results serve to validate existing VUV spectroscopic measurements of ^{15}N isotopomers in the wavelength range from 173 to 197 nm. However, most of the atmospheric N_2O photolysis occurs at wavelengths from 195 to 205 nm, warranting an extension of the high-resolution spectroscopic analyses of isotopically substituted N_2O species to longer wavelengths. This should cover the whole range of stratospherically relevant temperatures (200 to 300 K) and should also include ^{17}O and ^{18}O isotopologues.

6 Statistical nature of nitrogen isotope fractionation in N_2O photolysis: $^{15}N_2O$

The calculation of elemental isotope ratios from molecular mass spectra is based on the assumption that isotopes are distributed statistically (randomly) over different isotopologues (section 2.2). For example, the abundance of $^{14}N_2$ and $^{15}N_2$ should be the square of the abundance of ^{14}N and ^{15}N in a nitrogen sample with a statistical isotope distribution while that of $^{14}N^{15}N$ should be two times the product of ^{14}N and ^{15}N abundance. We rely on such statistical isotope distributions when we infer the $^{15}N/^{14}N$ isotope ratio of a N_2 sample from the measurement of N_2^+ ion currents at m/z 28 and 29. However, for work with artificially enriched samples of compounds with two or more nitrogen atoms, deviations from the statistical isotope distribution occur which are taken into account either by measuring the molecular isotope ratios of both substituted N_2 isotopologues (i.e. ^{29}R and ^{30}R) [*Stevens et al.*, 1993] or by first equilibrating the isotope distribution in an electric [*Buresh and Austin*, 1993] or microwave discharge [*Well et al.*, 1993].

In the case of N_2O, we relaxed the assumption of a statistical isotope distribution by distinguishing between the two isotopomers $^{14}N^{15}NO$ and $^{15}N^{14}NO$ and allowing for different isotope ratios at the terminal and central nitrogen position of the molecule (denoted $^{15}R_1$ and $^{15}R_2$, cf. Figure 2). A mass-spectrometric method based on NO^+ fragment analysis was developed to determine the position-dependent ^{15}N isotope ratios in N_2O [*Brenninkmeijer and Röckmann*, 1999] (cf. section 2.6). In the following, we will present evidence that nitrogen isotopes are fractionated in a statistical manner by N_2O photolysis. Therefore, the abundance of stratospheric $^{15}N_2O$ is expected to correspond to its statistically expected value.

6.1 Deviations from statistical isotope distributions

It was already mentioned that samples which are artificially enriched in stable isotopes do not obey statistical isotope distributions unless suitable equilibration methods are applied. However, deviations from statistical isotope distribution might also occur in atmospheric samples. Mroz *et al.* [1989] detected multiply deuterated methane (CD_4) in the atmosphere in excess of the very small abundance expected for a statistical distribution of deuterium over the different isotopologues, possibly due to the use of heavy water in nuclear power plants. Zyakun and co-workers [*Zyakun and Schidlowski*, 2000; *Zyakun and Brenninkmeijer*, 2001; *Zyakun and Schidlowski*, 1997] developed a mathematical formalism to show that kinetic isotope effects or mixing of two reservoirs

of isotopically substituted molecules can induce deviations from statistical isotope distributions. The authors suggested that measurement of $C^{18}O_2$ is a promising approach for the assessment of sources and turn-over of the atmospheric CO_2 reservoir, but requires development of a suitable mass spectrometric technique. According to a literature search though, it seems that applications of non-statistical isotope distributions in atmospheric trace gases are wanting, probably due to the small abundance of heavy isotopes in the most frequently encountered elements H, C, N and O which makes it very difficult to measure poly-substituted isotopologues.

The fact that mixing causes deviations from statistical isotope distributions is illustrated in Figure 31. Clearly, a mixture of two reservoirs with different initial isotopic composition does not correspond to the statistical isotope distribution described by the parabola $x(^{14}N^{15}N) = 2\,x(^{14}N)\,x(^{15}N) = 2x(^{15}N) - 2[x(^{15}N)]^2$. Of course, this is an extreme scenario. In reality, mixing of two reservoirs with differences in isotopic composition as suggested by Figure 31 do not normally occur in the atmosphere. Rather, samples with light elements such as H, C, O or N appear very close to the origin of a plot such as Figure 31 and relative differences in ^{15}N abundance rarely exceed 10 %. Therefore, the parabola can be very well approximated by a linear line so that the mixed sample cannot be distinguished from a sample with a statistical isotope distribution. A numerical example with $x_1(^{15}N) = 0.00366$ (corresponding to air-N_2) and $x_2(^{15}N) = 1.1\,x_1(^{15}N)$ shows that $x(^{14}N^{15}N)$ in the mixture never deviates more than 0.009 ‰ from the statistically dictated isotope distribution.

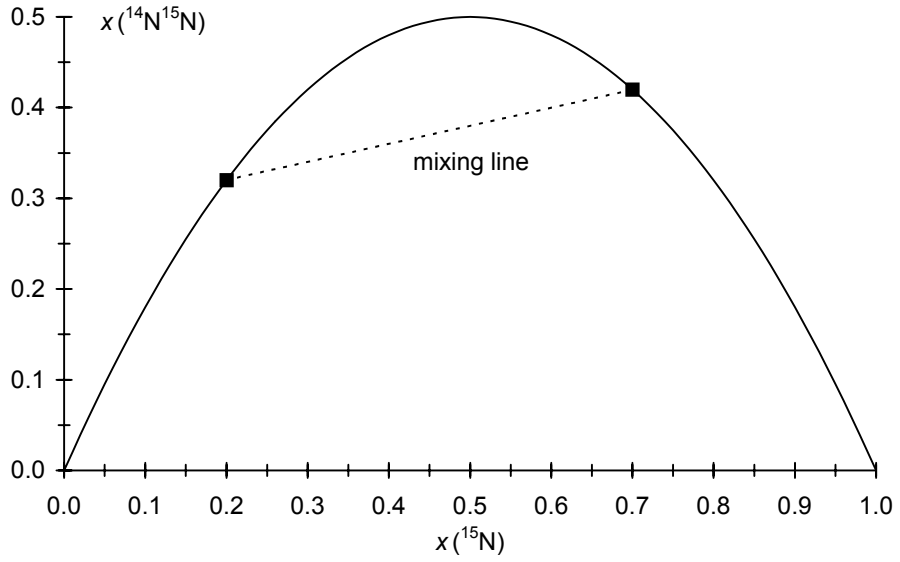

Figure 31: The parabola shows the abundance of $^{14}N^{15}N$ expected for a statistical isotope distribution in a sample of N_2 with a total ^{15}N abundance of $x(^{15}N)$. The mixing line indicates that the $^{14}N^{15}N$ abundance of a sample prepared by mixing different amounts of two reservoirs of different isotopic composition deviates from the parabola, even if the two reservoirs initially matched a statistical isotope distribution.

In the case of kinetic isotope effects, we have to consider which fractionation constant is expected for a statistical isotope distribution. Restricting ourselves to Rayleigh fractionation by N_2O photolysis in a closed system, we base our calculations on eqn. 57 (p. 50)

$$\ln \frac{R}{R_0} = \varepsilon \ln y \tag{57}$$

which is exact if we identify y with the remaining fraction of the light isotopologue. As indicated by equations 14 (p.20) and 24a (p. 23), the statistically expected isotope ratio of $^{15}N_2{}^{16}O$ in N_2O is given by the product of the $^{15}N/^{14}N$ isotope ratios at the terminal and central nitrogen atom, i.e. $R_1 \cdot R_2$. Writing R_{12} for the ratio of $^{15}N_2{}^{16}O$ to $^{14}N_2{}^{16}O$, we have

$$\ln \frac{R_{12}}{R_{12,0}} = \ln \frac{R_1 R_2}{R_{1,0} R_{2,0}} = (\varepsilon_1 + \varepsilon_2) \ln y = \varepsilon_{12} \ln y \tag{61}$$

This means that the $^{15}N_2{}^{16}O$ fractionation constant ε_{12} must equal the sum of individual fractionation constants at the terminal and central nitrogen sites in N_2O in order to maintain a statistical isotope distribution. It will be explored in the next section to which extent this is truly the case.

6.2 Isotopic fractionation of $^{15}N_2O$ in UV photolysis

The isotopic fractionation of $^{15}N_2O$ by UV photolysis was measured in the same way as described in section 4.1, i.e. photolysis of a mixture of 4 mmol/mol N_2O in N_2 by a 1 kW antimony lamp (*Heraeus*, Hanau). By the time of the experiments, we were not yet aware of the artefacts by $O(^1D)$ production at high degrees of conversion (section 4.2), so that rather than choosing a lower N_2O mixing ratio, we adopted the one used in previous experiments [*Röckmann et al.*, 2001]. The N_2O fraction in the photolysis mixture was prepared manometrically and consisted of (5.95±0.03) % $^{15}N_2O$ (isotopic purity > 99.5 %, cf. section 2.4.2) diluted into a sample of the N_2O working standard. The mixing ratio of $^{15}N_2O$ was adjusted in a way that the amplifier feedback resistors of the Faraday cup collectors on the isotope ratio mass spectrometer did not have to be exchanged.

The results of the photolysis experiments at room temperature are shown in Figure 32. Rather than the atomic fractionation constants $^{18}\varepsilon$ and $^{15}\varepsilon$, the effective fractionation constants for isotopic species of mass 45 and 46 are shown. $^{46}\varepsilon$ represents the amount-weighted average of the fractionation constants ε_{12} and $^{18}\varepsilon$ corresponding to $^{15}N_2{}^{16}O$ and $^{14}N_2{}^{18}O$ photolysis with negligible contributions from $^{14}N^{15}N^{17}O$ and $^{15}N^{14}N^{17}O$ (Table 3) whereas $^{45}\varepsilon$ is essentially the amount weighted average of ε_2 ($^{14}N^{15}N^{16}O$), ε_1 ($^{15}N^{14}N^{16}O$) and $^{17}\varepsilon(^{14}N_2{}^{17}O)$ photolysis stemming from the working standard. As noted previously (section 4.2), a decreasing trend of $|\varepsilon|$ towards

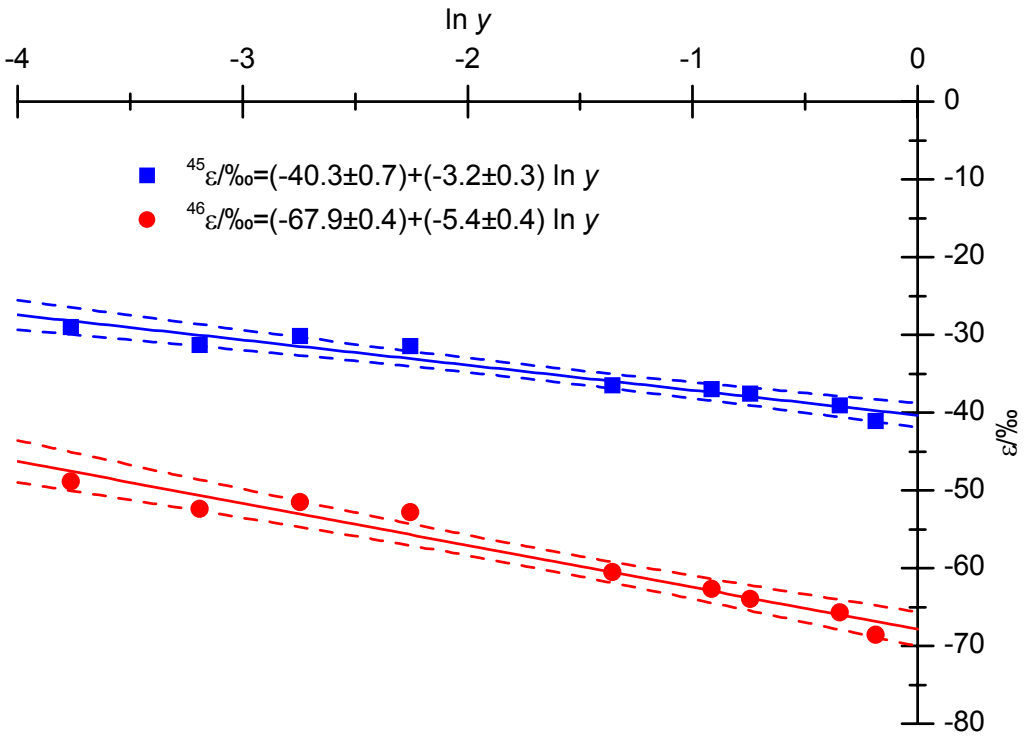

Figure 32: Directly calculated fractionation constants for photolysis of a mixture of N_2O working standard and $^{15}N_2O$. Values calculated from $\ln(1+^{45}\delta)/\ln y$ and $\ln(1+^{46}\delta)/\ln y$ are shown rather than atomic fractionation constants (e.g. $^{18}\varepsilon$, $^{15}\varepsilon$). Mass-spectrometric errors are smaller than the symbol sizes. A linear fit is applied; dashed lines indicate 95 % confidence intervals.

higher degrees of conversion is evident which can be attributed to $O(^1D)$ production from photolysis products of N_2O and subsequent reaction of N_2O with $O(^1D)$. The slope of the plot of $^{45}\varepsilon$ vs $\ln y$ is similar to previously determined values (Table 7) for the same reactor (B) and also the "true" fractionation constant estimated by the y-axis offset agrees well: Taking into account the contribution of $^{14}N_2{}^{17}O$ photolysis, one can derive $^{15}\varepsilon = (-41.5\pm0.7)$ ‰ from $^{45}\varepsilon$ as opposed to the value of (–40.4±0.2) ‰ measured before. Although a similar empirical correction for reaction of $O(^1D)$ could be applied in the case of $^{45}\varepsilon$, this is not possible for $^{46}\varepsilon$. since information on the fractionation constant of $^{15}N_2{}^{16}O$ in the reaction of N_2O with $O(^1D)$ in missing. However, this lack seems to be acceptable since the y-axis offset determined for $^{45}\varepsilon$ in the present case agrees well with the previously determined "true" fractionation constant.

Hence, the y-axis offset is also adopted as "true" fractionation constant in the case of $^{46}\varepsilon$. Then, ε_{12} can be calculated from $^{46}\varepsilon$ and the previously determined value of $^{18}\varepsilon = (-35.5\pm0.2)$ ‰ (Table 7) taking into account the amount of $^{15}N_2O$ in the N_2O/N_2 photolysis mixture as well as the purity of the $^{15}N_2O$ material (section 2.4.2) and the absolute isotopic composition of the working standard (Table 4). This gives $\varepsilon_{12} = (-79.1\pm1.3)$ ‰ which can be compared to the sum of ε_1 and ε_2 equal to (–80.8±0.4) ‰ (Table 7). Obviously, ε_{12} is very close to the statistically ex-

pected value which demonstrates that $^{15}N_2O$ photolysis should not introduce a deviation from a statistical isotope distribution in atmospheric N_2O.

6.3 Temperature dependence

Experiments to determine the $^{15}N_2{}^{16}O$ fractionation constants were also performed at temperatures lower than the ambient laboratory conditions. The same set-up and the same reactor (A) were used as in the previous experiments at low temperatures (section 4.1). Final degrees of conversion were between 13 and 18 %, corresponding to $-0.20 < \ln y < -0.14$. At these comparatively small degrees of conversion, the required correction of ε_{12} due to the influence of the N_2O + $O(^1D)$ reaction is negligible. Adopting the same slope of –5.4 as for $^{46}\varepsilon$ vs $\ln y$ and scaling it with the measured value of $^{46}\varepsilon$ during any of the low temperature experiments gives maximum deviations of 1.5 ‰ which are incorporated into the error of the final ε_{12} value.

Figure 33 shows a comparison between the measured values of ε_{12} and the sum of ε_1 and ε_2 (or, equivalently, $2^{15}\varepsilon$) calculated from the results obtained in previous experiments under comparable conditions. Temperatures were varied between 184 and 296 K. Except for the measure-

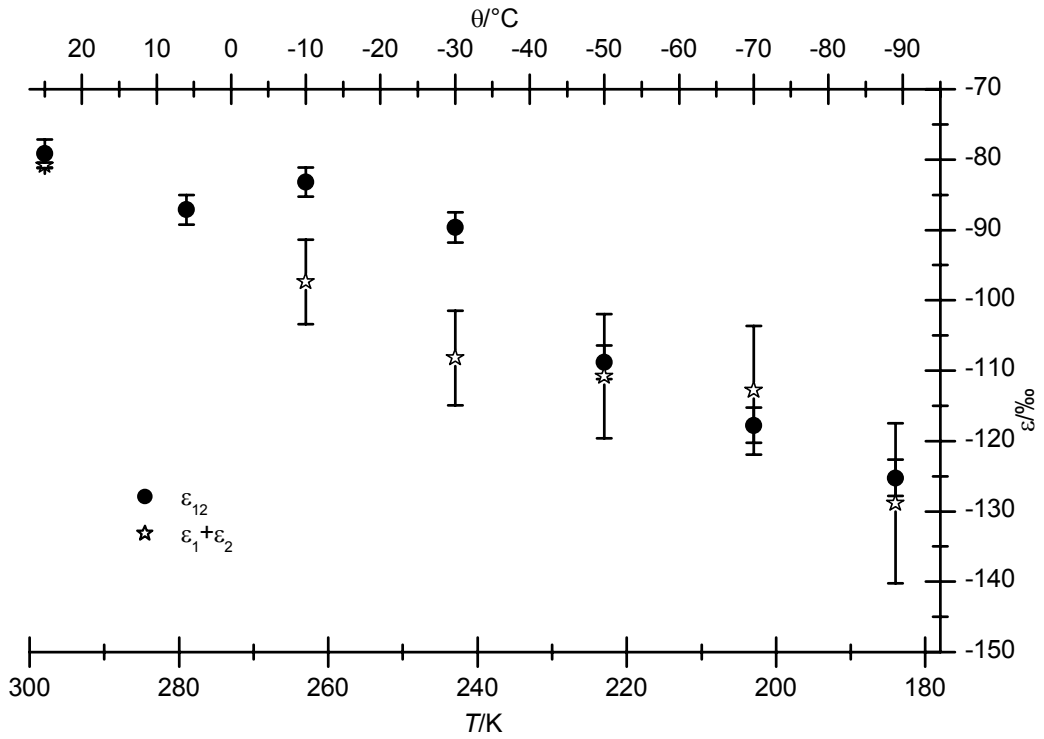

Figure 33: Comparison between measured fractionation constants of $^{15}N_2{}^{16}O$ and statistically expected values calculated from the results for ε_1 and ε_2 determined in previous experiments at low temperatures (cf. Figure 24). Broadband UV radiation from a 1 kW antimony lamp was used as a light source filtered through the same sample of aged water as in the previous experiments.

ments at 243 K and 263 K all values of ε_{12} are equal with the sum of ε_1 and ε_2 which strongly suggests that $^{15}N_2O$ photolysis occurs at rates consistent with a statistical distribution of ^{15}N in N_2O at all stratospherically relevant temperatures. We do not currently have an explanation for the deviating results at 243 K and 263 K, but note that these may be outliers since – other than in the extensive room temperature experiments – only one data point each was obtained at temperatures lower than 296 K.

6.4 Comparison with other data and theories

Figure 34 gives an overview of theoretically predicted and measured fractionation constants for $^{15}N^{16}O$ photolysis near room temperature, similar to the plots shown previously for $^{15}\varepsilon$, $^{18}\varepsilon$, $^{15}\varepsilon_1$ and $^{15}\varepsilon_2$. Apparently, no theory is capable of predicting the large enrichments at the wavelengths of the antimony lamp while the VUV spectroscopic measurements of Selwyn and Johnston [1981] do not extend beyond 197 nm. The deviations of the Hermite propagation (HP) theory [*Johnson et al.*, 2001] is likely due to the use of a two-dimensional potential energy surface in their calculations which only considers changes of NN–O bond length and bending angle (*Matt Johnson*, personal communication, 2002). Discrepancies between the measured value and the prediction by the zero point energy (ZPE) theory are of similar relative magnitude (i.e. about a factor

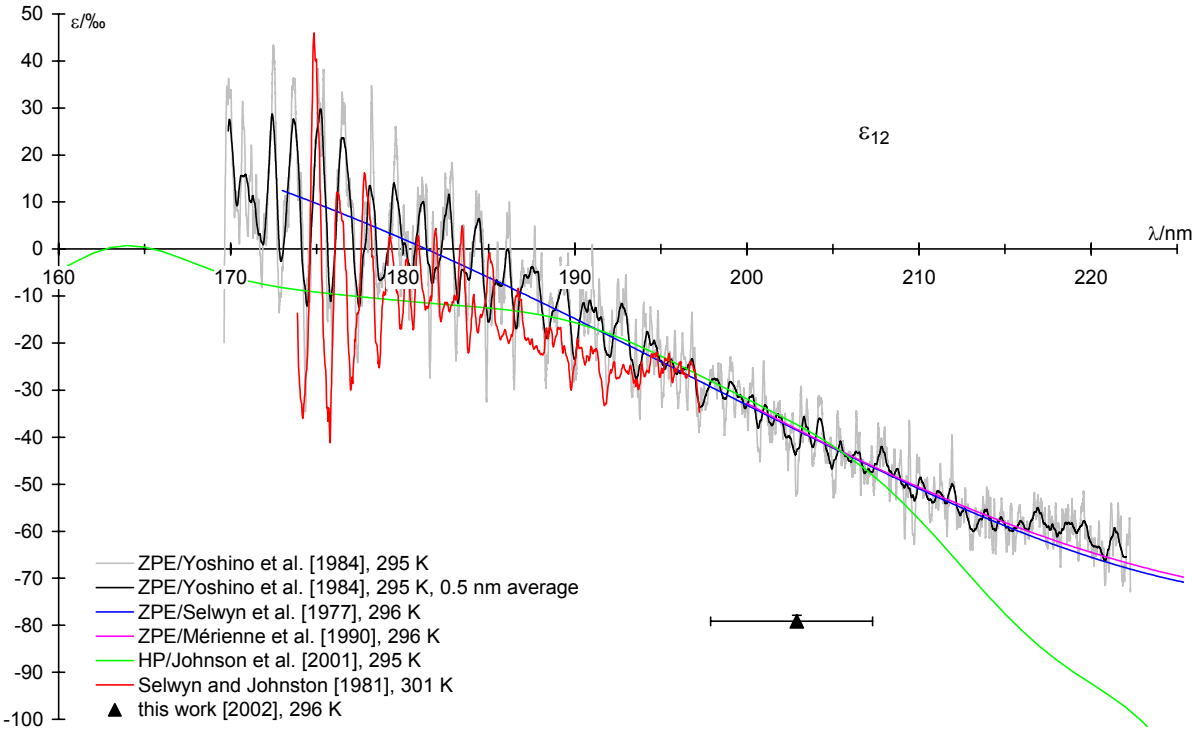

Figure 34: Overview of theoretically predicted and measured fractionation constants for $^{15}N^{16}O$ photolysis near room temperature (cf. Figure 28).

of 2) as for the other fractionation constants. However, we note that for both the HP and the ZPE theory the sum of ε_1 and ε_2 is nearly identical to ε_{12} which lends support to the experimental finding that $^{15}N_2{}^{16}O$ photolysis proceeds along the lines of a statistical isotope distribution.

Having realised that the "additivity law" of fractionation constants holds in the case of $^{15}N_2{}^{16}O$, one may want to ask whether this extends to other N_2O isotopomers and isotopologues as well. Considering that the predictions of the ZPE theory seem to be off from the measured values for $^{15}\varepsilon_1$, $^{15}\varepsilon_2$, $^{18}\varepsilon$, $^{17}\varepsilon$ and $^{15}\varepsilon_{12}$ by a constant factor of 2, it is reasonable to check the validity of the "additivity law" within the framework of this theory. To a very good degree of approximation, fractionation constants predicted by the ZPE theory are proportional to differences in zero point energy between the isotopically substituted species and $^{14}N_2{}^{16}O$. Recently, Łapiński *et al.* [2001] reported vibrational frequencies for all twelve N_2O isotopomers and isotopologues in solid nitrogen matrices and summarised the existing measurements in the gas phase. We have calculated the resulting gas phase zero point energies within the harmonic oscillator approximation via $U_0 = \frac{1}{2}h\sum_{n=1}^{3} g_n \nu_n$ where g_n is the degeneracy of the vibrational mode and ν_n are the frequencies of the fundamental stretching and bending vibrations. We then adopt the zero point energy differences of $^{14}N^{15}N^{16}O$, $^{15}N^{14}N^{16}O$, $^{14}N_2{}^{17}O$ and $^{14}N_2{}^{18}O$ to $^{14}N_2{}^{16}O$ in order to estimate the expected zero point energy differences for the remaining five double substituted and two triple substituted N_2O species. These are compared to the measured values in Figure 35. Evidently, the relative deviation of calculated to measured values is less than 1.5 % so that the fractionation constants in N_2O photolysis are expected to follow a pattern in line with a statistical isotope distribution. Isotopically substituted N_2O species are therefore expected to be present in the atmosphere at their statistically dictated amounts. Furthermore, the calculation of average ^{15}N fractionation constants as well as values for the position-dependent ^{15}N enrichment and oxygen isotope fractionation from measurements of ^{31}R, ^{45}R and ^{46}R isotope ratios can be reconciled with the statistical approximation made in the derivation of the corresponding relations between these isotope ratios and the elemental isotope ratios ^{15}R, $^{15}R_1$, $^{15}R_2$, ^{18}R and ^{17}R.

Future measurements of the stratospheric $^{15}N_2{}^{16}O$ abundance should show whether the expected statistically dictated amounts are truly present. However, as mentioned above, this is certainly a daunting task due to the low concentration of $^{15}N_2{}^{16}O$ in stratospheric air.

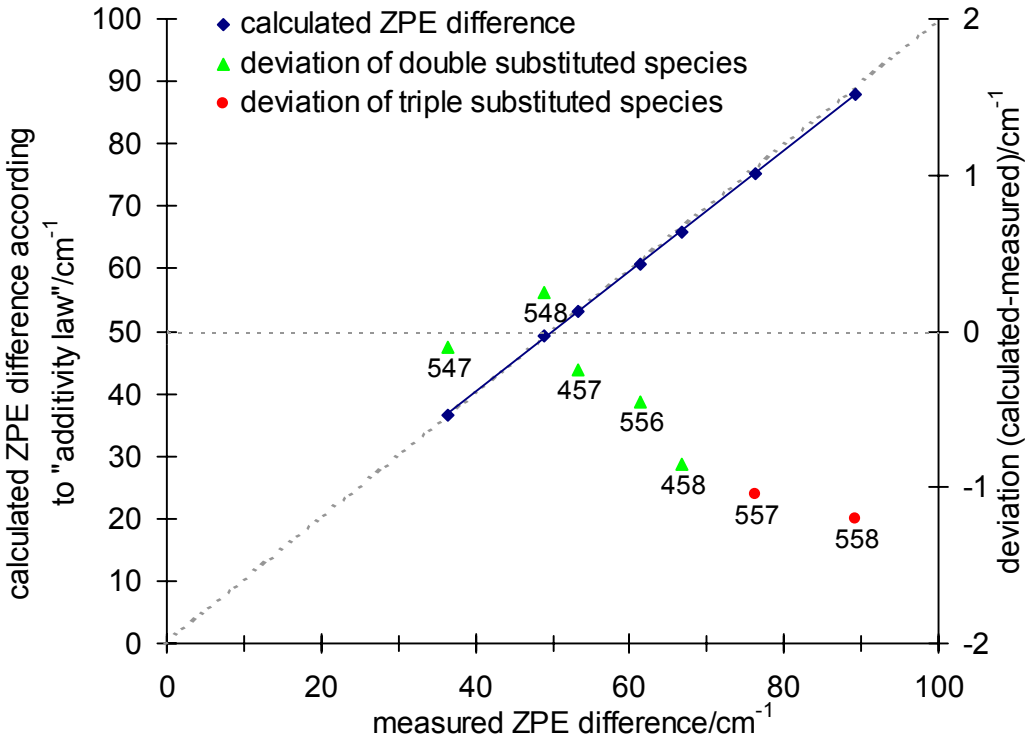

Figure 35: Comparison between measured ZPE differences and values calculated according to the "additivity law" proposed in the main text. N_2O species are abbreviated by their AFGL codes composed of the last digits of the integral isotope masses (Appendix B). On the right axis, the deviations of the calculated from the measured values are shown for double and triple substituted N_2O species.

7 N_2O in the stratosphere

This chapter is sub-divided into three parts: In the first part (section 3.1), the influence of the transport phenomena mixing and diffusion on the apparent fractionation constants and the ratios of fractionation constants ψ and η will be shown. In the second section, results from stratospheric balloon samples are presented. To this end, the technique for position-dependent ^{15}N isotope ratio analysis was adapted to continuous-flow mass spectrometry allowing isotope measurements on small stratospheric samples (≈1 nmol N_2O). The last section relates the actual stratospheric measurements to data obtained in the laboratory experiments (chapters 3–5) and presents results from a stratospheric 2D model which was forced by the laboratory data. The effects of transport, $O(^1D)$ sink, wavelength and temperature dependence on ε, ψ and η values will be discussed

7.1 Mixing effects on apparent isotope fractionation

For convenience, we formally introduce here two dimensionless quantities as diagnostic values: the ratio of the fractionation constants for the central (locant: 2; Figure 2) and for the terminal (locant: 1) nitrogen position in the N_2O molecule (η) and the ratio of the average ^{15}N and the ^{18}O fractionation constants (ψ):

$$\eta = {}^{15}\varepsilon_2/{}^{15}\varepsilon_1 \qquad\qquad \psi = {}^{15}\varepsilon/{}^{18}\varepsilon$$

We note that there are at least two other sets of N_2O isotopomer terminology in use at present [*Toyoda and Yoshida*, 1999; *Yung and Miller*, 1997] (see Appendix B) which lead to equivalent definitions of η and ψ. The merit of using ratios of ε is the possibility to distinguish dynamic and photochemical influences on observed isotopic fractionations. Although the fractionation constants associated with photolysis can apparently undergo significant changes by dynamic processes, their ratio is – to a first approximation – invariant throughout the stratosphere if transport and mixing are the only processes of importance. The accurate calculation in this section shows that ratios of ε are not entirely invariant to dynamic processes, but never deviate much from the observed end-member ratio.

We first show that mixing of two air masses containing a trace gas that is isotopically fractionated to different degrees by the same loss process decreases the apparent fractionation constant (ε_{app}) in the atmosphere relative to the real fractionation constant (ε) of the reaction causing the fractionation. This may serve as a simple model for stratosphere–troposphere or mid-

latitude–tropical exchange. In the case of diffusion, the value for ε_{app} depends on whether the reaction-diffusion system is rather reaction- or diffusion-limited.

Subsequently, simultaneous intramolecular fractionations at two sites of a molecule (such as $^{15}\varepsilon_{1,}\,^{15}\varepsilon_{2}$) are considered. It is shown that diffusion or mixing processes generally lead to only small decreases or increases of the ratio of apparent fractionation constants (e.g., $\eta_{app} = {}^{15}\varepsilon_{2,app}/{}^{15}\varepsilon_{1,app}$).

7.1.1 Influence of mixing on the apparent fractionation constant

First, we calculate the δ value of an air mass produced by mixing of two distinct air masses (A, B) in a volume ratio $x : (1–x)$. Air mass A and B could be identified, e.g., with tropospheric (non-photolysed) and stratospheric (photolysed) air. Then, the δ value of the mixed air mass is

$$\delta_{mix} = \frac{x c_A \delta_A + (1-x) c_B \delta_B}{x c_A + (1-x) c_B} \tag{62}$$

where c_A, c_B are the concentrations of light isotopologues in the two air masses and δ_A, δ_B are the pertinent δ values. The apparent fractionation constant of the mixed air mass (ε_{app}) is then calculated analogously to Rayleigh fractionation (3.1)

$$\varepsilon_{app} = \frac{\ln(1+\delta_{mix})}{\ln y} = \frac{\ln\left[x(1+\delta_A) + (1-x)\, y_B (1+\delta_B)\right]}{\ln\left[x + (1-x)\, y_B\right]} - 1 \tag{63}$$

By identifying y with the concentration ratio of the most abundant, light isotopologue (i.e., c/c_A) eqn. 63 is valid without any approximation. y runs from 1 (at $x = 1$) to $y_B = c_B/c_A$ (at $x = 0$) and is related to x via $y = x + (1-x)\, y_B$. Without loss of generality, δ_{mix} is transformed so that $\delta_A = 0$ (by subtraction of δ_A from all δ values). Then, eqn. 63 yields

$$\varepsilon_{app} = \frac{\ln\left[x + (1-x)\, y_B (1+\delta_B)\right]}{\ln\left[x + (1-x)\, y_B\right]} - 1 \tag{64}$$

Figure 36 shows a plot of $\ln(1+\delta)$ as it would be found for photolysis with a fractionation constant of $\varepsilon = –21$ ‰. A plot of $\ln(1+\delta_{mix})$ for a hypothetical mixture of non-photolysed (tropospheric) air (316 nmol/mol) with photolysed (stratospheric) air (arbitrarily chosen to have 100 nmol/mol) are also shown. At $x = 0$, $|\varepsilon_{app}|$ is at its maximum and identical to ε:

$$\max|\varepsilon_{app}| = \varepsilon_{app}(x=0) = \frac{\ln[\, y_B (1+\delta_B)]}{\ln y_B} - 1 = \frac{\ln(1+\delta_B)}{\ln y_B} = \varepsilon \tag{65}$$

Because of the monotony of logarithms, the initial $\varepsilon_{app}(x \to 1)$ is identical to the minimum $|\varepsilon_{app}|$ that can be observed:

$$\min|\varepsilon_{app}| = \lim_{x \to 1} \varepsilon_{app} = \frac{-\, y_B \delta_B}{1 - y_B} \tag{66}$$

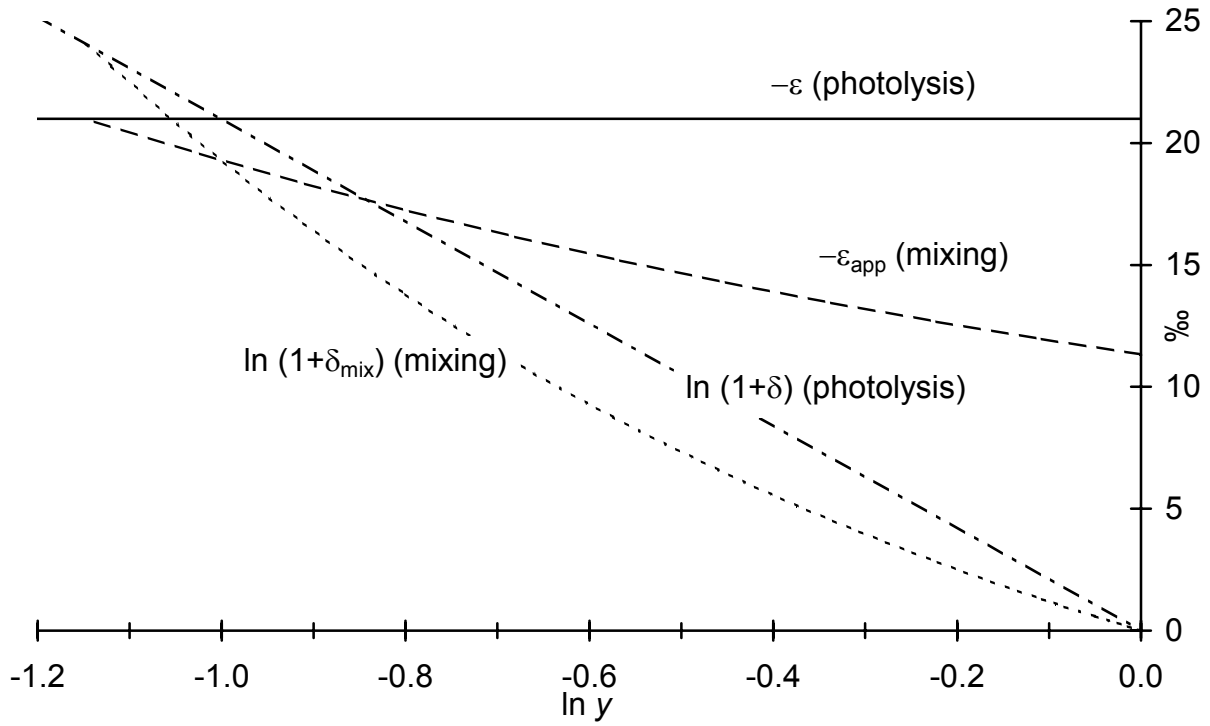

Figure 36: Simulation of ln(1+δ) during N_2O photolysis in one air mass (in accordance with Rayleigh fractionation) and of ln(1+δ_{mix}) for mixing of an air mass containing non-photolysed (unfractionated) N_2O with another air mass containing photolysed (Rayleigh-fractionated) N_2O. Also shown are the fractionation constants for photolysis (ε = –21 ‰) and the apparent fractionation constant of the mixed air mass (ε_{app}) calculated for each ln *y* (negative values shown for direct comparison).

7.1.2 Influence of diffusion on the apparent fractionation constant

The effect of pure one-dimensional diffusion on ε_{app} is illustrated in Figure 37. It follows from the solution of the reaction diffusion equation given in [*Kaye*, 1987]. With the parameter $Q = 4H_{av}^2/K_z$ (H_{av}: scale height, K_z: vertical eddy diffusion coefficient), one can derive a value of $\varepsilon_{app} = \frac{1-\sqrt{1+Qk'}}{1-\sqrt{1+Qk}} - 1$ for the apparent fractionation constant with diffusion where k' and k are the reaction rate constants of the isotopically heavy and light isotopologues, respectively. They are related to each other by $\alpha = 1 + \varepsilon = \frac{k'}{k}$ (eqn. 55). ε_{app} varies between ε and $\sqrt{1+\varepsilon} - 1$ for the cases $Q\,k << 1$ (fast diffusion, slow reaction: reaction-limited) and $Q\,k >> 1$ (slow diffusion, fast reaction: diffusion-limited).

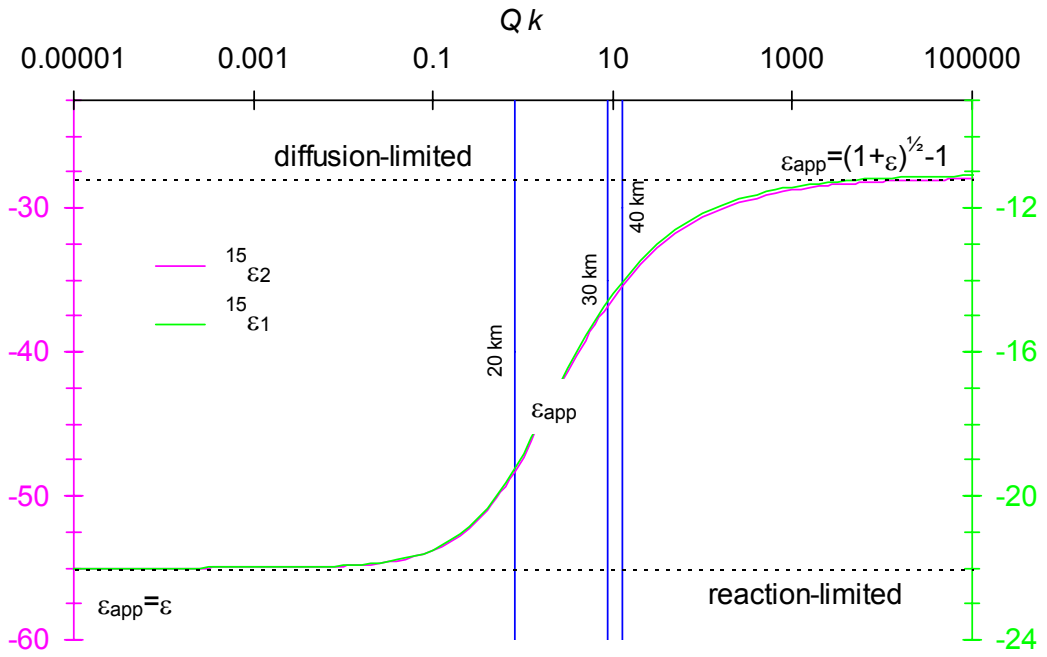

Figure 37: Effect of reaction rate constant (k) and vertical eddy diffusion constant (K_z) on the apparent fractionation constant (ε_{app}) as a function of $Q\,k = 4H_{av}^2 k/K_z$. $^{15}\varepsilon_2$ and $^{15}\varepsilon_1$ were assumed to be –55 ‰ and –22 ‰, respectively, and plotted on adjusted y-axes so that they can be compared directly. Obviously $^{15}\varepsilon_{2,app}$ and $^{15}\varepsilon_{1,app}$ almost collapse into a single curve which indicates that their ratio must be nearly constant. The exactly calculated ratio (η_{app}) is plotted in Figure 38. The blue vertical lines denote instantaneous (non-integrated) values of $Q\,k$ for different altitudes calculated from total N_2O loss rates [*Minschwaner et al.*, 1993] and a parameterisation of K_z [*Froideveaux and Yung*, 1982]. The scale height was assumed to be at a constant H_{av} value of 7 km, since it only varies ±15 % with different temperatures at different altitudes whereas K_z and k vary over several orders of magnitude.

7.1.3 Influence of diffusion and mixing on ratios of fractionation constants

Now, we consider ratios of apparent individual intramolecular fractionation constants such as $\eta = {}^{15}\varepsilon_2/{}^{15}\varepsilon_1 = ({}^{15}\alpha_2 - 1)/({}^{15}\alpha_1 - 1)$ in the case of N_2O, first for only the reaction, then for diffusion and finally for mixing. Similar relationships hold for $\psi = {}^{15}\varepsilon/{}^{18}\varepsilon$.

For a Rayleigh process η is – because of its definition – independent of the fraction of remaining reactant (y). In terms of atmospheric chemistry, η is independent of the mixing ratio, since y is calculated from the stratospheric mixing ratio relative to its tropospheric value.

No matter the remaining reactant, a similar constancy holds for one-dimensional diffusion which follows from the above solution for the apparent fractionation constant with diffusion, i.e. $\varepsilon_{app} = \dfrac{1-\sqrt{1+Qk'}}{1-\sqrt{1+Qk}} - 1$. Depending on the value of Q, the ratio of apparent fractionation constants ($\eta_{app} = \varepsilon_{2,app}/\varepsilon_{1,app}$) varies (Figure 38). For $Qk << 1$ (reaction-limited), $\eta_{app} = \eta$, whereas for

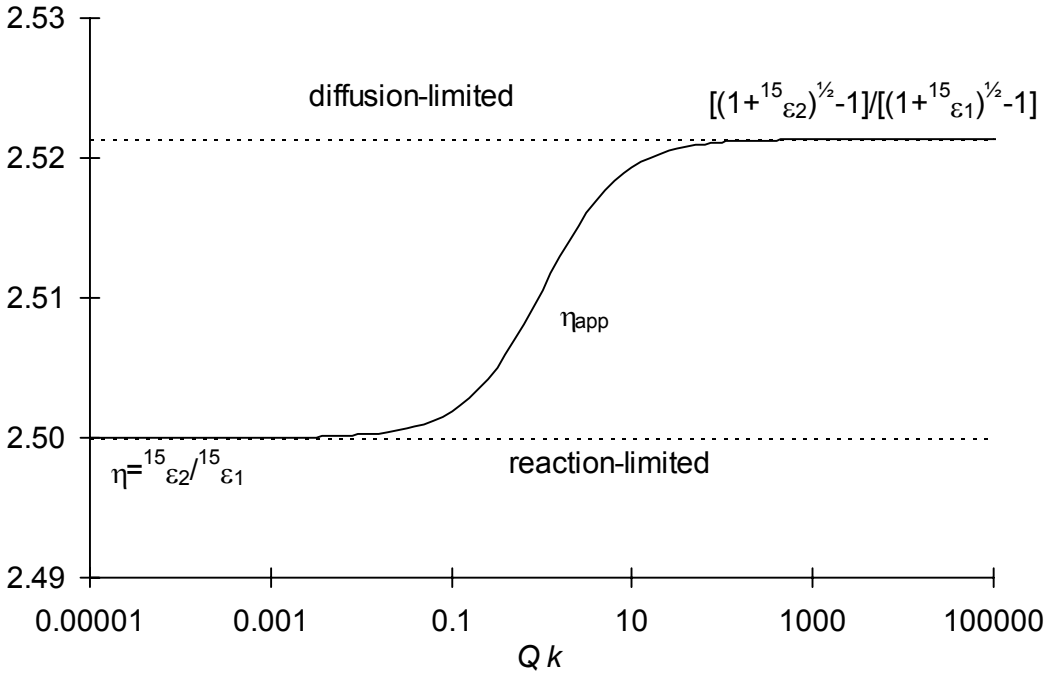

Figure 38: Simulation of η_{app} for one-dimensional vertical diffusion in steady state with a first-order loss process (rate constant k, $Q = 4\,H_{av}^2/K_z$, $^{15}\varepsilon_2 = -55$ ‰, $^{15}\varepsilon_1 = -22$ ‰). Also shown are the limiting values for $Q\,k << 1$ (fast diffusion, slow reaction: reaction-limited) and $Q\,k >> 1$ (slow diffusion, fast reaction: diffusion-limited).

$Qk >> 1$ (diffusion-limited), $\eta_{app} = \dfrac{\sqrt{1+\varepsilon_2}-1}{\sqrt{1+\varepsilon_1}-1} \approx \dfrac{\varepsilon_2}{\varepsilon_1}\dfrac{1-¼\varepsilon_2}{1-¼\varepsilon_1}$. For normal isotope effects ($\varepsilon < 0$) and larger fractionations at the central N atom than at the terminal N atom ($\varepsilon_2 < \varepsilon_1 < 0$), such as for N_2O photolysis, we have therefore $\eta_{app} \geq \eta$; for inverse isotope effects with $\varepsilon_2 > \varepsilon_1 > 0$, $\eta_{app} \leq \eta$. For $|\varepsilon_2| < |\varepsilon_1|$, such as in the case of the reaction $N_2O + O(^1D)$, the inverse relationships hold. Anyway, the variability of η (Figure 38) is much smaller than that of ε_{app} (Figure 37). Under the same reaction-diffusion regime, η_{app} does not vary at all with altitude.

In contrast to diffusion, in the case of pure mixing, η_{app} does not behave exactly as a conserved property. However, even then η_{app} does not deviate much from η. For two differently fractionated positions of the molecule (fractionation constants: ε_2, ε_1) the following constant relationship is derived from eqn. 62 for any x of the mixed air mass:

$$\frac{\delta_{2,\mathrm{mix}} - \delta_{2,\mathrm{A}}}{\delta_{1,\mathrm{mix}} - \delta_{1,A}} = \frac{\delta_{2,\mathrm{B}} - \delta_{2,\mathrm{A}}}{\delta_{1,\mathrm{B}} - \delta_{1,\mathrm{A}}} = const. \qquad (67)$$

$\delta_{1,\mathrm{mix}}$ varies monotonically between $\delta_{1,\mathrm{A}}$ and $\delta_{1,\mathrm{B}}$, whereas $\delta_{2,\mathrm{mix}}$ varies monotonically between $\delta_{2,\mathrm{A}}$ and $\delta_{2,\mathrm{B}}$. Without loss of generality, we can apply the transformation to $\delta_{1,\mathrm{A}} = \delta_{2,\mathrm{A}} = 0$ again:

$$\frac{\delta_{2,\mathrm{mix}}}{\delta_{1,\mathrm{mix}}} = \frac{\delta_{2,\mathrm{B}}}{\delta_{1,\mathrm{B}}} = const. \tag{68}$$

This means, that for mixing the ratio δ_2/δ_1 is constant. However, as opposed to Rayleigh fractionation with or without diffusion, $\eta_{app} = \varepsilon_{2,app}/\varepsilon_{1,app}$ is not constant, but function of x

$$\eta_{app}(x) = \frac{\ln(1+\delta_{2,\mathrm{mix}})}{\ln(1+\delta_{1,\mathrm{mix}})} \tag{69}$$

Nevertheless, there are upper and lower boundaries for $\eta_{app}(x)$ because of the monotonic character of δ_1, δ_2 and of the natural logarithm. The lower and upper boundaries are attained for $x = 0$ and $x = 1$:

$$\eta_{app}(x=0) = \frac{\ln(1+\delta_{2,\mathrm{B}})}{\ln(1+\delta_{1,\mathrm{B}})} \qquad \eta_{app}(x=1) = \frac{\ln(1+\delta_{2,\mathrm{A}})}{\ln(1+\delta_{1,\mathrm{A}})} \tag{70}$$

For $\delta_{1,A} = \delta_{2,A} = 0$, $\delta_{1,B} = (y_B)^{\varepsilon_1} - 1$ and $\delta_{2,B} = (y_B)^{\varepsilon_2} - 1$ (Rayleigh fractionation) we have:

$$\eta_{app}(x=0) = \frac{\varepsilon_2}{\varepsilon_1} = \eta \qquad \eta_{app}(x \to 1) = \frac{(y_B)^{\varepsilon_2} - 1}{(y_B)^{\varepsilon_1} - 1} = \frac{\delta_{2,B}}{\delta_{1,B}} \tag{71}$$

Figure 39 illustrates the relationship between ratios of true and apparent fractionation constants and the ratio of δ values for $\varepsilon > 0$ and $\varepsilon < 0$. Typical values for $^{15}\varepsilon_1$ and $^{15}\varepsilon_2$ in N_2O broadband photolysis have been assumed. One realises that for $\varepsilon > 0$ (and $|\varepsilon_2| > |\varepsilon_1|$)

$$\eta \le \eta_{app} \le \frac{\delta_{2,B}}{\delta_{1,B}} \tag{72}$$

It follows immediately that the inverse relationship holds for $\varepsilon < 0$.

7.1.4 Note on linear combinations of δ values

Some recent studies on intramolecular nitrogen isotope analysis of N_2O express the position-dependent fractionation by the difference of δ values at the central and terminal nitrogen site [*Griffith et al.*, 2000; *Pérez et al.*, 2001; *Yamulki et al.*, 2001; *Yoshida and Toyoda*, 2000]. This quantity (also called "site preference") has been used initially to highlight the newly available information from the position-dependent measurement of nitrogen isotope ratios as opposed to the conventional "bulk" nitrogen isotope ratio. Although this may be illustrative, one has to bear in mind that there is no additional physical insight gained from linear combinations of δ values, neither in Rayleigh fractionation where the ratio $\ln(1+\delta_2)/\ln(1+\delta_1)$ is conserved, nor in mixing where ratios of δ values are conserved. *Differences* of δ values ($\delta_1 - \delta_2$) are not correlated with differences of fractionation constants ($\varepsilon_2 - \varepsilon_1$). In contrast, *ratios* of fractionation constants (e.g., $\varepsilon_2/\varepsilon_1$) or ratios of δ values (δ_2/δ_1) appear to be more suitable as a diagnostic tool. They are characteristic for

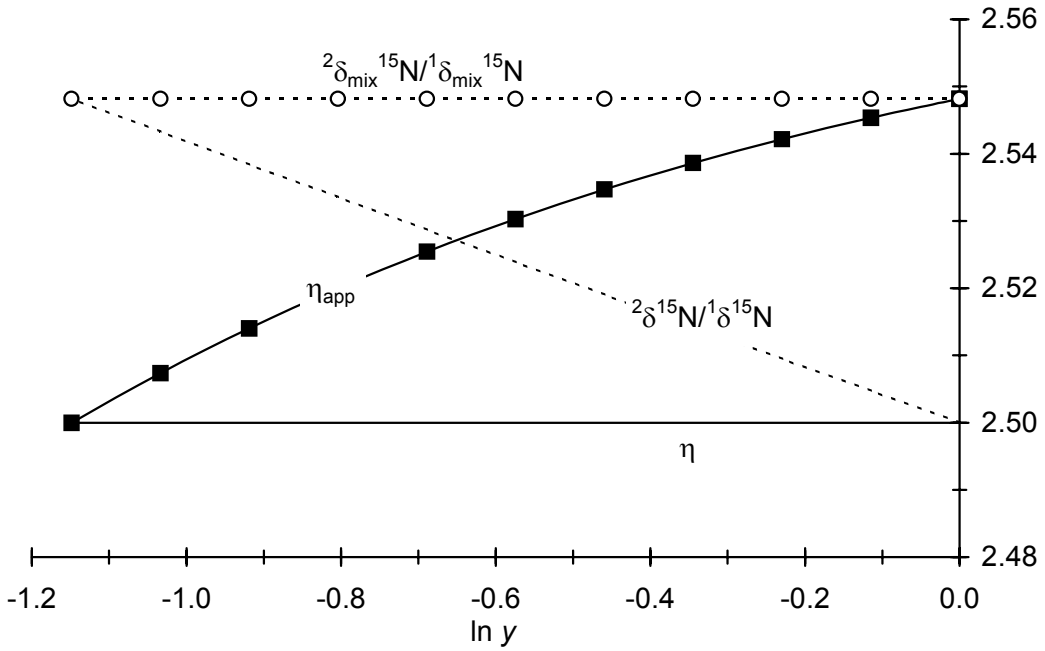

Figure 39: Simulation of η during N_2O photolysis ($^{15}\varepsilon_2 = -55$ ‰, $^{15}\varepsilon_1 = -22$ ‰) in a single air mass and of η_{app} for mixing of an air mass containing non-photolysed (unfractionated) N_2O with another air mass containing photolysed (Rayleigh-fractionated) N_2O. Displayed are both η and the ratio of δ values during photolysis ($^2\delta^{15}N/^1\delta^{15}N$) and for simulated mixing ($^2\delta_{mix}{}^{15}N/^1\delta_{mix}{}^{15}N$).

Rayleigh fractionation or mixing, respectively, and can be used interchangeably for small enrichments. Finally, distinct changes in these ratios signal independent variations of the fractionation constants through the change of environmental parameters or the influence of other reactions. For example, dynamic and photochemical influences on the observed ε ratios for N_2O should be distinguishable.

The above statement on linear combinations of δ values and fractionation constants means also that the value of the average ^{15}N fractionation constant in a Rayleigh process, i.e. $^{15}\varepsilon = (^{15}\varepsilon_1 + {}^{15}\varepsilon_2)/2$, is not exactly identical to the value derived from a $\ln(1+\delta^{15}N)$ vs $\ln y$ plot. $\delta^{15}N$, the observable quantity in isotope mass-spectrometry of the N_2O^+ molecule ion, corresponds to the arithmetic average of the isotope ratios at the two nitrogen sites in the N_2O molecule, $^{15}R = \frac{1}{2}(^{15}R_1 + {}^{15}R_2)$. More precisely, in a Rayleigh process, the geometric (not arithmetic) average of $^{15}R_1$ and $^{15}R_2$, should be used to calculate the average ^{15}N fractionation constant since

$$\sqrt{^{15}R_1\,{}^{15}R_2} \Big/ \sqrt{^{15}R_1(t=0)\,{}^{15}R_2(t=0)} = \sqrt{y^{\varepsilon_1} y^{\varepsilon_2}} = y^{(\varepsilon_1+\varepsilon_2)/2} = y^{\varepsilon} \qquad (73)$$

Otherwise, not necessarily linear relationships between $\ln(1+\delta)$ and $\ln y$ arise. However, if $^{15}\varepsilon_1$ and $^{15}\varepsilon_2$ are not too different, the arithmetic average is almost identical to the geometric average. E.g., for $^{15}\varepsilon_1 = -20$ ‰ and $^{15}\varepsilon_2 = -60$ ‰ and large extents of reaction ($\ln y = -4$), $^{15}\varepsilon$ calculated

from ^{15}R (–40.8 ‰) is very close to the true value (–40 ‰). Given the achievable experimental precision, the error in using ^{15}R directly to calculate $^{15}\varepsilon$ is therefore negligible.

7.2 Stratospheric measurements

7.2.1 Experimental methods

A total of 19 stratospheric and upper tropospheric whole air samples from altitudes between 10 and 28 km in the tropics, mid-latitudes and the polar region were obtained by balloon-borne cryogenic samplers. 10 tropical samples were obtained above Hyderabad, India (17.5°N, 78.6°E) in April 1999, one sample from September 1993 was taken in Aire sur l'Adour, France (43.7°N, 0.3°W) and the 9 polar samples are from different campaigns in Kiruna, Sweden (67.9°N, 21.1°E): During the SESAME campaign in 1993, 3 samples were obtained at altitudes between 17 and 19 km; the other samples from higher altitudes were taken during consecutive EASOE campaigns in January, February, and March 1992.

In the laboratory, N_2O was cryogenically extracted from 0.1 to 2 dm^3 of stratospheric air by a *Finnigan* MAT PreCon device [*Brand*, 1995]. The amount of processed air depended on the N_2O mixing ratio and the monitored ions, i.e. N_2O^+ or NO^+). CO_2 was removed with an efficiency of > 99.9% by *Ascarite* (*Sigma-Aldrich*). The trapped condensable gases were separated at a flow rate of 2 cm^3 min^{-1} on a Poraplot Q capillary column (*Chrompack*, 25 m length, i.d. 0.32 mm, 35 °C). The GC exhaust was coupled via an open split interface to a *Finnigan* DELTA^{plus} XL mass spectrometer. Simultaneous measurements of the ion currents at m/z 44, 45 and 46 (N_2O^+ molecular ion) or, alternately, m/z 30 and 31 (NO^+ fragment) were possible with the universal triple collector configuration. Elemental isotope ratios were calculated as described in section 2.1. The standard deviation of the isotope measurements at the 1σ level is 0.2‰ for $\delta^{15}N$, $\delta^{18}O$ and $^1\delta^{15}N$ at tropospheric mixing ratios and 0.6‰ below 50 nmol/mol, as established by multiple measurements of various fractionated gases. Results of N_2O samples analysed with this online method and the offline method (section 8.1) are identical within their errors.

N_2O mixing ratios were determined by GC-ECD with a precision of ≈ 1 nmol/mol. Non-linearity effects of the electron capture detector were accounted for by precise dilution of tropospheric air with N_2O-free synthetic air. The N_2O concentration measurements were in agreement to results obtained shortly after sampling within experimental errors (except for two samples), indicating no severe production/destruction of N_2O in the sampling containers over time. Although no isotope ratios were measured when the older samples were obtained, the stability of N_2O mixing ratios suggests no serious alteration of the isotopic composition during storage.

δ values are reported relative to our N_2O working standard gas which has an isotopic composition close to tropospheric N_2O (section 8.4). Its position-dependent isotopic composition on international scales is $^2\delta^{15}N = 21.2$ ‰, $^1\delta^{15}N = -19.2$ ‰ and $\delta^{18}O = 38.5$ ‰ vs air-N_2 and VSMOW, respectively (sections 2.3 and 2.4). However, it was not necessary to convert the stratospheric isotope ratios to international scales, because we are focusing on variations relative to the tropospheric value. Apparent stratospheric fractionation constants ε_{app} (or short: ε) are defined in analogy to the laboratory experiments as $\varepsilon = \ln(1+\delta)/\ln y$ (section 3.1) where y in this case means the ratio of stratospheric and tropospheric mixing ratio.

7.2.2 Results

Vertical profiles of the N_2O mixing ratio from tropospheric levels of 315 nmol/mol down to 6 nmol/mol (Figure 40) reflect the destruction of N_2O with increasing age of stratospheric air, i.e. towards higher altitudes and latitudes. Simultaneously, enrichments in all heavy isotopes are observed in the order $^{14}N^{15}NO > N_2{}^{18}O > {}^{15}N^{14}O$ which is the same pattern as for N_2O photolysis (Figure 28) and confirms the view that photolysis is responsible for the isotopic enrichment.

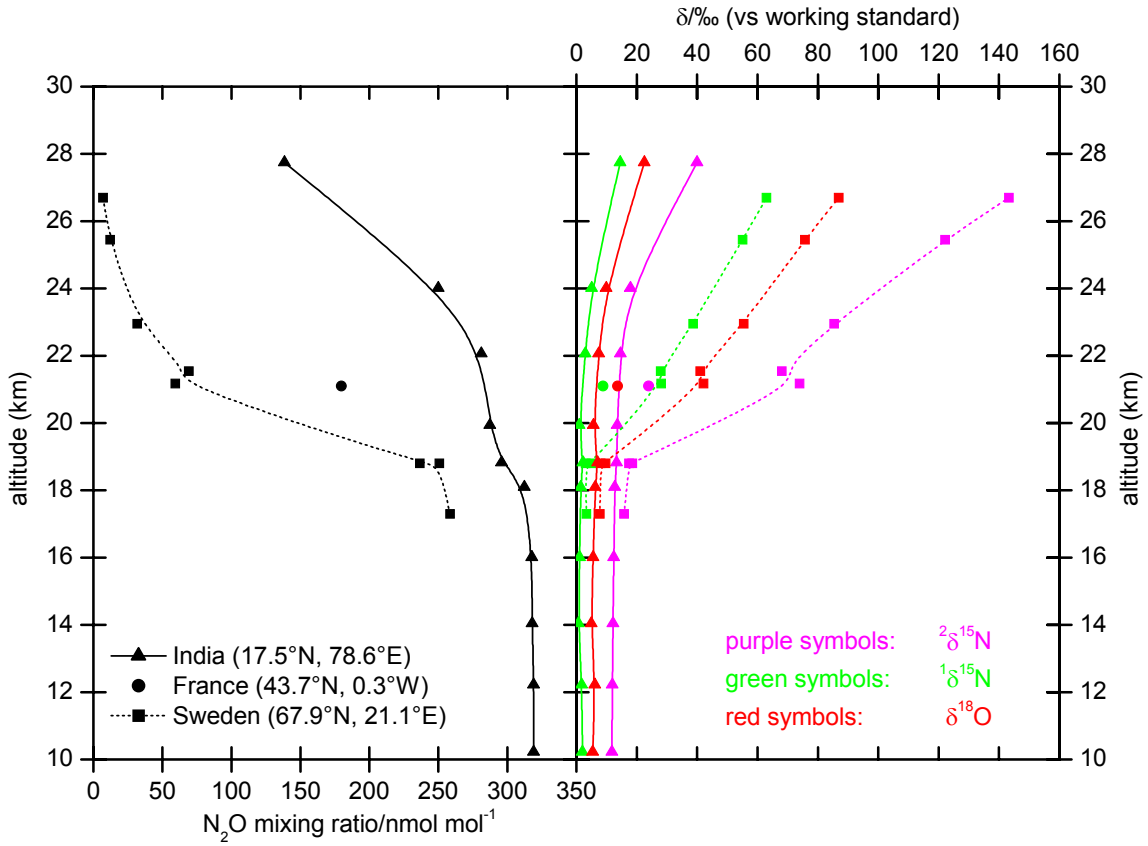

Figure 40: Vertical profiles of N_2O mixing ratio and isotopic composition for 19 upper tropospheric and stratospheric air samples from three different latitudes. Along with its removal by stratospheric sink reactions, N_2O becomes isotopically enriched. Cubic B-spline curves are used for interpolation.

Figure 41 presents the stratospheric isotope data as Rayleigh fractionation plots. The tight correlation between samples obtained at different locations and different times of the year is striking and indicates that the derived fractionation constants are likely a common characteristic of stratospheric N_2O. Apparent stratospheric fractionation constants are smaller than laboratory values (section 4.2.2) obtained by broadband photolysis with lamps of similar spectral characteristics as the actual stratospheric flux (Figure 30). Moreover, a small, but significant decrease in the apparent fractionation constants is noticed for the lower stratosphere (200 to 320 nmol/mol) as shown in the insert of Figure 41. Such deviations were already suspected to exist by Rahn and Wahlen [1997] and are in agreement with other results [*Toyoda et al.*, 2001b; *Yoshida and Toyoda*, 2000]. Using balloon-borne infrared remote sensing, Griffith *et al.* [2000] also see an attenuation of isotope fractionation constants in the lower stratosphere, but the derived values for ε_{app} are 1.5 to 2 times larger than the MS measurements. Part of this discrepancy is attributed to artefacts of the peak fitting procedure in FTIR analysis (*Dave Griffith*, personal communication, 2002).

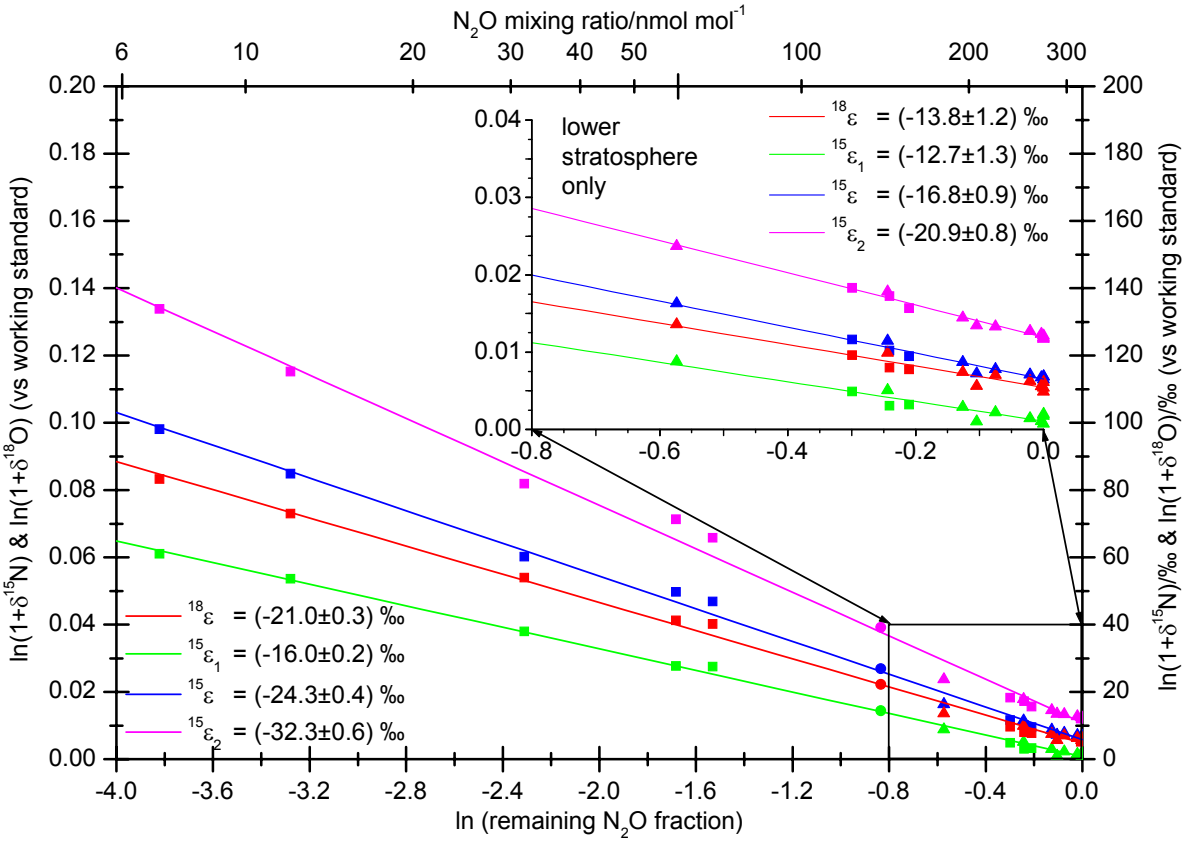

Figure 41: Rayleigh fractionation plots of the stratospheric samples shows the tight correlation between N_2O mixing ratios and isotopic composition. Linear least squares fits are applied to derive the apparent fractionation constants (ε_{app}) along with 2σ errors. The inset focuses on the lower stratosphere only (mixing ratios between 200 and 320 nmol/mol) and shows clearly smaller ε_{app} in this region. The average ^{15}N isotope fractionation has been included for comparison with other studies. The same shape of symbols as in Figure 40 has been used to identify the sampling site.

7.3 Data interpretation

The results obtained in this work [*Röckmann et al.*, 2001] and other published data have been compiled and re-evaluated (Table 12). Apparent fractionation constants were recalculated whenever they were originally derived from plots of δ vs ln *y* rather than ln(1+δ) vs ln *y*. η_{app} and ψ_{app} have been calculated from linear regression of ln(1+$^2\delta^{15}$N) vs ln(1+$^1\delta^{15}$N) and ln(1+δ^{15}N) vs ln(1+δ^{18}O), respectively, instead of the ratio $\varepsilon_{2,app}/\varepsilon_{1,app}$ and $^{15}\varepsilon_{app}/^{18}\varepsilon_{app}$. This gives a more precise estimate of the actual η_{app} and ψ_{app} value, because otherwise errors associated with ln *y* are introduced.

The data have been split into lower stratospheric values with –ln $y < 0.6$ and middle stratospheric values with –ln $y > 0.6$ (corresponding to N_2O mixing ratios of about 170 nmol/mol). These categories are based on the discontinuity in the Rayleigh plots of the mass-spectrometric data of the present work and from [*Toyoda et al.*, 2001b]. The maximum sampling altitude was 35 km [*Griffith et al.*, 2000; *Toyoda et al.*, 2001b].

The decrease of ε_{app} in the lower stratosphere noted above is clearly present in all data-sets. This effect is mainly due to effects of mixing and diffusion as noted earlier [*Rahn et al.*, 1998] and discussed in section 7.1. However, η_{app} and ψ_{app} also show significant differences between middle

Table 12: Intercomparison of apparent fractionation constants and values of η_{app} and ψ_{app} derived from data presented in this work and a re-evaluation of literature data. Results are mostly from mid to high northern latitudes (33–68°N) except for those obtained at 15°N in this work.

	$^{15}\varepsilon_{app}$/‰	$^{15}\varepsilon_{1,app}$/‰	$^{15}\varepsilon_{2,app}$/‰	$^{18}\varepsilon_{app}$/‰	η_{app}	ψ_{app}
"lower stratosphere" (–ln $y < 0.6$)						
Kim & Craig [1993]	–24±8	—	—	–22±12	—	0.98±0.20
Rahn & Wahlen [1997]	–13.8±0.7	—	—	–12.9±1.7	—	1.01±0.09
Yoshida & Toyoda [2000]	–19.4±0.5	–11.6±1.7	–26.7±1.3	–16.2±0.9	2.1±0.4	1.19±0.05
Toyoda *et al.* [2001]	–15.9±1.1	–8.8±1.4	–22.9±1.2	–11.5±1.8	2.2±0.4	1.26±0.15
this work	–16.8±0.8	–12.7±1.2	–20.9±0.7	–13.8±1.0	1.5±0.1	1.17±0.05
"middle stratosphere" (–ln $y > 0.6$)						
Rahn & Wahlen [1997]	–21.7‡	—	—	–13.5‡	—	1.61‡
Griffith *et al.* [2000]	–42.3±10	–27.3±14	–57.1±10	–42.6±29	2.1±1.1†	1.0±0.7†
Toyoda *et al.* [2001]	–28.6±0.6	–15.5±0.4	–40.9±1.3	–24.6±0.6	2.6±0.1	1.16±0.02
this work	–23.2±0.8	–15.5±0.4	–30.5±1.5	–20.0±0.6	2.0±0.1	1.16±0.03

† calculated from the ratio of fractionation constants; errors of η and ψ may be too high because errors of the fractionation constants are correlated

‡ one sample only

and lower stratospheric altitudes. Whereas the present study finds η_{app} values of 2.0±0.1/1.5±0.1 for middle/lower stratosphere, respectively, values of 2.6±0.1/2.2±0.4 can be derived from the work of Toyoda *et al.* [2001b]. The dependence of η_{app} on altitude cannot be explained by transport effects since the change of η_{app} associated with changes of photolysis rates and K_z is only small (section 7.1.3). Therefore, a change in photochemical parameters must be the cause. Such a change may also account for the differences between the results from the two studies: With one exception, our middle stratospheric samples were obtained at 68°N in winter/early spring, coinciding with maximum O_3 column densities. In contrast, the samples from Toyoda *et al.* were obtained at 39°N in late spring. Since $O(^1D)$ is produced by O_3 photolysis, we may expect a larger contribution of the $O(^1D) + N_2O$ sink in the high-latitude samples. This qualitative interpretation is supported by simulations with a 2D stratospheric chemistry and transport model (Figure 42).

Figure 43 shows simulated η values when the relative contribution of $N_2O + O(^1D)$ changes, assuming a negligible influence of wavelength and temperature variations on η (see below). The range covered by η extends from 0.25 to 2.4, which should render it a sensitive diagnostic to es-

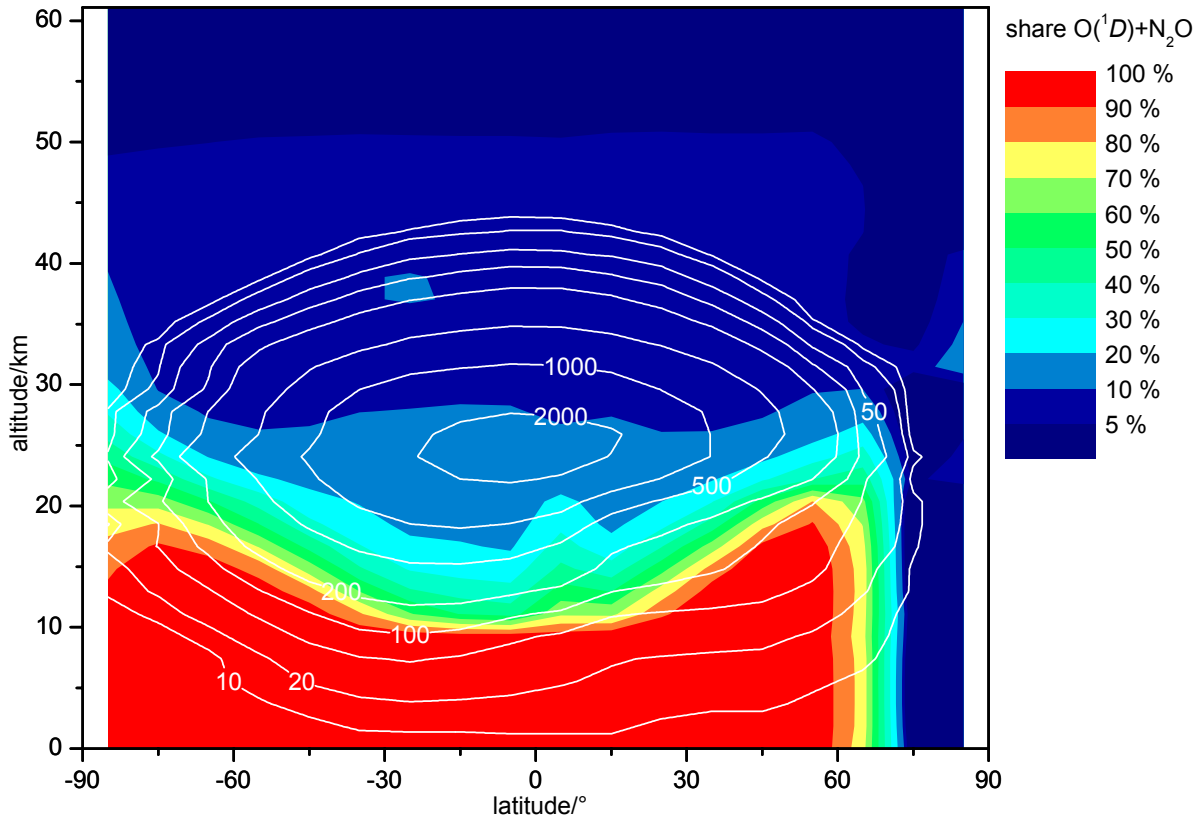

Figure 42: Results from 2D model runs for March 1999. The coloured contours show the relative contribution of the $O(^1D)$ sink to total N_2O loss (instantaneous rates). White contour lines indicate the total N_2O loss rate (cm^{-3} s^{-1}). The share of the $O(^1D)$ sink is larger at lower altitudes and higher altitudes. However, the largest total loss is at altitudes where its contribution is only 10 to 20 %.

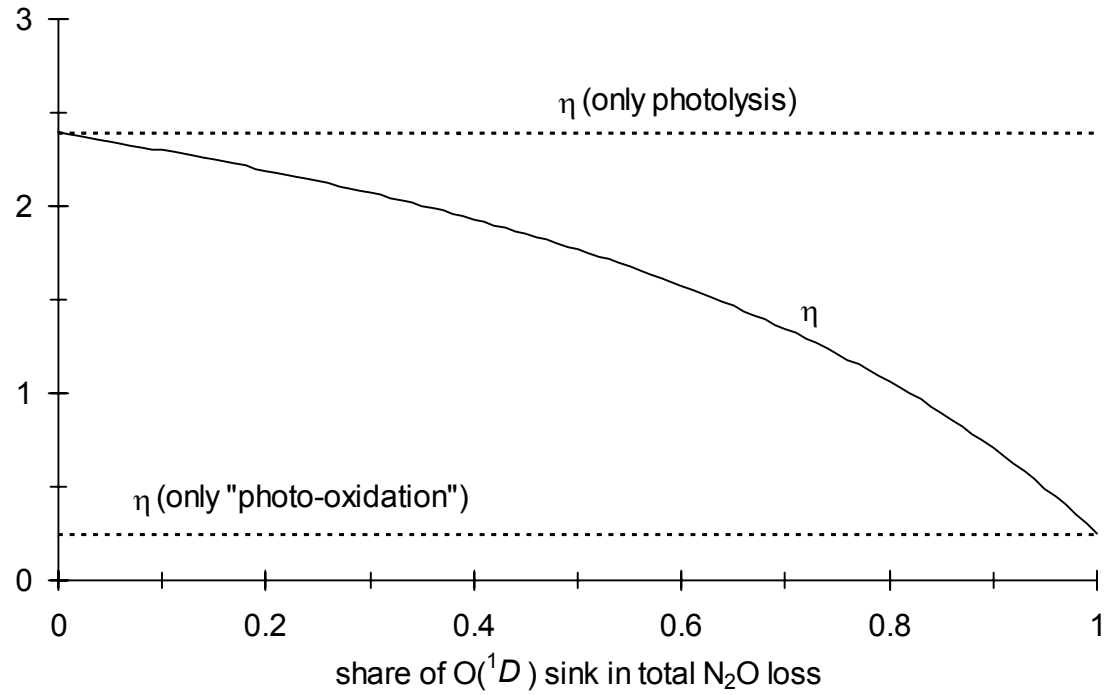

Figure 43: Simulation of $\eta = \varepsilon_2/\varepsilon_1$ for concurrent photolysis and photooxidation. Values for η("photooxidation") (chapter 3) and for η(photolysis) from UV broadband photolysis with an Sb lamp at room temperature (chapter 4) were used to derive the relationship shown here.

timate the influence of the $O(^1D)$ sink. Taking the average of the mass-spectrometric determinations of middle and lower stratospheric η_{app} values (2.3 and 1.85), we would expect a contribution of the $O(^1D)$ sink of ≈10 % for the middle stratosphere and ≈ 40 % for the lower stratosphere. The former value is in agreement with the integrated value for the total stratosphere (R1, p. 5).

Similar simulations as for η can be made for ψ. The experimental data give ψ(only "photooxidation") = 0.45 and ψ(only photolysis) = 1.10. With the same reservations as for η, atmospheric ψ values are therefore expected to vary from 0.45 to 1.10. Hence, ψ is probably not as sensitive a diagnostic as η to estimate the relative contribution of $N_2O + O(^1D)$ and N_2O photolysis to the overall N_2O sink, since the spread between η(only "photooxidation") = 0.25 and η(only "photolysis") = 2.48 is much larger. This is reflected by the stratospheric measurements which do not show any significant change of ψ with altitude in the data-sets of this work and Toyoda *et al.* [2001b].

Figure 44 shows the wavelength-dependence of η and ψ. Variations over the atmospherically most important region between 195 and 205 nm [*Minschwaner et al.*, 1993] are not very strong and much smaller than the influence which can be expected due to varying contribution of the $O(^1D)$ sink, confirmed by η values of 2.37/2.40/2.65 at 20/40/80 km calculated from the integration

over the entire wavelength spectrum of actinic flux (Table 11). The fractionation constants also show little variability between 20 and 40 km altitude, and even if some additional variation is introduced by changes of solar zenith angle the influence of wavelength changes on ε is likely to be small.

With respect to the differences in η_{app} between 68°N/winter and 39°N/late spring, the wavelength dependence of η works in the opposite direction than the contribution of the $O(^1D)$ sink: At low solar zenith angles and high O_3 column densities, solar light flux has to travel through a larger O_3 column which diminishes mainly the long wavelengths of the stratospheric UV "window". Thus, the effective photolysis wavelength will decrease and the η will increase. However, the expected variation is much smaller than what is expected from different contributions of $O(^1D)$.

From the data on the temperature dependence of N_2O photolysis (Figure 24), we expect decreasing isotope fractionation with increasing altitude, since stratospheric temperatures are lowest at the tropopause and increase monotonously with height. This trend is opposite to the changes seen in the lower and middle stratospheric samples confirming the overwhelming influence of transport on the differences in ε_{app} between these two altitude regions. Our lower stratospheric data from polar and tropical latitudes are not distinguishable (Figure 41), but the latitude data from Toyoda *et al.* [*Toyoda et al.*, 2001b] indicate larger values of $|\varepsilon_{app}|$. Temperature cannot ac-

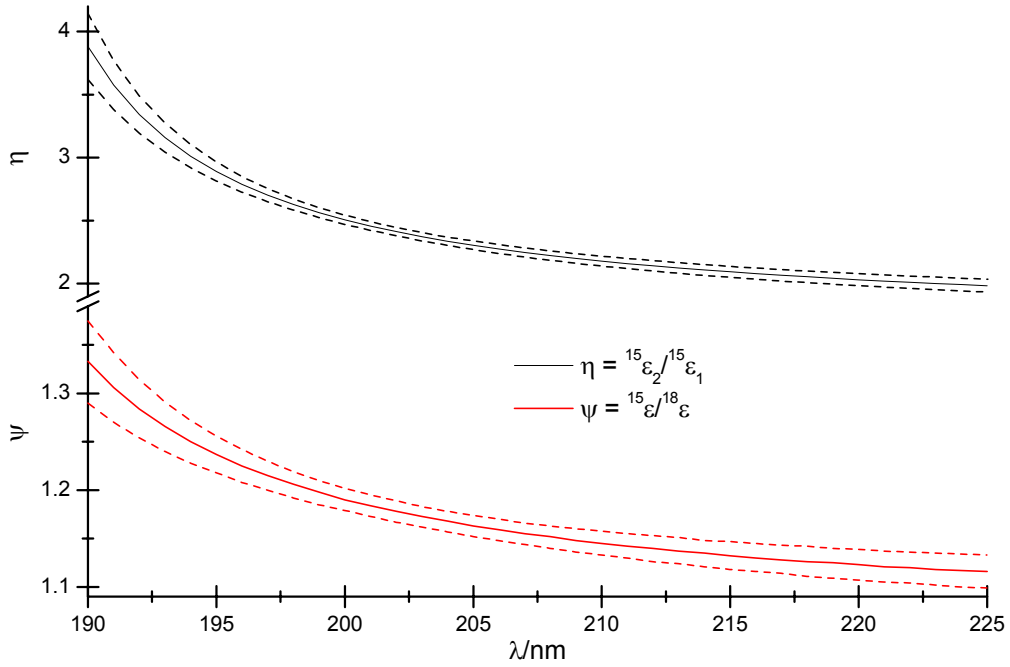

Figure 44: Influence of wavelength on η and ψ in N_2O photolysis derived from the linear fits of ε(λ) (Table 10) for room temperature. The dashed lines represent 2σ errors.

count for this pattern since it increases only little from the tropics to the poles at these altitudes. Fractionation constants should therefore rather decrease monotonously towards the poles. Again, differences in transport at different times of the year and different sampling locations are more likely to account for the variation of ε_{app}.

If temperature was the only parameter of influence, not only the fractionation constants themselves, but also the ratio of fractionation constants at the central to terminal nitrogen sites, $\eta = {}^{15}\varepsilon_2/{}^{15}\varepsilon_1$, should decrease along the vertical stratospheric temperature gradient (Figure 45). However, these temperature effects are only small and do not help to explain the lower η values observed in the lower stratosphere, but they are nevertheless essential ingredients for models of atmospheric isotope chemistry. Very high precision isotope ratio measurements would be required to detect the influence of temperature on ψ. For the moment a satisfying agreement between stratospheric ψ_{app} values and laboratory measurements of ψ can be noted which confirms the adequate simulation of actinic flux by the broadband photolysis lamp used to establish the temperature dependence of ε.

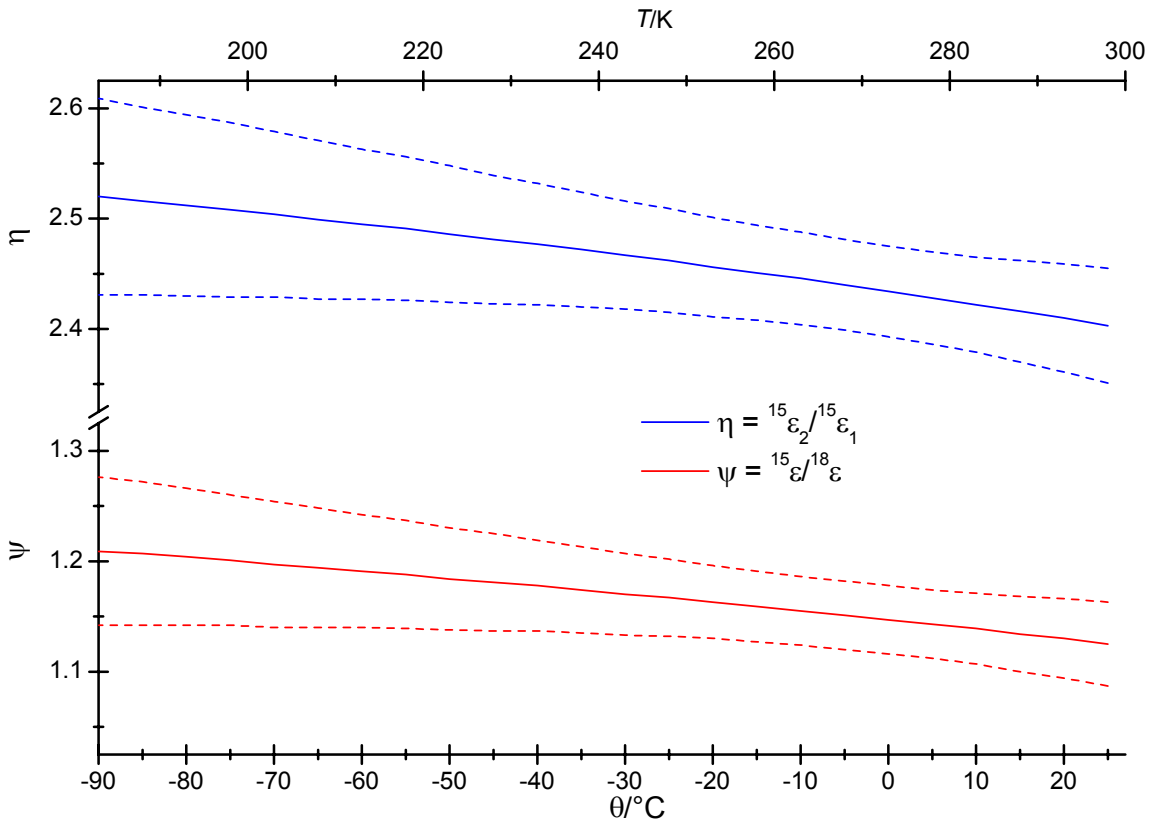

Figure 45: Influence of temperature on ratios of fractionation constants derived from the linear fit to the data obtained by photolysis with the antimony lamp. Both η and ψ decrease with increasing temperature, with a slightly stronger relative change for ψ than for η. The dashed lines represent 1σ confidence intervals.

Finally, it was investigated to what degree a 2D chemical transport model reflects the stratospheric data using the laboratory data as input [*Kaiser et al.*, 2001]. Following Johnson *et al.* [2001] we assume a temperature of 233 K as representative for the region of stratospheric photolysis. Work by Minschwaner *et al.* [1993] indicates that the photolysis rates are largest for 195 to 205 nm. From the photolysis rate spectra in Figure 30, we assume a half-photolysis wavelength of 202 nm. With the best fit to the wavelength dependence of ε (Table 10) and assuming the same relative temperature dependence as established for the broadband photolysis experiments (Figure 23), we adopt values of $^{15}\varepsilon_2 = -63.4$ ‰, $^{15}\varepsilon_1 = -25.4$ ‰ and $^{18}\varepsilon = -36.6$ ‰ for photolysis and the temperature-independent data for fractionation by $N_2O + O(^1D)$ (chapter 3).

The results of this modelling exercise are shown in Table 13. The model reproduces the general trend of lower fractionation constants in the lower stratosphere and is actually in quite good agreement with the stratospheric data from this work. This may be surprising at first sight, given the crude assumptions of a single temperature and wavelength for the parameterisation of N_2O photolysis, but is actually a confirmation of the important role of transport for the values of apparent fractionation constants in the atmosphere. While ψ values from the model agree well with the stratospheric data, η is clearly too high. Although higher η values have been reported [*Toyoda et al.*, 2001b], the reason for the *increase* of η in the model results for the lower stratosphere as compared to the middle stratospheric results is not clear. We note that the modelled η is actually even higher than the input value from photolysis. This may point to numerical problems in the model.

Table 13: N_2O fractionation constants in photolysis, $N_2O+O(^1D)$, stratosphere and a 2D model.

	laboratory measurements		stratospheric data		Mainz 2D model	
	photolysis	$N_2O+O(^1D)$	lower stratosphere	middle stratosphere	lower stratosphere	middle stratosphere
$^{15}\varepsilon$/‰	–44.4	–5.5	–16.8	–23.2	–16.8	–27.1
$^{15}\varepsilon_1$/‰	–25.4	–8.8	–12.7	–15.5	–9.1	–15.7
$^{15}\varepsilon_2$/‰	–63.4	–2.2	–20.9	–30.5	–24.6	–38.5
$^{18}\varepsilon$/‰	–36.6	–12.2	–13.8	–20.0	–14.8	–22.8
$\eta = {}^{15}\varepsilon_2/{}^{15}\varepsilon_1$	2.49	0.25	1.50	2.02	2.70	2.46
$\psi = {}^{15}\varepsilon/{}^{18}\varepsilon$	1.23	0.45	1.17	1.16	1.15	1.21

8 N_2O in the troposphere

The variability of atmospheric N_2O mixing ratios is very low (Figure 1) because of its long atmospheric lifetime (≈120 years). Variations in isotopic signatures are therefore expected to be likewise small over seasonal time scales. However, the imbalance between sources and sinks which accounts for the observed increase in the global N_2O burden (Table 1) is expected to cause changes in isotopic composition over a time frame of decades, because the global N_2O source is isotopically lighter than tropospheric N_2O (section 1.3). These long-term changes could be investigated by monitoring N_2O isotopes on a regular basis as done for CO_2 [*Trolier et al.*, 1996], but this is out of the scope of a 3-year doctoral thesis. We rather analysed samples of Antarctic firn air taken at various depth levels which allows reconstruction of past changes and the current atmospheric trend in N_2O isotope ratios by using a firn air transport model. The results of this approach will be presented in chapter 9.

In this chapter, we focus on the efforts which were made to improve analytical techniques of N_2O analysis in order to detect seasonal and spatial changes of N_2O isotopic composition at various sampling stations. All sample extraction and purification steps were made off-line, i.e. on vacuum manifolds which were not connected to the isotope ratio mass spectrometer. As opposed to the automatised on-line technique used for stratospheric and firn air samples (section 7.2.2), this requires large amounts of sample of the order of hundreds of dm^3 of air and standardised reproducible procedures in manual sample work-up. An unexpected interfering contamination was noticed in NO^+ fragment analysis (section 8.3.2) which made modifications of the vacuum manifold necessary. Despite all efforts, no clearly discernible temporal or spatial patterns in the tropospheric N_2O isotope signature were detected.

8.1 Experimental methods

8.1.1 Air sampling

Whole air samples were obtained at the locations in Table 14 with a scheduled sampling interval of one to three weeks. A modified diving compressor (*RIX Industries*) was used to fill 5 or 10 L aluminium high pressure cylinders to up to 120 bar [*Mak and Brenninkmeijer*, 1994]. Air was drawn through PFA tubing (outer diameter: $\frac{1}{2}$") connected to a drying unit filled with *Drierite* ($CaSO_4$, with $CoCl_2$ as moistness indicator) at the inlet of the air compressor. The air cylinders were shipped regularly to our laboratory in Mainz.

Table 14: Sampling locations for tropospheric N_2O samples

Station	Country	Location	Altitude	Operating agency
Spitsbergen	Norway	79°N 12°W	474 m	Norwegian Institute for Air Research
Kollumerwaard	Netherlands	53°N 6°E	0 m	University of Groningen
Mainz	Germany	50°N 8°E	128 m	MPI for Chemistry
Schauinsland	Germany	48°N 8°E	1205 m	Umweltbundesamt
Mt. Sonnblick	Austria	47°N 13°E	3106 m	Institute for Meteorology, Salzburg
Izaña, Tenerife	Spain	28°N 16°W	2370 m	Spanish Meteorological Service

8.1.2 Extraction of N_2O from bulk air

An off-line preparation technique was used to extract N_2O quantitatively from bulk air samples in order to measure the isotope ratios afterwards. A CO extraction system established in our laboratory served this purpose [*Brenninkmeijer*, 1993; *Brenninkmeijer et al.*, 2001]. It delivered not only CO-derived CO_2, but also all other gases in air with sufficiently low vapour pressures at the boiling point of liquid nitrogen (-196 °C). This "trace gas cocktail" consisted mainly of CO_2, H_2O and N_2O, but included also – among others – non-methane hydrocarbons (NMHCs), NO_2, chlorofluorocarbons (CFCs) and hydrofluorocarbons (HFCs). Some of these gases yield isobaric interferences during the isotopic analysis of N_2O and consequently had to be removed in two further purification steps using NaOH to remove CO_2 and a preparatory gas chromatographic separation system.

The extraction line comprised two highly efficient, Russian Doll-type cooling traps (RDT) [*Brenninkmeijer*, 1991] prior to the CO oxidation step which remove the condensable trace gases from the air stream at a flow rate of usually 5 ℓ/min. After the designated sample volume had been processed, the first RDT was isolated from the system and evacuated while it was still frozen. This RDT already retained more than 99.9 % of the CO_2 and 99.7 % of the N_2O [*Röckmann*, 1998], so that the contents of the second trap could be ignored. Although the surface area of the glass fibre thimbles inside the RDT was quite large, the contents of the first trap could be transferred quantitatively to a U-shaped glass tube by pumping on the first trap for 35 min. From the U-shaped trap the sample was frozen onto *Ascarite* (NaOH-coated silica, *Sigma*, 20-30 mesh).

8.1.3 Separation from CO_2 and H_2O

The sample flask containing *Ascarite* consisted of a lower body and an upper valve part (*Louwers Hapert* high vacuum stopcock). Both parts were assembled using a *Viton* seal and a *Rotulex* bracket. This design facilitated easy filling and removal of *Ascarite* from the bottle.

Each flask was supplied with 2.5 to 3.5 g of *Ascarite*. Before use, it was evacuated until the pressure did not decrease any more due to water desorbing from to the alkaline surface

(0.1 mbar). It was found that the reaction of CO_2 with NaOH proceeded faster when there was still some water present, i.e. when the flask was not evacuated any further. Usually > 99.99 % of the CO_2 reacted within minutes as monitored by the pressure change in the flask. However, sometimes it was necessary to heat the flask with a heat gun (to not more than 100 °C) to initiate the reaction, since, otherwise, it could take days to start (probably because the *Ascarite* was too dry). As soon as the reaction was initiated, the production of H_2O accelerated it by dissolving CO_2 and NaOH in the aqueous phase. After 24 h on *Ascarite*, the N_2O sample contained less than 0.1 % CO_2 which means that it was removed with more than 99.9999 % efficiency.

In order to remove water (stemming mainly from the reaction with *Ascarite*, not from the trace gas cocktail) from the sample, it was cryogenically distilled into another flask of similar size containing P_2O_5 as drying agent at its bottom. This method was preferred to trapping the H_2O by freezing because of the solubility of N_2O in water which might have caused the enclosure of some of the N_2O in the water ice formed. The dried gas was transferred afterwards to a smaller sample tube.

8.1.4 Gas chromatographic purification

After removal of CO_2 there were still other gases present which interfere with isotopic analyses of N_2O and the NO^+ fragment. Especially air samples from polluted stations contained significant amounts of hydrocarbons which can pose problems with the analysis of the N_2O molecule or NO^+ fragment ion. Propane (m/z 44, 45, 46 from $C_3H_8^+$ isotopologues), ethanol (m/z 46) or other hydrocarbons (m/z 44, 45, 46 from $C_3H_8^+$ fragments) might interfere with bulk N_2O analysis. Ethane (m/z 30, 31 from $C_2H_6^+$ isotopologues), fluorocarbons (m/z 31 from CF^+) or other hydrocarbons (m/z 30, 31 from $C_2H_6^+$ fragments) can interfere with NO^+ fragment analysis.

The sample with the highest amount of contaminating gases was from Kollumerwaard (KOL-025). More than 5 ppm of condensable gases other than N_2O, H_2O and CO_2 must have been present in the original bulk air sample to account for the amount of gas present after the CO_2/H_2O removal step. A significant amount of it was NO_2 as suggested by the intense brown colour of the gas. This indicated that NO_2 was not removed completely by basic *Ascarite*. If time had been sufficient, NO_2 would disproportionate into NO_2^- and NO_3^- as other tests with *Ascarite* had shown. Most other samples contained impurities between 1 and 2 % of the amount of N_2O.

A GC/MS-system was used to remove any possibly remaining CO_2 and other impurities (Figure 46). The system was initially made of glass, but changed later to stainless steel (with *Nupro* K series valves and *Swagelok* fittings), except for the Russian doll trap, the P_2O_5 flask and a calibrated small volume manometer ("microvolume", denoted P2 in Figure 46). This reduced the number of *Viton* o-rings which were a source of m/z 31 interference (section 8.3.2).

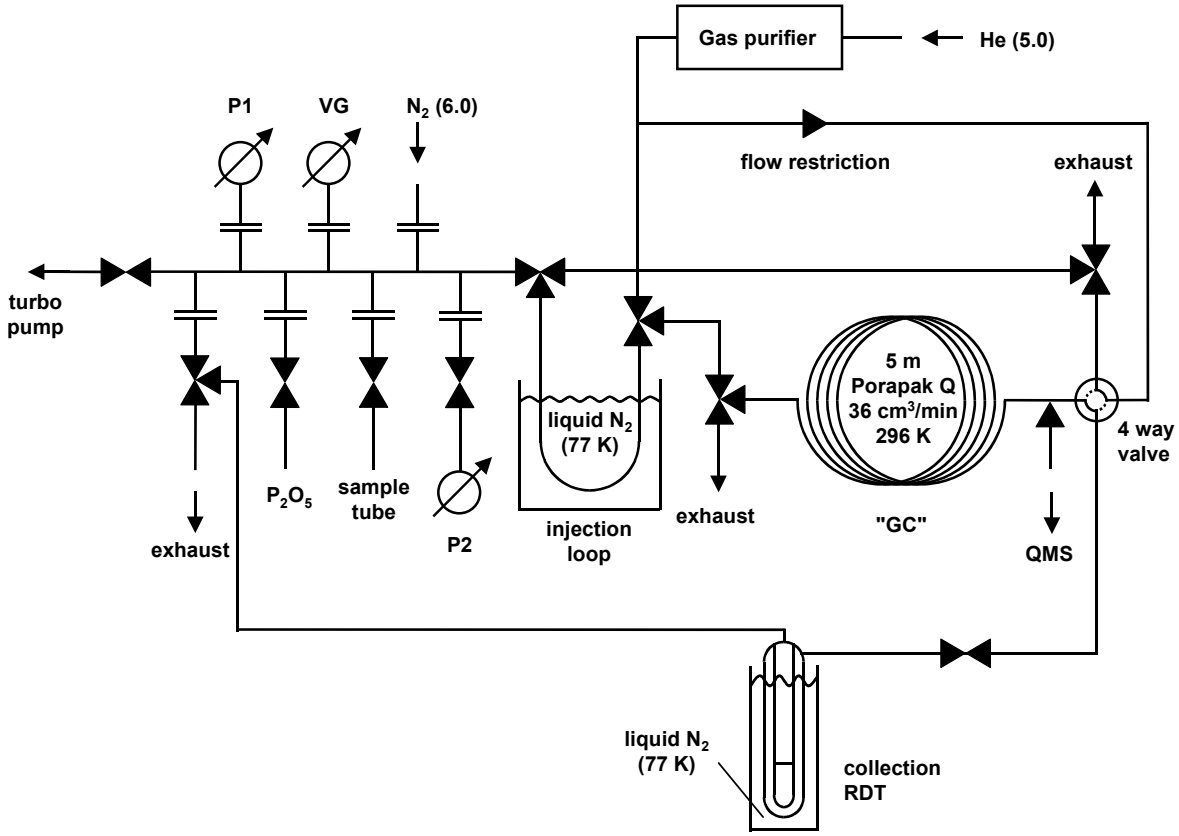

Figure 46: Gas chromatographic purification system for N_2O. P1, P2: piezoresistive manometers (*Institute of Geological & Nuclear Sciences*, New Zealand); VG: vacuum gauge (*Hastings*); QMS: quadrupole mass spectrometer (*Balzers*).

The amount of gas was determined prior to and after gas chromatographic separation in the microvolume with a piezoresistive sensor. The temperature was recorded at the time of pressure measurement in the microvolume. Knowing the amount of air that has been subject to the trace gas extraction process, we thus obtain an independent manometric estimate of the N_2O mixing ratio of the air analysed.

The samples are frozen into an injection loop (35 cm, $\frac{1}{8}$" stainless steel) and passed over the GC column (Porapak Q, 5 m $\frac{1}{8}$" stainless steel, *Alltech*) using a stream of purified helium (*Messer-Griesheim*, grade 5.0; *Supelco* High Capacity Carrier Gas Purifier). The gas flow is split after the GC and a minute portion is fed via a $\frac{1}{16}$" stainless steel capillary (1 m) into a quadrupole MS (*Balzers* QMS 200). Five to 20 s before the arrival of the N_2O peak at ≈7.5 min, the 4 way valve is switched over to the collection trap. As soon as N_2O is not detected any more on the MS, the 4 way valve is switched back. This procedure ensures that N_2O is collected quantitatively from the gas stream without alteration of its isotopic ratio and without contamination by other gases eluting before or after N_2O. The timing of the trapping procedure is crucial since CO_2 elutes about 1.5 min before N_2O and propane elutes 4.0 min after N_2O.

After trapping the purified N_2O, the collection trap is isolated from the GC and a backflush of the column is initiated. Helium remaining in the collection trap is pumped off. The trap is thawed, and its contents is transferred to the P_2O_5 tube for drying, then quantified manometrically in the microvolume (P2) and transferred back to the sample tube.

Recovery in blank tests with pure N_2O was (99.33±0.04) % with no detectable isotope fractionation. Tests with the collection trap only gave recovery rates close to 100 ‰. Closing the split valve did not increase the recovery rate which indicates that the remainder of the N_2O was presumably adsorbed onto the column and elutes only later. To avoid alterations of the isotopic composition by memory effects, only samples with similar δ values were measured in succession.

8.1.5 Mass spectrometric analysis

Analyses of $\delta^{15}N$ and $\delta^{18}O$ values as well as NO^+ fragment analysis were carried out as described in sections 2.5 and 2.6. $^{31}\delta$ was measured on a *Micromass* Prism II mass spectrometer with adjustable Faraday cups. Atmospheric samples were analysed with the cold-finger (microvolume) inlets of the mass spectrometers. Corrections for CO_2 interference in N_2O analysis and CHF_3 in NO^+ analysis were applied as describe in section 2.8 above and section 8.3.3 below.

On some occasions, $\delta^{17}O$ of atmospheric N_2O samples was analysed by conversion to CO_2 and N_2 (section 2.3.1) and subsequent reduction of CO_2 to O_2 with F_2/He [*Brenninkmeijer and Röckmann*, 1998]. The results of the $\delta^{17}O$ analyses are shown in section 10.1.

8.1.6 Sample size

The mixing ratio of N_2O in air samples (μ) was determined by gas chromatography with electron capture detection (ECD). The non-linearity of the detector was accounted for by fitting the response function to a dilution series. μ was about 315 nmol/mol for the year 1999 which represented the majority of the tropospheric air samples analysed. The average amount of processed air was 400 ℓ (STP) within a range of 300 to 1060 dm^3, corresponding to 139 μℓ (SATP) of N_2O (5.6 μmol). In the following sections, all sample amounts given in ℓ or μℓ refer to SATP.

8.2 Blank tests for $\delta^{15}N$ and $\delta^{18}O$ measurements

Before any atmospheric samples were run, several tests to check the efficiency of the analysis and purification system were performed.

8.2.1 Zero enrichment measurement of standard gas using bellows and cold finger

Working standard gas was admitted to the standard and sample side bellows of the mass spectrometer and the isotope ratios were measured. The standard errors of the results shown in

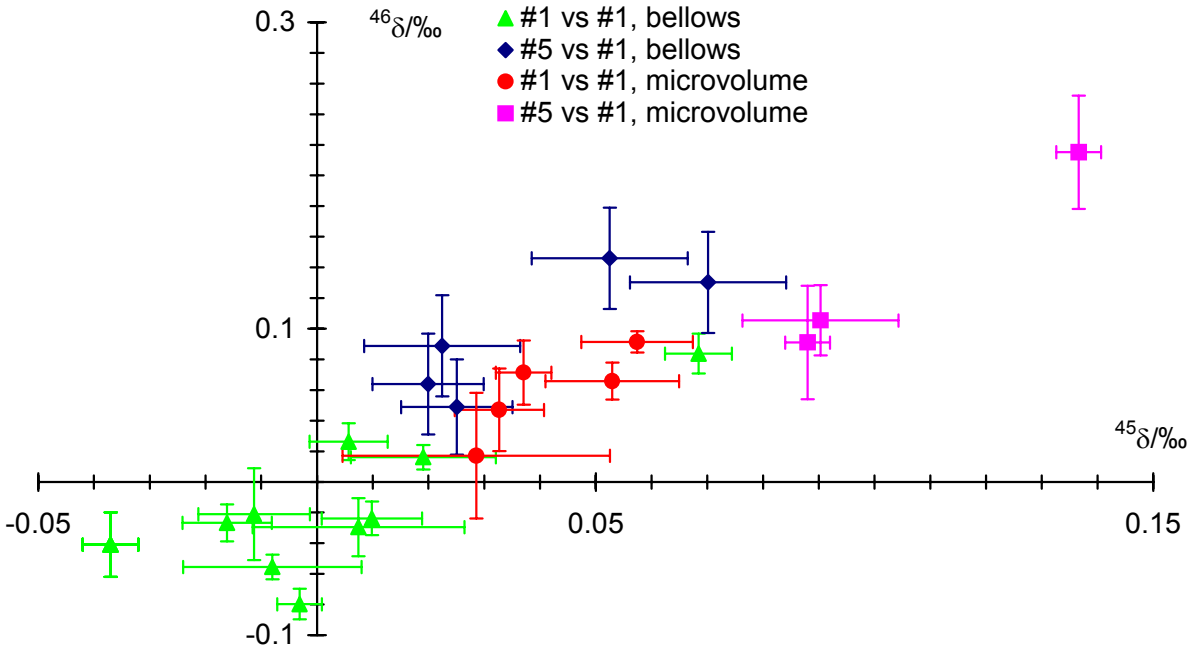

Figure 47: Zero enrichment measurement of N_2O working standard gas

	$^{45}\delta$/‰	$^{46}\delta$/‰	number of analyses (*n*)
#1 vs #1, bellows	0.00±0.02	–0.01±0.02	12
#5 vs #1, bellows	0.04±0.02	0.10±0.04	5
#1 vs #1, microvolume	0.05±0.01	0.07±0.03	5
#5 vs #1, microvolume	0.11±0.03	0.14±0.07	3

Figure 47 (standard #1 vs standard #1, bellows) represent the external precision of the mass spectrometric analysis and were 0.02 ‰ for both $^{45}\delta$ and $^{46}\delta$ and $n = 12$ measurements. A similar analysis of a slightly fractionated standard gas sample (standard #5 vs standard #1, bellows) gives similar results with standard deviations of 0.02 ‰ and 0.04 ‰ for $n = 5$.

The same set of measurements was performed for the microvolume inlet of the isotope mass spectrometer. Aliquots of 300 µℓ or less were admitted to the mass spectrometer. The standard deviations were similar to the measurement with bellows. However, the mean values of $^{45}\delta$ and $^{46}\delta$ have increased in all cases: The differences between microvolume and bellow analyses were (0.04±0.03) ‰ for standard #1 vs #1 and (0.07±0.05) ‰ for standard #5 vs #1 in $^{45}\delta$ whereas the respective changes in $^{46}\delta$ were (0.07±0.05) ‰ and (0.04±0.11) ‰. This seems to indicate some fractionation of the sample when measuring with the microvolume.

8.2.2 Freezing standard gas onto *Ascarite* and extraction

About 130 µℓ of pure N_2O working standard gas were frozen into a pre-evacuated *Ascarite* bottle and the same extraction procedure was carried out as for atmospheric air samples. However, the gas was not passed over the GC. This was a check whether N_2O isotope ratios are affected by freezing onto *Ascarite*. Since the sample size was made similar to the atmospheric sam-

ples, the same corrections for CO_2 contamination had to be applied (section 2.8). The final results from eight experiments gave $^{45}\delta = (0.05 \pm 0.03)$ ‰ and $^{46}\delta = (0.11 \pm 0.03)$ ‰. The average yield of N_2O was (99.9±0.5) %. The observed enrichments are not significantly larger for $^{45}\delta$ and $^{46}\delta$ than those for the zero enrichment measurement with the microvolume.

8.2.3 Gas chromatography of pure N_2O standard gas

In two series of experiments relatively large samples of N_2O standard gas that could be measured with the bellows of the mass spectrometer were measured repeatedly on the mass spectrometer, interspersed with GC purification runs. Each time the samples were frozen back from the bellow (which took about 5 min and which was stopped when the signal on mass 44 reached 1 mV). Sometimes GC purification steps were interspersed with the MS measurements to check whether the GC runs fractionated the samples (Figure 48). Obviously, the δ values increase from analysis to analysis by about 0.05 ‰ in $^{45}\delta$ and by about 0.1 ‰ in $^{46}\delta$. This is only due to fractionation by MS analysis/back-freezing of the sample since it does not matter significantly whether there are GC runs interspersed with the MS analyses or not.

Figure 49 shows the same data as Figure 48, but now $^{46}\delta$ is plotted against $^{45}\delta$ to show the mass dependence of the fractionation associated with repeated MS analysis/freeze back cycles. The similarity of both experimental series is apparent, too.

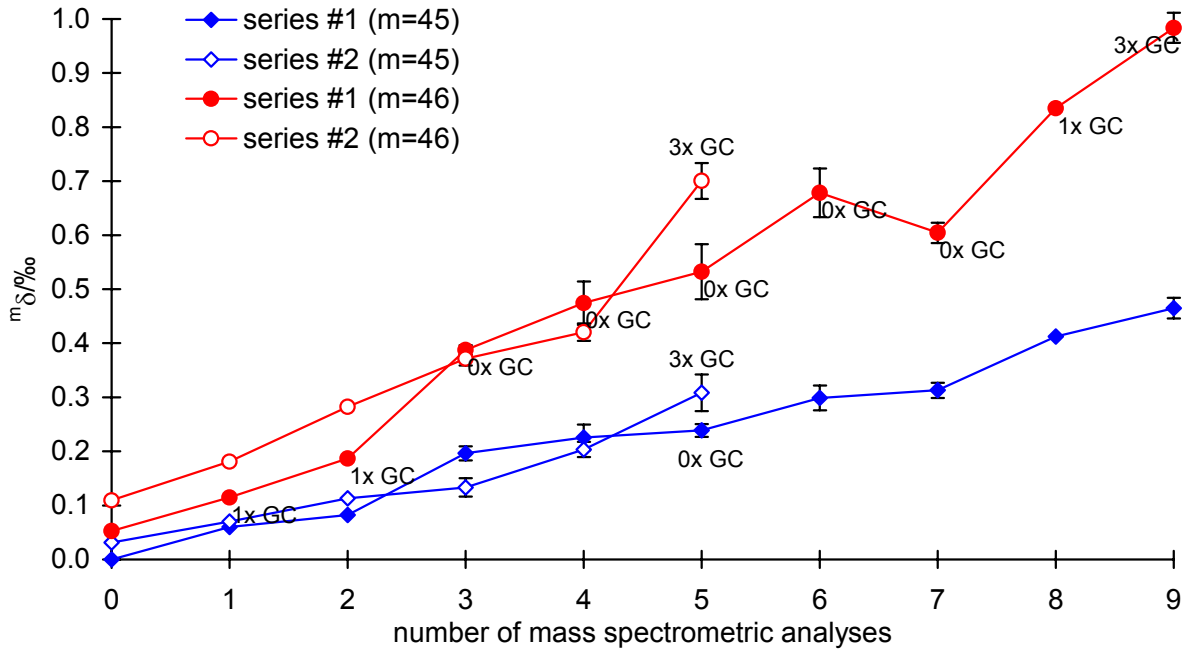

Figure 48: Repeated MS analyses and GC purification runs of two N_2O standard gas samples. Samples were treated in the same way in series #1 and #2 except for MS analysis number 5 where the N_2O sample underwent 3 GC runs in series #2, but none in series #1. The labels indicate the number of GC runs that were interspersed with the MS analyses, but for clarity only $^{46}\delta$ of series #1 is labelled at each point.

With this fractionation it became clear that any sample analysis should not involve too many repeated MS analyses. However, if necessary, it should not be a problem to run a sample several times over the GC in order to remove impurities that one could not get rid of in a single run.

Next, 12 small samples of N_2O working standard gas (≈130 µℓ) were run over the GC to check whether the GC purification would introduce any artefacts for smaller atmospheric samples. Again, $^{45}\delta$ and $^{46}\delta$ only show the expected enrichment due to microvolume use in the MS measurement, although the standard deviation is slightly higher in this case. Mean changes in $^{45}\delta$ are (0.04±0.04) ‰ and (0.08±0.07) ‰ in $^{46}\delta$. Both δ values are correlated (Figure 50), indicating a systematic fractionation.

8.2.4 Extraction of pure N_2O from N_2O + CO_2 mixtures with GC purification

About 130 µℓ of N_2O working standard gas and about 70 mℓ of CO_2 were frozen into a 120 mℓ valve flask containing 2.5 to 3.5 g of *Ascarite*. After CO_2 had reacted with NaOH, the flasks were processed alike the atmospheric samples, including gas chromatographic purification. The average yield of the *Ascarite* reaction step was (99.50±0.32) % ($n = 13$), that of the GC run was (98.9±0.2) % ($n = 13$). Hence, the overall yield was (98.5±0.4) % which is used later in order to estimate the N_2O concentration manometrically. On average, $^{45}\delta$ and $^{46}\delta$ values were altered by (–0.04±0.06) ‰ and (–0.08±0.08) ‰, respectively. Taken together with the results from sections

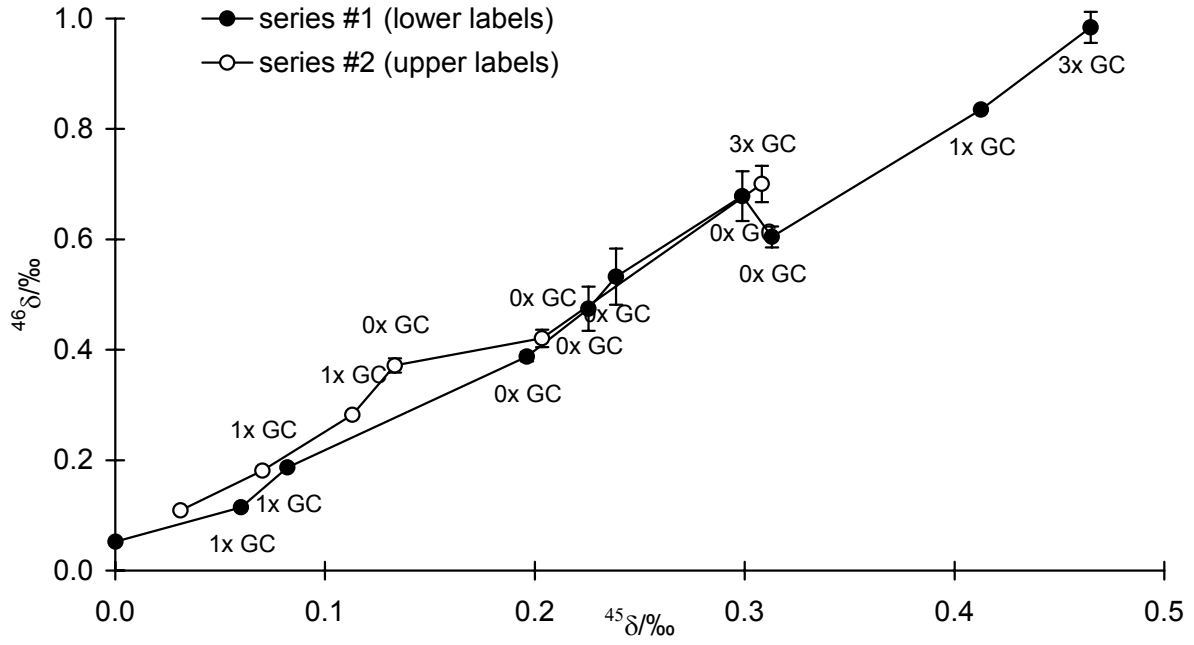

Figure 49: The same data as in Figure 48, but now $^{46}\delta$ plotted against $^{45}\delta$. The slope of about 2 indicates the mass dependence of the fractionation associated with repeated MS analysis/freeze back cycles.

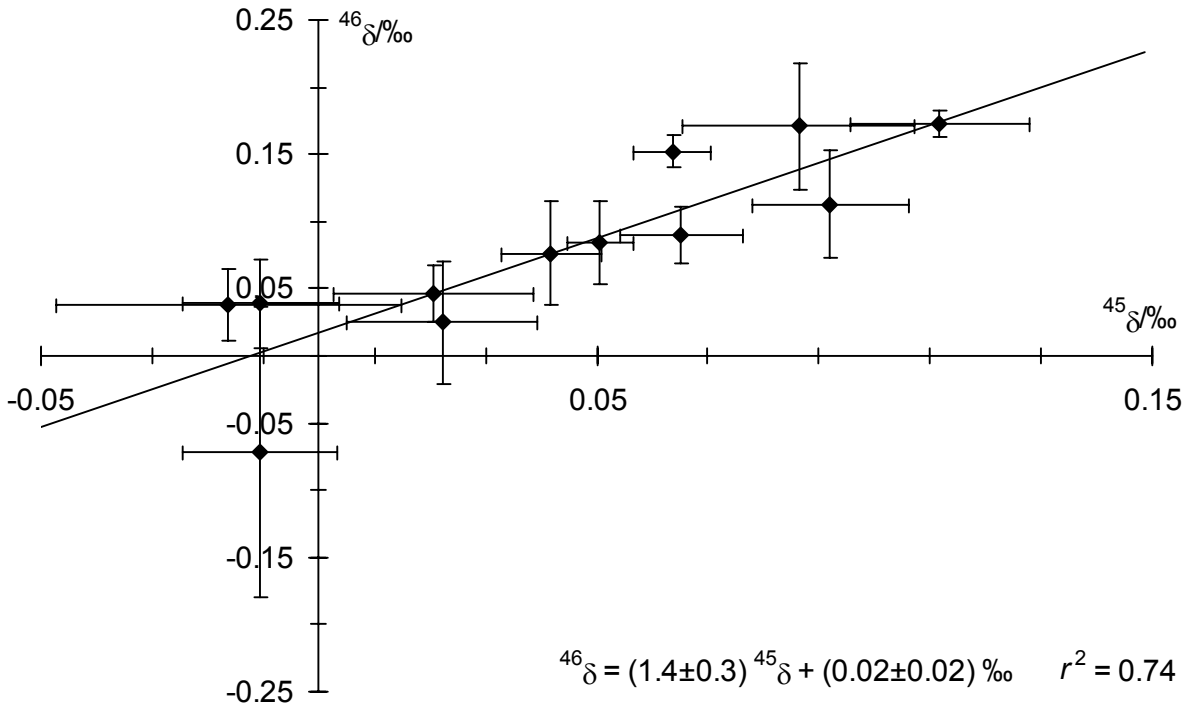

Figure 50: Correlation between $^{46}\delta$ and $^{45}\delta$ for analyses of standard gas passed over the GC. The slope does not correspond exactly to the expected one of ≈2 for a mass-dependent relationship. This may be either due to the small range of $^{46}\delta$ and $^{45}\delta$ or indicates vapour pressure/chromatographic effects that do not correlate with molecular mass, but depend on the intramolecular distribution of ^{15}N in N_2O [*Jancso and van Hook*, 1974].

8.2.1 to 8.2.3, this means that the presence of CO_2 caused a decrease of $^{45}\delta$ by about 0.09 ‰ and a decrease of $^{46}\delta$ by about 0.18 ‰. This may have to do with the additional production of H_2O by reaction of CO_2 with *Ascarite*. However, from mass balance calculations considering the solubility coefficient of about 25 mmol/ℓ/bar for N_2O in H_2O [*Weiss and Price*, 1980] and equilibrium isotope fractionation constants of $^{15}\varepsilon_{N_2O(g)/N_2O(aq)} = -0.75$ ‰ and $^{18}\varepsilon_{N_2O(g)/N_2O(aq)} = -1.06$ ‰ [*Inoue and Mook*, 1994] (all values at 25 °C), the resulting change in $\delta^{15}N$ and $\delta^{18}O$ should be less than 0.001 ‰. Furthermore, dissolved N_2O should be released again from H_2O after cryogenic distillation from the bottle with *Ascarite* to the P_2O_5 bottle (section 8.1.3). The minor isotopic fractionation in the CO_2 removal thus remains unexplained at the moment.

8.3 Mass spectrometry of NO^+ fragment ions

8.3.1 Zero enrichment measurements of $^{31}\delta$ values

Similar tests as for $\delta^{15}N$ and $\delta^{18}O$ analysis were performed in case of the NO^+ fragment of N_2O. Zero enrichment measurements (section 8.2.1) with the microvolume of the *Micromass*

Prism II mass spectrometer gave essentially unchanged mean $^{31}\delta$ values of (0.03±0.02) ‰ from a set of five analyses. However, problems appeared in early analyses of atmospheric samples (section 8.3.2) and further blank tests of the analytical system (section 8.3.4).

8.3.2 Contamination problems in $^{31}\delta$ analysis

Whereas initial analyses of atmospheric samples gave similar $^{45}\delta$ and $^{46}\delta$ values, the $^{31}\delta$ values varied by several ‰ absolutely. Furthermore, repetitive GC purification steps of the same sample revealed that $^{31}\delta$ generally decreased. However, the quadrupole mass spectrometer connected to the preparatory GC did not reveal any compounds that eluted before or after the N_2O peak. Varying the time frame during which gas was frozen out from the GC effluent showed that the contaminant must elute after N_2O. Upon close inspection of mass spectra of severely contaminated samples taken on the MAT 252 instrument peaks were found at m/z 69 and sometimes also at m/z 50 and 51 that did not exist in the reference gas spectrum (though this approach was often thwarted by an unidentified broad background at m/z 50 to m/z 52 in the MS). With the help of a mass spectral database (Wiley/NIST, 1990) trifluoromethane (CHF_3, Freon F-23) was identified as the most likely candidate for this kind of contamination (distinct peaks at m/z 31, 51 and 69 due to CF^+, CHF_2^+ and CF_3^+). Therefore tests of CHF_3 and other fluorine containing gaseous compounds were run on the GC. Retention times were 8.8 min for CHF_3, 2.5 min for CF_4, 14.0 min for CH_2F_2 and 14.8 min for CF_3Cl. The retention time of N_2O in the set-up as described above is about 8.0 min. For an amount of 130 µℓ (SATP) that is representative of a real atmospheric sample, we have to sample the effluent of the GC from 7.5 to 9.0 min which overlaps with the CHF_3 peak. Thus, CHF_3 is the contaminant responsible for the observed variation of $^{31}\delta$.

8.3.3 CHF_3 correction

In order to account for the CHF_3 contamination interfering masses were measured at m/z 51 and m/z 69, but the correction via m/z 69 is preferred because of an unidentified broad background at m/z 50 to m/z 52 in the MS. This correction can be derived along the lines of the CO_2 correction (section 2.8). One has to consider the measured ionisation efficiencies of $^{14}N^{16}O^+$ relative to $^{14}N_2{}^{16}O^+$ ($^{30}r = {}^{30}I/{}^{44}I \approx 0.32$) and of CHF_2^+/CF_3^+ to CF^+ ($^{51}r = {}^{51}I/{}^{31}I \approx 1.7$, $^{69}r = {}^{69}I/{}^{31}I \approx 2.9$). The exact approach is described here (see section 2.8 for an explanation of the symbols):

$$^{31}\delta = (1+{}^{31}\delta')\frac{1-\frac{{}^{31}u}{{}^{31}U'}}{1-\frac{{}^{31}v}{{}^{31}V'}}-1 \qquad (74)$$

which results with the same approximations as for the CO_2 correction in

$$
\begin{aligned}
{}^{31}\delta &= {}^{31}\delta' - \frac{{}^{46}R_{st}(N_2O)}{{}^{31}R_{s,st}(N_2O)}\frac{1}{{}^{30}r}\frac{1}{{}^{69}r}\left[(1+{}^{46}\delta' N_2O)\frac{{}^{69}u}{{}^{46}U'} - \frac{{}^{69}v}{{}^{46}V'}\right] \\
{}^{31}\delta &= {}^{31}\delta' - \frac{{}^{46}R_{st}(N_2O)}{{}^{31}R_{s,st}(N_2O)}\frac{1}{{}^{30}r}\frac{1}{{}^{69}r}\left[(1+{}^{46}\delta' N_2O)\frac{{}^{51}u}{{}^{46}U'} - \frac{{}^{51}v}{{}^{46}V'}\right]
\end{aligned}
\qquad (75)
$$

The expressions before the bracket term are denoted ${}^{69}C$ and ${}^{51}C$, the bracket terms ${}^{69}b$ and ${}^{51}b$, respectively. They amount to ${}^{69}C = 9.70$ ‰/% and ${}^{51}C = 5.70$ ‰/% which compares favourably to the results of a dilution series of CHF_3 in N_2O (Figure 51). The pertinent ratios ${}^{69}C/{}^{51}C$ are 1.703 (theory) and 1.665±0.003 (experiment).

8.3.4 Further blank tests and modifications to the analytical system

Checks of the ${}^{31}\delta$ integrity upon freezing pure N_2O on *Ascarite* (section 8.2.2) gave similar zero enrichments as for ${}^{45}\delta$ and ${}^{46}\delta$ analyses, but with a higher standard deviation: (0.10±0.33) ‰ ($n = 8$). Almost no correlation could be found between ${}^{45}\delta$ and ${}^{31}\delta$ ($r^2 = 0.12$). Furthermore, there was no correlation between measured values ${}^{31}\delta'$ and ${}^{69}b$ either, rendering the CHF_3 correction established above apparently useless. Possibly, there are other contaminants present in the analytical system that produce ions of m/z 31 (such as CF^+) and cause a greater variability of ${}^{31}\delta$. It was hoped that the gas chromatographic purification step would solve this problem.

However, after the GC purification step, the raw, uncorrected ${}^{31}\delta'$ values turned out to be significantly enriched relative to the standard gas and still displayed a higher standard deviation than the zero enrichment tests (section 8.3.1): ${}^{31}\delta' = (0.39\pm0.17)$ ‰ ($n = 12$). ${}^{31}\delta'$ was not correlated to ${}^{45}\delta$ (Figure 52). Moreover, ${}^{31}\delta'$ was not correlated to ${}^{69}b$, either. A tentative CHF_3 correc-

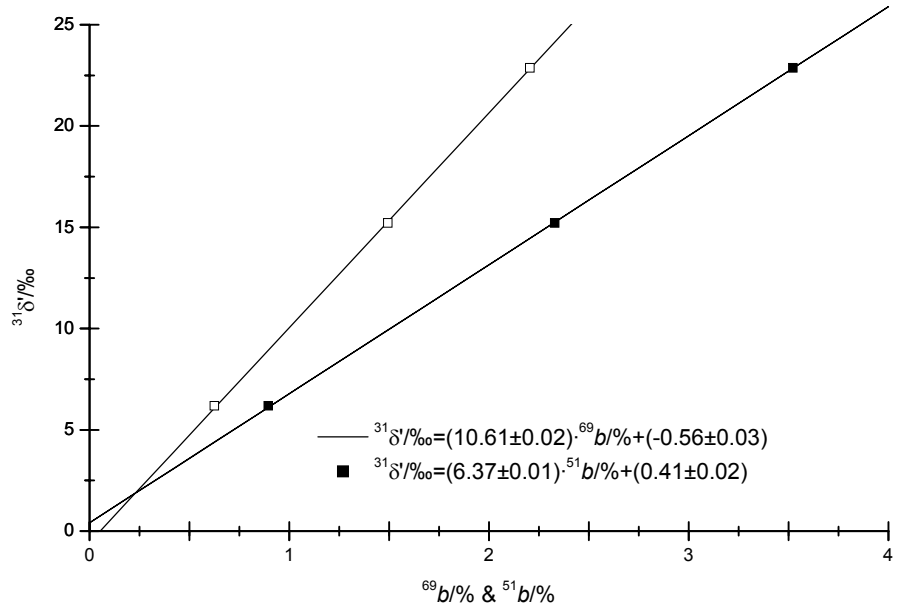

Figure 51: Dilution series showing the influence of CHF_3 contamination on the measured ${}^{31}\delta'$ value. ${}^{69}b = 2.3\%$ corresponds to a molar fraction of 0.01 % CHF_3 in N_2O.

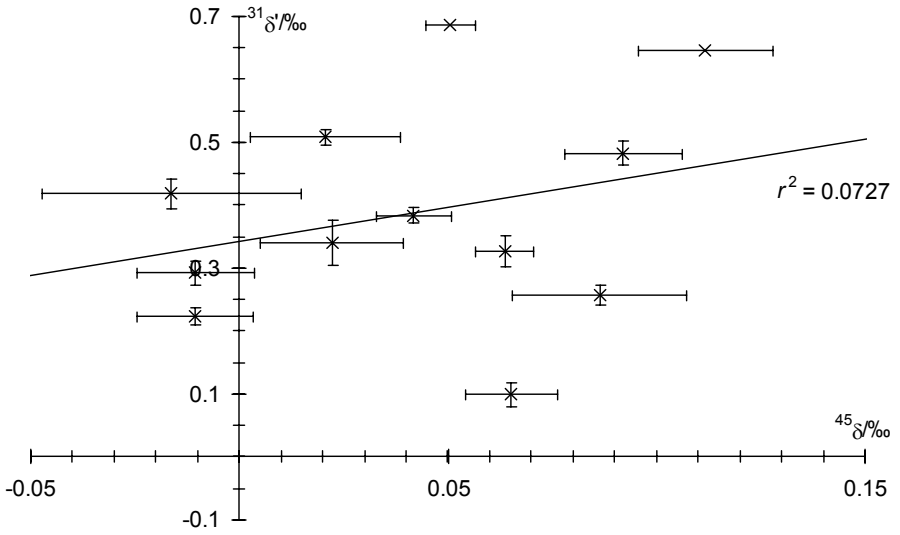

Figure 52: Absence of correlation between $^{45}\delta$ and $^{31}\delta'$ for analyses of standard gas that was run over the GC.

tion of the data as established in section 8.3.3 gave a corrected value of $^{31}\delta = (0.05 \pm 0.29)$ ‰. Although the mean $^{31}\delta$ value is closer to zero now, the standard deviation even increased.

To investigate this phenomenon further, the samples were analysed a second time on the *Finnigan* MAT 252 instrument after $^{31}\delta$ analysis on the *Micromass* Prism II. $^{45}\delta$ and $^{46}\delta$ showed an increase in line with expectations from section 8.2.3 (+0.09 ‰ and +0.15 ‰), but ^{69}b and ^{51}b clearly increased, too. This must be attributed either to impurities that were frozen out from the MS or to some contaminant being released from the *Viton* o-rings used in the sample flask valves. To estimate the amount of m/z 69 impurity at the time of $^{31}\delta$ measurement, the average of ^{69}b for both analyses on the MAT 252 was taken and $^{31}\delta'$ corrected accordingly. The corrected mean $^{31}\delta$ now had a satisfactory value of (0.09 ± 0.08) ‰ (cf. section 8.3.1). A plot of $^{31}\delta$ vs $^{45}\delta$ (Figure 53) showed that much less scattered data compared to the plot of uncorrected $^{31}\delta'$ vs $^{45}\delta$ (Figure 52).

By repeated MS analysis/freeze back cycles on the Prism II, we could rule out that impurities were present in the MS itself which caused continuous increases in $^{31}\delta$. However, we suspected that out-gassing o-rings could be the reason. Therefore, in addition to changing the vacuum manifold for GC purification from glass (with *Viton* o-rings in the valves) to an all stainless steel system (section 8.1.4), all *Viton* o-rings including those in the valves of the *Ascarite* flasks were replaced by butyl rubber o-rings and the CFC based vacuum grease (*Fomblin, BOC Edwards*) used until then for the o-rings was replaced by silicone grease (*Dow Corning*). The glass sample flasks were replaced by stainless steel flasks with *Nupro* valves for the most recent analyses of atmospheric N_2O. $^{45}\delta$ and $^{46}\delta$ values are not affected by the described artefacts and were therefore retained for the older analyses.

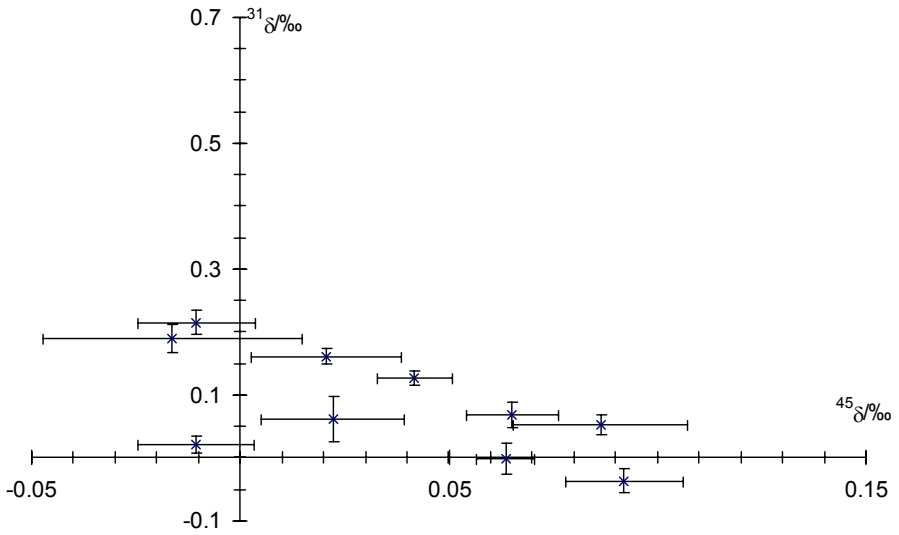

Figure 53: Plot of corrected $^{31}\delta$ values vs $^{45}\delta$ for standard gas run over the GC. Samples were analysed first on the MAT 252 MS for $^{45}\delta$ and $^{46}\delta$, then for $^{31}\delta$ on the Prism II and finally a second time on the MAT 252. The mean value of the two ^{69}b was used to correct the $^{31}\delta$ values. Only 10 out of the original 12 samples could be subjected to this evaluation because the other two were not analysed for a second time

8.4 Tropospheric N_2O samples

8.4.1 Analyses of four Mainz air samples taken on a single day

Having established accuracy and precision of the overall method for standard gas samples, it was now possible to apply it to atmospheric samples. The problems due to CHF_3 contamination shall be illustrated on a set of atmospheric air samples taken from the roof (height above ground: ≈12 m) of the Max Planck Institute for Chemistry in Mainz on a single day in November 1999. The prevailing moderate westerly winds on that day excluded contamination by near-by point sources, corroborated by normal urban CO mixing ratios of ≈200 nmol/mol.

Samples were drawn through PFA tubing (perfluoroalkoxy copolymer, *Dupont*) and directly processed over the CO extraction line. The final results after two GC runs are shown in Table 15.

$\delta^{15}N$ and $\delta^{18}O$ bear similar errors as the blank runs. Therefore, the methodology is considered to be valid for atmospheric samples, too, and we assume that the standard deviation of the mean from the four samples represents the total uncertainty of the analytical method. The values have been corrected for the small interference of residual CO_2 impurities, but not for the ^{17}O isotope anomaly of atmospheric N_2O (sections 2.5, 2.6 and 10.1) and the little fractionation encountered in the check runs of standard gas samples (section 8.2.4). Correcting for the O isotope anomaly requires a downward revision of $\delta^{15}N$ by –0.05 ‰ (and –0.09 ‰ for $^2\delta^{15}N$).

Table 15: Analyses of four air samples taken in Mainz on November 10, 1999

Analysis #	$\delta^{15}N$/‰	$^{1}\delta^{15}N$/‰	$^{2}\delta^{15}N$/‰	$\delta^{18}O$/‰	mixing ratio/ nmol mol^{-1}
1	5.53	–4.54	15.20	5.69	312
2	5.62	–4.56	15.39	5.78	313
3	5.53	–4.96	15.60	5.74	308
4	5.52	–4.63	15.26	5.69	309
mean	5.55±0.05	–4.67±0.20	15.36±0.18	5.72±0.04	311±2
rel. to air/VSMOW	6.56±0.08	–23.8±0.6	36.9±0.6	44.40±0.23	

δ values in rows 2–6 are relative to $^{18}O/^{16}O$ and average $^{15}N/^{14}N$ isotope ratios of the working standard. δ values in the last row are relative to international standards and include the uncertainty of the working standard calibration (cf. Table 4**)**. Mixing ratios were determined by volumetric analysis in the N_2O extraction system and compare well to the value of (315.0±0.5) nmol/mol determined by GC-ECD (section 8.1.6).

$^{2}\delta^{15}N$ and consequently also $^{1}\delta^{15}N$ have comparatively higher standard deviations. This is partly due to the first sample: It contained 22 % impurities (determined manometrically) that had to be removed by the preparatory GC. A contribution of more than 10 % to these impurities stems from CHF_3 and we assume that this is caused by the PFA sampling line, possibly by gaseous decomposition products of PFA or by gases dissolved in or adsorbed to PFA.

The correlation of $^{31}\delta'$ with ^{69}b for the first GC runs (Figure 54) shows the expected slope of ≈10 ‰/% (Figure 51), but the results for the second GC run deviate significantly (≈5 ‰/%)

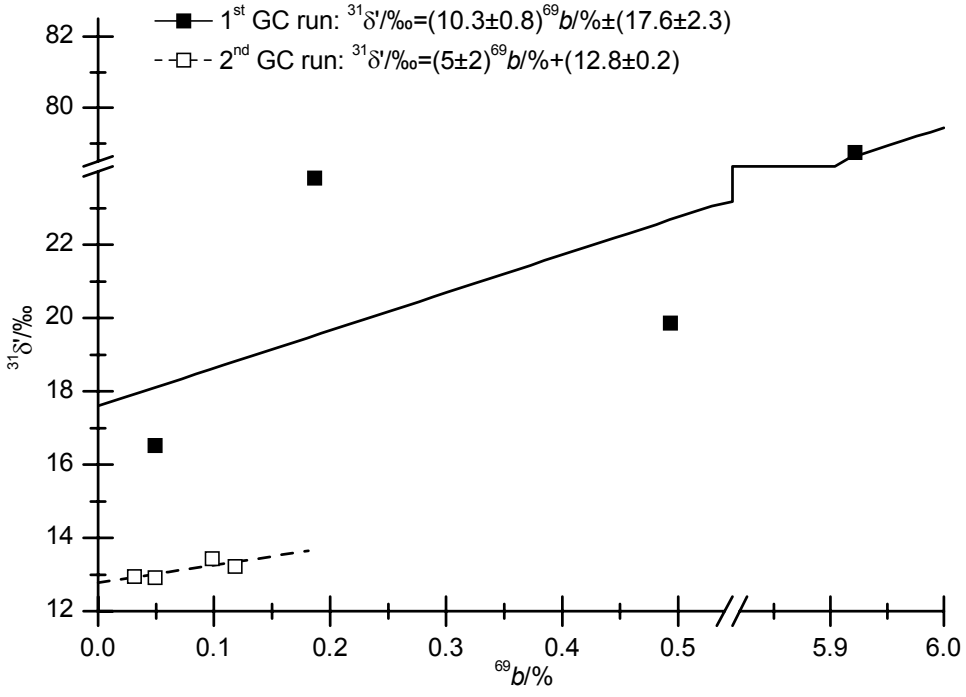

Figure 54: Correlation of $^{31}\delta'$ with ^{69}b (cf. section 8.3.3) for two GC runs of Mainz air samples

Table 16: Overview on tropospheric N_2O analyses from six sampling locations. $\delta^{15}N$ values are relative to air, $\delta^{18}O$ is relative to VSMOW. Standard deviations represent variation of the results for individual sampling locations and do not include uncertainty of working standard calibrations.

Location	Latitude	$\delta^{15}N$	$^{1}\delta^{15}N$	$^{2}\delta^{15}N$	$\delta^{18}O$
Spitsbergen	79°N	6.80±0.14 $n = 23$	–23.7±0.4 $n = 16$	37.4±0.4 $n = 16$	44.72±0.25 $n = 23$
Kollumerwaard	53°N	6.58±0.03 $n = 3$	–23.3±0.3 $n = 2$	36.5±0.2 $n = 2$	44.39±0.04 $n = 3$
Mainz	50°N	6.61±0.07 $n = 8$	–23.6±0.4 $n = 7$	36.8±0.4 $n = 7$	44.49±0.15 $n = 8$
Schauinsland	48°N	6.69±0.09 $n = 11$	–23.6±0.5 $n = 7$	36.9±0.4 $n = 7$	44.61±0.15 $n = 11$
Mt. Sonnblick	47°N	6.69±0.09 $n = 36$	–23.8±0.7 $n = 27$	37.1±0.7 $n = 27$	44.55±0.18 $n = 35$
Izaña	28°N	6.78±0.11 $n = 9$	–23.8±0.6 $n = 8$	37.3±0.5 $n = 8$	44.62±0.13 $n = 9$
mean of all		6.72±0.12 $n = 91$	–23.7±0.6 $n = 67$	37.1±0.6 $n = 67$	44.62±0.21 $n = 90$

although the slope is less well defined. It is assumed that other impurities than CHF_3 are responsible for this fact. $^{31}\delta'$ is therefore corrected by the latter slope rather than the former.

The mixing ratio determined by GC-ECD (section 8.1.6) was (315±0.5) nmol/mol. The results of the manometric determination in the microvolume of the vacuum line gave on average (311±2) nmol/mol which is in reasonable agreement with the gas chromatographic analysis.

8.4.2 Time series of N_2O measurements at various stations

An overview over the results of N_2O isotope measurements in tropospheric air from six sampling stations (Table 14) over two years of measurements is given in Table 16 and Figure 55. Obviously, the variability of the isotopic composition of N_2O is rather low compared to the strong gradients observed in the stratosphere (Figure 40), but larger than the analytical precision estimated from the analysis of four tropospheric air samples obtained in Mainz on a single day (Table 15). Local variations of source fluxes might account for this, but should influence N_2O mixing ratios as well. However, N_2O mixing ratios were virtually invariant (315.8±1.8 nmol/mol) and did not show any correlation to δ values. Only one sample obtained at Mt. Sonnblick on 12.08.99 was found to be significantly depleted in heavy isotopes ($\delta^{15}N = 5.3$ ‰, $\delta^{18}O = 42.2$ ‰; not shown in Figure 55) and a high mixing ratio of 328 nmol/mol. Although it was attempted to exclude pollution by local point sources during sampling, these excursions must be attributed to such a source. Another outlier in Figure 55 is the sample with lowest $\delta^{18}O$ (43.7 ‰) which is the one containing substantial NO_2 impurities (KOL-025) as mentioned in section 8.1.4.

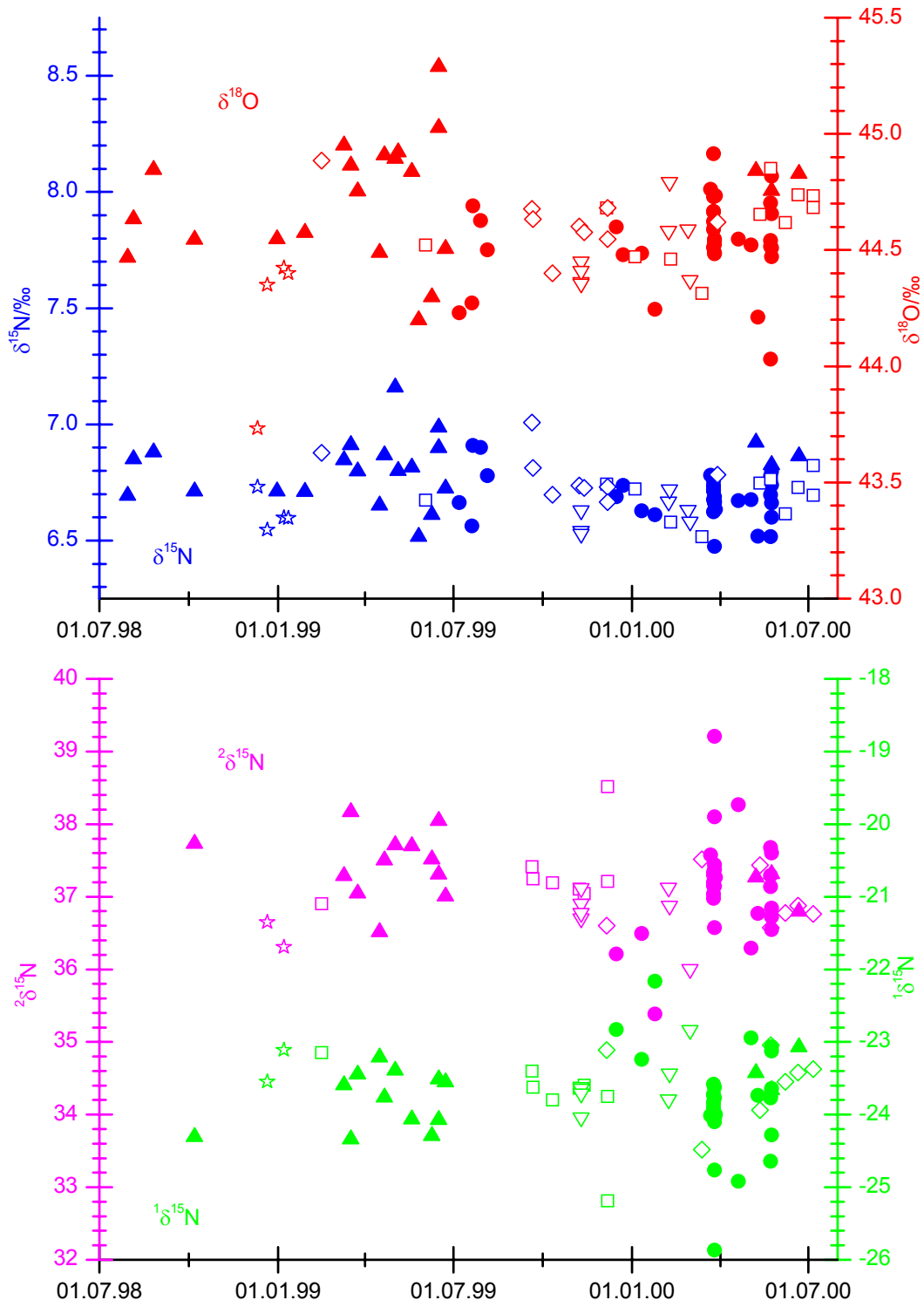

Figure 55: Time series of $\delta^{15}N$, $\delta^{18}O$, $^{2}\delta^{15}N$ and $^{1}\delta^{15}N$ in tropospheric N_2O (▲ Spitsbergen; ☆ Kollumerwaard; ▽ Mainz; ◇ Schauinsland; ● Mt. Sonnblick; □ Izaña, Tenerife)

No clearly discernible temporal or spatial trends are present in the tropospheric data in Figure 55. Nevertheless, we note that $\ln(1+\delta^{15}N)$ and $\ln(1+\delta^{18}O)$ are correlated to each other (Figure 56), just as in the stratosphere. However, the slope of (0.46±0.03) differs from the values of Ψ_{app} obtained in the most recent studies of stratospheric N_2O (1.16–1.26, cf. Table 12). It is

also different from the slope of about 2 found in isotope measurements of soil emissions (Figure 65), the largest single N_2O source (Table 1). This seems to indicate that the correlation between $\delta^{15}N$ and $\delta^{18}O$ is a sampling artefact and neither of stratospheric nor of surface origin. For example, kinetic isotope effects due to diffusion should induce a slope close to 0.5 (because of the mass differences of ^{18}O to ^{16}O and ^{15}N to ^{14}N). No such correlation between $^1\delta^{15}N$ and $^2\delta^{15}N$ could be found however. Rather, a $^1\delta^{15}N$ vs $^2\delta^{15}N$ plot gives an anti-correlation of the two values (slope -0.88 ± 0.05; $r^2 = 0.82$) which reflects the way by which $^1\delta^{15}N$ is calculated ($^1\delta^{15}N = 2\delta^{15}N - {}^2\delta^{15}N$) and the absence of large variations in $\delta^{15}N$.

Our results for the mean oxygen and average nitrogen isotope ratios of tropospheric N_2O (last row in Table 16) agree within errors with most previous studies (see [*Rahn and Wahlen*, 2000] for an overview) and the values reported by Yoshida and Toyoda [2000] ($\delta^{15}N/‰ = 7.0\pm0.6$ and $\delta^{18}O/‰ = 43.7\pm0.9$) which were obtained by on-line gas chromatography-isotope ratio mass spectrometry. Although the mean mixing ratio of our samples is identical to the value of Yoshida and Toyoda (315.7±2.4 nmol/mol), we observe much smaller variations of $\delta^{15}N$ and $\delta^{18}O$. This indicates that it is possible to obtain a higher precision with the off-line technique used here, although at the expense of a more laborious sample preparation.

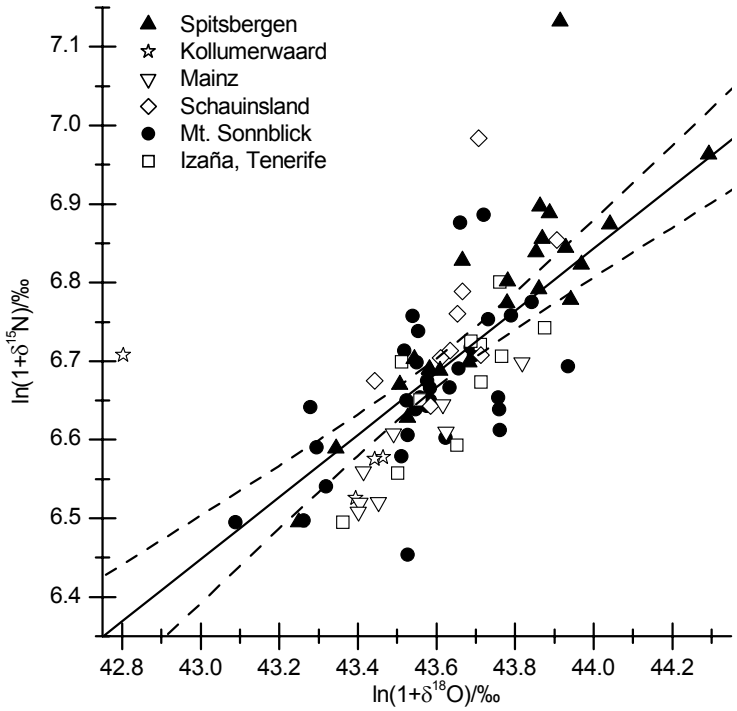

Figure 56: Correlation between $\ln(1+\delta^{18}O)$ and $\ln(1+\delta^{15}N)$ of N_2O in tropospheric samples. A linear least squares fit through all data weighted by assumed errors of 0.05‰ in both $\ln(1+\delta^{15}N)$ and $\ln(1+\delta^{18}O)$ is shown with 95% confidence intervals: $\ln(1+\delta^{15}N) = (-13.2\pm1.4)‰ + (0.46\pm0.03)\ln(1+\delta^{18}O)$ ($r^2 = 0.49$).

The so-called "site preference" ($\equiv {}^2\delta^{15}N - {}^1\delta^{15}N$) is clearly different in both studies: (60.7±1.1) ‰ were found in the present case as opposed to (18.7±2.2) ‰ reported by Yoshida and Toyoda. The large deviation is a consequence of the position-dependent isotopic composition of our working standard. Assuming hypothetically that our N_2O working standard gas was symmetric in $^{15}N/^{14}N$ isotope ratios, we would obtain a value of (20.0±1.1) ‰. This emphasises the need for a direct intercomparison of both working standard gas calibrations which were obtained by completely independent techniques. We have tried to account for the uncertainty of all relevant parameters in the position-dependent calibration of our working standard gas (section 2.4.2), but if there are unknown systematic errors in, for example, ^{18}R(SMOW), the results may nevertheless be incorrect. For the present work, these discrepancies are of little importance since we virtually use tropospheric N_2O as a reference for the interpretation of stratospheric isotope ratios (chapter 7) and also for the variation of δ values in firn air (see next chapter).

Summarising, we note – as expected – little variation in the stable isotope composition of tropospheric N_2O between 79°N and 15°N and over time-scales of 2 years. The variability is slightly larger than the total uncertainty of the off-line analysis system. Judging from the observed correlation between $\delta^{15}N$ and $\delta^{18}O$, this may be caused by residual sampling artefacts which have not yet been accounted for in the error analysis. However, no such correlation is observed between ${}^1\delta^{15}N$ and ${}^2\delta^{15}N$.

9 Firn air record of N_2O isotopes

Temporal trends of atmospheric trace gases are of crucial importance in the construction of global budgets, and by the same token trends in isotopic composition are required for isotope budgets (chapter 11). In chapter 8 it was shown that current changes of the isotopic composition of tropospheric N_2O are too small to be detected over a time-scale of two years with the achievable analytical precision. Rahn and Wahlen [2000] recently predicted annual trends in $^{15}N/^{14}N$ and $^{18}O/^{16}O$ isotope ratios of about –0.03 ‰/a using a simple one-box model. However, they concluded that the direct measurements reported in the literature of the last 20–30 years were too scattered to permit a verification of these postulated trends.

We therefore made use of the natural archive of the past atmosphere represented by air trapped in Antarctic firn to estimate the history of isotope ratios in N_2O. The firn profile cannot be used directly for this purpose since gravitational fractionation and diffusion processes change mixing and isotope ratios [*Schwander et al.*, 1988]. Firn air models take these effects into account and allow the reconstruction of changes in the atmospheric composition from the firn profile. Here, we use a forward model developed at the Laboratoire de Glaciologie et Géophysique in Grenoble, France [*Rommelaere et al.*, 1997] which requires atmospheric scenarios as input data and then calculates the depth profile of the considered trace gas taking into account molecular weight and diffusion coefficients, firn density and porosity profiles as well as mean annual temperature and snow accumulation rate at the respective drilling site.

9.1 Measurements

Within the framework of the European Project FIRETRACC (Firn Record of Trace Gases Relevant to Atmospheric Chemical Change), 16 large air samples were obtained from Dronning Maud Land (DML) in January 1998, and 13 samples were obtained at Dome Concordia (Dome C) in January 1999 (Figure 57). DML has a mean annual temperature of –38°C and an relatively high snow accumulation rate of 60 kg m^{-2} a^{-1} whereas Dome C is an extremely cold site (–53 °C) with a low snow accumulation rate (30 kg m^{-2} a^{-1}). Therefore, the firn-ice transition zone in DML is located at about 73.5 m and at about 99.5 m at Dome C: This results in broader age distributions at Dome C as compared to DML (Figure 58), and although the firn-ice transition is located at a shallower depth in DML, the mean age for the sample from the greatest depth is larger in DML than at Dome C. Actually, Figure 58 shows the age distribution calculated for CO_2, but the corresponding distribution for N_2O is expected to look alike, because both trace gases share

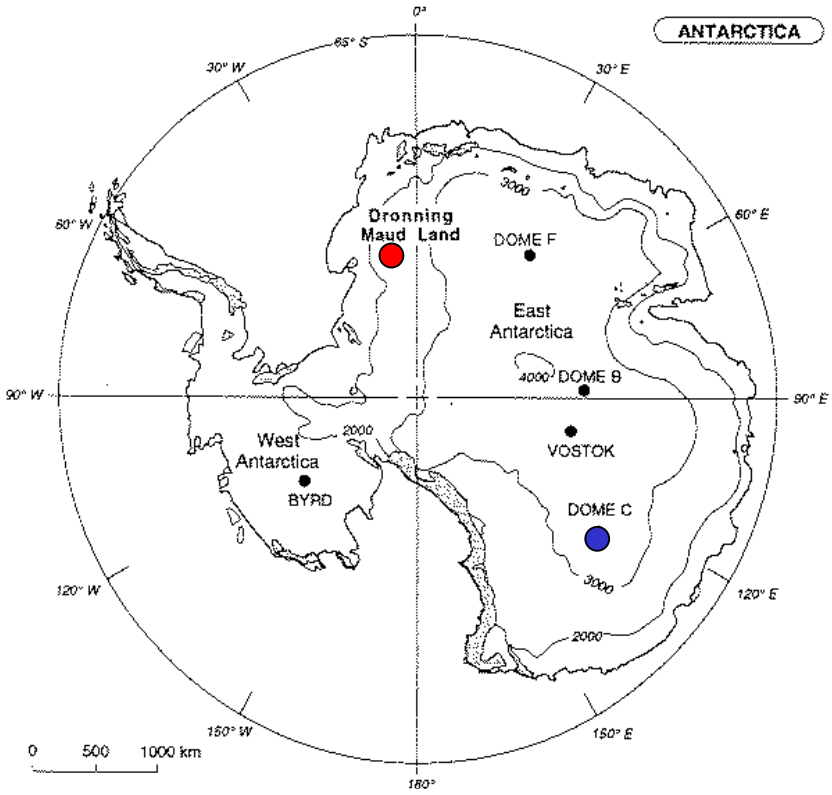

Figure 57: FIRETRACC drilling sites in Antarctica (Dronning Maud Land: 77°S 10°W, 2300 m above sea level; Dome C: 75°S 123°W, 3240 m).

quasi-exponential increases in mixing ratio and similar molecular properties. For example, the diffusion coefficient of N_2O is very close to that of CO_2: $D(N_2O) = 1.004\ D(CO_2)$ [*Trudinger et al.*, 1997] since both gases have nearly equal molecular masses and comparable interaction potentials.

In the air samples extracted from the firn, N_2O mixing ratios were determined by GC-ECD (section 8.1.6) and the isotopic composition was analysed by the same continuous-flow GC-MS method described for the stratospheric samples (section 7.2.1). Depth profiles of mixing ratios and isotope ratios relative to the isotope ratios of contemporary tropospheric N_2O at the sampling sites are shown in Figure 60 (p. 143). Obviously, N_2O mixing ratios decrease with depth, in accordance with the atmospheric evolution (Figure 1, p. 2) whereas isotope ratios increase with depth which indicates the input of isotopically light N_2O from its sources. It was already noted that the firn air measurements cannot be used directly to derive the history of trace gas mixing ratios, and that firn air models must be used for this purpose as explained in the following section.

9.2 Firn air modelling and results

Both inverse and forward models allow reconstruction of past atmospheric trends in trace gas mixing ratios. Inverse methods infer parameters of a given model from the observations

whereas forward models predict the expected results for a given set of model parameters. In the case of isotope ratios, inversion techniques cannot be applied because the comparatively high measurement errors are magnified by the model inversion and result in a reconstructed history of considerable uncertainty.

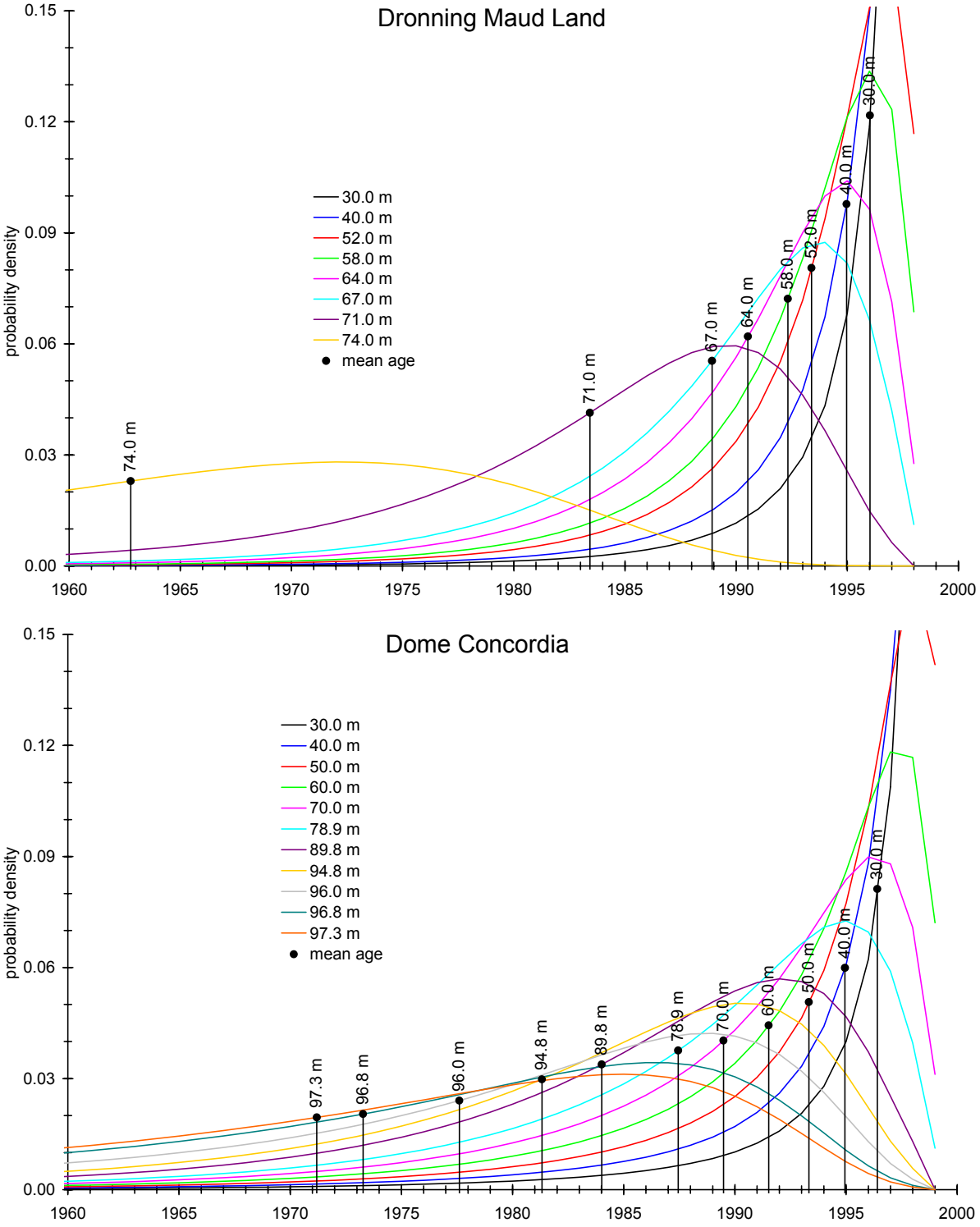

Figure 58: Firn air age distributions for CO_2 at different depths in Dronning Maud Land and at Dome Concordia as calculated by the firn air model forced with the well-known atmospheric evolution of the CO_2 mixing ratio [*Etheridge et al.*, 1996]. The mean age is indicated by vertical lines connecting the age profile to the calendar year-axis.

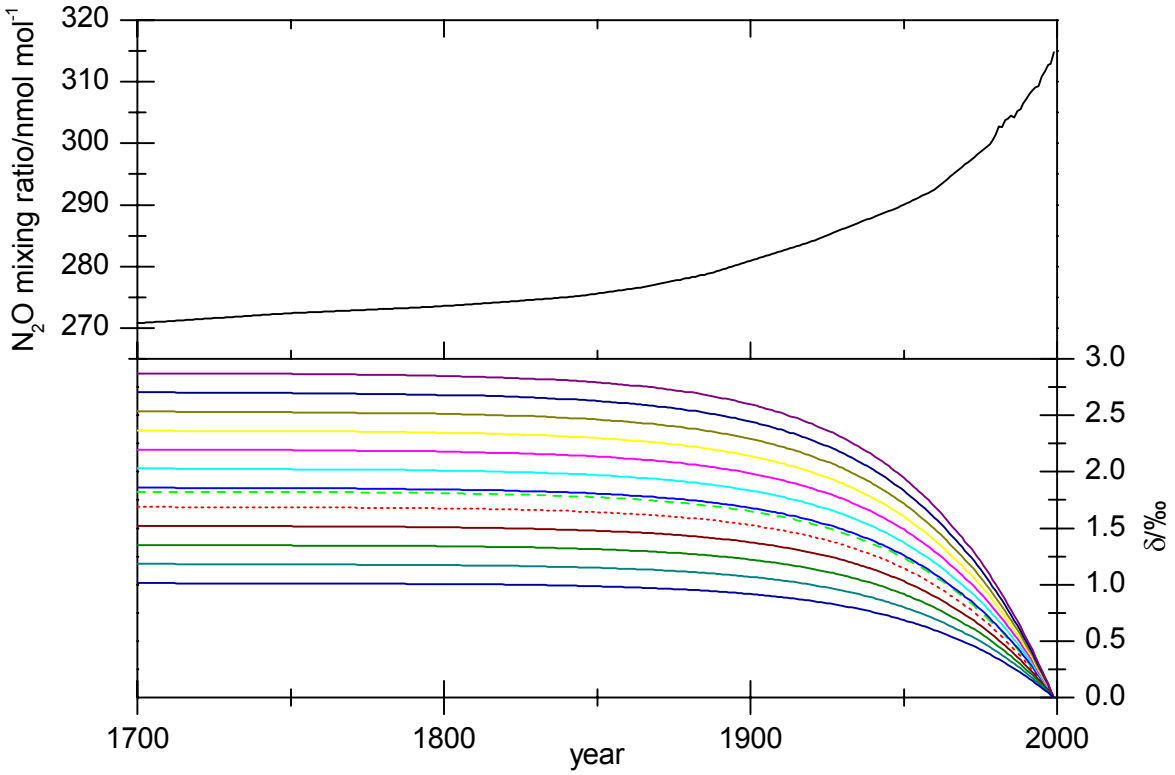

Figure 59: Scenarios of past N_2O mixing and isotope ratios used in the firn air diffusion model. N_2O mixing ratios are constructed from an interpolation of ice core data [*Flückiger et al.*, 1999], firn air measurements at South Pole [*Battle et al.*, 1996] an direct observations at Cape Grim, Tasmania [*Prinn et al.*, 2000] (cf. Figure 1). The isotope scenarios are based on the "depleted ocean" (- - - - - -) and "enriched ocean" scenarios (– – –) from Rahn and Wahlen [2000]. The "depleted ocean" scenario is scaled up and down in steps of 10 % to match the observations.

We already argued that it is reasonable to assume the same diffusivity profile for CO_2 and N_2O because both gases have similar molecular weights and diffusion coefficients. In addition, the atmospheric history of N_2O mixing ratios is relatively well-known (Figure 1), so that the firn profile can be readily calculated with the scenario shown in Figure 59 (top panel).

For DML, the calculated firn profile from this scenario matches the observations well (Figure 60), but for Dome C the modelled N_2O mixing ratios decrease slightly faster with depth than the observations which means that the modelled diffusivity of N_2O is lower than in reality. This discrepancy may arise from adopting the same diffusivity profile for CO_2 and N_2O, if, for example, interactions between the trace gas and the firn matrix play a role. We note that CO_2 is more soluble in water than N_2O, but such an effect on diffusivity should be more important at the warmer DML site. Hence, the origin of the small deviation is not yet understood, but the agreement obtained between model and observations is satisfactory.

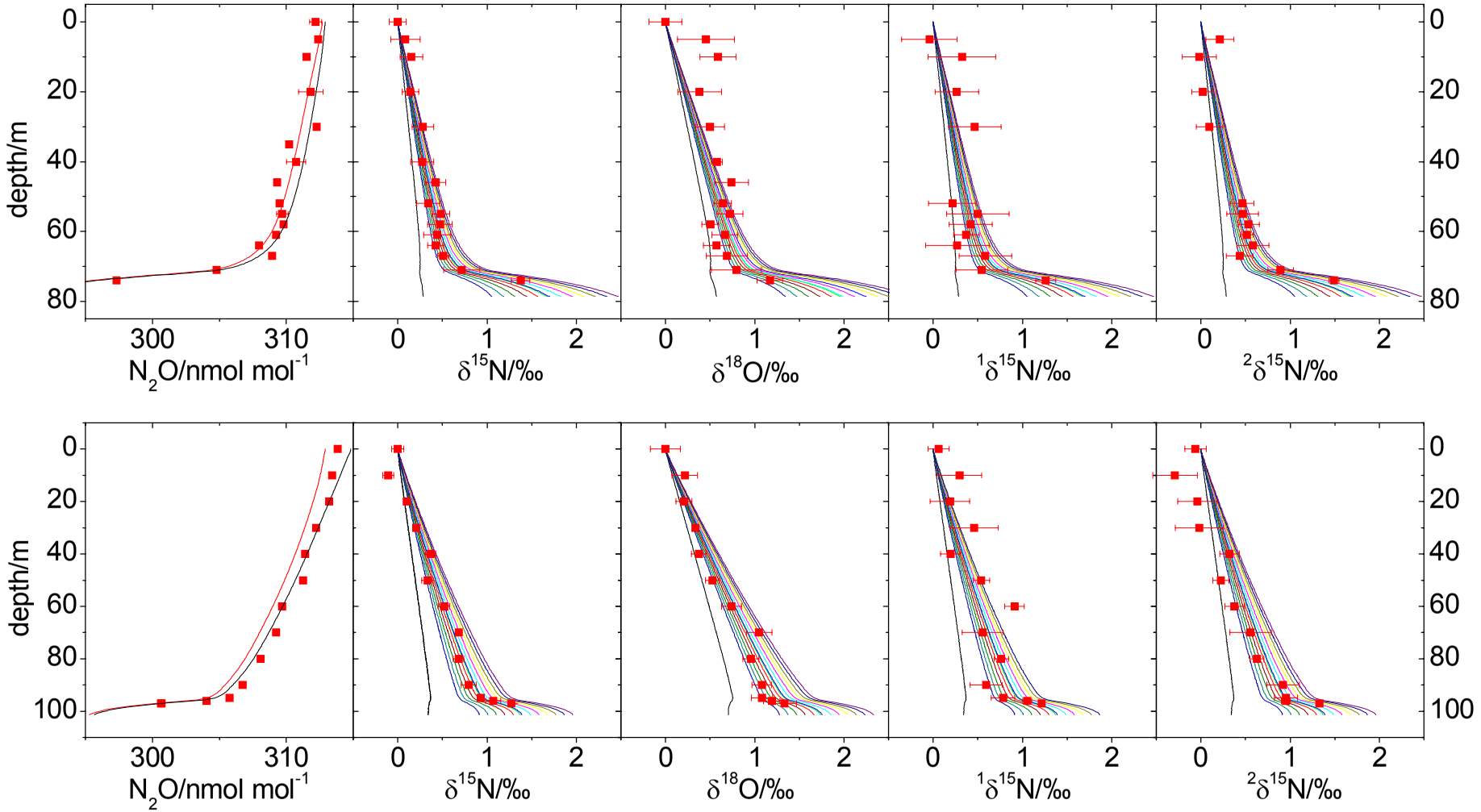

Figure 60: Depth profiles of N_2O mixing ratios and isotopic composition in Antarctic firn air from Dronning Maud Land (top row) and Dome Concordia (bottom row). The leftmost panels show firn model derived mixing ratios for the year of sampling (—) and the previous year (—). The coloured lines in the following panels show the modelled change of isotope ratios using the scenarios in Figure 59 as input. The black line is the firn isotope profile from a scenario with constant isotopic composition since pre-industrial times.

For the isotope ratios, atmospheric scenarios were constructed based on model results from Rahn and Wahlen [2000] who split the total N_2O source into an anthropogenic and a natural part. The magnitude of the anthropogenic N_2O source (P_{anth}) is constrained by an exponential model ($dP_{anth}/dt = w P_{anth} = \text{const.}$) whereas the natural source (P_{nat}) is assumed to be constant. Direct observations of N_2O mixing ratios as well as measurements in ice cores and firn air can then be used to constrain this model by least-squares regression, assuming a constant atmospheric lifetime τ. We note parenthetically that the model described can be solved in closed form:

$$\mu = \mu_0 + \frac{P_{anth,0} / N}{1/w + 1/\tau}\left[e^{w(t-t_0)} - 1\right] \tag{76}$$

where N is the total number of molecules in the atmosphere (cf. Appendix A). Constraining this equation by natural (pre-industrial) and present mixing ratios (μ_0, μ) as well as the present trend ($d\mu/dt$), allows calculation of w. The value of w is independent of the lifetime τ. τ only determines the magnitude of the natural source (P_{nat}) and of $P_{anth,0}$ ($<< P_{nat}$). Such a calculation was performed to derive the red curve in Figure 1 (p. 2) which is similar to the result of Rahn and Wahlen.

The modelled increase of the anthropogenic source was used to calculate the expected variation in isotope ratios assuming two scenarios for the isotopic composition of the ocean source ("enriched" and "depleted ocean", cf. Figure 59). Obviously, the major part of change in isotopic composition occurs in the 20th century. A set of additional scenarios is created by scaling the "depleted ocean" scenario up and down in steps of 10 % to give the best match to the observations. This is equivalent to adjusting the off-set between pre-industrial and present isotopic composition of N_2 (i.e., the δ values of pre-industrial vs present N_2O isotopes).

The most stringent constraints on the isotopic composition of N_2O in the past come from the samples obtained at the greatest depths (Figure 60), since even down to 70 m at Dome C and 67 m in DML the mean age of the N_2O is less than 10 years (Figure 58). Furthermore, the top part of the profile is affected by thermal diffusion which can introduce larger variations on seasonal time-scales [*Severinghaus et al.*, 2001]. The oldest samples of the firn profiles clearly show that an isotope scenario without any change of isotope signatures (black lines in Figure 60) does not reproduce the observations. The best match between modelled and observed profiles is obtained for decreases of ≈2.0 ‰ in $\delta^{15}N$ and ≈1.2 ‰ in $\delta^{18}O$ since pre-industrial times with uncertainties corresponding to the error of the lowest samples given in Table 17. The position-dependent ^{15}N depletion is quite similar for both nitrogen atoms. The consistent isotope changes derived from DML and Dome C samples represent the isotopic fingerprint of the average global N_2O source causing the observed increase in N_2O mixing ratios. Measurements of N_2O isotopes in firn air at

Table 17: Best estimates and uncertainties for the difference between present and pre-industrial isotopic composition of atmospheric N_2O and for the present annual trends, derived from firn air model scenarios

	$(\delta_{present}-\delta_{pre\text{-}ind})\ (1+\delta_{pre\text{-}ind})^{-1}$		$d\delta_{present}/dt\ (1+\delta_{present})^{-1}$	
	best guess/‰	range/‰	best guess/‰ a^{-1}	range/‰ a^{-1}
$\delta^{15}N$	–2.0	–1.8 to –2.2	–0.041	–0.038 to –0.046
$^1\delta^{15}N$	–1.9	–1.7 to –2.2	–0.038	–0.035 to –0.039
$^2\delta^{15}N$	–2.1	–1.9 to –2.3	–0.044	–0.039 to –0.049
$\delta^{18}O$	–1.2	–1.0 to –1.5	–0.025	–0.021 to –0.031

South Pole have shown similar decreases of 1.8 ‰ and 1.4 ‰ in $\delta^{15}N$ and $\delta^{18}O$, respectively, over the last century [*Sowers et al.*, 2001]. However, the position-dependent change of ^{15}N is not very well resolved due to higher measurement uncertainties.

In addition to the difference between present and pre-industrial isotope ratios, it is possible to determine the present annual N_2O isotope trends which was not possible by direct measurements. The inferred decreases are also shown in Table 17 and slightly differ from the values of –0.03 ‰/a for $\delta^{15}N$ and $\delta^{18}O$ in the "depleted ocean" scenario of Rahn and Wahlen [2000]. Although these trends are small, they correspond to large changes in the global source signature because they affect the entire atmospheric N_2O burden of 1510 Tg N in 1998 [*Prather et al.*, 2001] (cf. eqn. A14, Appendix A). These trends will be used to infer a global N_2O isotope budget in chapter 11.

10 Anomalous oxygen isotope fractionation

"Mass-independent" oxygen isotope effects were initially quantified in an operational way by $\Delta^{17}O' \equiv \delta^{17}O - \gamma\,\delta^{18}O$ (42). The factor γ represents some representative value close to the three-isotope exponent β (sections 1.3.1, 1.3.2). This definition was sufficient as long as measurement precision was restricted, but leads to inconsistencies if accurate results are required. The definition given in eqn. 41 is therefore preferred because it is derived without approximations from the mass-dependent fractionation laws given in sections 1.3.1 and 1.3.2 and uses the standard addition theorems for δ values (footnote 4, p. 17):

$$\Delta^{17}O = \frac{1+\delta^{17}O}{\left(1+\delta^{18}O\right)^{\beta}} - 1 \tag{41}$$

β is the three-isotope exponent for mass-dependently fractionated N_2O and equals 0.516 (section 2.7.2). δ values are relative to VSMOW. If $\delta^{17}O$ is expressed relative to another standard (e.g., air) which lies on another mass-dependent fractionation line with VSMOW (0.510 in the case of air-O_2, cf. section 2.7.3), a correction term has to be included in eqn. 41:

$$\Delta^{17}O = \frac{1+\delta^{17}O_{air}}{\left(1+\delta^{18}O_{air}\right)^{\beta}}\left[1+\delta^{18}O_{VSMOW}(air)\right]^{0.510-0.516} - 1 \tag{77}$$

The required correction for $\Delta^{17}O$ in absolute terms is approximately $(0.510-0.516)\cdot\delta^{18}O_{VSMOW}(air) = (-0.006)\cdot 23.68\ ‰ = -0.14\ ‰$. Previous studies on the mass-independent oxygen anomaly used $\Delta^{17}O'$ and definition 42 and expressed δ values relative to air [*Cliff et al.*, 1999; *Cliff and Thiemens*, 1997]. In light of the new definition and the discovery that a correction to $\Delta^{17}O$ is required, we re-evaluated the results from the quoted studies and also performed new analyses ourselves.

10.1 Atmospheric measurements

Oxygen isotopes of N_2O were measured on molecular O_2 derived from tropospheric N_2O by combustion to N_2 and CO_2 (section 2.3.1) and subsequent reduction of CO_2 to O_2 with F_2 [*Brenninkmeijer and Röckmann*, 1998]. N_2O was extracted from large air samples at various remote sampling locations and purified by the gas chromatographic off-line method describe in section 8.1. The results are presented in Figure 61 together with data from Cliff and Thiemens [*Cliff and Thiemens*, 1997] which were obtained by decomposition of N_2O to N_2 and O_2 on a gold surface (section 2.3.1).

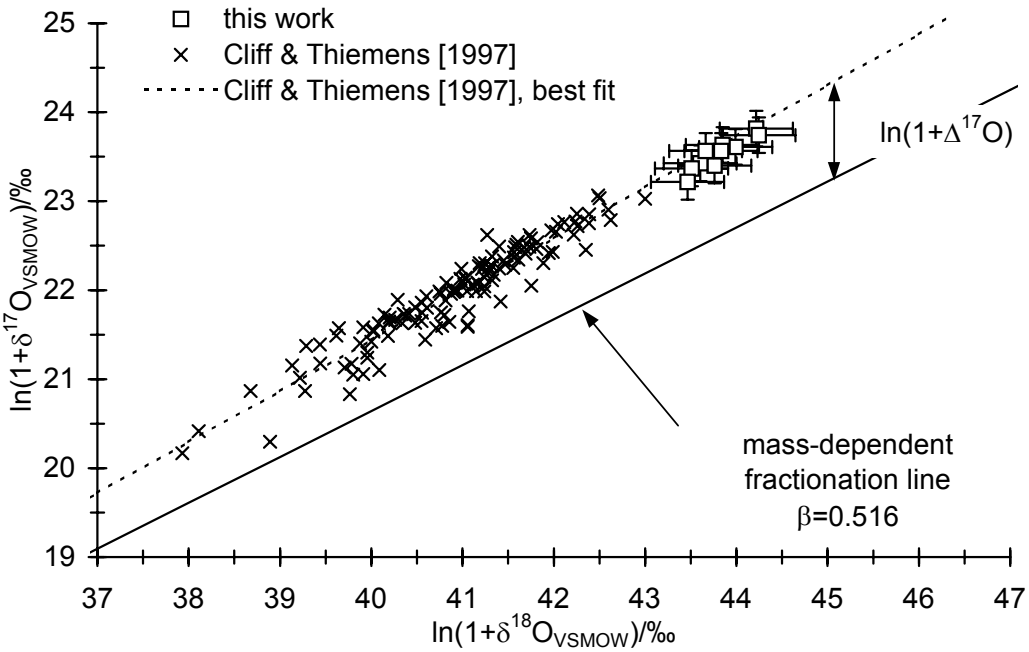

Figure 61: $\ln(1+\delta^{17}O)$ vs $\ln(1+\delta^{18}O)$ plot for N_2O extracted from air samples obtained at Spitsbergen, Norway (March, May, June 1999); Mainz, Germany (February, March 2000); Mt. Sonnblick, Austria (December 1999, March 2000); Izaña, Tenerife (April 1999); Kollumerwaard, Netherlands (January 1999) and Schauinsland, Germany (February 2000). Mixing ratios for all samples are in the range 312.8-316.5 ppb. The results from [*Cliff and Thiemens*, 1997] have been re-scaled to the VSMOW scale using their most recent values of $\delta^{17}O_{VSMOW}(\text{air-}O_2) = 11.92$ ‰ and $\delta^{18}O_{VSMOW}(\text{air-}O_2) = 23.50$ ‰ [*Luz et al.*, 1999].

All samples exhibit a clear ^{17}O excess. Our results give $\Delta^{17}O = (0.93\pm0.08)$ ‰ ($n = 10$) which agrees well with the value of (0.85 ± 0.19) ‰ ($n = 124$) derived from Cliff and Thiemens' data on a larger set of samples. Had we used definition 42, values of $\Delta^{17}O' = (1.01\pm0.08)$ ‰ and (0.98 ± 0.19) ‰ would have been obtained. The difference between these two values is actually smaller than between the values for $\Delta^{17}O$ because our O_2 working standard is about 29 ‰ lighter in ^{18}O than tropospheric N_2O.

The most prominent difference between the two datasets is the range of observed $\delta^{18}O$ values. Whereas the new data show $\delta^{18}O$ values between 44.4 and 45.2 ‰ (consistent with Table 16), the older measurements from Cliff and Thiemens.[*Cliff and Thiemens*, 1997] show a large spread and are generally lower. This variability of $\delta^{18}O$ is only conceivable in the vicinity of strong N_2O sources, because N_2O is generally well-mixed in the troposphere owing to its long lifetime of ≈120 years. However, variations of sample size were deemed to be absent by Cliff and Thiemens within their error of 1 % and are unlikely at the remote sites where part of their samples were obtained which may point to a lack of precision in sampling (precision of the N_2O decomposition method was estimated to be better than 0.1 ‰ for $\delta^{17}O$ and $\delta^{18}O$ [*Cliff and Thiemens*,

1994]). The differences in magnitude of the results might be attributed to a calibration problem. The new results are in good agreements with other reports of $\delta^{18}O$ values for tropospheric N_2O, but the results from Cliff and Thiemens are the lowest of all [*Rahn and Wahlen*, 2000; *Yoshida and Toyoda*, 2000]. In conclusion from the measurements presented we find a well-defined $\delta^{18}O$ value of 44.8±0.3 ‰ vs VSMOW and a ^{17}O excess of $\Delta^{17}O = 0.9 \pm 0.1$ ‰ (assuming $\beta = 0.516$).

Due to the importance of N_2O in the atmosphere as a major greenhouse gas and primary source of NO_x in the stratosphere, questions arise regarding the origin of the small, but significant oxygen anomaly. A number of reactions have been put forward to explain it. These include, to name a few, $N_2 + NO_2^*/NO_3^*$ [*Zellner et al.*, 1992], $N_2 + CO_3^*$ [*McElroy and Jones*, 1996], $N_2 + O_3^*$ [*Prasad and Zipf*, 2000; *Zipf and Prasad*, 1998], UV photolysis [*Johnson et al.*, 2001; *Miller and Yung*, 2000], $N_2 + O(^1D)$ [*Estupiñán et al.*, 2002]. Subsequent experiments have partly ruled out the importance of some of these sources such as $N_2 + NO_2^*$ [*Estupiñán et al.*, 2000], $N_2 + CO_2^*$ [*Wingen and Finlayson-Pitts*, 1998] and $N_2 + O_3^*$ [*Estupiñán et al.*, 2002]. In the following, we present experiments which exclude UV photolysis as an important source and propose an alternative mechanism for the origin of the anomalous fractionation in N_2O.

10.2 UV photolysis

Samples of N_2O were photolysed to various degrees with an ArF laser at 193 nm [*Röckmann et al.*, 2000] and by a broadband UV lamp (section 5.3). The experimental results are shown in Figure 62 and Table 18. In case of Rayleigh fractionation (such as the photolysis experiments), the slope of a $\ln(1+\delta^{17}O)$ vs $\ln(1+\delta^{18}O)$ plot (i.e. the ratio of fractionation constants $^{17}\varepsilon/^{18}\varepsilon$) does not coincide with the definition of $\beta = \ln(^{17}\alpha)/\ln(^{18}\alpha)$ (eqn. 7). We rather have to take the non-linearity between isotope ratios and fractionation factors into account ($\delta = y^{\varepsilon} - 1 = y^{\alpha - 1} - 1$) which gives the following relation:

$$\beta = \frac{\ln^{17}\alpha}{\ln^{18}\alpha} = \frac{\ln(1+^{17}\varepsilon)}{\ln(1+^{18}\varepsilon)} = \frac{\ln\left[1 + \ln(1+\delta^{17}O)/\ln y\right]}{\ln\left[1 + \ln(1+\delta^{18}O)/\ln y\right]} \tag{78}$$

Table 18: Results from UV photolysis experiments

Light source	λ/nm	Conversion (*y*)	ln *y*	$\delta^{17}O$/‰	$\delta^{18}O$/‰	β (eqn. 78)
ArF laser	193.3	71.3 %	–0.338	3.7	7.2	0.510
ArF laser	193.3	51.6 %	–0.662	7.7	15.2	0.504
Sb lamp	202.9±5.3†	57.6 %	–0.552	10.3	19.8	0.519
Sb lamp	202.9±5.3†	59.2 %	–0.524	9.4	18.2	0.515
Sb lamp	202.9±5.3†	29.1 %	–1.234	23.1	44.5	0.519

† half-photolysis wavelength and mean deviation of lower and upper quartiles (cf. section 5.3)

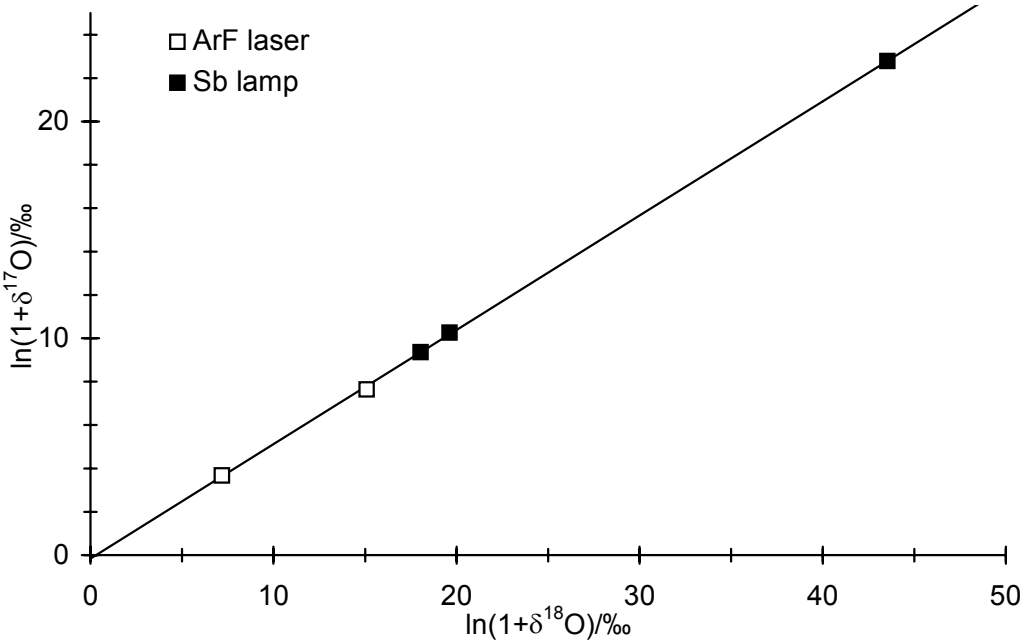

Figure 62: Oxygen isotope data from UV photolysis experiments with an ArF excimer laser and a broadband Sb lamp. A linear fit yields a slope of (0.527±0.004) and a y-axis offset of (–0.15±0.09).

Thus, the average β values are (0.507±0.004) and (0.518±0.006) for the ArF laser and Sb lamp experiments. The β value for the Sb lamp is close to the value of 0.516 for mass-dependently fractionated N_2O (section 2.7.2) and the value 0.521 expected from simple transition-state theory considerations (section 1.3.2). The significance of the results for the ArF laser should be tested by additional measurements.

Johnston *et al.* [1995] concluded from their data that there was no oxygen isotope anomaly in N_2O photolysis at 185 nm. However, a close inspection of their data gives a slope of –1.5±0.4 in a $\ln(1+\delta^{17}O)$ vs $\ln(1+\delta^{18}O)$ plot. Calculating β in the way suggested by eqn. 78 gives an average of –0.5±1.8. Both values don't appear to be reasonable results. Possibly systematic errors were introduced in sample analysis due to incomplete separation of N_2 from O_2 which may disturb the oxygen isotope measurements on the mass spectrometer (section 2.3.2, p. 29).

Previous theoretical predictions of the three-isotope exponent in N_2O photolysis were thought to indicate a small oxygen isotope anomaly. Using a quantum-chemical approach, Johnson *et al.* [2001] have calculated fractionation constants for N_2O isotopomers and isotopologues. Their results give an increasing trend in $^{17}\varepsilon/^{18}\varepsilon$ from 185 to 225 nm with an average of (0.525±0.002) which deviates slightly from the value of 0.521 from transition-state theory. However, re-analysis of their data using eqn. 78 gives $\beta = 0.521\pm0.001$ with no discernible trend and in perfect agreement with simple transition-state theory calculations. Using the ZPE theory, Miller

and Yung [2000] predicted a constant value for $^{17}\varepsilon/^{18}\varepsilon$ of 0.545, but this ratio is based on zero-point energies rounded to 0.5 cm^{-1}. Using zero-point energies calculated from unrounded vibrational frequencies [*Łapiński et al.*, 2001] (cf. section 6.4) rather gives a ratio of 0.529±0.004 (assuming a precision of 0.1 cm^{-1}) which is in much better agreement with measurements and other theoretical predictions.

In order to assess whether photolysis introduces a significant ^{17}O excess into N_2O, we adopt an upper limit for β of 0.521 (judging from our experimental data and the theoretical considerations above). Assuming that the slope of 0.516 derived from the experiments of Cliff and Thiemens [1997] (cf. section 2.7.2) represents mass-dependently fractionated N_2O, we can estimate an upper limit for $\Delta^{17}O$ of 0.06 ‰ using a simple box model (eqn. A16, see Appendix A), a typical lower stratospheric fractionation constant of 14 ‰ (Table 12) and a characteristic ratio of lower stratospheric to tropospheric mixing ratios of 0.75 [*Holton*, 1990]. Thus, photolysis contributes at most 7 % to the observed oxygen isotope anomaly in tropospheric N_2O. Assuming this upper limit for excess ^{17}O from N_2O photolysis, one can predict a $\Delta^{17}O$ value for the lower stratosphere of 0.24 ‰ which should be checked by high-precision measurements in addition to those of Cliff *et al.* [1999] where such a trend was hardly distinguishable from experimental error.

Re-evaluation of the $N_2O + O(^1D)$ experiments of Johnston *et al.* [1995] which were designed to detect oxygen isotope anomalies in this reaction, gives a slope of 0.59±0.05 in a $\ln(1+\delta^{17}O)$ vs $\ln(1+\delta^{18}O)$ plot and an average value for β of 0.57±0.05. The small deviation from the expected slope of 0.511 as derived from collision theory (section 1.3.2) is probably not statistically significant. The deviation may be caused by N_2 interference with O_2 isotope analysis as suspected for the photolysis experiments in the same paper (see above).

The presence of oxygen isotope anomalies in the dominant N_2O sources (microbial nitrification and denitrification reactions in waters and soils) is unlikely, because all biological reactions measured to date were mass dependent (e.g., [*Glickman et al.*, 1997]). From the experimental evidence accumulated above, it also unlikely that such anomalies are due to the "conventional" N_2O sinks (photolysis and reaction with excited atomic oxygen). We therefore propose an alternative, tropospheric origin of the ^{17}O anomaly in N_2O.

10.3 Transfer of the ^{17}O anomaly in O_3 to N_2O

A critical examination of known N_2O sources suggests an indirect chemical pathway for transfer of heavy oxygen from O_3 to N_2O to explain the anomalous $\Delta^{17}O$ signature of atmospheric N_2O. O_3 is enriched in ^{17}O and ^{18}O and the prime example for "mass independent" frac-

tionation in the atmosphere with an extraordinarily large ^{17}O excess of ≈ 30‰ in the troposphere [*Johnston and Thiemens*, 1997; *Krankowsky et al.*, 1995]. The mechanism proposed here starts with transfer of oxygen from O_3 to NO_x via the O_3–NO_x cycle, i.e. oxidation of NO by O_3 (R10) and subsequent NO_2 photolysis (R11). In the absence of further fractionation, this leads to a ^{17}O excess of NO_x in the atmosphere. The other important pathway for oxidation of atmospheric NO proceeds via peroxy radicals, according to R13 and R14. O atoms in the peroxy radicals stem from atmospheric O_2. Although indirect evidence points to the possible existence of oxygen isotope anomalies in HO_2 [*Savarino and Thiemens*, 1999a], we treat peroxy radicals as mass dependently fractionated here. A potential ^{17}O excess will only increase the overall effect.

$$NO + O_3 \rightarrow NO_2 + O_2 \qquad k_{10} = 1.7 \cdot 10^{-14}\ cm^3 s^{-1} \qquad (R10)$$

$$NO + HO_2 \rightarrow NO_2 + HO \qquad k_{13} = 8.8 \cdot 10^{-12}\ cm^3 s^{-1} \qquad (R13)$$

$$NO + RO_2 \rightarrow NO_2 + RO \qquad (R14)$$

$$NO_2 + h\nu \rightarrow NO + O(^3P) \qquad (R11)$$

Cycling between NO and NO_2 in the atmosphere (Figure 63) is fast compared to the NO emission rate and the rate of NO_x removal in the form of HNO_3 and N_2O_5. Thus, the isotopic composition of NO_2 is determined by the relative importance R10 and R13 + R14 assuming that O isotopes are mixed between O_3, NO_x, HO_x and RO_x. For example, if R10 and R13 + R14 were equally efficient, the isotopic composition of NO_2 would simply be the average of the O_3 and the per-oxy radical isotopic composition.

The relative importance of the two pathways depends on the availability of reactants. In our simplified scheme (Figure 63), the ratio of NO_2 formed via O_3, $P(NO_2^*)$ and via HO_2, $P(NO_2)$, is

$$\frac{P(NO_2^*)}{P(NO_2)} = \frac{k_{10} c(O_3)}{k_{13} c(HO_2)} \qquad (79)$$

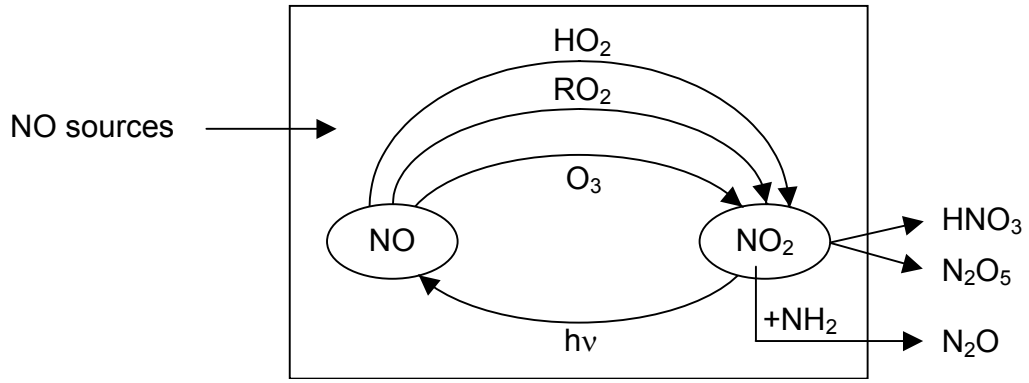

Figure 63: Simplified scheme of NO–NO_2 cycling in the atmosphere. The relative importance of the NO oxidation pathway involving ozone and the pathways involving peroxy radicals is crucial for the isotopic composition of the atmospheric NO_x pool. Only the most important reactions are shown and the detailed pathways involving other species like NO_3 or N_2O_5 are left out.

RO_2 has been neglected because HO_2 is usually the most important peroxy radical. Using typical mixing ratios of 50 nmol/mol O_3 and 10 pmol/mol HO_2 with rate constants k_{10} and k_{13} at 298 K [*Atkinson et al.*, 2001] gives a $P(NO_2^*)/P(NO_2)$ of ≈10 and still 1.2 for an extreme scenario of low O_3 (30 nmol/mol) and high HO_2 (50 pmol/mol). Hence, the oxidation pathway via O_3 dominates in the atmosphere. On the global scale, we adopt the result from a 3-D atmospheric chemistry model (MATCH) giving an average ratio $P(NO_2^*)/P(NO_2)$ of about 4 (*Rolf von Kuhlmann*, personal communication, 2000). This means that in the absence of further fractionation the expected ^{17}O excess for atmospheric NO_2 is about 80 % of the effect in O_3, i.e. $\Delta^{17}O \approx 24‰$.

The second step of the proposed mechanism is the transfer of the oxygen isotope anomaly from NO_2 to N_2O via reaction of NO_2 with NH_2 radicals (R16) which originate from ammonia oxidation by OH (R15). In the atmosphere, NH_2 can react with O_3, NO_2, HO_2, NO, OH and SO_2 [*Dentener and Crutzen*, 1994; *Kohlmann and Poppe*, 1999], but only channel R16 leads to N_2O formation:

$$NH_3 + OH \rightarrow NH_2 + H_2O \qquad k_{15} = 1.6 \cdot 10^{-13}\ cm^3 s^{-1} \qquad (R15)$$

$$NH_2 + NO_2 \rightarrow N_2O + H_2O \qquad (R16)$$

In this reaction, oxygen is transferred directly from NO_2 to N_2O, thus completing the transfer process from O_3 to N_2O. The importance of reaction R16 depends critically on the relative atmospheric concentrations of the main reaction partners of NH_2, i.e. O_3 and NO_2. It is favoured in the tropics, in particular in biomass burning plumes. Estimates of the contribution of this reaction to the global N_2O source strength range from 2 to 7 % [*Dentener and Crutzen*, 1994] with a best estimate of 3.4 % (0.6 Tg/a) (Table 1). Since R10 and R16 together represent a source of N_2O with a ^{17}O excess of about 24 ‰, a contribution of 3.4 % can explain almost the entire $\Delta^{17}O$ value of 0.9 %.

There are a few caveats to the above suggested magnitude of the $\Delta^{17}O$ contribution by this reaction: In accordance with the kinetic data evaluation by DeMore *et al.* [1997], Dentener and Crutzen [*Dentener and Crutzen*, 1994] have assumed that the reaction channel leading to N_2O accounts for 95 % of the reaction rate of $NH_2 + NO_2$ ($k_{16} + k_{17} = 2.0 \cdot 10^{-11}$ $cm^3 s^{-1}$), the remainder being due to the following reaction:

$$NH_2 + NO_2 \rightarrow H_2NO + NO \qquad (R17)$$

In a more recent model by Kohlmann and Poppe [1999], a re-measured value of the branching ratio $k_{16}/k_{16}+k_{17}$ of $NH_2 + NO_2$ of 60 % [*Meunier et al.*, 1996] was incorporated together with a number of other revisions and yielded an estimate of the $NH_2 + NO_2 \rightarrow N_2O$ source of 0.2 Tg N/a. Other studies report even lower branching ratios [*Lindholm and Hershberger*, 1997; *Park and Lin*, 1996; *Park and Lin*, 1997] of 19 to 24 % which have led to an evaluated value

of (25±15) % (IUPAC Subcommittee on Gas Kinetic Data Evaluation: Data Sheet NOx22, http://www.iupac-kinetic.ch.cam.ac.uk). On the other hand, $\Delta^{17}O$ values of NO_2 may well be higher than 24 ‰. Recent reports of $\Delta^{17}O \approx 25$ ‰ in nitrates [*Michalski et al.*, 2001] point to a value of $\Delta^{17}O(NO_2) \approx 38$ ‰, assuming that one of the O atoms in HNO_3 is derived from OH which is mass-dependently fractionated due to isotope exchange with H_2O.

A recent report has suggested that reaction of $N_2 + O(^1D) \rightarrow N_2O$ could contribute about 1.4 % to the global N_2O source [*Estupiñán et al.*, 2002]. Since $O(^1D)$ is produced by O_3 photolysis, it should inherit the ^{17}O excess of ≈ 30 ‰ from O_3. Although a small source, this reaction could thus account for ≈ 0.4 ‰ of the oxygen isotope anomaly in N_2O. Since two thirds of the reaction $N_2 + O(^1D) \rightarrow N_2O$ are supposed to occur in the stratosphere, an increase of the ^{17}O anomaly with altitude is expected. Although such an increase in stratospheric N_2O was suggested by Cliff *et al.* [1999], it is difficult to quantify such a trend between stratospheric and tropospheric $\Delta^{17}O$ values from their data. Further stratospheric measurements of the $\delta^{17}O$ signature in N_2O should help to decide which mechanism explains the origin of the oxygen isotope anomaly in N_2O best. Possibly it is a combination of the $NH_2 + NO_2$ and the $N_2 + O(^1D)$ sources.

11 Global N_2O isotope budget

The construction of the global budget of N_2O still shows large uncertainties in both the total flux from natural and anthropogenic sources as well as in the stratospheric losses (Table 1). Isotopes do provide additional constraints on global trace gas budgets and may help to make budgets more precise. However, uncertainties on the average isotopic composition of the aggregated global N_2O source are also large. In the concluding chapter of this thesis, it will be shown nevertheless that the presently available data on the isotopic composition of N_2O are in agreement with the current understanding of the global N_2O cycle.

11.1 Pre-industrial and anthropogenic N_2O sources

It was noted previously that construction of global N_2O isotope budgets requires knowledge of the stratospheric N_2O isotope fractionation [*Kim and Craig*, 1993; *Kim et al.*, 2000; *Yoshida and Toyoda*, 2000]. However, none of the previous isotope budgets could draw on constraints from the tropospheric isotope trends (Table 17) since the required data were not yet available. Instead, it was attempted to *calculate* the expected isotope trends from assumed isotopic signatures of N_2O sources. For example, Kim *et al.* [2000] predicted trends of –0.06 ‰/a for $\delta^{15}N$ and –0.08 ‰ for $\delta^{18}O$ in tropospheric N_2O. Obviously, these trends overestimate the real trends now established by the firn air measurements. Here, we will incorporate the measured trends in a simple box-model for N_2O and derive the isotopic signatures of the pre-industrial and the anthropogenic N_2O sources.

The mass balance for tropospheric N_2O in a simple 2-box model divided into troposphere and stratosphere as given in Appendix A is

$$N x_T \frac{d\mu_T}{dt} = P - L = P - F_{TS} + F_{ST} \tag{A5}$$

where the term $N x_T$ represents the number of tropospheric molecules. F_{TS} and F_{ST} are N_2O fluxes from troposphere to stratosphere and vice versa. The mass balance requires that the N_2O production from all sources, $P = \Sigma P_i \approx 0.59$ Tmol/a $\hat{=}$ 16.4 Tg N/a (TAR; Table 1) is equal to the sum of the observed imbalance $N x_T d\mu_T/dt \approx 0.14$ Tmol/a $\hat{=}$ 3.8 Tg N/a and the stratospheric loss $L \approx 0.45$ Tmol/a $\hat{=}$ 12.6 Tg N/a. For the individual isotopologues eqn. A5 can be rewritten in terms of δ values using equations A14 and A15:

$$\mu_T x_T N \frac{1}{1+\delta_T} \frac{d\delta_T}{dt} = \delta'_P P + \delta'_S F_{ST} \tag{80}$$

The differential quotient is the change in the isotopic composition of tropospheric N_2O. Average isotopic composition of the global N_2O source (δ_P') and a representative value for the stratosphere (δ_S') are expressed relative to the tropospheric isotopic composition (δ_T) which simplifies further calculations. The term $(1+\delta_T)$ is required to normalise the isotope scale and the term $\mu_T x_T N$ simply represents the present tropospheric N_2O reservoir which can be inferred from the total atmospheric N_2O reservoir. The total atmospheric N_2O reservoir was given by *Prather et al.* [2001] as 1510 Tg N ≙ 53.9 Tmol in 1998.

Representative values for δ_S' can be obtained from the measured lower stratospheric fractionation constants (Table 12) and eqn. A10 (Appendix A) if a representative stratospheric mixing ratio (μ_S) is assumed. μ_S can be calculated from eqn. A7 with the following constraints: global N_2O lifetime $\tau = 120$ a, total number of molecules in the atmosphere $N = 1.8 \cdot 10^{20}$ mol [*Trenberth and Guillemot*, 1994], stratospheric N_2O loss $L = F_{TS} - F_{ST} = F(\mu_T - \mu_S) = 0.45$ Tmol/a and an average share of the stratosphere of $x_S = 15$ % [*Warneck*, 1999]. Assuming $\mu_T = 315$ nmol/mol, this gives $\mu_S = 248$ nmol/mol and requires an exchange flux between troposphere and stratosphere and vice versa of $F = 0.22$ Tmol/s, in reasonable agreement with estimates of F and μ_S from Holton [1990]. The resulting values for δ_S' are shown column 3 of Table 19..

Knowing the present tropospheric trends in δ_T, it is now possible to solve eqn. 80 for δ_P', i.e. the present isotopic composition of the global N_2O source relative to the isotopic composition of tropospheric N_2O (columns 5 and 6, Table 19). Obviously, the global average source must be significantly depleted relative to tropospheric N_2O in order to balance the isotopic enrichments in stratospheric N_2O. We can compare the present situation to a hypothetical isotopic equilibrium by assuming the absence of any trends in δ_T (column 7, Table 19). Subtracting the equilibrium situation from eqn. 80 shows that for every –0.01 ‰/a of the present trend, the global

Table 19: δ_P' values for the present global average source based on the lower stratospheric fractionation constants and the annual trends derived from the firn data, including the ranges given in Table 17. The last column shows the results obtained without annual trends, i.e. for a hypothetical isotopic equilibrium in the present atmosphere.

	ε_{app}/‰	δ_S'/‰	$\frac{d\delta_T/dt}{(1+\delta_T)}$/‰ a^{-1}	δ_P'/‰, firn derived trends		δ_P'/‰, no trends
				best guess	range	best guess
1	2	3	4	5	6	7
^{15}N	–16.8	4.02	–0.041	–14.7	–14.5 to –15.1	–11.4
terminal ^{15}N	–12.7	3.04	–0.038	–11.7	–11.5 to –12.6	–8.6
central ^{15}N	–20.9	5.00	–0.044	–17.8	–17.4 to –18.2	–14.2
^{18}O	–13.8	3.30	–0.025	–11.4	–11.1 to –11.9	–9.4

source signature decreases by about 0.8 ‰, assuming constant values for the total source flux P (= 0.59 Tmol/a) and tropospheric N_2O burden of 47.4 Tmol (calculated with $x_S = 15$ ‰, $\mu_S = 248$ nmol/mol and $\mu_T = 315$ nmol/mol).

Similar budget calculations can be performed for the pre-industrial atmosphere assuming that the N_2O budget was in equilibrium then (i.e. $P = L$) and the isotopic composition of the average source flux was constant (causing isotopic equilibrium). We further assume that the stratospheric fractionation constants remained invariable between 1700 and today and that the lifetime of N_2O has not changed which allows the annual sink strength to be scaled from its present value of 12.6 Tg N/a at 315 nmol/mol to a pre-industrial N_2O mixing ratio of 10.8 Tg N/a at 270 nmol/mol. Thus, also the relative enrichments due to fractionation in the stratosphere must remain constant. Using eqn. 80 and $\frac{d\delta_T/dt}{(1+\delta_T)} = 0$, we can calculate the pre-industrial isotope signature of the global average source (Table 20, column 2).

In order to compare this signature to the present values, we convert the values to the modern tropospheric signature (Table 20, column 3) using the best estimates for the difference between present and pre-industrial isotopic composition of tropospheric N_2O (Table 17). Slight decreases of all source signature can be ascertained. Relative changes are in the order $\delta^{18}O < {}^2\delta^{15}N < \delta^{15}N < {}^1\delta^{15}N$ which is different than the order of stratospheric values where ${}^1\delta^{15}N < \delta^{18}O < \delta^{15}N < {}^2\delta^{15}N$. Actually, it is not evident that the source signatures have to become isotopically lighter since the atmosphere is not in equilibrium between sources and sinks. The excess of isotopically light N_2O from the increasing source flux forces the tropospheric N_2O signature to lower values, even if the source isotopic composition remains constant, because the stratospheric return flux (F_{ST}) does not increase proportionally. Figure 64 shows the evolution of N_2O mixing ratios and tropospheric isotope signature in such a scenario where the isotopic com-

Table 20: δ'_P values for the pre-industrial global average source assuming isotopic equilibrium. δ'_P values for the present global average source are from Table 19. The anthropogenic source signatures are derived from a mass balance between pre-industrial (natural) and present sources for the anthropogenic source flux given in IPCC-SAR and IPCC-TAR (see main text).

	δ'_P(pre-ind.)/‰		δ'_P(pres.)/‰	δ'_P(anthrop.)/‰ vs δ_T(pres.)	
	vs δ_T(pre-ind.)	vs δ_T(pres.)	vs δ_T(pres.)	SAR	TAR
1	2	3	4	5	6
^{15}N	-14.9	-12.9	–14.7	-18.3	-17.4
terminal ^{15}N	-11.2	-9.4	–11.7	-16.2	-15.1
central ^{15}N	-18.5	-16.4	–17.8	-20.3	-19.7
^{18}O	-12.2	-11.0	–11.4	-12.1	-12.0

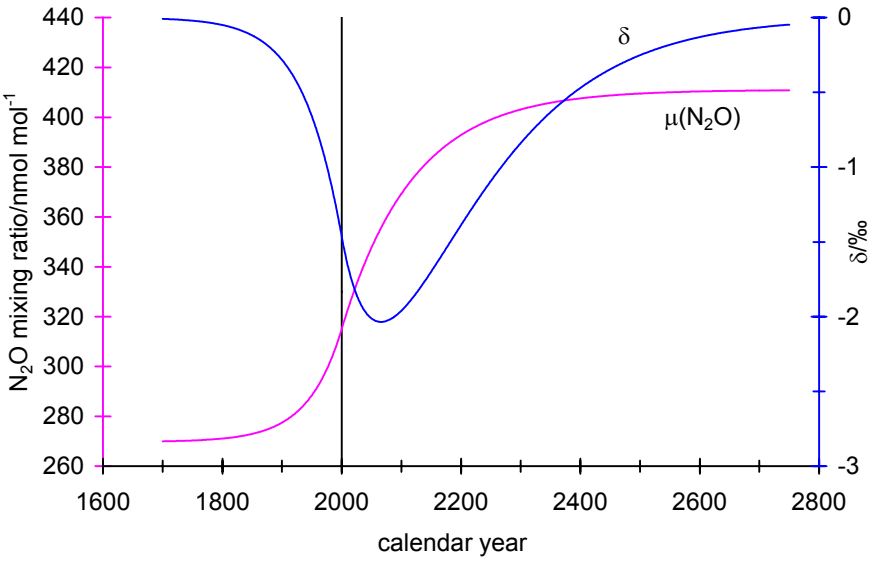

Figure 64: Hypothetical scenario for N_2O mixing ratio and isotopic composition assuming a constant average source signature, but exponentially increasing anthropogenic source fluxes and a development of N_2O mixing ratios as in eqn. 76 (p. 144). In 2000, the increase of the anthropogenic source is suddenly stopped, so that mixing ratio and isotope ratios can relax to their respective equilibrium values.

position of the source remains constant, but the return flux lags behind. Starting in the year 2000, the system is allowed to relax to equilibrium by stopping the increase of the anthropogenic source. Obviously, the time-scale for changes in δ values is much slower than for changes of mixing ratio. The slow relaxation of δ is a consequence of the high degree of cancellation between changes of isotopically substituted and unsubstituted species since the lifetimes are very similar for different isotopologues (cf. eqn. A11) [*Manning*, 1999; *Tans*, 1997].

Assuming that the isotope signature of the pre-industrial N_2O source represents the isotope signature of the present natural source, we can estimate the global average anthropogenic source by simple mass balance considerations. Two values are adopted for the strength of the anthropogenic source: 1. the difference between the present source and the calculated pre-industrial one (5.6 Tg N a^{-1}) which agrees well with the IPCC-SAR (5.7 Tg N a^{-1}), cf. Table 1; 2. the revised value from IPCC-TAR of 6.7 Tg N a^{-1} which requires a reduction of the natural source to 9.7 Tg N a^{-1} to close the N_2O budget. The results in Table 20, columns 5 and 6, show that the total anthropogenic source is isotopically lighter than the pre-industrial (natural) source. This general trend is robust to changes in individual parameters (e.g., the stratospheric enrichments or the stratosphere-troposphere fluxes) since present and pre-industrial inventories are affected alike.

In conclusion, global N_2O isotope budget calculations using observed apparent stratospheric fractionation constants (Table 12) as well as present atmospheric trends derived from firn air measurements (Table 17) enable an isotopic characterisation of the present and pre-industrial

(natural) global average N_2O source. The inferred anthropogenic emissions are significantly depleted relative to the pre-industrial N_2O source. This is in agreement with recent data from soil measurements which indicate that N_2O from agricultural soils (i.e. the largest source of anthropogenic N_2O according to Table 1) may be more depleted than natural soil emissions [*Pérez et al.*, 2001].

11.2 Isotope signatures of individual N_2O sources

In the final section of this thesis, the global average source is divided into an ocean component and a residual component dominated by soil emissions. The relatively well-characterised ocean source is used to infer the isotopic composition of the poorly known residual (soil) source. We focus on the $^{18}O/^{16}O$ and average $^{15}N/^{14}N$ isotope ratios since the vast majority of existing source measurements have only assayed these values. To this end, the inferred global average source signatures (Table 20) are converted to VSMOW and air-N_2 scales using the average isotopic composition of tropospheric N_2O (Table 16). The results are shown in Table 21.

Table 1 shows that the largest N_2O sources on the global scale are soils and oceans. A compilation of the presently available information on $\delta^{15}N$ and $\delta^{18}O$ values of emissions from these sources is given in Figure 65. It illustrates the difficulty to assign representative isotope signatures to individual sources due to the relatively small number of existing measurements and their large scatter. Especially the isotope ratios of soil emissions (green symbols) seem to be very variable and span the whole range of measured values if landfill soils are included. Isotope signatures of oceanic emissions are better known. In a recent modelling study, Rahn and Wahlen [2000] defined two scenarios for the global average oceanic source: A relatively "depleted ocean" with $\delta^{15}N = 5$ ‰ and $\delta^{18}O = 39$ ‰ as proposed by Kim and Craig [1993] at the low end (close to values observed in open ocean surface water) and an "enriched ocean" with values of $\delta^{15}N = 10$ ‰ and $\delta^{18}O = 54$ ‰ (corresponding to the upper end of near-surface water values). The end points of the red ellipsis in Figure 65 are defined by these two scenarios. Taking the area enclosed by this ellipsis as a possible range for the global oceanic source, the flux-weighted average of the

Table 21: Global average isotope signatures of tropospheric N_2O (Table 16) and pre-industrial, present and anthropogenic N_2O sources (Table 19, Table 20) relative to air-N_2 and VSMOW.

	δ_T(pres.)	δ'_P(pre-ind.)/‰	δ'_P(pres.)/‰	δ'_P(anthrop.)/‰	
				SAR	TAR
^{15}N	6.7	-6.3	-8.1	-11.7	-10.8
^{18}O	44.6	33.1	32.7	31.9	32.1

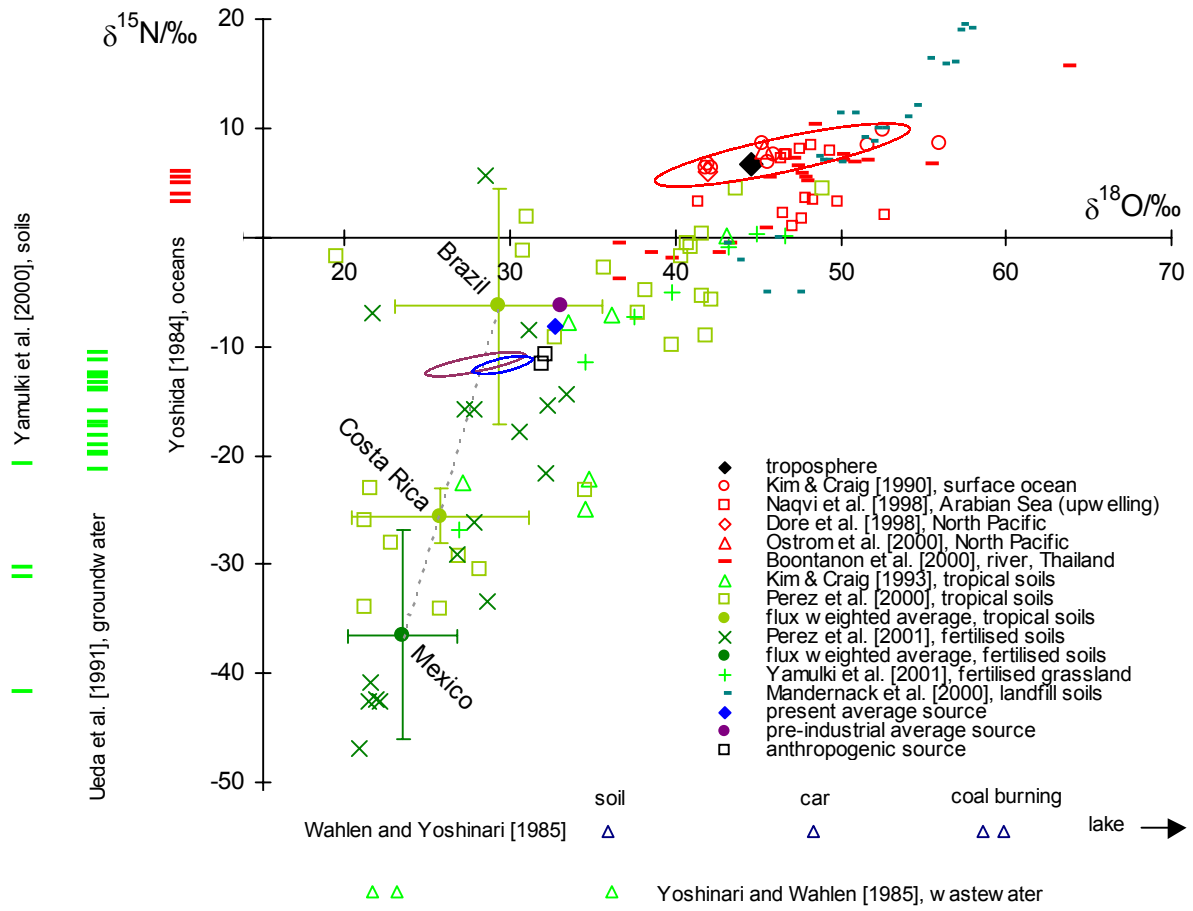

Figure 65: Compilation of $^{18}O/^{16}O$ and average $^{15}N/^{14}N$ isotope ratios of N_2O sources relative to VSMOW and air-N_2. Not all data are discussed in detail, but they are shown to give a comprehensive overview of presently available data. Data points from studies where only O or N isotopes were measured are shown at the bottom and to the left of the co-ordinate system. Also shown are the mean modern tropospheric isotope ratios (◆) as well as present (◆) and pre-industrial (●) global average source signatures derived from stratospheric and firn data. The anthropogenic source signature (□) is deduced from these values and the IPCC-SAR/TAR budgets. Assuming ocean emissions to be within the red ellipsis (end-members correspond to the depleted and enriched ocean sources defined in [*Rahn and Wahlen*, 2000]), the purple and blue ellipses show the isotopic composition of the residual source (mainly soils) for pre-industrial and present times. Flux-weighted average source signatures (with country names and ±1σ errors) for soil emissions fall on a single line that passes through the ellipses designating the isotope ratios of the residual source.

residual source can be calculated from the best estimates of the oceanic and the total N_2O source (Table 1) and the global average source signature derived from the isotope budgets for the present and the pre-industrial atmospheres which are also shown in Figure 65.

Evidently, the average signature of the residual sources can be well constrained by this approach, even allowing for the wide range of oceanic isotope values. This is a consequence of the relatively small contribution of the oceans to the total N_2O source flux which is even smaller for the present atmosphere than the pre-industrial one. The isotopic signature of the residual source

lies on the nodal line connecting the flux weighted average of natural and agricultural tropical soils [*Pérez et al.*, 2000; *Pérez et al.*, 2001] suggesting that it is dominated by emissions from these sources. Interestingly, the isotope signatures of the residual source for the present and pre-industrial atmosphere are almost identical in apparent contradiction to the previous notion that the anthropogenic contribution must be isotopically lighter than the natural N_2O source. However, this is also explained by the smaller contribution of the relatively heavy ocean source in the present atmosphere compared to pre-industrial times. Actually, the residual N_2O in the present atmosphere seems to be even slightly heavier than its pre-industrial equivalent in contradiction to the previous notion that the isotopic signature of industrial sources (such as fossil fuel combustion or nitric and adipic acid production) should be close to that of tropospheric air ($\delta^{15}N = 0$ ‰; $\delta^{18}O \approx 23.7$ ‰) [*Rahn and Wahlen*, 2000] and that agricultural soils should rather emit isotopically light N_2O [*Pérez et al.*, 2001].

The required contribution by an isotopically heavier N_2O source might be the NH_2+NO_2 reaction which effects not only the ^{17}O excess of atmospheric N_2O, but also increases the average $^{18}O/^{16}O$ ratio because of the extreme isotopic enrichment of atmospheric ozone (chapter 10). This source is likely to have increased from pre-industrial to present times due to rising anthropogenic NH_3 and NO_x emissions. If this is the case, it should be reflected by an accompanying increase of the oxygen isotope anomaly in N_2O which could be ascertained by ice core measurements of $^{17}O/^{16}O$ isotope ratio in N_2O.

Of course, the latter suggestion is rather speculative. Figure 65 also shows high isotope ratios in N_2O emissions from landfill sites [*Mandernack et al.*, 1998] and rivers [*Boontanon et al.*, 2000]. If these had increased together with isotopically light emissions from agricultural soils, the near constant residual source signature could be explained. Further work is needed to establish representative values for the isotope signatures of the poorly characterised N_2O sources which could then be used in a bottom-up approach to quantify individual source contributions. Within the range of errors, the present understanding of the global N_2O cycle is in line with measurements of the isotopic composition of N_2O sources.

Appendix A: Box modelling of isotopes

In the following, the mathematical treatment of simple 1- and 2-box models of stable isotopes in atmospheric N_2O is formulated. The focus is set on the influence of a loss process (sink reaction) on the isotopic composition of tropospheric N_2O. The results are used in the global budget calculations of chapter 11.

1-box model

The atmosphere is treated as a single box with a uniform N_2O mixing ratio μ in a constant total number of molecules N with production and loss rates P and L, respectively. The loss process is assumed to be of first order with lifetime τ. The mass balance equation then reads

$$\frac{d(\mu N)}{dt} = N\frac{d\mu}{dt} = P - L \qquad \text{with } L = \frac{\mu N}{\tau} \tag{A1}$$

For an isotopically substituted molecule a similar equation applies:

$$\frac{d(\mu' N)}{dt} = N\frac{d\mu'}{dt} = P' - L' \qquad \text{with } L' = \frac{\mu' N}{\tau'} \tag{A2}$$

Note that we do not assume steady-state which would imply $P-L=0$ and $P'-L'=0$. The atmospheric isotope ratio (μ'/μ) is used as reference value for the δ values of the source and sink:

$$\delta'_P \equiv \frac{P'}{P}\Big/\frac{\mu'}{\mu} - 1 \tag{A3}$$

$$\delta'_L \equiv \frac{L'}{L}\Big/\frac{\mu'}{\mu} - 1 = \frac{\tau}{\tau'} - 1 \tag{A4}$$

In principle, the lifetime τ' could be calculated from the fractionation factor associated with the assumed global sink by $\tau' = \tau/\alpha = \tau/(1+\varepsilon)$ [*Rahn and Wahlen*, 2000]. However, this fractionation factor is *a priori* not identical to the one pertaining to the loss reactions as they occur in nature, since these losses are not evenly distributed throughout the atmosphere (as in a 1-box model) and furthermore, are subject to variations caused by transport processes. Actually, Rahn and Wahlen did not use an average value for the fractionation factor α to calculate the lifetime of the isotopically substituted N_2O, since – at that time – the temperature and wavelength dependence of isotopic fractionation in N_2O photolysis (chapters 4 and 5) as well as the fractionation by $O(^1D)$ (chapter 3) were not sufficiently characterised. They rather drew on measurements of *apparent* fractionation factors in the lower stratosphere. This approach is not immediately understandable, but can be justified in the framework of a 2-box model as explained below (eqn. A13).

2-box model

A 2-box model dividing the atmosphere into stratosphere and troposphere promises to be a more realistic way to analyse tropospheric isotope ratios. Defining F_{TS} and F_{ST} as the N_2O fluxes from troposphere to stratosphere and vice versa as well as $x_T = N_T/N = \text{const.}$ as the fraction of tropospheric (N_T) to total number (N) of molecules in the atmosphere, we have the following mass balance for tropospheric N_2O:

$$N x_T \frac{d\mu_T}{dt} = P - L = P - F_{TS} + F_{ST} \tag{A5}$$

Assuming that the average exchange flux F of air masses between stratosphere and troposphere and vice versa is equal in both directions, we can calculate F_{TS} and F_{ST} from the corresponding mixing ratios, i.e. $F_{TS} = \mu_T F$ and $F_{ST} = \mu_S F$. The global lifetime τ is then calculated from the global N_2O burden $N(x_T\mu_T + x_S\mu_S)$ with $x_S = 1 - x_T$ and the net loss $L = F_{TS} - F_{ST}$:

$$\tau = \frac{N(x_T\mu_T + x_S\mu_S)}{L} = \frac{N(x_T\mu_T + x_S\mu_S)}{F_{TS} - F_{ST}} = \frac{N(x_T\mu_T + x_S\mu_S)}{F(\mu_T - \mu_S)} \tag{A6}$$

Solving for μ_S yields

$$\mu_S = \mu_T \frac{F\tau - N x_T}{F\tau + N x_S} \tag{A7}$$

For the limit of $x_S \to 0$, we recover the 1-box model with a hypothetical value for μ_S

$$\lim_{x_S \to 0} \mu_S = \mu_T \left(1 - \frac{N}{F\tau}\right) \tag{A8}$$

N is well known from measurements of the mean pressure at earth's surface and calculations of the geopotential and equals $1.77 \cdot 10^{20}$ mol for the dry atmosphere [*Trenberth and Guillemot*, 1994]. A value of $\tau = 120$ a is adopted from more sophisticated 2D- and 3D-atmospheric chemistry models [*Prather et al.*, 1995]. However, the variability in estimates of F is large. F also depends on the height level assumed to be representative for troposphere-stratosphere exchange. E.g., Holton [1990] used the 100 mbar isobar, corresponding to a value of x_S of approximately 0.1. With his values of $\mu_T = 330$ nmol/mol and $F = 2.0 \cdot 10^{11}$ mol/s (corresponding to 5.8 Tg/s), we find $\mu_S = 243$ nmol/mol.

The stratospheric mixing ratio of isotopically substituted N_2O, μ'_S, can be calculated similarly. The relative isotope ratio of stratospheric vs tropospheric N_2O is defined as:

$$\delta'_S \equiv \frac{\mu'_S}{\mu_S} \Big/ \frac{\mu'_T}{\mu_T} - 1 \tag{A9}$$

Observations have shown that δ'_S in the lower stratosphere (which is the region relevant for isotope exchange and which mixing ratio also dominates the average stratospheric mixing ratio because of the exponential decrease of total number density with height) can be described by a Rayleigh fractionation equation with an apparent fractionation constant ε_{app} (cf. section 7.2):

$$\delta'_S = \left(\frac{\mu_S}{\mu_T} \right)^{\varepsilon_{app}} - 1 \tag{A10}$$

Equations A6, A9 and A10 can be solved for the lifetime of isotopically substituted N_2O:

$$\tau' = \tau \frac{\dfrac{1}{1-(\mu_S/\mu_T)^{1+\varepsilon_{app}}} - x_S}{\dfrac{1}{1-\mu_S/\mu_T} - x_S} \tag{A11}$$

This is the lifetime τ' which should be used in eqn. A4 to make the 2-box model equivalent to a 1-box model. The relative lifetime of isotopically substituted N_2O molecule depends not only on the fractionation constant ε, but also on the relative distribution of total atmospheric mass and the speed of exchange between stratosphere and troposphere

Recovering the 1-box case by the limit $x_S \to 0$, we have

$$\lim_{x_S \to 0} \tau' = \tau \frac{1-\mu_S/\mu_T}{1-(\mu_S/\mu_T)^{1+\varepsilon_{app}}} \tag{A12}$$

This corresponds to the 1-box solution only in case of negligible stratospheric destruction (corresponding to a very long lifetime τ or a very fast stratosphere-troposphere exchange):

$$\lim_{\mu_S \to \mu_T} \tau' = \lim_{\mu_S \to \mu_T} \tau \frac{-1/\mu_T}{-(1+\varepsilon_{app})(\mu_S/\mu_T)^{\varepsilon_{app}}/\mu_T} = \frac{\tau}{1+\varepsilon_{app}} \tag{A13}$$

Incidentally, this equation was used by Rahn and Wahlen [2000] to calculate the lifetime of heavy isotopologues of N_2O.

Isotope budgets

For the purpose of isotope budgets, we rewrite eqn. A5 using definitions A4 and A3:

$$\mu_T x_T N \frac{1}{1+\delta_T} \frac{d\delta_T}{dt} = \delta'_P P - \delta'_L L \tag{A14}$$

where δ_T stands for the tropospheric isotope ratio relative to any standard (such as VSMOW or air-N_2). In order to derive the isotopic composition of lost N_2O (i.e., δ'_L), we use δ'_S (A10) which can be derived from stratospheric measurements and substitute L for $F_{TS} - F_{ST} = F(\mu_T - \mu_S)$. One obtains

$$\delta'_S F_{ST} = -\delta'_L L \tag{A15}$$

$$\delta'_L = \frac{1-\left(\frac{\mu_S}{\mu_T}\right)^{\varepsilon_{app}}}{\frac{\mu_T}{\mu_S}-1} \tag{A16}$$

In steady state, sources and sinks balance ($P = L$) and we have $\frac{d\delta_T}{dt} = 0$ and $\delta'_L = \delta'_P$ corresponding to isotopic equilibrium.

Appendix B: A note on nomenclature

Some discrepancies in definitions and nomenclature have appeared among previous publications on kinetic isotope effects in N_2O photolysis. We cannot resolve these issues, but summarise the differences.

To distinguish the two non-equivalent nitrogen atoms in N_2O we assign arbitrary locants: 1 for the terminal and 2 for the central nitrogen [*Brenninkmeijer and Röckmann*, 1999]. We can thus distinguish two δ values: $^{1}\delta^{15}N$, $^{2}\delta^{15}N$ (shorter: $^{1}\delta$, $^{2}\delta$). The fractionation constants are designated $^{15}\varepsilon_1$ and $^{15}\varepsilon_2$ (or: ε_1, ε_2) . This leads to a compact symbolism, but at least three other sets of terminology are also in use:

1. the so-called "AFGL code" of isotopologues and isotopomers developed at the Air Force Geophysics Laboratory (AFGL, Hanscom Air Force Base, Massachusetts, USA) which is based on the last digit of the integer isotope mass [*Rothman et al.*, 1998; *Yung and Miller*, 1997], e.g. (456) for $^{14}N^{15}N^{16}O$
2. α and β prefixes for the central and terminal N atom, thus treating the oxygen atom as a substituent and applying organic chemistry nomenclature [*Toyoda and Yoshida*, 1999], e.g. $\delta^{15}N^{\alpha}$
3. μ and τ prefixes for the middle (Greek: mesos) and terminal (Greek: telos) N atom (*Thom Rahn*, personal communication, 1999)

None of these four nomenclatures is encompassed with current IUPAC (International Union of Pure and Applied Chemistry) recommendations. Application of existing IUPAC rules would lead to hardly manageable names such as (1-^{15}N,2-^{14}N)dinitrogen 1-oxide for $^{14}N^{15}NO$ and (1-^{15}N,2-^{14}N)dinitrogen 2-oxide for $^{15}N^{14}NO$ (using the systematic name for N_2O and the numbering rules for isotopically modified compounds), respectively 1-oxa-2,3-diazaprop-1-en-2-yne (treatment as heteroatomic chain; isotopic substitutions would have to be indicated by the appropriate locants) (*Warren Powell*, personal communication 2001). In the first IUPAC-compliant case the ^{15}N atom always has been assigned locant 1, whereas in the second case the central and terminal nitrogen atoms are numbered 2 and 3, respectively. None of these latter solutions seems satisfactory if concise, intuitive symbols are desired.

References

Aregbe, Y., S. Valkiers, K. Mayer, P. De Bièvre, R.M. Wessel, and A. Alink (1998): Measuring amount ratios of gas isotopes by two primary methods, *Metrologia*, **35** (1), 7-16.

Atkinson, R., D.L. Baulch, R.A. Cox, J.N. Crowley, R.F. Hampson, Jr., J.A. Kerr, M.J. Rossi, and J. Troe (2001): Summary of Evaluated Kinetic and Photochemical Data for Atmospheric Chemistry: Web Version December 2001 - IUPAC Subcommittee on Gas Kinetic Data Evaluation for Atmospheric Chemistry, http://www.iupac-kinetic.ch.cam.ac.uk.

Atkinson, R., D.L. Baulch, R.A. Cox, R.F. Hampson, J.A. Kerr, M.J. Rossi, and J. Troe (1997): Evaluated kinetic and photochemical data for atmospheric chemistry: Supplement VI - IUPAC Subcommittee on Gas Kinetic Data Evaluation for Atmospheric Chemistry, *J. Phys. Chem. Ref. Data*, **26** (6), 1329-1499.

Baertschi, P. (1976): Absolute ^{18}O content of standard mean ocean water, *Earth Planet. Sci. Lett.*, **31**, 341-344.

Bange, H.W., S. Rapsomanikis, and M.O. Andreae (1996): Nitrous oxide in coastal waters, *Global Biogeochem. Cycles*, **10** (1), 197-207.

Battle, M., M. Bender, T. Sowers, P.P. Tans, J.H. Butler, J.W. Elkins, J.T. Ellis, T. Conway, N. Zhang, P. Lang, and A.D. Clarke (1996): Atmospheric gas concentrations over the past century measured in air from firn at the South Pole, *Nature*, **383**, 231-235.

Begun, G.M., and L. Landau (1961): Mass spectra and metastable transitions in isotopic nitrous oxides, *J. Chem. Phys.*, **35** (2), 547-551.

Bender, M., T. Sowers, and L. Labeyrie (1994): The Dole effect and its variations during the last 130,000 years as measured in the Vostok ice core, *Global Biogeochem. Cycles*, **8** (3), 363-376.

Bigeleisen, J. (1949): The relative reaction velocities of isotopic molecules, *J. Chem. Phys.*, **17** (8), 675-678.

Bigeleisen, J. (1952): The effects of isotopic substitution on the rates of chemical reactions, *J. Phys. Chem.*, **56**, 823-828.

Bigeleisen, J. (1955): Statistical mechanics of isotopic systems with small quantum corrections. I. General considerations and the rule of the geometric mean, *J. Chem. Phys.*, **23** (12), 2264-2267.

Bigeleisen, J. (1996): Nuclear size and shape effects in chemical reactions. Isotope chemistry of the heavy elements, *J. Am. Chem. Soc.*, **118** (15), 3676-3680.

Bigeleisen, J., and M.G. Mayer (1947): Calculation of equilibrium constants for isotopic exchange reactions, *J. Chem. Phys.*, **15** (5), 261-267.

Bigeleisen, J., and M. Wolfsberg (1958): Theoretical and experimental aspects of isotope effects in chemical kinetics, *Adv. Chem. Phys.*, **1**, 15-76.

Böhlke, J.K., and T.B. Coplen (1995): Interlaboratory comparison of reference materials for nitrogen-isotope-ratio measurements, in *Reference materials and intercomparison materials for stable isotopes of light elements*, edited by IAEA, pp. 51-66, International Atomic Energy Agency, Vienna.

Boontanon, N., S. Ueda, P. Kanatharana, and E. Wada (2000): Intramolecular stable isotope ratios of N_2O in the tropical swamp forest in Thailand, *Naturwissenschaften*, **87**, 188-192.

Brand, W.A. (1995): PreCon: A fully automated interface for the pre-GC concentration of trace gases in air for isotopic analysis, *Isotopes Environ. Health Stud.*, **31**, 277-284.

Brasseur, G.P., J.J. Orlando, and G.S. Tyndall (1999): *Atmospheric Chemistry and Global Change*, 655 pp., Oxford University Press, New York.

Brenninkmeijer, C.A.M. (1991): Robust, high-efficiency, high-capacity cryogenic trap, *Anal. Chem.*, **63** (11), 1182-1184.

Brenninkmeijer, C.A.M. (1993): Measurement of the abundance of ^{14}CO in the atmosphere and the $^{13}C/^{12}C$ and $^{18}O/^{16}O$ ratio of atmospheric CO with applications in New Zealand and Antarctica, *J. Geophys. Res.*, **98** (D6), 10595-10614.

Brenninkmeijer, C.A.M., and I. Hemmingsen (1988): Sheathed thermocouples as heater elements, *Journal of Physics E-Scientific Instruments*, **21** (5), 502-503.

Brenninkmeijer, C.A.M., C. Koeppel, T. Röckmann, D.S. Scharffe, M. Bräunlich, and V. Gros (2001): Absolute measurement of the abundance of atmospheric carbon monoxide, *Journal of Geophysical Research*, **106** (D9), 10003-10010.

Brenninkmeijer, C.A.M., and T. Röckmann (1996): Russian doll type cryogenic traps: Improved design and isotope separation effects, *Anal. Chem.*, **68** (17), 3050-3053.

Brenninkmeijer, C.A.M., and T. Röckmann (1998): A rapid method for the preparation of O_2 from CO_2 for mass spectrometric measurement of $^{17}O/^{16}O$ ratios, *Rapid Commun. Mass Spectrom.*, **12** (8), 479-483.

Brenninkmeijer, C.A.M., and T. Röckmann (1999): Mass spectrometry of the intramolecular nitrogen isotope distribution of environmental nitrous oxide using fragment-ion analysis, *Rapid Commun. Mass Spectrom.*, **13** (20), 2028-2033.

Brown, W.A., P. Gardner, M. Perez Jigato, and D.A. King (1995): Characterization and orientation of adsorbed NO dimers on Ag{111} at low temperatures, *J. Chem. Phys.*, **102** (18), 7277-7280.

Buresh, R.J., and E.R. Austin (1993): Measuring nitrogen-15 content of gases: Comparison of direct and arc-redistribution methods, *Soil Sci. Soc. Am. J.*, **57** (1), 93-95.

Cantrell, C.A., R.E. Shetter, and J.G. Calvert (1994): Branching ratios for the $O(^1D) + N_2O$ reaction, *J. Geophys. Res.*, **99** (D2), 3739-3743.

Cantrell, C.A., A. Zimmer, and G.S. Tyndall (1997): Absorption cross sections for water vapor from 183 to 193 nm, *Geophys. Res. Lett.*, **24** (17), 2195-2198.

Chang, T.-L., and W.-J. Li (1990): A calibrated measurement of the atomic weight of carbon, *Chin. Sci. Bull.*, **35** (4), 290-296.

Cicerone, R.J. (1989): Analysis of sources and sinks of atmospheric nitrous oxide (N_2O), *J. Geophys. Res.*, **94** (D15), 18265-18271.

Clayton, R.N., L. Grossman, and T.K. Mayeda (1973): A component of primitive nuclear composition in carbonaceous meteorites, *Science*, **182**, 485-488.

Clayton, R.N., and T. Mayeda, K. (1988): Formation of ureilites by nebular processes, *Geochim. Cosmochim. Acta*, **52**, 1313-1318.

Cliff, S.S., C.A.M. Brenninkmeijer, and M.H. Thiemens (1999): First measurement of the $^{18}O/^{16}O$ and $^{17}O/^{16}O$ ratios in stratospheric nitrous oxide: A mass-independent anomaly, *J. Geophys. Res.*, **104** (D13), 16171-16175.

Cliff, S.S., and M.H. Thiemens (1994): High-precision isotopic determination of the $^{18}O/^{16}O$ and $^{17}O/^{16}O$ ratios in nitrous oxide, *Anal. Chem.*, **66** (17), 2791-2793.

Cliff, S.S., and M.H. Thiemens (1997): The $^{18}O/^{16}O$ and $^{17}O/^{16}O$ ratios in atmospheric nitrous oxide: A mass-independent anomaly, *Science*, **278** (5344), 1774-1776.

Coplen, T.B., H.R. Krouse, and J.K. Böhlke (1992): Reporting of nitrogen-isotope abundances, *Pure Appl. Chem.*, **64** (6), 907-908.

Craig, H. (1957): Isotopic standards for carbon and oxygen and correction factors for mass-spectrometric analysis of carbon dioxide, *Geochim. Cosmochim. Acta*, **12**, 133-149.

Crutzen, P.J. (1970): The influence of nitrogen oxides on the atmospheric ozone content, *Quart. J. R. Met. Soc.*, **96**, 320-325.

Crutzen, P.J. (2002): Geology of mankind, *Nature*, **415**, 23.

De Bièvre, P., S. Valkiers, H.S. Peiser, P.D.P. Taylor, and P. Hansen (1996): Mass-spectrometric methods for determining isotopic composition and molar mass traceable to the SI, exemplified by improved values for nitrogen, *Metrologia*, **33** (5), 447-455.

DeMore, W.B., S.P. Sander, D.M. Golden, R.F. Hampson, M.J. Kurylo, C.J. Howard, A.R. Ravishankara, C.E. Kolb, and M.J. Molina (1997): *Chemical kinetics and photochemical data for use in stratospheric modeling. Evaluation number 12*, 269 pp., Jet Propulsion Laboratory, California Institute of Technology, Pasadena, California.

Dentener, F., and P.J. Crutzen (1994): A three-dimensional model of the global ammonia cycle, *J. Atmos. Chem.*, 331-369.

Elkins, J.W., S.C. Wofsy, M.B. McElroy, C.E. Kolb, and W.A. Kaplan (1978): Aquatic sources and sinks for nitrous oxide, *Nature*, **275**, 602-606.

Esler, M.B., D.W.T. Griffith, F. Turatti, S.R. Wilson, T. Rahn, and H. Zhang (2000): N_2O concentration and flux measurements and complete isotopic analysis by FTIR spectroscopy, *Chemosphere: Global Change Sci.*, **2**, 445-454.

Estupiñán, E.G., R.E. Stickel, J.M. Nicovich, and P.H. Wine (2002): Investigation of N_2O production from 266 and 532 nm laser flash photolysis of $O_3/N_2/O_2$, *J. Phys. Chem. A*, **106** (24), 5880-5890.

Estupiñán, E.G., R.E. Stickel, and P.H. Wine (2000): Is quenching of electronically excited NO_2 by N_2 an important atmospheric source of N_2O?, *Chemosphere: Global Change Sci.*, **2**, 247-253.

Etheridge, D.M., L.P. Steele, R.L. Langenfelds, R.J. Francey, J.M. Barnola, and V.I. Morgan (1996): Natural and anthropogenic changes in atmospheric CO_2 over the last 1000 years from air in Antarctic ice and firn, *J. Geophys. Res.*, **101** (D2), 4115-4128.

Firestone, M.K., and E.A. Davidson (1989): Microbiological basis of NO and N_2O production and consumption in soil, in *Exchange of Trace Gases between Terrestrial Ecosystems and the Atmosphere*, edited by M.O. Andreae, and D.S. Schimel, pp. 7-21, John Wiley & Sons, Ltd., Berlin-Dahlem, Germany.

Flückiger, J., A. Dällenbach, T. Blunier, B. Stauffer, T.F. Stocker, D. Raynaud, and J.-M. Barnola (1999): Variations in atmospheric N_2O concentration during abrupt climatic changes, *Science*, **285**, 227-230.

Flückiger, J., E. Monnin, B. Stauffer, J. Schwander, T.F. Stocker, J. Chappellaz, D. Raynaud, and J.-M. Barnola (2002): High-resolution Holocene N_2O ice core record and its relationship with CH_4 and CO_2, *Global Biogeochem. Cycles*, **16** (1), 8.

Friedman, L., and J. Bigeleisen (1950): Oxygen and nitrogen isotope effects in the decomposition of ammonium nitrate, *J. Chem. Phys.*, **18** (10), 1325-1331.

Fritz, P., and J.C. Fontes (1980): *Handbook of Environmental Isotope Geochemistry: The Terrestrial Environment, A*, 545 pp., Elsevier Scientific Publishing Company, Amsterdam.

Froideveaux, L., and Y.L. Yung (1982): Radiation and chemistry in the stratosphere: Sensitivity to O_2 absorption cross sections in the Herzberg continuum, *Geophys. Res. Lett.*, **9** (8), 854-857.

Frolking, S.E., A.R. Mosier, D.S. Ojima, C. Li, W.J. Parton, C.S. Potter, E. Priesack, R. Stenger, C. Haberbosch, P. Dörsch, H. Flessa, and K.A. Smith (1998): Comparison of N_2O emissions from soils at three temperate agricultural sites: simulations of year-round measurements by four models, *Nutr. Cycl. Agroecosyst.*, **52**, 77-105.

Fujii, T., T. Yamamoto, J. Inagawa, K. Watanabe, and K. Nishizawa (1998): Influences of nuclear size and shape and nuclear spin on chemical isotope effect of zirconium-crown complex, *Ber. Bunsen-Ges. Phys. Chem.*, **102** (4), 663-669.

Gao, Y.Q., and R.A. Marcus (2001): Strange and unconventional isotope effects in ozone formation, *Science*, **293**, 259-263.

Glickman, M.H., S. Cliff, M. Thiemens, and J.P. Klinman (1997): Comparative study of ^{17}O and ^{18}O isotope effects as a probe for dioxygen activation: Application to the soybean lipoxygenase reaction, *J. Am. Chem. Soc.*, **119** (47), 11357-11361.

Gonfiantini, R. (1978): Standards for stable isotope measurements in natural compounds, *Nature*, **271**, 534-536.

González, M., R. Valero, J.M. Anglada, and R. Sayós (2001): *Ab initio* $^1A'$ ground potential energy surface and transition state theory kinetics study of the $O(^1D)+N_2O \rightarrow 2NO$, $N_2+O_2(a\ ^1\Delta_g)$ reactions, *J. Chem. Phys.*, **115** (15), 7015-7031.

Griffith, D.W.T., G.C. Toon, B. Sen, J.-F. Blavier, and R.A. Toth (2000): Vertical profiles of nitrous oxide isotopomer fractionation measured in the stratosphere, *Geophys. Res. Lett.*, **27** (16), 2485-2488.

Güllük, T., F. Slemr, and B. Stauffer (1998): Simultaneous measurements of CO_2, CH_4, and N_2O in air extracted by sublimation from Antarctic ice cores: Confirmation of the data obtained using other extraction techniques, *J. Geophys. Res.*, **103** (D13), 15971-15978.

Hall, S.J., and P.A. Matson (1999): Nitrogen oxide emissions after nitrogen additions in tropical forests, *Nature*, **400** (6740), 152-155.

Hathorn, B.C., and R.A. Marcus (1999): An intramolecular theory of the mass-independent isotope effect for ozone. I., *J. Chem. Phys.*, **111** (9), 4087-4100.

Hathorn, B.C., and R.A. Marcus (2000): An intramolecular theory of the mass-independent isotope effect for ozone. II. Numerical implementation at low pressures using a loose transition state, *J. Chem. Phys.*, **113** (21), 9497-9509.

Heidner III, R.F., and D. Husain (1974): A study of the collisional quenching of $O(2^1D_2)$ by the noble gases employing time-resolved attenuation of atomic resonance radiation in the vacuum ultraviolet, *Int. J. Chem. Kinet.*, **6**, 77-87.

Hoefs, J. (1997): *Stable Isotope Geochemistry*, 201 pp., Springer-Verlag, Berlin.

Holton, J.R. (1990): On the global exchange of mass between stratosphere and troposphere, *J. Atmos. Sci.*, **47** (3), 392-395.

Houghton, J.T., L.G. Meira Filho, J. Bruce, H. Lee, B.A. Callander, E. Haites, N. Harris, and K. Maskell (1994): *Climate Change 1994: Radiative Forcing of Climate Change and an Evaluation of the IPCC IS 92 Emission Scenarios*, Cambridge University Press, Cambridge, UK.

Hut, G. (1987): *Consultants' Group Meeting on stable isotope reference samples for geochemical and hydrological investigations*, 42 pp., IAEA, Vienna.

IAEA (1995): *Reference and intercomparison materials for stable isotopes of light elements*, 165 pp., International Atomic Energy Agency, Vienna.

Inoue, H., Y., and W.G. Mook (1994): Equilibrium and kinetic nitrogen and oxygen isotope fractionations between dissolved and gaseous N_2O, *Chemical Geology (Isotope Geoscience Section)*, **113**, 135-148.

Jancso, G., and W.A. van Hook (1974): Condensed phase isotope effects (especially vapor pressure isotope effects), *Chem. Rev.*, **74** (6), 689-750.

Johnson, M.S., G.D. Billing, A. Gruodis, and M.H.M. Janssen (2001): Photolysis of nitrous oxide isotopomers studied by time-dependent Hermite propagation, *J. Phys. Chem. A*, **105** (38), 8672-8680.

Johnston, J.C., S.S. Cliff, and M.H. Thiemens (1995): Measurement of multioxygen isotopic ($\delta^{18}O$ and $\delta^{17}O$) fractionation factors in the stratospheric sink reactions of nitrous oxide, *J. Geophys. Res.*, **100** (D8), 16801-16804.

Johnston, J.C., and M.H. Thiemens (1997): The isotopic composition of tropospheric ozone in three environments, *J. Geophys. Res.*, **102** (D21), 25395-25404.

Junk, G., and H.J. Svec (1958): The absolute abundance of the nitrogen isotopes in the atmosphere and compressed gas from various sources, *Geochim. Cosmochim. Acta*, **14**, 234-243.

Kaiser, J., C.A.M. Brenninkmeijer, and T. Röckmann (2002a): Intramolecular ^{15}N and ^{18}O fractionation in the reaction of N_2O with $O(^1D)$ and its implications for the stratospheric N_2O isotope signature, *J. Geophys. Res.*, **107** (D14), 4214, doi: 10.1029/2001JD001506.

Kaiser, J., T. Röckmann, and C.A.M. Brenninkmeijer (2002b): Temperature dependence of isotope fractionation in N_2O photolysis, *Phys. Chem. Chem. Phys.*, **4** (18), 10.1039/B204837J, 4220-4230.

Kaiser, J., T. Röckmann, C. Brühl, and C.A.M. Brenninkmeijer (2001): Isotopic enrichment in stratospheric N_2O: 2-D model results linked to laboratory measurements of N_2O photochemistry, *Geophys. Res. Abs.*, **3**, 5784.

Kaye, J.A. (1987): Mechanisms and observations for isotope fractionation of molecular species in planetary atmospheres, *Rev. Geophys.*, **25** (8), 1609-1658.

Keeling, R.F. (1995): The atmospheric oxygen cycle: The oxygen isotopes of atmospheric CO_2 and O_2 and the O_2/N_2 ratio, *Rev. Geophys.*, **33** (Supplement), 1253-1262.

Kim, K.-R., and H. Craig (1990): Two-isotope characterization of nitrous oxide in the Pacific Ocean and constraints on its origin in deep water, *Nature*, **347** (6288), 58-61.

Kim, K.-R., and H. Craig (1993): Nitrogen-15 and oxygen-18 characteristics of nitrous oxide: A global perspective, *Science*, **262** (5141), 1855-1857.

Kim, K.-R., F. Joos, M. Keller, P. Matson, and H. Craig (2000): Balancing the N_2O (nitrous oxide) budgets: Constraints from two-isotope characterization, in *Non-CO_2 Greenhouse Gases: Scientific Understanding, Control and Implementation*, edited by J. van Ham, A.P.M. Baede, L.A. Meyer, and R. Ybema, pp. 179-184, Kluwer Academic Publishers, Noordwijkerhout, The Netherlands.

Kim, S.-T., and J.R. O'Neil (1997): Equilibrium and nonequilibrium oxygen isotope effects in synthetic carbonates, *Geochim. et Cosmochim. Acta*, **61** (16), 3461-3475.

Kohlmann, J.-P., and D. Poppe (1999): The tropospheric gas-phase degradation of NH_3 and its impact on the formation of N_2O and NO_x, *J. Atmos. Chem.*, **32**, 397-415.

Krankowsky, D., F. Bartecki, G.G. Klees, K. Mauersberger, K. Schellenbach, and J. Stehr (1995): Measurement of heavy isotope enrichtment in tropospheric ozone, *Geophys. Res. Lett.*, **22** (13), 1713-1716.

Krankowsky, D., P. Lämmerzahl, and K. Mauersberger (2000): Isotopic measurements of stratospheric ozone, *Geophys. Res. Lett.*, **27** (17), 2593-2595.

Kroeze, C., A. Mosier, and L. Bouwman (1999): Closing the N_2O budget: A retrospective analysis 1500-1994, *Global Biogeochem. Cycles*, **13** (1), 1-8.

Kroopnick, P., and H. Craig (1972): Atmospheric oxygen: Isotopic composition and solubility fractionation, *Science*, **175**, 54-55.

Lämmerzahl, P., T. Röckmann, C.A.M. Brenninkmeijer, D. Krankowsky, and K. Mauersberger (2002): Oxygen isotope composition of stratospheric carbon dioxide, *Geophys. Res. Lett.*, **29** (12), 10.1029/2001GL014343.

Lanzendorf, E.J., T.F. Hanisco, N.M. Donahue, and P.O. Wennberg (1997): Comment on: "The measurement of tropospheric OH radicals by laser-induced fluorescence spectroscopy during the POPCORN field campaign" by Hofzumahaus *et al.* and "Intercomparison of tropospheric OH radical measurements by multiple folded long-path laser absorption and laser induced fluorescence" by Brauers *et al.*, *Geophys. Res. Lett.*, **24** (23), 3037-3038.

Łapiński, A., J. Spanget-Larsen, J. Waluk, and J.G. Radziszewski (2001): Vibrations of nitrous oxide: Matrix isolation Fourier transform infrared spectroscopy of twelve N_2O isotopomers, *J. Chem. Phys.*, **115** (4), 1757-1764.

Laurent, T., P.D. Naik, H.-R. Volpp, J. Wolfrum, T. Arusi-Parpar, I. Bar, and S. Rosenwaks (1995): Absolute rate constants, reactive cross-sections and isotopic branching ratio for the reaction of $O(^1D)$ with HD, *Chem. Phys. Lett.*, **236**, 343-349.

Lee, C.C.-W., and M.H. Thiemens (2001): The $\delta^{17}O$ and δ^{18O} measurements of atmospheric sulfate from a coastal and high alpine region: A mass-independent isotopic anomaly, *J. Geophys. Res.*, **106** (D15), 17359-17373.

Leuenberger, M., P. Nyfeler, H.P. Moret, P. Sturm, and C. Huber (2000): A new gas inlet system for an isotope ratio mass spectrometer improves reproducibility, *Rapid Commun. Mass Spectrom.*, **14**, 1543-1551.

Li, W.J., and H.A.J. Meijer (1998): The use of electrolysis for accurate $\delta^{17}O$ and $\delta^{18}O$ isotope measurements in water, *Isotopes Environ. Health Stud.*, **34**, 349-369.

Li, W.-J., B. Ni, D. Jin, and T.-L. Chang (1988): Measurement of the absolute abundance of oxygen-17 in V-SMOW, *Chin. Sci. Bull.*, **33** (19), 1610-1613.

Lide, D.R. (1999): *CRC Handbook of Chemistry Physics*, CRC Press, Boca Raton.

Lindholm, N., and J.F. Hershberger (1997): Product branching ratios of the $NH_2(X^2B_1) + NO_2$ reaction, *J. Phys. Chem. A*, **101** (27), 4991-4995.

Luz, B., E. Barkan, M.L. Bender, M.H. Thiemens, and K.A. Boering (1999): Triple-isotope composition of atmospheric oxygen as a tracer of biosphere productivity, *Nature*, **400**, 547-550.

Machida, T., T. Nakazawa, Y. Fujii, S. Aoki, and O. Watanabe (1995): Increase in the atmospheric nitrous oxide concentration during the last 250 years, *Geophys. Res. Lett.*, **22** (21), 2921-2924.

Mak, J.E., and C.A.M. Brenninkmeijer (1994): Compressed-air sample technology for isotopic analysis of atmospheric carbon monoxide, *J. Atmos. Ocean. Technol.*, **11** (2), 425-431.

Mandernack, K.M., T. Rahn, and M. Wahlen (1998): The d15N and d18O of N2O produced by pure cultures of methanotrophic bacteria, in *AGU Spring Meeting*, edited by AGU, AGU, San Francisco.

Manning, M.R. (1999): Characteristic modes of isotopic variations in atmospheric chemistry, *Geophys. Res. Lett.*, **26** (9), 1263-1266.

Marić, D., J.P. Burrows, and G.K. Moortgat (1992): A study of the formation of N_2O in the reaction of $NO_3(A^2E')$ with N_2, *J. Atmos. Chem.*, **15**, 157-169.

Mariotti, A. (1983): Atmospheric nitrogen is a reliable standard for natural ^{15}N abundance measurements, *Nature*, **303**, 685-687.

Mariotti, A. (1984): Natural ^{15}N abundance measurements and atmospheric nitrogen standard calibration, *Nature*, **311**, 251-252.

Mariotti, A., J.C. Germon, P. Hubert, P. Kaiser, R. Letolle, A. Tardieux, and P. Tardieux (1981): Experimental determination of nitrogen kinetic isotope fractionation some principles; illustration for the denitrification and nitrification processes, *Plant Soil*, **62**, 413-430.

Mariotti, A., J.C. Germon, and A. Leclerc (1982): Nitrogen isotope fractionation associated with the $NO_2^- \rightarrow N_2O$ step of denitrification in soils, *Can J Soil Sci*, **62** (2), 227-241.

Matson, P.A., and P.M. Vitousek (1990): Ecosystem approach to global nitrous oxide budget, *Bioscience*, **40** (9), 667-672.

Matson, P.A., P.M. Vitousek, G.P. Livingston, and N.A. Swanberg (1990): Sources of variation in nitrous oxide flux from Amazonian ecosystems, *J. Geophys. Res.*, **95** (D10), 16789-16798.

Matsuhisa, Y., J.R. Goldsmith, and R.N. Clayton (1978): Mechanisms of hydrothermal crystallization of quartz at 250 °C and 15 kbar, *Geochimica and Cosmochimica Acta*, **42**, 173-182.

Matsumi, Y., and A.M.S. Chowdhury (1996): Translational relaxation and electronic quenching of hot $O(^1D)$ by collisions with N_2, *J. Chem. Phys.*, **104** (18), 7036-7044.

Matsumi, Y., S.M. Shamsuddin, Y. Sato, and M. Kawasaki (1994): Velocity relaxation of hot $O(^1D)$ atoms by collisions with rare gases, N_2, and O_2, *J. Chem. Phys.*, **101** (11), 9610-9618.

Matsuta, H., and K. Hirokawa (1986): SERS observation of the effects of pressure and water on the adsorbed state of nitrogen dioxide on a silver powder surface, *Surf. Sci.*, **172**, L555-L560.

Mauersberger, K. (1987): Ozone isotope measurements in the stratosphere, *Geophys. Res. Lett.*, **14** (1), 80-83.

McElroy, M.B., and D.B.A. Jones (1996): Evidence for an additional source of atmospheric N_2O, *Global Biogeochem. Cycles*, **10** (4), 651-659.

Mérienne, M.F., B. Coquart, and A. Jenouvrier (1990): Temperature effect on the ultraviolet absorption of $CFCl_3$, CF_2Cl_2, and N_2O, *Planet. Space Sci.*, **38** (5), 617-625.

Meunier, H., P. Pagsberg, and A. Sillesen (1996): Kinetics and branching ratios of the reactions $NH_2 + NO_2 \rightarrow N_2O + H_2O$ and $NH_2 + NO_2 \rightarrow H_2NO + NO$ studied by pulse radiolysis combined with time-resolved infrared diode laser spectroscopy, *Chem. Phys. Lett.*, **261**, 277-282.

Michalski, G., L. Hernandez, T. Meixner, M. Fenn, and M.H. Thiemens (2001): Tracing nitrate deposition using $\Delta^{17}O$, *Eos Transactions AGU, Fall Meeting Supplement*, **82** (47), Abstract H11D-0256.

Miller, C.E., and Y.L. Yung (2000): Photo-induced isotopic fractionation of stratospheric N_2O, *Chemosphere: Global Change Sci.*, **2**, 255-266.

Miller, M.F. (2002): Isotopic fractionation and quantification of ^{17}O anomalies in the oxygen three-isotope system: an appraisal and geochemical significance, *Geochim. et Cosmochim. Acta*, **66** (11), 1881-1889.

Minschwaner, K., G.P. Anderson, L.A. Hall, and K. Yoshino (1992): Polynomial coefficients for calculating O_2 Schumann-Runge cross sections at 0.5 cm^{-1} resolution, *J. Geophys. Res.*, **97** (D9), 10103-10108.

Minschwaner, K., R.J. Salawitch, and M.B. McElroy (1993): Absorption of solar radiation by O_2: Implications for O_3 and lifetimes of N_2O, $CFCl_3$, and CF_2Cl_2, *J. Geophys. Res.*, **98** (D6), 10543-10561.

Mook, W.G. (2000): *Environmental isotopes in the hydrological cycle: Principles and applications*, 280 pp., **1**, UNESCO, Paris.

Mook, W.G., and S. van der Hoek (1983): The N_2O correction in the carbon and oxygen isotopic analysis of atmospheric CO_2, *Isot. Geosci.*, **1**, 237-242.

Moore, H. (1974): Isotopic measurement of atmospheric nitrogen compounds, *Tellus*, **26** (1/2), 169-174.

Mosier, A., C. Kroeze, C. Nevison, O. Oenema, S. Seitzinger, and O. van Cleemput (1998): Closing the global N_2O budget: nitrous oxide emissions through the agricultural nitrogen cycle, *Nutr. Cycl. Agroecosyst.*, **52**, 225-248.

Mroz, E.J., M. Alei, J.H. Cappis, P.R. Guthals, A.S. Mason, and D.J. Rokop (1989): Detection of multiply deuterated methane in the atmosphere, *Geophys. Res. Lett.*, **16** (7), 677-678.

Müller, P. (1994): Glossary of terms used in physical organic chemistry, *Pure Appl. Chem.*, **66**, 1077-1184.

Murray, J.E., K. Yoshino, J.R. Esmond, W.H. Parkinson, Y. Sun, A. Dalgarno, A.P. Thorne, and G. Cox (1994): Vacuum ultraviolet Fourier transform spectroscopy of the $\delta(0,0)$ and $\beta(7,0)$ bands of NO, *J. Chem. Phys.*, **101** (1), 62-73.

Muzio, L.J., and J.C. Kramlich (1988): An artifact in the measurement of N_2O from combustion sources, *Geophys. Res. Lett.*, **15** (12), 1369-1372.

Nakicenovic, N., J. Alcamo, G. Davis, B.d. Vries, J. Fenhann, S. Gaffin, K. Gregory, A. Grübler, T.Y. Jung, T. Kram, E.L.L. Rovere, L. Michaelis, S. Mori, T. Morita, W. Pepper, H. Pitcher, L. Price, K. Riahi, R.A. Roehrl, H.-H. Rogner, A. Sankovski, M. Schlesinger, P. Shukla, S. Smith, R. Swart, S.v. Rooijen, N. Victor, and Z. Dadi (2000): *IPCC Special Report on Emission Scenarios*, 599 pp., Cambridge University Press, Cambridge, UK.

Nevison, C., and E. Holland (1997): A reexamination of the impact of antropogenically fixed nitrogen on atmospheric N_2O and the stratospheric O_3 layer, *J. Geophys. Res.*, **102** (D21), 25519-25535.

Newton, A.S., and A.F. Sciamanna (1970a): Metastable peaks in the mass spectra of N_2O and NO_2, *J. Chem. Phys.*, **44** (11), 4327-4332.

Newton, A.S., and A.F. Sciamanna (1970b): Metastable peaks in the mass spectra of N_2O and NO_2, II, *J. Chem. Phys.*, **52** (1), 327-336.

Nørgaard, J.V., H. Kipphardt, S. Valkiers, and P.D.P. Taylor (1999): *IMEP-8: Carbon and oxygen isotope ratios in CO_2*, 46 pp., Institute for Reference Materials and Measurements, Geel.

Olivier, J.G.J., A.F. Bouwman, K.W. van der Hoek, and J.J.M. Berdowski (1998): Global air emission inventories for anthropogenic sources of NO_x, NH_3 and N_2O in 1990, *Environ. Pollut.*, **102** (S1), 135-148.

Park, J., and M.C. Lin (1996): Mass-spectrometric determination of product branching probabilities for the $NH_2 + NO_2$ reaction at temperatures between 300 and 990 K, *Int. J. Chem. Kinet.*, **28**, 879-883.

Park, J., and M.C. Lin (1997): A mass spectrometric study of the $NH_2 + NO_2$ reaction, *J. Phys. Chem. A*, **101** (14), 2643-2647.

Pérez, T., S.E. Trumbore, S.C. Tyler, E.A. Davidson, M. Keller, and P.B. De Camargo (2000): Isotopic variability of N_2O emissions from tropical forest soils, *Global Biogeochem. Cycles*, **14** (2), 525-535.

Pérez, T., S.E. Trumbore, S.C. Tyler, P.A. Matson, I. Ortiz-Monasterio, T. Rahn, and D.W.T. Griffith (2001): Identifying the agricultural imprint on the global N_2O budget using stable isotopes, *J. Geophys. Res.*, **106** (D9), 9869-9878.

Prasad, S.S. (1997): Potential atmospheric sources and sinks of nitrous oxide: 2. Possibilities from excited O_2, "embryonic" O_3, and optically pumped excited O_3, *J. Geophys. Res.*, **102** (D17), 21527-21536.

Prasad, S.S., and E.C. Zipf (2000): Atmospheric production of nitrous oxide from excited ozone and its significance, *Chemosphere: Global Change Sci.*, **2**, 235-245.

Prather, M., R. Derwent, D. Ehhalt, P. Fraser, E. Sanhueza, and X. Zhou (1995): Radiative forcing of climate change - Other trace gases and atmospheric chemistry, in *Climate Change 1995 - The Science of Climate Change*, edited by J.T. Houghton, L.G. Meira Filho, B.A. Callander, N. Harris, A. Kattenberg, and K. Maskell, pp. 86-103, Cambridge University Press, Cambridge.

Prather, M., D. Ehhalt, F. Dentener, R. Derwent, E. Dlugokencky, E. Holland, I. Isaksen, J. Katima, V. Kirchhoff, P. Matson, P. Midgley, and M. Wang (2001): Atmospheric chemistry and greenhouse gases, in *Climate Change 2001: The Scientific Basis: Contribution of Working Group I to the Third Assessment Report of the Intergovernmental Panel of Climate Change*, edited by J.T. Houghton, Y. Ding, D.J. Griggs, M. Noguer, P.J. van der Linden, X. Dai, K. Maskell, and C.A. Johnson, pp. 239-287, Cambridge University Press, Cambridge, United Kingdom and New York, NY, USA.

Prather, M.J. (1998): Time scales in atmospheric chemistry: Coupled perturbations to N_2O, NO_y, and O_3, *Science*, **279**, 1339-1341.

Prinn, R.G., R.F. Weiss, P.J. Fraser, P.G. Simmonds, D.M. Cunnold, F.N. Alyea, S. O'Doherty, P. Salameh, B.R. Miller, J. Huang, R.H.J. Wang, D.E. Hartley, C. Harth, L.P. Steele, G. Sturrock, P.M. Midgley, and A. McCulloch (2000): A history of chemically and radiatively important gases in air deduced from ALE/GAGE/AGAGE, *J. Geophys. Res.*, **105** (D14), 17751-17792.

Rahn, T., and M. Wahlen (1997): Stable isotope enrichment in stratospheric nitrous oxide, *Science*, **278** (5344), 1776-1778.

Rahn, T., and M. Wahlen (2000): A reassessment of the global isotopic budget of atmospheric nitrous oxide, *Global Biogeochem. Cycles*, **14** (2), 537-543.

Rahn, T., H. Zhang, M. Wahlen, and G.A. Blake (1998): Stable isotope fractionation during ultraviolet photolysis of N_2O, *Geophys. Res. Lett.*, **25** (24), 4489-4492.

Ramaswamy, V., O. Boucher, J. Haigh, D. Hauglustaine, J. Haywood, G. Myhre, T. Nakajima, G.Y. Shi, and S. Solomon (2001): Radiative forcing of climate change, in *Climate Change 2001: The Scientific Basis: Contribution of Working Group I to the Third Assessment Report of the Intergovernmental Panel of Climate Change*, edited by J.T. Houghton, Y. Ding, D.J. Griggs, M. Noguer, P.J. van der Linden, X. Dai, K. Maskell, and C.A. Johnson, pp. 349-416, Cambridge University Press, Cambridge, United Kingdom and New York, NY, USA.

Randeniya, L.K., P.F. Vohralik, and I.C. Plumb (2002): Stratospheric ozone depletion at northern mid latitudes in the 21st century: The importance of future concentrations of greenhouse gases nitrous oxide and methane, *Geophys. Res. Lett.*, **29** (4), 4.

Rayleigh, J.W.S. (1896): Theoretical considerations respecting the separation of gases by diffusion and similar processes, *Philos. Mag.*, **S. 5, Vol. 42**, 493-498.

Reader, J., C.J. Sansonetti, and J.M. Bridges (1996): Irradiances of spectral lines in mercury pencil lamps, *Appl. Opt.*, **35** (1), 78-83.

Redlich, O. (1935): Eine allgemeine Beziehung zwischen den Schwingungsfrequenzen isotoper Molekeln (nebst Bemerkungen über die Berechnung harmonischer Kraftkonstanten), *Zeitschrift für Physikalische Chemie B*, **28** (5), 371-382.

Richet, P., Y. Bottinga, and M. Javoy (1977): A review of hydrogen, carbon, nitrogen, oxygen, sulphur, and chlorine stable isotope fractionation among gaseous molecules, *Ann. Rev. Earth Planet. Sci.*, **5**, 65-110.

Röckmann, T.(1998): Measurement and interpretation of ^{13}C, ^{14}C, ^{17}O and ^{18}O variation in atmospheric carbon monoxide, Ph. D. thesis, Ruprecht-Karls-Universität Heidelberg, Heidelberg.

Röckmann, T., C.A.M. Brenninkmeijer, P. Neeb, and P.J. Crutzen (1998a): Ozonolysis of nonmethane hydrocarbons as a source of the observed mass independent oxygen isotope enrichment in tropospheric CO, *J. Geophys. Res.*, **103** (D1), 1463-1470.

Röckmann, T., C.A.M. Brenninkmeijer, G. Saueressig, P. Bergamaschi, J.N. Crowley, H. Fischer, and P.J. Crutzen (1998b): Mass-independent oxygen isotope fractionation in atmospheric CO as a result of the reaction CO + OH, *Science*, **281** (5376), 544-546.

Röckmann, T., C.A.M. Brenninkmeijer, M. Wollenhaupt, J.N. Crowley, and P.J. Crutzen (2000): Measurement of the isotopic fractionation of $^{15}N^{14}N^{16}O$, $^{14}N^{15}N^{16}O$ and $^{14}N^{14}N^{18}O$ in the UV photolysis of nitrous oxide, *Geophys. Res. Lett.*, **27** (9), 1399-1402.

Röckmann, T., J. Kaiser, C.A.M. Brenninkmeijer, J.N. Crowley, R. Borchers, W.A. Brand, and P.J. Crutzen (2001): The isotopic enrichment of nitrous oxide ($^{15}N^{14}NO$, $^{14}N^{15}NO$, $^{14}N^{14}N^{18}O$) in the stratosphere and in the laboratory, *Journal of Geophysical Research*, **106** (D10), 10403-10410.

Rommelaere, V., L. Arnaud, and J.-M. Barnola (1997): Reconstructing recent atmospheric trace gas concentrations from polar firn and bubbly ice data by inverse methods, *J. Geophys. Res.*, **102** (D25), 30069-30083.

Rothman, L.S., C.P. Rinsland, A. Goldman, S.T. Massie, D.P. Edwards, J.-M. Flaud, A. Perrin, C. Camy-Peyret, V. Dana, J.-Y. Mandin, J. Schroeder, A. McCann, R.R. Gamache, R.B. Wattson, K. Yoshino, K.V. Chance, K.W. Jucks, L.R. Brown, V. Nemtchinov, and P. Varanasi (1998): The HITRAN molecular spectroscopic database and HAWKS (HITRAN Atmospheric Workstation): 1996 Edition, *Journal of Quantitative Spectroscopy and Radiative Transfer*, **60** (5), 665-710.

Ryden, J.C. (1981): N_2O exchange between a grassland and the atmosphere, *Nature*, **292**, 235-237.

Saito, T., and S. Ito (1998): Gas contaminant effect in a discharge-excited ArF excimer laser, *Applied Physics B-Lasers and Optics*, **66** (5), 579-583.

Sansonetti, C.J., M.L. Salit, and J. Reader (1996): Wavelengths of spectral lines in mercury pencil lamps, *Appl. Opt.*, **35** (1), 74-77.

Saueressig, G.(1999): Bestimmung von kinetischen Isotopentrennfaktoren in den atmosphärischen Methanabbaureaktionen, Ph. D. thesis, Johannes-Gutenberg-Universität, Mainz.

Savarino, J., and M.H. Thiemens (1999a): Analytical procedure to determine both $\delta^{18}O$ and $\delta^{17}O$ of H_2O_2 in natural water and first measurements, *Atmos. Environ.*, **33** (22), 3683-3690.

Savarino, J., and M.H. Thiemens (1999b): Mass-independent oxygen isotope (^{16}O, ^{17}O, ^{18}O) fractionation found in H_x, O_x reactions, *J. Phys. Chem. A*, **103**, 9221-9229.

Schütze, M. (1940): Ein neues Verfahren zur direkten Sauerstoffbestimmung in organischen Substanzen, *Z. Anal. Chem.*, **118** (7/8), 245-258.

Schwander, J., B. Stauffer, and A. Sigg (1988): Air mixing in firn and the age of the air at pore close-off, *Ann. Glaciol.*, **10**, 141-145.

Selwyn, G., J. Podolske, and H.S. Johnston (1977): Nitrous oxide ultraviolet absorption spectrum at stratospheric temperatures, *Geophys. Res. Lett.*, **4** (10), 427-430.

Selwyn, G.S.(1974): The ultraviolet spectroscopy of nitrous oxide (N_2O), Dissertation thesis, University of California, Berkeley.

Selwyn, G.S., and H.S. Johnston (1981): Ultraviolet absorption spectrum of nitrous oxide as function of temperature and isotopic substitution, *J. Chem. Phys.*, **74** (7), 3791-3803.

Severinghaus, J.P., A. Grachev, and M. Battle (2001): Thermal fractionation of air in polar firn by seasonal temperature gradients, *Geochem Geophy Geosy*, **2**, U1-U24.

Siemens, W.v. (1857): Über die elektrostatische Induktion und die Verzögerung des Stroms in Flaschendrähten, *Ann. Phys. Chem.*, **102**, 66-122.

Simonaitis, R., R.I. Greenberg, and J. Heicklen (1972): The photolysis of N_2O at 2139 Å and 1849 Å, *Int. J. Chem. Kinet.*, **4**, 497-512.

Smith, I.W.M. (1995): Neutral/neutral reactions without barriers: comparisons with ion/molecule systems and their possible role in the chemistry of interstellar clouds, *Int. J. Mass Spectrom. Ion Processes*, **149-150**, 231-249.

Sowers, T., A. Rodebaugh, N. Yoshida, and S. Toyoda (2001): Extending records of the isotopic composition of atmospheric N_2O back to 1900 A. D. from air trapped in snow at South Pole, in *Proceedings of 1st International Symposium on Isotopomers, 23-26 July 2001*, Yokohama, Japan.

Stevens, R.J., R.J. Laughlin, G.J. Atkins, and S.J. Prosser (1993): Automated determination of nitrogen-15-labeled dinitrogen and nitrous oxide by mass spectrometry, *Soil Sci. Soc. Am. J.*, **57** (4), 981-988.

Stuhl, F., and H. Niki (1971): Measurements of rate constants for termolecular reactions of $O(^3P)$ with NO, O_2, CO, N_2, and CO_2 using a pulsed vacuum-uv photolysis-chemiluminescent method, *J. Chem. Phys.*, **55** (8), 3943-3953.

Sun, F., G.P. Glass, and R.F. Curl (2001): The photolysis of NO_2 at 193 nm, *Chem. Phys. Lett.*, **337** (1-3), 72-78.

Tanaka, N., D.M. Rye, R. Rye, H. Avak, and T. Yoshinari (1995): High precision mass spectrometric analysis of isotopic abundance ratios in nitrous oxide by direct injection of N_2O, *Int. J. Mass Spectrom. Ion Processes*, **142** (3), 163-175.

Tans, P.P. (1997): A note on isotopic ratios and the global atmospheric methane budget, *Global Biogeochem. Cycles*, **11** (1), 77-81.

Thiemann, M., E. Scheibler, and K.W. Wiegand (1991): Nitric acid, nitrous acid, and nitrogen oxides, in *Ullmann's encyclopedia of industrial chemistry*, edited by B. Elvers, S. Hawkins, and G. Schulz, pp. 293-339, VCH Verlagsgesllschaft, Weinheim.

Thiemens, M.H. (1999): Mass-independent isotope effects in planetary atmospheres and the early solar system, *Science*, **283** (5400), 341-345.

Thiemens, M.H., and J.E. Heidenreich III (1983): The mass-independent fractionation of oxygen: a novel isotope effect and its possible cosmochemical implications, *Science*, **219**, 1073-1075.

Thiemens, M.H., T. Jackson, K. Mauersberger, B. Schueler, and J. Morton (1991): Oxygen isotope fractionation in stratospheric CO_2, *Geophys. Res. Lett.*, **18** (4), 669-672.

Thiemens, M.H., T. Jackson, E.C. Zipf, P.W. Erdman, and C. van Egmond (1995): Carbon dioxide and oxygen isotope anomalies in the mesosphere and stratosphere, *Science*, **270**, 969-972.

Thiemens, M.H., J. Savarino, J. Farquhar, and H. Bao (2001): Mass-independent isotopic compositions in terrestrial and extraterrestrial solids and their applications, *Acc. Chem. Res.*, **34** (8), 645-652.

Tiemann, E., H. Knöckel, and J. Schlembach (1982): Influence of the finite nuclear size on the electronic and rotational energy of diatomic molecules, *Ber. Bunsen-Ges. Phys. Chem.*, **86** (9), 821-824.

Toumi, R. (1993): A potential new source of OH and odd-nitrogen in the atmosphere, *Geophysical Research Letters*, **20** (1), 25-28.

Toyoda, S., and N. Yoshida (1999): Determination of nitrogen isotopomers of nitrous oxide on a modified isotope ratio mass spectrometer, *Anal. Chem.*, **71** (20), 4711-4718.

Toyoda, S., N. Yoshida, T. Suzuki, K. Tsuji, and K. Shibuya (2001a): Isotopomer fractionation during photolysis of nitrous oxide by ultraviolet of 206 to 210 nm, in *International Conference on the Study of Environmental Change Using Isotope Techniques*, edited by IAEA, International Atomic Energy Agency, Vienna, Austria.

Toyoda, S., N. Yoshida, T. Urabe, S. Aoki, T. Nakazawa, S. Sugawara, and H. Honda (2001b): Fractionation of N_2O isotopomers in the stratosphere, *J. Geophys. Res.*, **106** (D7), 7515-7522.

Trenberth, K.E., and C.J. Guillemot (1994): The total mass of the atmosphere, *J. Geophys. Res.*, **99** (D11), 23079-23088.

Trolier, M., J.W.C. White, P.P. Tans, K.A. Masarie, and P.A. Gemery (1996): Monitoring the isotopic composition of atmospheric CO_2: Measurements form the NOAA global air sampling network, *J. Geophys. Res.*, **101** (D20), 258972-5916.

Trudinger, C.M., I.G. Enting, D.M. Etheridge, R.J. Francey, V.A. Levchenko, L.P. Steele, D. Raynaud, and L. Arnaud (1997): Modeling air movement and bubble trapping in firn, *J. Geophys. Res.*, **102** (D6), 6747-6763.

Turatti, F., D.W.T. Griffith, S.R. Wilson, M.B. Esler, T. Rahn, H. Zhang, and G.A. Blake (2000): Positionally dependent ^{15}N fractionation factors in the UV photolysis of N_2O determined by high resolution FTIR spectroscopy, *Geophys. Res. Lett.*, **27** (16), 2489-2492.

Uehara, K., K. Yamamoto, T. Kikugawa, and N. Yoshida (2001): Isotope analysis of environmental substances by a new laser- spectroscopic method utilizing different pathlengths, *Sens. Actuator B-Chem.*, **74** (1-3), 173-178.

Umemoto, H. (1999): $^{14}N/^{15}N$ isotope effect in the UV photodissociation of N_2O, *Chem. Phys. Lett.*, **314**, 267-272.

Urey, H.C. (1947): The thermodynamic properties of isotopic substances, *J. Chem. Soc.*, 562-581.

Wahlen, M., and T. Yoshinari (1985): Oxygen isotope ratios in N_2O from different environments, *Nature*, **313** (6005), 780-782.

Warneck, P. (1999): *Chemistry of the Natural Atmosphere*, 923 pp., Academic Press, San Diego.

Watson, R.T., L.G. Meira Filho, E. Sanhueza, and A. Janetos (1992): Greenhouse gases: Sources and sinks, in *Climate Change: The IPCC Scientific Assessment*, edited by J.T. Houghton, B.A. Callander, and S.K. Varney, pp. 29-46, Cambridge University Press, Cambridge, UK.

Watson, R.T., H. Rodhe, H. Oeschger, and U. Siegenthaler (1990): Greenhouse gases and aerosols, in *Climate Change: The IPCC Scientific Assessment*, edited by J.T. Houghton, G.J. Jenkins, and J.J. Ephraums, pp. 5-40, Cambridge University Press, New York.

Weiss, R.F. (1981): The temporal and spatial distribution of tropospheric nitrous oxide, *J. Geophys. Res.*, **86** (C8), 7185-7195.

Weiss, R.F., and B.A. Price (1980): Nitrous oxide solubility in water and seawater, *Mar. Chem.*, **8**, 347-359.

Well, R., K.-W. Becker, and B. Meyer (1993): Equilibrating of ^{15}N-gases by electrodeless discharge: a method of indirect mass spectrometric analysis of $^{30}N_2$ for denitrification studies in soils, *Isotopenpraxis*, **29** (1/2), 175-180.

Werner, R.A., and W.A. Brand (2001): Referencing strategies and techniques in stable isotope ratio analysis, *Rapid Commun. Mass Spectrom.*, **15**, 501-519.

Weston, R.E., Jr. (1999): Anomalous or mass-independent isotope effects, *Chem. Rev.*, **99** (8), 2115-2136.

White, W.M. (2000): Isotope Geochemistry (Geology 656), http://www.geo.cornell.edu/geology/classes/GEO656.HTML.

Williamson, J.H. (1968): Least-squares fitting of a straight line, *Can. J. Phys.*, **46**, 1845-1847.

Wingen, L.M., and B.J. Finlayson-Pitts (1998): An upper limit on the production of N_2O from the reaction of $O(^1D)$ with CO_2 in the presence of N_2, *Geophys. Res. Lett.*, **25** (4), 517-520.

WMO (1999): *Scientific Assessment of Ozone Depletion: 1998. Global Ozone Research and Monitoring Project*, 732 pp., World Meteorological Organization, Geneva, Switzerland.

Yamulki, S., S. Toyoda, N. Yoshida, E. Veldkamp, B. Grant, and R. Bol (2001): Diurnal fluxes and the isotopomer ratios of N_2O in a temperate grassland following urine amendment, *Rapid Commun. Mass Spectrom.*, **15**, 1263-1269.

York, D. (1966): Least-squares fitting of a straight line, *Can. J. Phys.*, **44** (5), 1079-1086.

Yoshida, N. (1988): ^{15}N-depleted N_2O as a product of nitrification, *Nature*, **335** (6190), 528-9.

Yoshida, N., A. Hattori, T. Saino, S. Matsuo, and E. Wada (1984): $^{15}N/^{14}N$ ratio of dissolved N_2O in the eastern tropical Pacific Ocean, *Nature*, **307**, 442-444.

Yoshida, N., and S. Matsuo (1983): Nitrogen isotope ratio of atmospheric N_2O as a key to the global cycle of N_2O, *Geochem. J.*, **17**, 231-239.

Yoshida, N., H. Morimoto, M. Hirano, I. Koike, S. Matsuo, E. Wada, T. Saino, and A. Hattori (1989): Nitrification rates and ^{15}N abundances of N_2O and NO_3^- in the western North Pacific, *Nature*, **342** (6252), 895-897.

Yoshida, N., and S. Toyoda (2000): Constraining the atmospheric N_2O budget from intramolecular site preference in N_2O isotopomers, *Nature*, **405**, 330-334.

Yoshinari, T. (1990): Emissions of N_2O from various environments - the use of stable isotope composition of N_2O as tracer for the studies of N_2O biogeochemical cycling, in *Denitrification in Soil and Sediment*, edited by N.P. Revsbech, and J. Sørensen, pp. 129-150, Plenum Press, New York.

Yoshinari, T., and M. Wahlen (1985): Oxygen isotope ratios in N_2O nitrification at a wastewater treatment facility, *Nature*, **317** (6035), 349-350.

Yoshino, K., J.R. Esmond, A.S.C. Cheung, D.E. Freeman, and W.H. Parkinson (1992): High-resolution absorption cross-sections in the transmission window region of the Schumann-Runge bands and Herzberg continuum of O_2, *Planet. Space Sci.*, **40** (2-3), 185-192.

Yoshino, K., D.E. Freeman, and W.H. Parkinson (1984): High resolution absorption cross section measurements of N_2O at 295-299 K in the wavelength region 170-222 nm, *Planet. Space Sci.*, **32** (10), 1219-1222.

Young, E.D., A. Galy, and H. Nagahara (2002): Kinetic and equilibrium mass-dependent isotope fractionation laws in nature and their geochemical and cosmochemical significance, *Geochim. Cosmochim. Acta*, **66** (6), 1095-1104.

Yung, Y.L., and C.E. Miller (1997): Isotopic fractionation of stratospheric nitrous oxide, *Science*, **278** (5344), 1778-1780.

Yung, Y.L., W.C. Wang, and A.A. Lacis (1976): Greenhouse effect due to atmospheric nitrous oxide, *Geophys. Res. Lett.*, **3** (10), 619-621.

Zellner, R., D. Hartmann, and I. Rosner (1992): N_2O formation in the reactive collisional quenching of NO_3^* and NO_2^* by N_2, *Ber. Bunsen-Ges. Phys. Chem.*, **96** (3), 385-390.

Zhang, H., P.O. Wennberg, V.H. Wu, and G.A. Blake (2000): Fractionation of $^{14}N^{15}N^{16}O$ and $^{15}N^{14}N^{16}O$ during photolysis at 213 nm, *Geophys. Res. Lett.*, **27** (16), 2481-2484.

Zipf, E.C., and S.S. Prasad (1998): Experimental evidence that excited ozone is a source of nitrous oxide, *Geophys. Res. Lett.*, **25** (23), 4333-4336.

Zyakun, A., and M. Schidlowski (2000): Determination of ^{16}O and ^{18}O abundance ratios in natural carbon dioxide reservoirs, *Int. J. Mass Spectrom.*, **203**, 83-92.

Zyakun, A.M., and C.A.M. Brenninkmeijer (2001): Determination of isotopomers in pools of molecules with polyisotopic content (IAEA-CN-80/74), in *International Conference on the Study of Environmental Change Using Isotope Techniques*, edited by IAEA, International Atomic Energy Agency, Vienna, Austria.

Zyakun, A.M., and M. Schidlowski (1997): Intramolecular $^{16}O/^{18}O$ variation in carbon dioxide: potential for assessment of environmental CO_2 fluxes - A feasibility study, *Int. J. Mass Spectrom. Ion Processes*, **161**, 97-112.